

Study of the Underlying Event in pp collisions with the ALICE detector at the LHC

Sara Vallero
Physikalisches Institut
University of Heidelberg

A thesis submitted for the degree of

Doctor of Natural Sciences

January 2012

Dissertation
submitted to the
Combined Faculties of the Natural Sciences and Mathematics
of the Ruperto-Carola-University of Heidelberg, Germany
for the degree of
Doctor of Natural Sciences

Put forward by
Sara Vallero
born in: *Cirié (TO), Italy*
Oral examination: *January 31, 2012*

Study of the Underlying Event with the ALICE detector in pp collisions at the LHC

Referees:

Prof. Dr. Johanna Stachel

Prof. Dr. Hans-Christian Schultz-Coulon

Alla mia famiglia.

Untersuchung des *Underlying Event* in pp-Kollisionen am LHC mit dem ALICE-Detektor Der überwiegende Teil der in hochenergetischen Kollisionen von Hadronen produzierten Teilchen stammt aus Prozessen mit kleinen Impulsüberträgen. Diese Prozesse entziehen sich einer störungstheoretischen Behandlung und müssen über phänomenologische Modelle beschrieben werden. In dieser Arbeit wird eine Messung des *Underlying Event* (UE) in pp-Kollisionen bei $\sqrt{s} = 0.9$ und 7 TeV am LHC als Funktion der harten Skala präsentiert. Relativ zur Teilchenspur mit dem größten Transversalimpuls (führende Spur bzw. *leading track*) lassen sich in azimuthaler Richtung verschiedene Bereiche definieren: *Toward* (in Richtung des führenden Teilchens), *Transverse* (transversal dazu), *Away* (entgegen der Richtung des führenden Teilchens). Die Untersuchung wird mit geladenen Teilchen oberhalb der folgenden drei p_T -Schwellen durchgeführt: 0.15, 0.5 und 1 GeV/ c . Es wird beobachtet, dass die Aktivität des UE für Transversalimpulse der führenden Teilchenspur oberhalb von 3–4 GeV/ c unabhängig von der harten Skala des Ereignisses ist. Im transversalen Bereich steigt die Teilchenmultiplizität von $\sqrt{s} = 0.9$ GeV zu 7 TeV abhängig von der betrachteten p_T -Schwelle um einen Faktor 2–3 an. Die Daten werden mit den Ereignisgeneratoren PYTHIA 6.4, PYTHIA 8.1 und PHOJET verglichen. Im Mittel unterschätzen diese Modelle die Aktivität des UE um 10–30 %.

Study of the Underlying Event in pp collisions with the ALICE detector at the LHC The bulk of particles produced in a high-energy hadronic collision originates from low-momentum-transfer processes, which are not amenable to a perturbative treatment and need to be modelled phenomenologically. In this thesis we present a measurement of the bulk event-activity or Underlying Event (UE) in pp collisions at $\sqrt{s} = 0.9$ and 7 TeV at the LHC as a function of the hard scale. Different regions are defined with respect to the azimuthal direction of the leading (highest p_T) track: *Toward*, *Transverse* and *Away*. The *Toward* and *Away* regions collect the fragmentation products of the hardest interaction. The *Transverse* region is most sensitive to the UE. The study is performed with charged particles above three different p_T thresholds: 0.15, 0.5 and 1.0 GeV/ c . We observe that for values of the leading-track p_T above 3–4 GeV/ c the bulk particle production becomes independent of the hard scale. In the *Transverse* region the multiplicity increases by a factor 2–3 between the lower and higher collision energies, depending on the p_T threshold considered. Data are compared to PYTHIA 6.4, PYTHIA 8.1 and PHOJET. On average, all models underestimate the UE activity by about 10–30%.

Contents

Preface	1
1 High-energy hadronic collisions	5
1.1 Factorization notions	5
1.2 QCD-improved Parton Model	6
1.2.1 Factorization of the hard cross-section	6
1.2.2 Kinematic variables	7
1.2.3 Jet cross-section	8
1.2.4 Higher order approaches	12
1.2.5 Initial state	13
1.2.6 Hadronization	15
1.3 The Underlying Event	16
1.3.1 Multi-Partonic Interactions	19
1.3.2 Underlying Event modelling	21
1.3.2.1 PHOJET and the Dual Parton Model	21
1.3.2.2 PYTHIA 6.4	23
1.3.2.3 PYTHIA 8.1	27
1.3.2.4 Considerations on PYTHIA tunes	28
2 The ALICE detector at the LHC	31
2.1 The Large Hadron Collider (LHC)	31
2.1.1 Collision parameters	33
2.2 A Large Ion Collider Experiment (ALICE)	34
2.2.1 Detector layout	34
2.2.1.1 Time Projection Chamber (TPC)	37

CONTENTS

2.2.1.2	Inner Tracking System (ITS)	40
2.2.1.3	V0A and V0C	42
2.2.2	Trigger system	43
2.2.3	Off-line framework	45
2.2.4	Performance	47
2.2.4.1	Primary vertex reconstruction	47
2.2.4.2	Track reconstruction	49
3	Transition Radiation Detector and Read-out Board testing	53
3.1	Detector design	54
3.2	Front-end electronics	56
3.2.1	Pre-amplifier and Shaping Amplifier (PASA)	57
3.2.2	Tracking Processor (TRAP)	58
3.2.3	Multi Chip Module (MCM)	58
3.2.4	Read-out Board (ROB)	59
3.3	Read-out Board testing procedure	61
3.3.1	System set-up	62
3.3.2	System software	64
3.3.3	Analog tests	66
3.3.4	Multi Chip Module identification	71
4	The Transverse regions method	77
4.1	Historical overview	77
4.2	Choice of scale	88
4.3	Physics processes	97
5	Measurement of the UE with the ALICE detector	101
5.1	Analysis strategy	101
5.1.1	Settings	101
5.1.2	Analysis flow	103
5.1.3	Software implementation	104
5.2	Data samples	108
5.3	Event and track selection	109
5.3.1	Event selection	109

5.3.1.1	Pile-up and beam-gas events	113
5.3.2	Track selection	115
5.4	Data correction procedure	118
5.4.1	Leading-track misidentification	122
5.4.2	Contamination from secondaries	125
5.4.3	Tracking efficiency	131
5.4.4	Vertex reconstruction	133
5.4.5	Two tracks effects	135
5.5	Systematic uncertainties	135
6	Results	147
6.1	Number density	148
6.2	Summed p_T	149
6.3	Azimuthal correlations	150
6.4	Comparison with ATLAS results	162
6.5	Energy scaling	163
6.6	Conclusions	167
A	Corrections on real data	169
A.1	Number density	170
A.2	Summed p_T	171
A.3	Azimuthal correlations	172
B	Comparison with ATLAS results	175
B.1	ATLAS limited phase-space: $ \eta < 0.8$	176
B.2	ATLAS full phase-space: $ \eta < 2.5$	180
	Acronyms	183
	List of Figures	187
	List of Tables	195
	Bibliography	197

CONTENTS

Preface

In November 2009 the Large Hadron Collider (LHC) at CERN delivered the first stable proton-proton collisions at a center-of-mass energy of 0.9 TeV. Since then, unprecedented interaction energies have been achieved: 2.36 TeV and 7 TeV, compared to the maximum 1.96 TeV provided by the Tevatron collider. Therefore a sound investigation of the TeV energy scale is essential in order to verify and extend the Standard Model (SM) of elementary interactions.

The particles produced in a proton-proton interaction can be classified according to the energy scale of the elementary process involved. At high momentum-transfers ($p_T \gtrsim 2 \text{ GeV}/c$) Quantum ChromoDynamics (QCD) is the appropriate tool to describe partonic scatterings. Quantitative solutions can be calculated with a perturbative approach. On the other hand, the bulk of particle production comes from low-momentum-transfer processes. When Λ_{QCD} is of the order of hundreds of MeV, a perturbative treatment is no longer feasible. Moreover, already at momentum transfers of few GeV/c , the QCD cross-section for an elementary 2-to-2 scattering exceeds the total hadronic cross-section. This observation is usually reconciled in terms of Multi Partonic Interactions (MPI). The bulk event-activity is correlated to the hardest scattering via gluon radiation and MPI. As a consequence, a high-transverse-momentum-transfer hadronic collision cannot simplistically be assimilated to two back-to-back jets plus a minimum bias event. Therefore, the overall event dynamics needs to be modelled and measured with suited observables.

One possible approach is to measure the bulk event-activity as a function of the hard scale, which is the strategy adopted in this PhD research, and it is generally referred to as the Underlying Event (UE) analysis. The UE is defined as

the component of the particle flow in hadronic collisions that does not originate from the hardest partonic-scattering. In our approach the relevant observables to characterize the UE are the number density and the summed p_T of charged particles in a topological region azimuthally perpendicular to the particle with the highest momentum in the event (called the leading particle).

A measurement of the UE is mandatory at LHC because its activity influences any physics measurement implying jet reconstruction or isolation cuts. It is also worth noticing that the UE observables are a powerful tool to constrain phenomenological models of hadronic collisions (i.e. tuning of Monte Carlo generators).

The outline of this thesis is the following: in Chapter 1 we introduce the theoretical concepts motivating the UE analysis. We summarize the main ideas of the QCD-improved parton model and give an experimental definition of the UE. Moreover, we describe the Monte Carlo models with which we compare our measurement. Chapter 2 describes the ALICE detector, used for the measurement presented in this thesis. Chapter 3 is not related to the UE analysis. It describes one of the ALICE sub-systems, the Transition Radiation Detector (TRD), and one step of the testing procedure of its read-out electronics. The reason is that part of this thesis was dedicated to the upgrade of this testing procedure. In Chapter 4 we give an overview of the historical measurements of the UE. Moreover, we show the results of a preliminary study based on reconstructed jets with which we illustrate the effects of different scale choices on the final UE observables. Finally, we investigate the contribution of different physics processes (QCD radiation, MPI and fragmentation of beam remnants) on the same final observables, as predicted by one particular model (PYTHIA 6.4). In Chapter 5 we define the analysis strategy and describe the software framework. The data-correction procedure and the estimate of the systematic uncertainties are also described. In Chapter 6 we present the final results of this thesis, which constitute the first measurement of the UE by the ALICE collaboration. A comparison with the ATLAS measurement is also discussed as well as the scaling of the UE observables with the collision energy. These results are the original work of this thesis.

In Appendix A we show the effect of each data-correction step on the measured distributions. Finally, in Appendix B we show the ratio between the ALICE and ATLAS measurements of the UE.

An abridged version of this thesis is the subject of a publication which is being prepared [16].

1

High-energy hadronic collisions

1.1 Factorization notions

Factorization is a method to simplify a complex theory by decomposing it in building-blocks, assuming no correlation between them. Each block describes a particular aspect of the process of interest. For instance, this concept can be used to calculate hard scattering cross-sections in hadronic collisions. Historically, the idea was developed for the description of Deep Inelastic Scattering (DIS) [62] in terms of Parton Model [98]. In this framework the total hadronic cross-section for a given process is calculated by weighting the partonic cross-section, describing elementary interactions of quarks and gluons, with the parton distributions in the nucleon (Parton Distribution Functions (PDFs)). Therefore, the hadronic cross-section will include a short-distance hard-scattering term, that can be calculated in the framework of Quantum Chromodynamics (QCD) with perturbative techniques, and a long-distance term describing the hadronic structure. The scale separating the two regimes is in principle arbitrary and is called *factorization scale* μ_F . A parton emitted with a transverse momentum smaller than μ_F is considered part of the hadronic structure.

Factorization is a fundamental property of QCD that makes it a predictive theory with controllable approximations. Moreover, the concept can be extended to the description of the overall hadronic collision. At LHC energies, apart from the hard scattering generating a pair of back-to-back jets at Leading Order (LO),

1. HIGH-ENERGY HADRONIC COLLISIONS

we expect other processes to contribute to the final multi-particle state. For instance, the fragmentation of beam remnants (i.e. those partons that did not participate in the hardest scattering) and eventually Multi Partonic Interactions (MPI). These aspects will be treated in more detail in Sections 1.3.1 and 1.3.2. In general, such processes involve energy scales smaller than the hardest scattering. Therefore, one can apply factorization also in this case and divide the overall event in a short-distance jet-production part, that can be described with perturbative QCD (pQCD), and a long-distance one. The latter is the main constituent of what we generally call the Underlying Event (UE). Nevertheless, we must be aware of some remaining correlation between hard scattering and soft bulk-activity. This is introduced by QCD radiation, which in our measurement is partially included in the UE, and MPI.

1.2 QCD-improved Parton Model

In this section we describe the extension of the Parton Model to processes with two incoming hadrons in the initial state. We refer to [93] and [76] to large extent.

1.2.1 Factorization of the hard cross-section

Given our introductory considerations on factorization, we can write the cross-section for a hard scattering like:

$$\sigma(P_1, P_2) = \sum_{i,j} \int dx_1 dx_2 f_i(x_1, \mu_F^2) f_j(x_2, \mu_F^2) \hat{\sigma}_{i,j}(p_1, p_2, \alpha_S(\mu_R^2), \frac{Q^2}{\mu_F^2}, \frac{Q^2}{\mu_R^2}) \quad (1.1)$$

The process is sketched in Fig. 1.1. In the formula the incoming hadrons' 4-momenta are indicated with P_1 and P_2 . The 4-momenta of the partons participating in the hard scattering are $p_1 = x_1 P_1$ and $p_2 = x_2 P_2$, where x_i are the Bjorken- x values of the partons. The process characteristic scale, i.e. the outgoing jet p_T , is indicated with Q . The parton distribution functions $f_i(x, \mu_F^2)$ are defined at a factorization scale μ_F introduced earlier. The quantity μ_R is the so-called *renormalization scale*. It is introduced in QCD in order to cure the ultra-violet (UV) divergences of the theory. These divergences are absorbed in

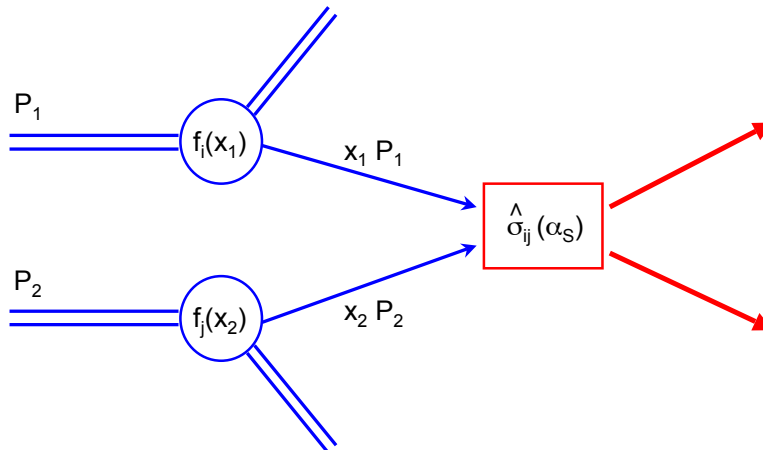


Figure 1.1: Schematic representation of the hard cross-section factorization. The proton PDFs are indicated with $f_{i,j}$, the momenta of the partons participating to the hard scattering are $x_i P_i$ and $\hat{\sigma}_{i,j}$ is the short distance cross-section. Figure adapted from [93].

a re-definition of the coupling constant α_S , which then becomes a running "constant". The quantity $\hat{\sigma}_{i,j}$ is the *short-distance cross-section* for the scattering of partons i and j . At leading order it corresponds to the parton-scattering cross-section. At higher orders long distance terms are factored-out. Therefore, this is a pure short-distance construct. Because of the asymptotic freedom property of QCD, small coupling at high energies, the short distance cross-section can be expressed as a perturbative expansion in α_S .

1.2.2 Kinematic variables

We introduce now a set of variables which will be used in the following sections. The center-of-mass of the partonic scattering is generally boosted with respect to the incoming hadrons' center-of-mass. Therefore, we classify the final state with variables that transform in a simple way under longitudinal boost: rapidity y , transverse momentum p_T and azimuthal angle ϕ . In terms of these variables, the 4-momentum of a particle of mass m is expressed as:

$$p^\mu = (E, p_x, p_y, p_z) = (m_T \cosh y, p_T \sin \phi, p_T \cos \phi, m_T \sinh y) \quad (1.2)$$

1. HIGH-ENERGY HADRONIC COLLISIONS

where z is the beam direction and $m_T = \sqrt{m^2 + p_T^2}$ is the so-called *transverse mass*.

The rapidity is defined as:

$$y = \frac{1}{2} \ln \left(\frac{E + p_z}{E - p_z} \right) \quad (1.3)$$

and is related to the longitudinal motion of the particle. This quantity is additive under boosts along z , therefore Δy is boost-invariant.

Experimentally the rapidity is often substituted by the *pseudo-rapidity*:

$$\eta = -\ln \tan \left(\frac{\theta}{2} \right) \quad (1.4)$$

where θ is the angle with respect to the beam direction and is directly measurable.

The two quantities y and η coincide in the limit $m \rightarrow 0$.

Moreover, in the rest of this chapter we indicate with s the total energy squared of the two incoming hadrons ($\simeq (P_1 + P_2)^2$) and with x the Bjorken- x .

1.2.3 Jet cross-section

Let us consider first the case in which the hard-collision outcome is a pair of high- p_T partons. We define this process a *2-to-2* ($2 \rightarrow 2$) *scattering*. The two final-state partons are observed as jets, which are collimated sprays of hadrons. Throughout this paragraph we will neglect effects like detector efficiency, resolution or details of the jet-finder algorithm and we will assume an exact correspondence between partons and jets. If we neglect the small intrinsic transverse momentum of partons in the nucleon (often called k_T), the two jets are produced back-to-back in azimuth and balanced in p_T in the laboratory frame.

The two-jet cross-section in terms of the boost-invariant variables defined above is:

$$\frac{d^3\sigma}{dy_3 dy_4 dp_T^2} = \frac{1}{16\pi \hat{s}^2} \sum_{i,j,k,l=q,\bar{q},g} \frac{f_i(x_1, \mu^2)}{x_1} \frac{f_j(x_2, \mu^2)}{x_2} \cdot \overline{\sum} |\mathcal{M}(ij \rightarrow kl)|^2 \frac{1}{1 + \delta_{kl}} \quad (1.5)$$

and is represented schematically in Fig. 1.2. The quantities y_3 and y_4 are the outgoing partons' rapidities in the laboratory frame. The squared momentum

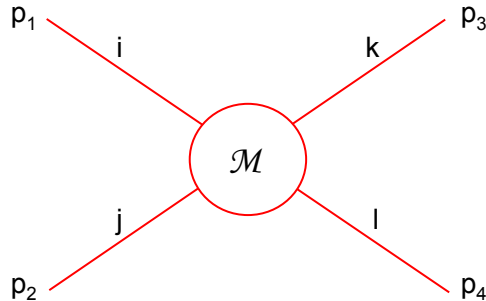


Figure 1.2: Schematic representation of a 2-to-2 scattering. The momenta of the incoming partons are indicated with $p_{1,2}$, \mathcal{M} indicates the matrix elements for the elementary scattering and $p_{3,4}$ are the momenta of the outgoing partons.

available in the partonic center-of-mass is indicated with \hat{s} and is one of the Mandelstam variables:

$$\hat{s} = (p_1 + p_2)^2 \quad \hat{t} = (p_1 - p_3)^2 \quad \hat{u} = (p_2 - p_3)^2 \quad (1.6)$$

The first sum in Eq. 1.5 runs over all the combinations of incoming (i, j) and outgoing (k, l) partons. The PDFs f_i are evaluated at a unified scale $\mu = \mu_F = \mu_R$. The sum $\overline{\sum}$ represents the average on all initial spin and color states and the sum on all final ones. The symbol \mathcal{M} indicates the matrix elements for the elementary partonic scatterings. The diagrams contributing to the matrix element at lowest order are shown in Fig. 1.3, where we have omitted their crossed partners. Analytical expressions of those diagrams can be found in [93]. The processes involving gluons in the initial state have higher probability because of the larger color factor of gluons with respect to quarks.

We consider now the more general case of more than two partons in the final state, which means processes of the type $2 \rightarrow 3,4,5$ and so on. One can define an n -partons cross-section σ^n at LO, thus considering only tree-level diagrams (no internal loops). This means that we are taking into account additional real quarks and gluons attached to the outgoing legs of Fig. 1.3. The cross-section

1. HIGH-ENERGY HADRONIC COLLISIONS

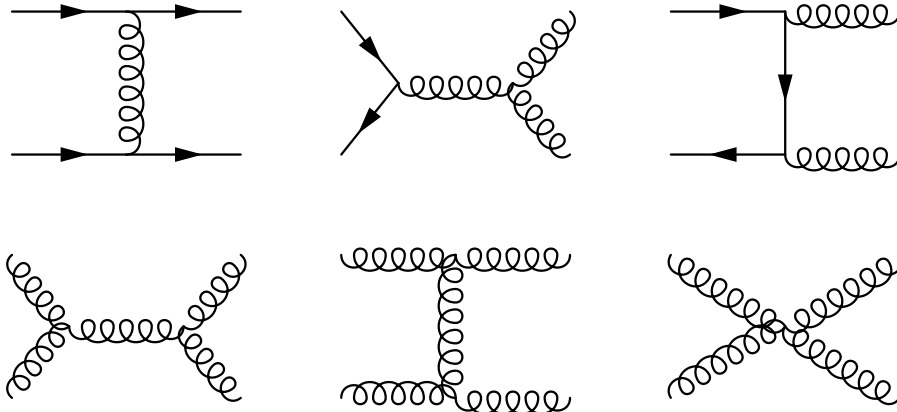


Figure 1.3: Lowest order diagrams contributing to the two jets cross-section. Crossed diagrams are not shown.

can be written as:

$$\sigma^n = \sum_{i,j,k_1,\dots,k_n=q,\bar{q},g} \int dx_1 dx_2 f_i(x_1, \mu^2) f_j(x_2, \mu^2) \hat{\sigma}^{i,j \rightarrow k_1 \dots k_n} \quad (1.7)$$

which is a generalization of Eq. 1.1. The LO matrix elements are known [117]. They show a typical bremsstrahlung structure, dominated by soft and collinear gluon emission. Each n -jet cross-section is proportional to α_S^n .

From an experimental point of view, a jet is operatively defined by the algorithm used for its reconstruction. When comparing theoretical predictions with real data, it is then necessary to run the same jet-finding algorithm at hadronic and partonic level. A particularly useful quantity in order to compare data and predictions is the jet p_T distribution. At LO it is obtained by integrating out of the two-jets cross-section (left term in Eq. 1.8) the dependence on one of the two jet momenta, which gives the inclusive cross-section for jet production (right term in Eq. 1.8):

$$\frac{d^3\sigma}{dy_3 dy_4 dp_T^2} \rightarrow \frac{d^2\sigma}{2\pi p_T dp_T dy} \quad (1.8)$$

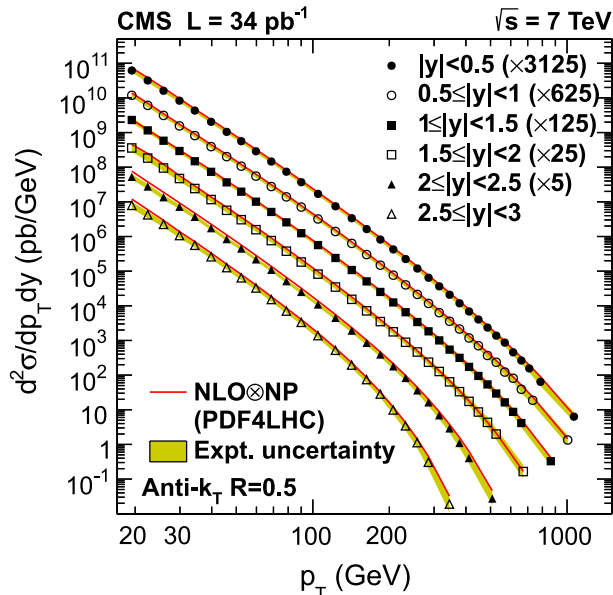


Figure 1.4: Inclusive jet cross-section measured with the CMS detector in 6 different rapidity ranges. Data are compared to a NLO pQCD prediction. More details in the text. Figure from [80].

Fig. 1.4 shows the inclusive jet cross-section measured by the CMS experiment in 6 different rapidity ranges. All the details of the measurement are explained in [80]. Jets are reconstructed with the anti- k_T jet algorithm [72]. The data are unfolded to take into account the finite detector resolution and are compared to a next-to-leading order (NLO) pQCD prediction from fastNLO [109]. The PDFs used are the CT10 [113]. The remarkable result is that data and QCD predictions agree over 10 orders of magnitude within experimental and theoretical uncertainties. The high- p_T region (up to 1 TeV/ c) corresponds to the shortest distance scale ever observed: 10^{-19} m. An excess of events in this region (not observed so far) or at higher momenta could be an indication of quark substructure or physics beyond the Standard Model.

1. HIGH-ENERGY HADRONIC COLLISIONS

1.2.4 Higher order approaches

In a lowest-order calculation, large uncertainties may arise due to the choice of the factorization and renormalization scales, to huge logarithms that need to be re-summed at highest orders or to extra partonic-processes. Therefore, it is mandatory to compare LHC data with at least NLO theoretical predictions. A NLO calculation takes into account diagrams contributing to the cross-section with an additional power of α_S . This procedure reduces the dependence of the results on non-physical scales. Specifically, an observable predicted to the order α_S^n is independent from the scale choice up to the order α_S^{n+1} .

One might proceed to calculate the next-to-next-to-leading order (NNLO) matrix elements to further reduce the scale dependence and verify the convergence of the perturbation series, but it is not the method generally used because the amount of calculation needed increases almost factorially with the order of α_S . Nonetheless, there are phase-space regions where higher-order contributions cannot be neglected (i.e. collinear parton emission). Therefore, one prefers to use the so-called *all orders approaches*. Resummation is a clear example of this type of approach: the leading logarithmic contributions are extracted from every perturbative order and are re-summed using an evolution equation.

An alternative technique is the *parton shower* formalism. This is generally implemented numerically in Monte Carlo generators like for instance PYTHIA [87, 130, 131]. The idea is to correlate few high-energy partons produced in a hard interaction with partons at a scale of the order of Λ_{QCD}^1 , to which one can then append a given hadronization model. The evolution is regulated by the DGLAP evolution equations [48, 92, 104, 116]. Solutions to such equations can be formulated in terms of *Sudakov form factors*. They represent the probability to evolve to a lower scale without emitting a gluon with a value of the evolution variable higher than a threshold. The evolution variable can be either the parent parton virtuality (PYTHIA 6.1/6.2 [129]) or the p_T^2 (PYTHIA 6.3/6.4 [130] and PYTHIA 8 [87, 131]), which also has intrinsic angular ordering. Angular ordering

¹ Λ_{QCD} is the scale at which the strong coupling starts to diverge, its value is of the order of 200 MeV.

is important because it simulates in a realistic way color coherence effects.

Sudakov form factors are the base of both parton showers and resummation techniques. For instance the Sudakov form factor for an initial-state shower is given by:

$$\Delta(t) \equiv \exp \left\{ - \int_{t_0}^t \frac{dt'}{t'} \int \frac{dz}{z} \frac{\alpha_S}{2\pi} P(z) \frac{f(x/z, t)}{f(x, t)} \right\} \quad (1.9)$$

where t is the hard scale and t_0 its cut-off value. $P(z)$ is the splitting function, or kernel probability, for the particular branching. It is a function of z , the fraction of energy of the parent parton carried by one of the splitting products.

With this formalism two new scales are introduced, one for the initial and one for the final-state showers. The peculiarity of the Sudakov form factors is that they re-sum all the effects of soft and collinear gluon emission. These are dominant terms, enhanced logarithmically. On the other hand, the parton shower formalism does not correctly include gluon emissions at high energies or angles.

Therefore we would like to exploit the parton showers capability to describe soft gluon emission and to use the matrix elements formalism when partons are geometrically and energetically well separated. There exist various techniques to interface the two methods so that each is used in its optimal phase-space region (for instance [78]). If we consider the multi-jet cross-section for a typical matching scale, about 10% of the n -jets cross-section is produced via parton showers from the scattering matrix at $(n - 1)$ jets [76].

1.2.5 Initial state

Another ingredient of the Parton Model are the distributions of partons in the nucleus. The PDFs cannot be calculated perturbatively and are determined via global fits to data. There are different groups evaluating the PDFs and updating them whenever new data are available: CTEQ [136], MRST [120], Alekhin [46] and the HERA experiments [38, 39, 82, 83]. Various experiments/processes provide informations on different kinematic regions. For instance HERA data are prevalently low- x , while DIS and Drell Yan (DY) data constrain higher x values. Collider jet data cover a wide range of x and Q^2 and are particularly important to determine the gluon distributions at high- x . Fig. 1.5 shows the LHC coverage in Bjorken- x and transferred momentum Q^2 compared to HERA and fixed target

1. HIGH-ENERGY HADRONIC COLLISIONS

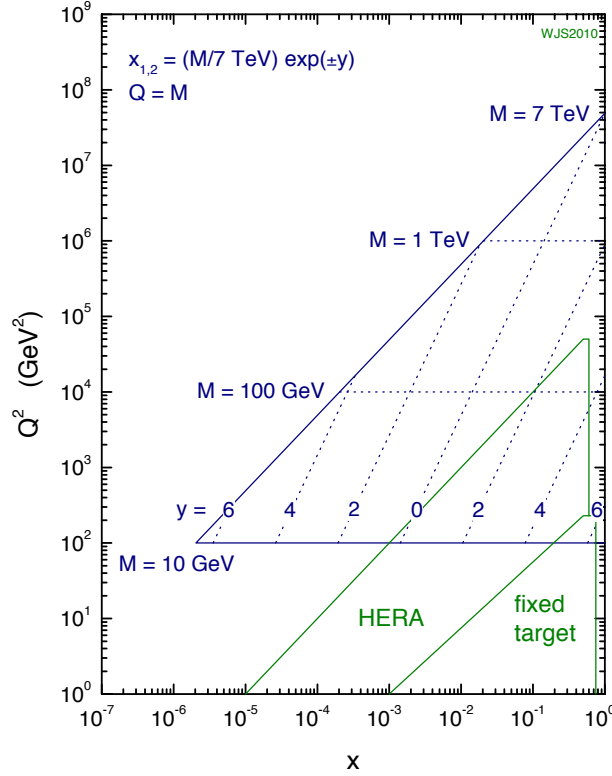


Figure 1.5: Parton kinematics at LHC ($\sqrt{s} = 7$ TeV), HERA and fixed target experiments. Figure from [90].

experiments. LHC covers almost 6 orders of magnitude in both variables. A closer look to the PDFs shows that the region $x < 0.1$ is dominated by gluons and sea-quarks, while in the remaining kinematic range the main contribution comes from valence quarks.

The accuracy of the PDFs knowledge has a certain impact on the UE modelling. For instance the amount of MPI strongly depends on the slope of the gluon distribution at low x and at NLO the slope is shallower than at LO. Moreover, a correct treatment of MPI should take into account multi-partonic PDFs, which at present are poorly constrained by measurements.

1.2.6 Hadronization

Up to this point we have considered only partonic-level cross-sections. In order to compare these predictions to hadronic-level data, we have to consider also fragmentation. The inclusive production of single hadrons is described by means of parton Fragmentation Functions (FFs). The FF gives the probability for a parton produced at a short distance $1/\mu$ (where μ is the factorization scale introduced earlier) to form a jet that includes a hadron carrying a fraction z of the longitudinal momentum of the parton. Although FFs are genuinely non-perturbative objects, they have two important properties that follow from perturbative considerations within the QCD-improved parton model. Firstly their dependence on μ is supposed to be determined by the DGLAP equations. Therefore, once their z dependence is measured at a given scale, the evolution can be evaluated perturbatively. The second fundamental property of the FFs is that they only depend on the fragmenting parton and on the produced hadron, but not on the details of the process from which they were determined.

Measurements of the FFs rely on a variety of data collected in e^+/e^- annihilation (LEP1 [29, 30, 33, 69, 70], LEP2 [24, 31], SLAC [28], PEP [41], DORIS [45, 65], PETRA [67]), hadron colliders ($Spp\bar{p}S$ [56, 64], Tevatron [25]), γp scattering (HERA [37, 91]) or $\gamma\gamma$ scattering (LEP2 [32]). The scaling violation property of the FFs and their universality are confirmed by global analyses of these data [110]. Generally FFs are given in a parametrized form so that they can be used conveniently without solving the DGLAP equations (see for example the KKP parametrization [111]).

Monte Carlo generators implement fragmentation using phenomenological schemes that model the carry over of momentum and flavour from the multi-parton final state (produced by matrix element calculations and parton showers) to the hadrons. The model parameters have to be adjusted to agree with the data. At present, the two most commonly used models are the *cluster fragmentation* [137] and the Lund *string fragmentation* [49, 128], the latter being implemented in PHOJET [95, 96] and PYTHIA [87, 130, 131] generators.

1. HIGH-ENERGY HADRONIC COLLISIONS

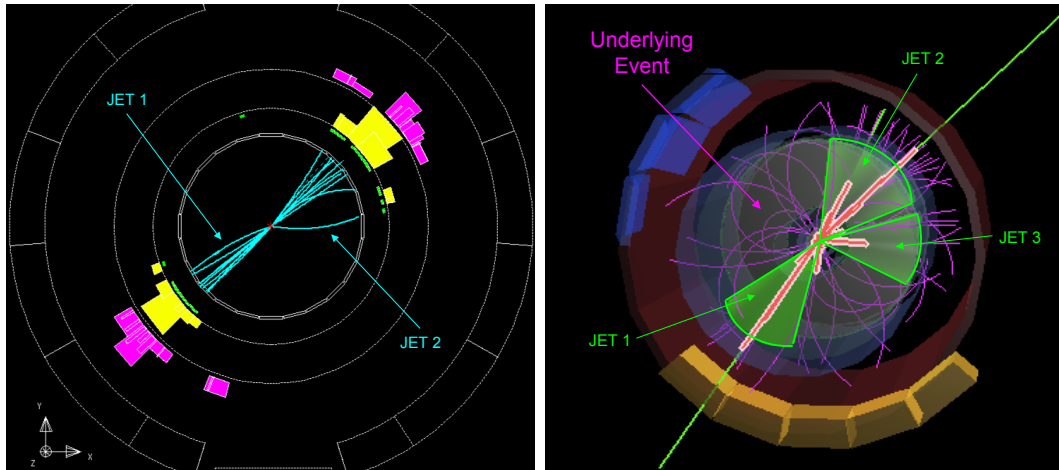


Figure 1.6: Left: a di-jet event in e^+/e^- collisions at LEP (as seen by the OPAL experiment). Two back-to-back jets are produced from the decay of the exchanged vector boson. No UE is present. Right: hadronic collision at $\sqrt{s} = 7$ TeV seen by the ALICE detector. Three jets are reconstructed (green areas and red tracks). The fragmentation of beam remnants and MPI also contribute to the multi-particle final state (magenta tracks).

1.3 The Underlying Event

In order to understand the UE in hadronic collisions, we first consider the simple case of jet production in e^+/e^- collisions. The left picture in Fig. 1.6 is an event display recorded by the OPAL experiment at LEP [43] (in the figure the beam axis is perpendicular to the page). The two colliding leptons annihilate in a virtual vector boson (γ^* or Z^*) producing a quark/anti-quark pair which then fragments into two back-to-back jets. The outgoing jets are visible in light-blue in the picture. QCD radiation could give rise to additional jets, but no other process contributes to the multi-particle final state.

In the right side of Fig. 1.6 we show an event display (in the $r\phi$ plane) of a pp collision recorded by the ALICE detector at a collision energy of 7 TeV. In this case three jets have been reconstructed (we ignore at this point the details of the jet finder algorithm): the jet areas are marked by the green shaded enclosures and the tracks belonging to each jet are marked in red. Additionally, the event

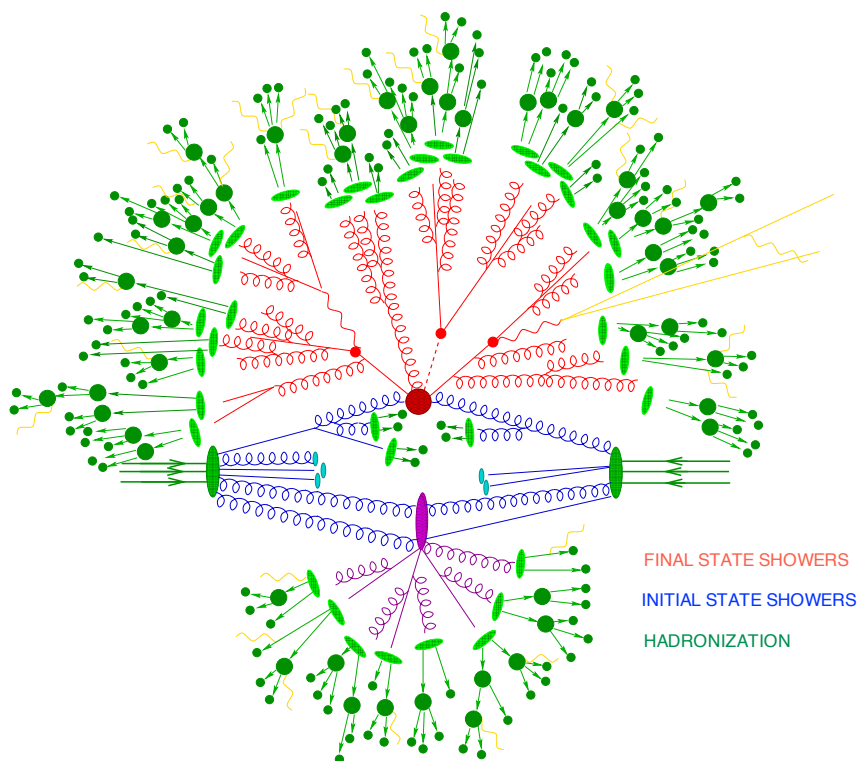


Figure 1.7: Sketch of a realistic pp collision. Figure from [112].

is populated by a bulk of soft particles (magenta lines) not belonging to the jets (and not present in the LEP case). These contributions constitute a background to any jet measurement: for instance they can be clustered by the jet-finding algorithms together with the particles really belonging to the jet, thus biasing the determination of the jet shape and energy.

In a completely general way, we define the UE as the component of the particle flow in hadronic collisions that does not originate from the hardest partonic scattering. This is, however, an ambiguous definition. For instance, Initial State Radiation (ISR) and Final State Radiation (FSR) need to be taken into account. Particles coming from these processes are often included in the definition of the

1. HIGH-ENERGY HADRONIC COLLISIONS

UE (this is the case of our analysis), instead of being considered part of the hardest scattering. More generally, the final hadronic state derives from the hadronization of partons possibly coming from different processes and it is therefore difficult to define the real origin of a final-state particle. The situation is sketched in Fig. 1.7. Blue/red lines represent initial/final state showers respectively. Hadronization and successive hadronic decays are sketched in green. This picture is further complicated by the fact that the initial protons are color-neutral objects. Therefore during fragmentation there will be a color flux connecting the beam remnants and the hardest scattering.

An alternative solution is to define the UE *ad hoc* for the process under consideration. For instance, in the case of jet events we need an operational strategy to associate part of the measured particles to the hard process and part to the other processes described above. In this thesis we will use the *Transverse Region* method (described in Chapter 4).

It is common belief that the origin of the bulk of soft particles accompanying jet production are the fragmentation of the beam remnants and MPI. Given their soft regime, these processes are only partially amenable to a perturbative treatment¹ (see Sect. 1.3.1). Therefore, the over-all event dynamics cannot be determined from first principles only, but it needs to be modelled with phenomenological calculations. Measurements of the bulk event-activity are therefore mandatory to test and constrain these models, especially at the unprecedented collision energies provided by the LHC. The main topic of this thesis is indeed a measurement of this underlying activity associated with jet production. All the processes described so far (hard scattering, QCD radiation, MPI and fragmentation of the beam remnants) are commonly implemented in multi-purpose Monte Carlo generators, which are the subject of Section 1.3.2. In the next Section (1.3.1) we take a closer look to the MPI phenomenology.

¹ Indeed perturbative QCD breaks down at scales comparable with Λ_{QCD} ($\mathcal{O}(100\text{ MeV})$).

1.3.1 Multi-Partonic Interactions

Given the high-energy regime and the large parton flux accessible at LHC, we expect more than one single pair of incoming partons to give rise to a hard scattering. This phenomenon emerges in a totally intuitive way if we consider the composite nature of hadrons. Fig. 1.8, from reference [132], gives a schematic representation of an event counting two 2-to-2 scatterings. UE and minimum bias features at hadronic colliders cannot be explained without introducing the MPI formalism in Monte Carlo generators [35, 54, 130, 133]. In such a scenario the hadron is probed simultaneously in different points, which gives a closer look to the parton distributions in the hadrons and their correlations (multi-parton distributions). For what concerns correlations among different collisions, it has been shown [75] that each single collision has a different localization in the transverse space. Different collisions in the same event do not interfere among each other (neglecting soft exchanges) and the final cross-section is given by a simple superposition of the different contributions. Therefore, the transverse momenta of outgoing partons are balanced independently in each collision. This feature has allowed the experimental identification of double parton scattering, mainly in the $\gamma+3$ -jets channel [23, 26, 27, 42].

Multiple radiation (see Sect. 1.2.3) can compete with multiple-interaction processes to create the same number of final-state partons. Nevertheless, we can distinguish between the two by considering that multiple radiation, opposite to MPI, introduces azimuthal correlations among final jets. Moreover, the two processes have a different dependence on the minimum jet- p_T choice and on the center-of-mass energy [74]. In particular, MPI are a power correction to the leading QCD mechanism of single scattering.

In the following we will outline a general approach to get a quantitative description of MPI. We refer to [132] for further details. It has been shown [133] that perturbation theory can be extended down to quite low p_T values, but still above Λ_{QCD} . In this way one can calculate perturbatively more than one interaction per event in the Parton Model framework. The QCD hard 2-to-2 cross-section

1. HIGH-ENERGY HADRONIC COLLISIONS

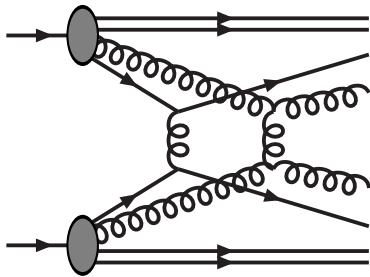


Figure 1.8: Schematic representation of an interaction with two 2-to-2 hard scatterings. Figure from [132].

can [132] be written as function of the p_T^2 scale:

$$\frac{d\sigma_{int}}{dp_T^2} = \sum_{i,j,k,l} \int dx_1 \int dx_2 \int d\hat{t} f_i(x_1, Q^2) f_j(x_2, Q^2) \frac{d\hat{\sigma}^{i,j \rightarrow k,l}}{d\hat{t}} \delta\left(p_T^2 - \frac{\hat{t}\hat{u}}{\hat{s}}\right) \quad (1.10)$$

where $\hat{s} = x_1 x_2 s$ is the available momentum in the partonic center-of-mass frame, $\hat{t} = (p_1 - p_3)^2$ and $\hat{u} = (p_2 - p_3)^2$ (with p_i defined in Fig. 1.2). We assume that the process hardness is given by the p_T scale, namely $Q^2 = p_T^2$. Eq. 1.10 derives from Eq. 1.1 approximated at first order. In the limit of small transferred momenta $|\hat{t}| \ll \hat{s}$ where $p_T^2 = \frac{\hat{t}\hat{u}}{\hat{s}} \simeq |\hat{t}|$ for constant α_S and neglecting the x -dependence, we can write the integrated interaction cross-section as:

$$\sigma_{int}(p_{T,\min}) = \int_{p_{T,\min}}^{\sqrt{s}/2} \frac{d\sigma}{dp_T} \propto \frac{1}{p_{T,\min}^2} \quad (1.11)$$

In the limit $p_{T,\min} \rightarrow 0$ this cross-section diverges. Already for values of $p_{T,\min}$ of few GeV/c the integrated interaction cross-section exceeds the total hadronic cross-section σ_{TOT} [132]. This is naturally explained by the fact that if an event contains n interactions, it will count n times in σ_{int} but only once in σ_{TOT} . Therefore we can say that the average number of interactions as function of the $p_{T,\min}$ value is given by:

$$\langle n \rangle(p_{T,\min}) = \frac{\sigma_{int}(p_{T,\min})}{\sigma_{TOT}} \quad (1.12)$$

Nevertheless the interaction cross-section still contains a non-physical divergence for vanishing p_T , which can be explained with a screening effect. Perturbative QCD calculations assume free incoming and outgoing partons, but in fact the incoming hadrons are color singlets. Therefore when the exchanged gluon has a very low p_T , or equivalently a large transverse wavelength, it can not resolve single color charges and the coupling is reduced. One can introduce a color-screening length scale, corresponding to the distance in which a color charge is compensated. This distance has to be smaller than the proton radius, which in first approximation would give $p_{T,\min} \simeq \Lambda_{QCD}$ [132], but in general it is not a known quantity. Therefore it is justified to introduce a cut-off value in the calculations, usually in p_T space, in order to reproduce the experimental results.

All these considerations on MPI do "not imply that the physics of the underlying event has to be an inherently non-perturbative quagmire", to quote [132]. On the contrary, MPI are a perturbative starting point in the description of the event activity associated with high- p_T jet production.

1.3.2 Underlying Event modelling

In the following sections we will focus on the different implementations of the UE in the Monte Carlo models with which we will compare our experimental results: PHOJET 1.1 [94, 95, 96], PYTHIA 6.4 [130] and PYTHIA 8.1 [87, 131].

1.3.2.1 PHOJET and the Dual Parton Model

PHOJET [94, 95, 96] is a two-component event generator: soft particle production is described by the Dual Parton Model (DPM) [77], while high- p_T production is based on perturbative QCD. Even though small-momentum-transfer processes are in principle described by the QCD Lagrangian, in this regime the large value of α_S does not justify a perturbative approach. An alternative strategy is to consider the large N limit of the theory, where N can be either the number of colours N_C or the number of flavours N_F . In this limit the interaction amplitudes can be expressed as $1/N$ -expansions. This approach is called *topological expansion* because each term of the expansion corresponds to an infinite set of Feynman

1. HIGH-ENERGY HADRONIC COLLISIONS

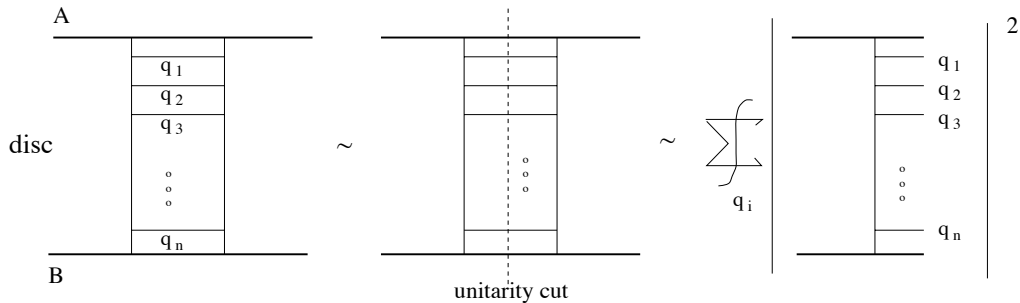


Figure 1.9: Graphical representation of the optical theorem: the discontinuity of the elastic scattering amplitude at vanishing momentum transfer corresponds to the total cross-section. Figure from [94].

diagrams with well defined topology. The first terms (Born approximation) correspond to planar diagrams. The DPM is a phenomenological realization of this approach based on the Regge Field Theory (RFT) [86] and incorporating the general concepts of duality and unitarity.

High-energy hadronic collisions are described with the exchange of effective Pomerons. A singularity in the Pomeron exchange amplitude at small transferred momenta can be considered like a unitarity cut through all intermediate propagators, assuming that such particles are on the mass-shell. The sum and integration of all those intermediate states gives the total cross-section. The procedure is represented schematically in Fig. 1.9 and is just an alternative description of the *optical theorem* [107]. The cross-section evaluation is divided in two ranges of intermediate states transverse momenta: $p_T < p_T^{\text{cut-off}}$ and $p_T > p_T^{\text{cut-off}}$. The cut-off value $p_T^{\text{cut-off}}$ is the main model parameter and artificially divides the graphs in two classes: soft and hard. One chooses $p_T^{\text{cut-off}} \gg \Lambda_{QCD}$ so that the hard part can be treated with the QCD-improved Parton Model (see Section 1.2).

We remind here that the model division in soft and hard is quite arbitrary, nevertheless the parameters are adjusted in a way that the sum of the hard and soft cross-sections is almost independent of the $p_T^{\text{cut-off}}$. In our comparison to data the chosen value for $p_T^{\text{cut-off}}$ is 3 GeV/c.

The p_T distribution of partons belonging to the soft part is parametrized by an exponential function:

$$\frac{dN_{soft}}{d^2p_T} \simeq e^{-\beta m_T} \quad (1.13)$$

The parameter β comes from the requirement of a smooth transition from soft constituents and hard scattered partons at the $p_T^{\text{cut-off}}$ value.

For what concerns hard processes, parton configurations derive from the lowest-order QCD matrix elements. Moreover, the program can generate ISR for hard scatterings according to DGLAP evolution equations and with angular ordering. The evolution is limited to the emission of partons with $p_T > p_T^{\text{cut-off}}$. The FSR is generated with the Lund program JETSET [58], also used for fragmentation.

By imposing unitarity constraints in the model one is able to obtain quantitative predictions for total, elastic and diffractive cross-sections. Moreover, MPI emerge in a natural way from the unitarization scheme. The soft and hard cross-sections in Born approximation grow like powers of s , violating the Froissart bound [101]. The dominant absorptive correction to this high-energy behaviour is given by graphs with multi-Pomeron exchanges. As a consequence, the average number of soft and hard interactions in one event increases with the energy. Finally, we remind that PHOJET produces also a set of diffractive topologies with the same framework described above. In particular, it includes single and double-diffractive dissociation and central diffraction.

Few parameters can be adjusted in the model. One of those is the $p_T^{\text{cut-off}}$ and other parameters describing the couplings of Pomeron and Reggeon with the proton. They are determined from fits to data and can not be changed individually without re-arranging also the other parameters.

1.3.2.2 PYTHIA 6.4

PYTHIA [130] is a multi-purpose event generator. The simulation of a high-energy hadronic collision starts with a hard QCD process of the type depicted in Fig. 1.3. Only LO QCD matrix elements are taken into account, which correspond to processes of the type $2 \rightarrow 2$. In order to generate multi-jet topologies

1. HIGH-ENERGY HADRONIC COLLISIONS

like $2 \rightarrow 3$, $2 \rightarrow 4$ and so on, the program employs the parton shower formalism. The same technique is used for the simulation of ISR and FSR. Hadronization is implemented through the Lund string fragmentation model, like in PHOJET. In order to correctly reproduce the total cross-section, also diffractive processes are considered, but contrary to PHOJET they are intrinsically soft and central diffraction is not included.

In the rest of this paragraph we will focus on those aspects of the event simulation relevant for the UE study: MPI and beam remnants. In particular we describe the so-called *new scenario* for the UE.

PHYTHIA 6.4 includes the possibility of characterizing every collision by a different impact parameter b : the distance of closest approach between the two colliding hadrons. Small b values correspond to a large overlap of the two colliding hadrons and therefore to an increased probability for MPI. In first approximation there is a linear proportionality between the overlap function and the mean number of interactions. In order to quantify the concept of matter overlap we need to make a choice on the matter distribution in the hadron at rest. In general, this choice will influence the distribution of the number of interactions and the UE magnitude. In the next section we describe the two particular choices corresponding to the considered tunes.

For each b value we assume that the number of interactions \tilde{n} is distributed according to a Poissonian:

$$P_{\tilde{n}} = \langle \tilde{n} \rangle^{\tilde{n}} \frac{\exp\{-\langle \tilde{n} \rangle\}}{\tilde{n}!} \quad (1.14)$$

before including restrictions like energy and momentum conservation.

Since the matter distribution can have tails to infinity we can have interactions with values of b arbitrarily large. To avoid the divergence of the total cross-section, we impose that each event must contain at least one semi-hard interaction. In this way the \tilde{n} distribution gets narrower than a Poissonian. Therefore, the probability that the two hadrons, passing through each other with impact parameter b , produce a collision of the required type is:

$$P_{\text{int}}(b) = \sum_{\tilde{n}=1}^{\infty} P_{\tilde{n}}(b) = 1 - P_0(b) = 1 - \exp\{-\langle \tilde{n} \rangle\} = 1 - \exp\{-k\mathcal{O}(b)\} \quad (1.15)$$

1.3 The Underlying Event

where $O(b)$ is the overlap function and k a proportionality factor. Now the average number of interactions per event is:

$$\langle n(b) \rangle = \frac{\langle \tilde{n}(b) \rangle}{P_{\text{int}}(b)} \quad (1.16)$$

where we have removed the possibility of no interaction. An average on all the b values gives:

$$\langle n \rangle = \frac{\sigma_{\text{int}}}{\sigma_{\text{ND}}} \quad (1.17)$$

where the difference from Eq. 1.12 lays in the fact that PYTHIA considers the non-diffractive (ND) cross-section instead of the total one. Elastic and diffractive events are treated separately.

Scatterings are ordered in a falling sequence of p_{T} . Eventually the procedure has to stop at small values of p_{T} , as mentioned in Sect. 1.3.1, because of colour-screening effects. Since the jet cross-section diverges like [132]:

$$\frac{\alpha_S^2(p_{\text{T}}^2)}{p_{\text{T}}^4} \quad (1.18)$$

we introduce a factor:

$$\frac{\alpha_S^2(p_{\text{T},0}^2 + p_{\text{T}}^2)}{\alpha_S^2(p_{\text{T}}^2)} \frac{p_{\text{T}}^4}{(p_{\text{T},0}^2 + p_{\text{T}}^2)^2} \quad (1.19)$$

which regularizes divergences by strongly damping the QCD cross-section for $p_{\text{T}} \ll p_{\text{T},0}$. The regularization value $p_{\text{T},0}$ is one of the main model parameters and needs to be tuned to data.

A hadron undergoing MPI should be described by multi-parton densities but, since our current experimental knowledge is not so advanced, PYTHIA introduces a particular technique to re-scale the single-parton PDFs. In general the interaction number i will be correlated with the previous $i - 1$, which have larger values of p_{T} because of the particular ordering scheme chosen. Therefore all the lower p_{T} -scales can be integrated-out. This can be understood by considering two different interactions: a really hard and a really soft one. The hardest interaction corresponds to a very short formation time and we expect it to be able to influence the softer one, but not vice-versa. During the evolution towards lower p_{T} values, partons that have already interacted are removed from the hadron. What

1. HIGH-ENERGY HADRONIC COLLISIONS

remains in the beam remnant is a number of partons given by the remaining valence content plus a number of sea quarks required by the conservation of total flavour. Moreover, colour re-arrangements (or *colour reconnections*) can occur in the final state. For instance the model includes an option for a *colour annealing* scenario, where one assumes that at hadronization time, the details of the colour evolution history are irrelevant. The only important factor is the minimization of the potential energy stored in the hadronization strings (or string length minimization).

Concerning longitudinal-momentum conservation, it is not implemented exactly for each single incoming proton, but only for the system as a whole.

Moreover, we expect the partons to carry a primordial transverse momentum k_T of some hundred MeV/ c , given by Fermi motion in the incoming protons. This is another important model parameter. In the shower evolution a comparison to data shows that a value of k_T of some GeV/ c is needed, hence we talk about an effective primordial k_T . The model also requires a null total beam k_T .

Each multiple interaction is associated with a set of initial and final-state radiation. The transverse momentum is the common evolution scale for the three processes: MPI, ISR and FSR. To good approximation FSR can be delayed until MPI and ISR are completely considered. FSR does not modify the energy carried by the perturbative initial-state partons, it simply re-distributes such energy among more partons in the final-state. On the contrary an additional ISR branching or another interaction imply more perturbative energy to be taken from the beam remnants. Therefore, the two mechanisms are in direct competition and should be interleaved in a common sequence of decreasing p_T . For example a second hard interaction should be considered before a softer ISR branching associated to the first interaction.

Finally, we should make some consideration on the $p_{T,\min}$ scale. Since MPI and ISR are interleaved, we should choose the same regularization procedure. We use the same smooth cut-off $p_{T,0}$ introduced earlier, but for ISR the regularization factor is the square root of the MPI case since only one Feynman vertex enters in

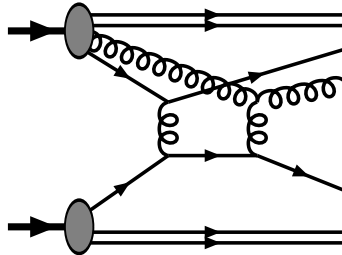


Figure 1.10: Schematic representation of a 2-to-2 scattering followed by a rescattering. Figure from [131].

the shower branching. For what concerns FSR, the cut-off can be at a lower value. This scale concerns the matching between perturbative physics and hadronization, hence it has a different meaning.

1.3.2.3 PYTHIA 8.1

PYTHIA 8 [87, 131] is the natural continuation of PYTHIA 6.4, the latter being no longer developed. The bulk of the simulation framework is the same in both models, but version 8 introduces some major changes: FSR is interleaved together with ISR and MPI, parton rescatterings are considered as well as an enhanced colour screening picture.

Rescattering happens when an already scattered parton is allowed to participate in another scattering. The situation is sketched in Fig. 1.10. The magnitude of this effect has been estimated to be negligible if compared to disjoint MPI at Tevatron energies[123]. In general, we expect rescattering to influence collective features like multiplicity or p_T distributions. In addition, it is a new source of 3-jet events and contributes to additional p_T in the perturbative region. This process is in competition with primordial k_T and colour reconnections in explaining the data.

Finally, we would like to mention that PYTHIA 8.1 takes into account initial-state partonic fluctuations before the collision. In such a picture the amount of colour-screening can change event-by-event.

1. HIGH-ENERGY HADRONIC COLLISIONS

1.3.2.4 Considerations on PYTHIA tunes

PYTHIA counts hundreds of parameters that can be set, more or less independently from each other, to reproduce the data¹. In this section we give a brief description of the two PYTHIA tunes with which we are comparing our experimental results. Next to each physics property we indicate in parenthesis the name of the relevant parameter in the respective model. These informations will be useful in the interpretation of the matching with real data. We remind here that the definition of an optimal tune to describe the measured data is outside the scope of this thesis.

PYTHIA 6.4 - Tune Perugia 0 [134] uses the CTEQ5L [114] set of leading-order PDFs. As already mentioned, the new UE model is used (MSTP(81)=21). The regularization scheme for ISR branchings is the same used for MPI (MSTP(70)=2). The $p_{T,0}$ value for both MPI and ISR is 2 GeV/ c (PARP(82)=2) at the reference energy of 1800 GeV (PARP(89)). The $p_{T,0}$ is rescaled with the collision energy proportionally to:

$$p_{T,0} \propto E_{CM}^{0.26} \quad (1.20)$$

where the exponent is given by PARP(90).

For what concerns the hadronic matter overlap, the model adopts a generic form:

$$\mathcal{O}(b) \propto \exp(-b^d) \quad (1.21)$$

where b is the varying impact parameter. The parameter d (PARP(83)) can range between the two extreme values of 1, corresponding to an exponential distribution, and 2, corresponding to a Gaussian. In this particular tune $d = 1.7$.

The primordial k_T distribution in the hadron has Gaussian shape (MSTP(91)=1) of width 2 GeV/ c (PARP(91)) and upper cut-off of 10 GeV/ c (PARP(93)).

For what concerns colour reconnections, the tune employs a specific scheme of string length minimization (MSTP(95)=6). This scheme improves the agreement with the $\langle p_T \rangle(N_{ch})$ distribution and with the high- p_T tail of the charged-particle

¹In this respect PHOJET is less flexible than PYTHIA, given its limited number of tunable parameters. In this analysis we used its default values.

spectrum at Tevatron energies [134].

PYTHIA 8.1 - Tune 1 [131] also uses the LO set of PDFs CTEQ5L. The regularization of ISR and MPI evolution has different values of $p_{T,0}$ for the two processes (`SpaceShower:samePTasMI=false`). In the ISR case $p_{T,0} = 2 \text{ GeV}/c$ (`SpaceShower:pT0Ref=2`) independently of the collision energy (`SpaceShower:ecmPow=0`). For MPI the reference value at 1800 GeV is $2.25 \text{ GeV}/c$ (`MultipleInteractions:pT0Ref=2.25`) and the power of the energy scaling defined in Eq. 1.20 is 0.24 (`MultipleInteractions:ecmPow=0.24`).

The impact parameter profile for MPI is a Gaussian without free parameters.

The primordial k_T distribution has a Gaussian shape independently in p_x and p_y .

The distributions amplitudes depend on the hard scale and on the mass of the two initiators.

1. HIGH-ENERGY HADRONIC COLLISIONS

2

The ALICE detector at the LHC

2.1 The Large Hadron Collider (LHC)

The Large Hadron Collider (LHC) [97] at CERN is the world biggest particle accelerator in operation at present. It is located in the area near Geneva, at the French/Swiss border. The LHC tunnel is built at a depth between 45 and 170 m and has a circumference of 26.7 km. The LHC was designed to accelerate protons at a maximum center-of-mass energy (\sqrt{s}) of 14 TeV and lead (Pb) ions at $\sqrt{s} = 5.5$ TeV per nucleon (ATeV) at maximum. These will be the highest energies ever reached in particle collisions. The machine started its operation the 10th of September 2008 and at the moment in which this thesis is being written the machine already delivered collisions at $\sqrt{s} = 0.9$ and 7 TeV for proton beams and at 2.76 ATeV for Pb beams.

The LHC machine is a synchrotron accelerating two beams in opposite directions and in distinct beam-pipes. Each beam is composed of compact *bunches* of particles. Before being injected in the LHC ring, proton bunches are pre-accelerated in the LINAC2, PS-booster, PS and SPS accelerators (Pb beams have a slightly difference sequence) to an energy per nucleon of 450 GeV. Various injections are needed before all the beam bunches are filled in the LHC. After injection, the LHC accelerates the beams up to the required energy while keeping them focused. This is achieved with a combination of electric and magnetic fields. The bending of the trajectories along the circumference is provided by a

2. THE ALICE DETECTOR AT THE LHC

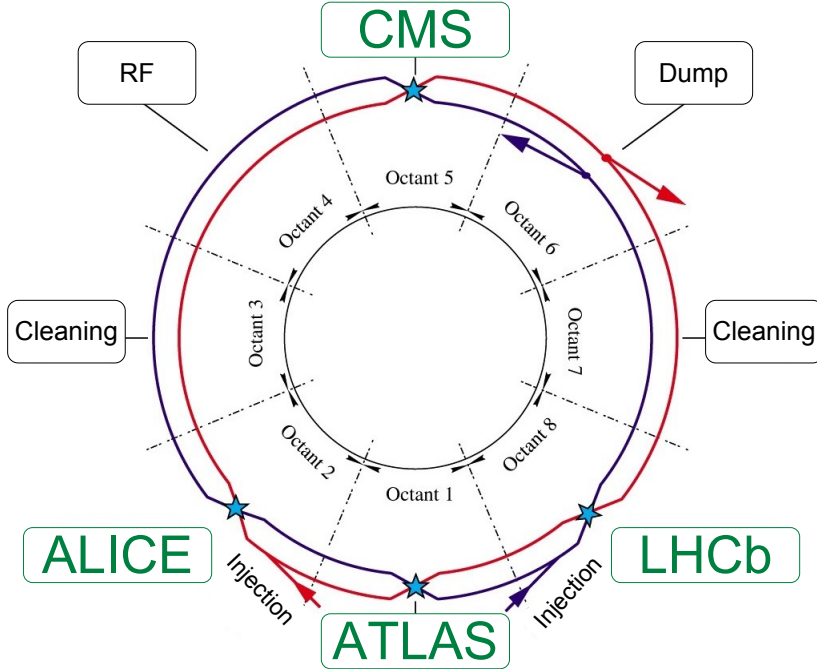


Figure 2.1: Schematic view of the LHC. The position of the 4 major experiments is indicated, as well as the injection, collimation (cleaning) and dumping regions. Blue stars locate the collision points.

set of 1,232 dipoles. Each dipole contains super-conducting magnets operating at a temperature of 1.9 K and drawing a maximum current of about 12 kA. The dipoles can deliver a maximum magnetic field of 8.33 T during pp collisions. The beams are accelerated by 8 Radio Frequency (RF) cavities, which operate at a frequency of 400 MHz. The RF power, besides accelerating the beams, keeps them localized and compensates the energy loss due to synchrotron radiation. Moreover, the LHC infrastructure has two collimation systems that remove the beam particles which have too large spatial distance from their own bunch (*beam-halo* particles) or that are separated in momentum space (too fast/slow). In this way one avoids the uncontrolled circulation of particles lost from the bunch. In four locations of the collider circumference, the beams are allowed to cross and collide. These are also the points where the four major LHC experiments are built: ALICE (see Sect. 2.2), ATLAS [8], LHCb [53] and CMS [79]. Finally, there is a

dumping system for each beam. The LHC circumference is divided in octants, shown in Fig. 2.1, where the position of the major experiments is also indicated, as well as the injection, collimation and dumping regions.

2.1.1 Collision parameters

The bunch spatial dimensions should be minimized in order to achieve a high number of collisions per time interval. This concept is quantified by the *luminosity*:

$$\mathcal{L} = \frac{fnN^2}{A} \quad (2.1)$$

where n is the number of bunches in both beams, N is the number of particles per bunch, A is the beam transverse area and f the revolution frequency. The luminosity is measured in $\text{cm}^{-2} \text{s}^{-1}$ and is related to the interaction frequency in the following way:

$$\frac{dN}{dt} = \mathcal{L}\sigma \quad (2.2)$$

where σ is the cross-section for the process of interest.

In the nominal LHC operation conditions [97], each beam is made of 2,808 bunches, each containing $1.15 \cdot 10^{11}$ protons. Bunches are spaced in time by 25 ns. The design luminosity for the pp runs is $10^{34} \text{ cm}^{-2} \text{ s}^{-1}$ ($10^{27} \text{ cm}^{-2} \text{ s}^{-1}$ for PbPb runs). The ALICE detector operates at a lower luminosity ($5 \cdot 10^{27} \text{ cm}^{-2} \text{ s}^{-1}$) in hadronic collisions to limit the probability of multiple collisions in the same bunch-crossing (pile-up effect), which is particular critical for the slow drift detectors (see Sect. 2.2).

We assume that the pile-up probability is given by a Poissonian distribution:

$$P(n) = \frac{\mu^n e^{-\mu}}{n!} \quad (2.3)$$

where n is the number of interactions. The parameter μ is usually quoted as an indicator of the pile-up probability.

2.2 A Large Ion Collider Experiment (ALICE)

A Large Ion Collider Experiment (ALICE) [15] is a general purpose experiment at the CERN LHC. It was designed to study the physics of strongly interacting matter and the formation of a quark-gluon-plasma (QGP) [66] at extreme values of energy density and temperature in nuclear collisions (PbPb). ALICE focuses on the region around mid-rapidity, where low baryon density and maximal energy density are expected. In case of proton-proton collisions, ALICE is complementary to the other LHC detectors. This is due to its tracking capabilities from very low p_T (150 MeV/ c) up to more than 100 GeV/ c and Particle IDentification (PID) over a comparable range. The low momentum reach is achieved with a small material budget to reduce multiple scattering (13% of X_0 up to a radius of ~ 2.8 m [15]), whereas a large lever arm (up to 3.5 m) ensures good resolution at high p_T (see Sect. 2.2.4.2).

The most stringent design constraint is the very high particle multiplicity expected in a PbPb collision. For instance, about 1,600 charged particles per unit pseudo-rapidity have been measured [18] at mid-rapidity in central PbPb collisions at $\sqrt{s} = 2.76$ ATeV. The experiment was optimized for $dN_{ch}/d\eta = 4000$ around mid-rapidity and tested with simulations up to $dN_{ch}/d\eta = 8000$ [15].

The tracking is particularly robust because it is based on 3-dimensional information with up to 160 points and a moderate magnetic field of 0.5 T¹ (compared to the 2 T and 4 T of the ATLAS [8] and CMS [79] detectors respectively).

2.2.1 Detector layout

Fig. 2.2 shows the layout of the ALICE detector, housed in the L3 magnet (red). Tracking in the ALICE central barrel relies on the Time Projection Chamber (TPC) described in Sect. 2.2.1.1, on the Inner Tracking System (ITS) described in Sect. 2.2.1.2 and on the Transition Radiation Detector (TRD) described in Chapter 3.

¹The field is generated by a solenoidal magnet, previously used in the L3 experiment at LEP, which houses the central detectors.

2.2 A Large Ion Collider Experiment (ALICE)

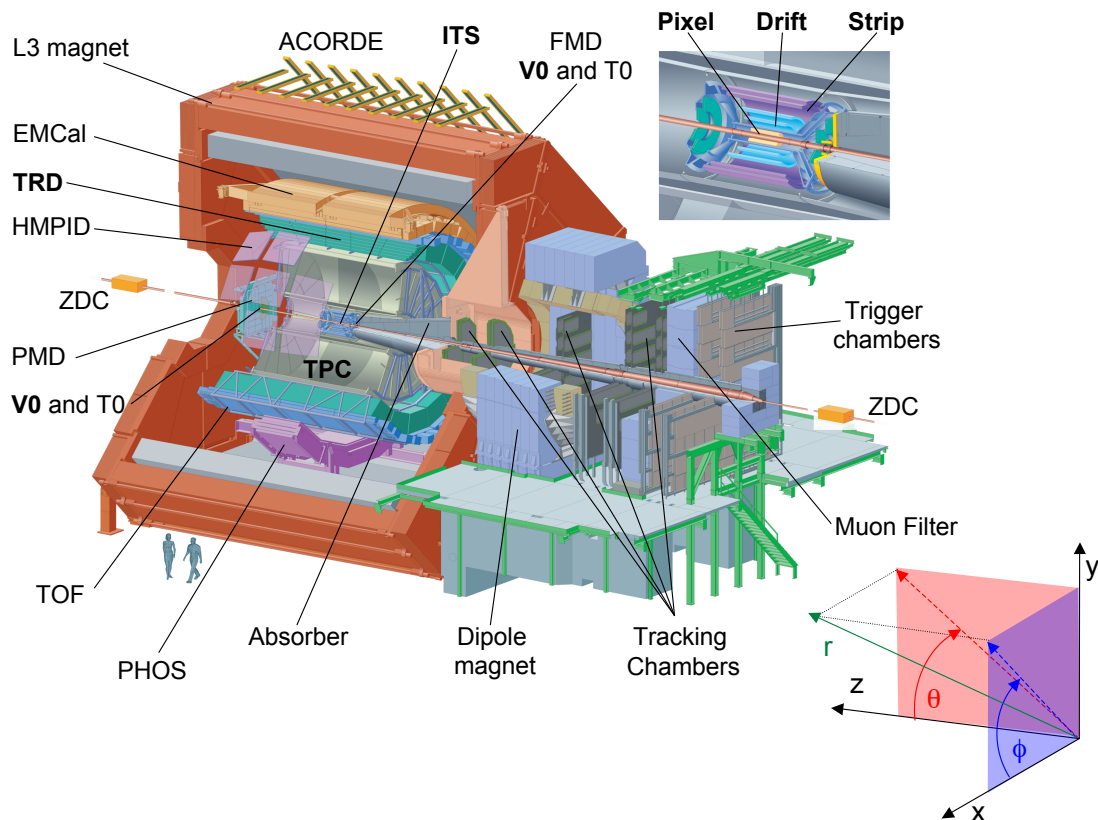


Figure 2.2: Schematic representation of the ALICE detector. Top-right insertion: enlargement of the Inner Tracking System (ITS) showing its sub-systems. Bottom-right insertion: ALICE cartesian and spherical coordinate systems. The $z > 0$ region is the so called detector A-side and the $z < 0$ region is the C-side.

One of the main features of ALICE is the large number of detectors dedicated to charged-particle identification. TPC and ITS provide PID via energy loss (dE/dx) measurements in the low p region (below $1 \text{ GeV}/c$). Moreover, the TPC can extend this measurement to the relativistic rise of the Bethe-Bloch distribution [127], ideally up to about $100 \text{ GeV}/c$. In the intermediate momentum range (up to about $4 \text{ GeV}/c$) PID is achieved with the Time Of Flight (TOF) detector, which is an array of Multi-gap Resistive Plate Chambers (MRPCs) optimized for large acceptance ($|\eta| < 0.9$). The TOF has a time resolution below

2. THE ALICE DETECTOR AT THE LHC

100 ps. The High Multiplicity PID (HMPID) is an array of proximity focusing ring imaging Cherenkov counters, which extends the identification of hadrons up to about 5 GeV/ c . Its acceptance is limited to 10% of the central barrel. Moreover, the TRD can identify electrons with momenta above 1 GeV/ c .

ALICE has two electromagnetic calorimeters. The PHOTon Spectrometer (PHOS) is a single arm system composed of dense PbWO₄ scintillating crystals. It has a good energy resolution (about 1.4% for a 20 GeV jet [47]) and a segmentation smaller than the Molière¹ radius. A set of Multiwire Proportional Chambers in front of PHOS acts as Charged Particle Veto (CPV).

The ElectroMagnetic Calorimeter (EMCal) is a Pb-scintillator sampling calorimeter. It has a 6 times wider acceptance than PHOS, but lower granularity (the transverse cell size is about 2 times the Molière radius) and energy resolution (about 6% for a 20 GeV jet [57]). The EMCal is positioned at approximately opposite azimuth than the PHOS and has been optimized for the measurement of jet production rates and fragmentation functions.

The Muon Spectrometer is a forward system designed for the study of heavy quarks resonances (J/ψ , Υ etc.) with sufficient mass resolution (100 MeV/ c^2 at the Υ mass) to separate the different states and momentum coverage down to zero p_T . It consists of a composite absorber, a bipolar magnet creating an integrated field of 3 Tm, 10 planes of cathode-strip tracking-stations, a second muon filter and 4 layers of Resistive Plate Chambers (RPC) for muon identification and trigger.

Moreover, ALICE includes detectors used for trigger purposes or to measure global event properties. For instance, the T0 detector is composed of 2 sets of Cherenkov detectors installed directly around the beam pipe². They measure the

¹The Molière radius is a characteristic constant of a material that quantifies the transverse dimension of electromagnetic showers. It is defined as the radius of a cylinder containing 90% of the shower's energy. A small Molière radius corresponds to a good position resolution and good shower separation due to a smaller degree of overlapping.

²The ALICE beam-pipe is a beryllium cylinder 800 μm thick and with an external diameter of 6 cm.

2.2 A Large Ion Collider Experiment (ALICE)

event time with a resolution of less than 25 ps. The V0 detector is used as minimum bias trigger and to reject beam-gas events. It is described in more detail in Sect. 2.2.1.3.

ACORDE is an array of 60 large scintillators located on top of the ALICE magnet. It is used as cosmic rays trigger and to align and calibrate the other sub-systems. The Forward Multiplicity Detector (FMD) is composed of rings of silicon strip detectors located at 3 different positions along the beam pipe. It measures the multiplicity in a large acceptance ($-3.4 < \eta < -1.7$ and $1.7 < \eta < 5.0$).

The Photon Multiplicity Detector (PMD) measures multiplicity and spatial distribution of photons. It is composed of two layers of gas proportional counters, preceded by lead converter plates.

The Zero Degree Calorimeter (ZDC) system is equipped with 2 sets of compact hadronic calorimeters used to trigger on the collision impact parameter. Moreover, the ZDC includes 2 small electromagnetic calorimeters (ZEM) installed on one side of the interaction point to improve the centrality measurement.

In Fig. 2.2 we also show the ALICE cartesian coordinate system. The system origin coincides with the nominal interaction point in the middle of the central barrel and has been shifted in the picture for visualization purpose. Alternatively, we will sometimes refer to a spherical coordinate system, also centred at the nominal interaction point. The polar angle θ increases from z ($\theta = 0$) to $-z$ ($\theta = \pi$). The azimuthal angle ϕ increases clockwise from x ($\phi = 0$), passing y ($\phi = \pi/2$) to x ($\phi = 2\pi$) with the observer standing at negative z and looking towards the origin.

For a more detailed description of the ALICE detector see [15]. In the following sections we describe the main features of the detectors used in the analysis, referring mainly to [15]. Some characteristics are also summarized in Table 2.2.

2.2.1.1 Time Projection Chamber (TPC)

The TPC is the main tracking detector of the ALICE central barrel. It provides tracking in the p_T range from 0.2 (at nominal magnetic field) to 100 GeV/ c and

2. THE ALICE DETECTOR AT THE LHC

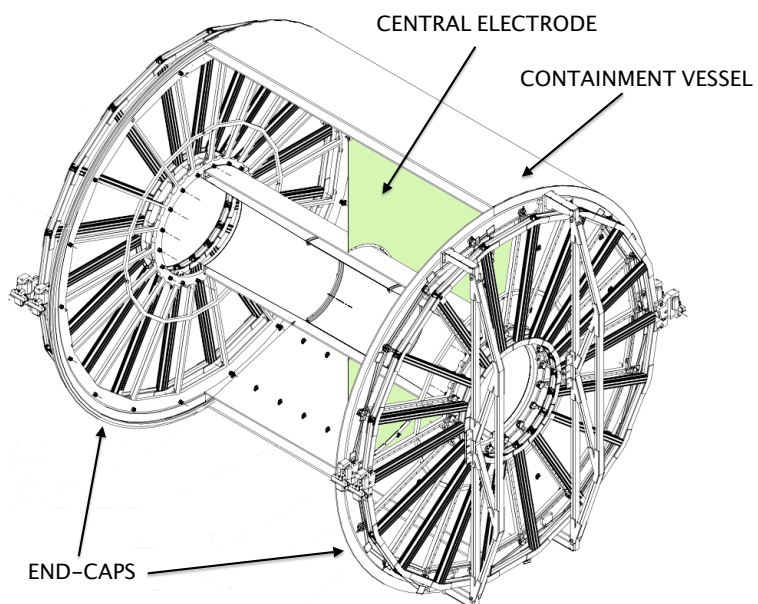


Figure 2.3: 3D view of the TPC field cage. The containment vessel and the central electrode are indicated in the figure, as well as the end-caps sustaining the read-out chambers (not shown). Figure adapted from [15].



Figure 2.4: The TPC before installation.

2.2 A Large Ion Collider Experiment (ALICE)

particle identification via dE/dx in the low momentum region ($dE/dx \sim 1/\beta^2$) and in the relativistic rise of the Bethe-Bloch distribution. The detector is made of a large cylindrical field cage, where ionization electrons are transported on either sides of a central electrode (at 100 kV) to the end plates (see Fig. 2.3). The active volume has an inner radius of about 0.85 m, an outer radius of about 2.5 m and it extends for 5 m along the beam direction. The position resolution varies from 1100 to 800 μm along the $r\phi$ coordinate (inner and outer radius respectively) and from 1250 to 1100 μm along the beam direction. The momentum resolution is better than 2.5% for tracks with momenta below 4 GeV/ c . The TPC drift time is about 90 μs , which is the limiting factor on the acquisition rate in proton-proton collisions.

The active volume is filled with a mixture of Ne/CO₂/N₂ in the proportions 90/10/5. The gas system is optimized to achieve high drift speed, low diffusion, low multiple scattering, small space-charge effects and good ageing and stability properties. The N₂ improves quenching and allows high gas gains [103]. The NeCO₂ mixture has a steep dependence of the drift velocity on temperature [138], therefore the thermal stability has to be below 0.1 K in the drift volume. This requires an elaborate system of heat screens and cooling systems: there are screens at the inner and outer radius shielding from neighbouring detectors (ITS, TRD) and screening and cooling of the Front End Electronics (FEE). The pressure follows the ambient pressure.

The TPC read-out is performed with 72 multi-wire proportional chambers with cathode pad read-out, which are mounted into 18 trapezoidal sectors at each end of the drift volume (see Fig. 2.3). The total number of read-out channels is 557,568. To follow the radial dependence of the track density, the read-out is segmented radially into two chambers with different wire geometry. The read-out chambers are normally protected by a gating grid against electrons coming from the drift volume and ions from the amplification region. The grid is opened only after an L1 trigger (more in Sect. 2.2.2) for the entire drift time. In about 10% of the azimuthal angle the detector is not sensitive because of inactive areas between neighbouring chambers. This mainly affects high p_{T} (straight)

2. THE ALICE DETECTOR AT THE LHC

tracks, while low and intermediate p_T tracks are bent out of the insensitive areas by the magnetic field.

2.2.1.2 Inner Tracking System (ITS)

The ITS directly surrounds the beam-pipe and is composed of 6 cylindrical layers of silicon detectors. The main task of the detector is to localize the primary vertex with a resolution better than $100\ \mu\text{m}$ (in PbPb collisions) and to reconstruct secondary vertexes from decays of hyperons and D and B mesons. Moreover, it extends the tracking and PID capabilities of the TPC to particles with momentum below $200\ \text{MeV}/c$. The outermost 4 layers have analog read-out to perform PID via dE/dx in the non-relativistic region ($dE/dx \propto 1/\beta^2$). The first layer has an extended pseudo-rapidity coverage ($|\eta| < 1.98$) to ensure, together with the FMD, a complete coverage for the measurement of charged particles multiplicity. The ITS momentum resolution is better than 2% for pions with transverse momentum ranging from $100\ \text{MeV}/c$ to $3\ \text{GeV}/c$. The spatial resolution is some tens of μm , with the highest precision close to the primary vertex. For momenta higher than $3\ \text{GeV}/c$ the ITS spatial resolution is a key element for the global momentum resolution (see Sect. 2.2.4.2).

The ITS layers are located between 4 and 43 cm in radial distance. They cover the range $|\eta| < 0.9$ for all vertices within the interaction diamond length ($\pm 1\sigma$ i.e. $\pm 5.3\ \text{cm}$ along the beam direction). The outermost radius was designed to match ITS tracks with TPC tracks. The cooling system of the most external layers was optimized to provide the temperature stability and uniformity required by the TPC. The material budget in the active volume is minimized in order to reduce multiple scattering: the effective thickness of the ITS system including support and services is 7.7% of radiation length [17]. Sensors partially overlap in order to cover the solid angle completely. The total number of read-out channels is almost 13 millions. The ITS layout is shown in Fig. 2.5. The single sub-systems are further discussed in the following.

2.2 A Large Ion Collider Experiment (ALICE)

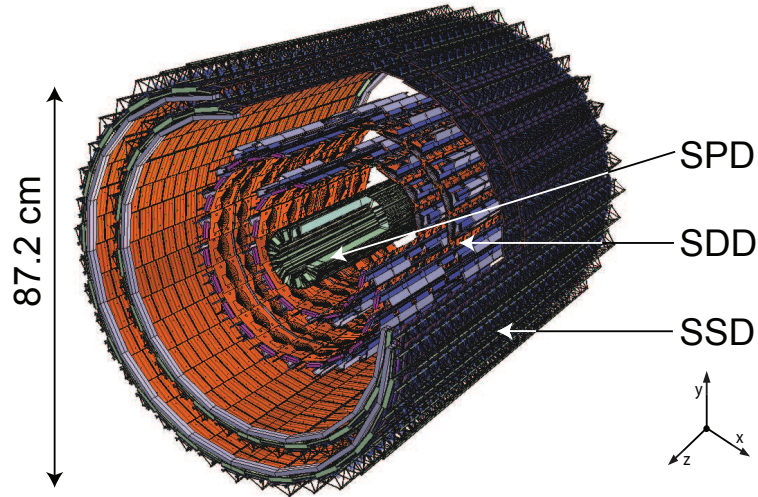


Figure 2.5: Layout of the ITS system. The 3 subsystems are indicated in the figure: Silicon Pixel Detector (SPD), Silicon Drift Detector (SDD) and Silicon Strip Detector (SPD). Each subsystem is composed by 2 cylindrical layers. Figure from [17].

	Silicon Pixel	Silicon Drift	Silicon Strip
Spatial resolution $r\phi$ (μm)	12	35	20
Spatial resolution z (μm)	100	25	830
Two-track resolution $r\phi$ (μm)	100	200	300
Two-track resolution z (μm)	850	600	2400
Modules	240	260	1,698
Read-out channels	9,835 k	133 k	2,608 k

Table 2.1: Spatial resolution and number of modules and read-out channels for the various ITS subsystems. Table adapted from [15].

2. THE ALICE DETECTOR AT THE LHC

The two inner Silicon Pixel Detector (SPD) layers were designed to cope with a track density as high as 50 tracks/cm² in relatively high radiation levels (estimated total dose of 2.7 kGy in 10 years of standard running [122]). The sensors have an active area of 12.8 mm ($r\phi$) x 70.7 mm (z) and a thickness of 200 μm . The system is supported by a carbon-fibre frame and the material traversed by straight tracks perpendicular to the detector surface is about 1% X_0 per layer. The SPD barrel is surrounded by an Al-coated carbon-fibre external shield to protect the SDD layers from the SPD heat flow.

The Silicon Drift Detector (SDD) layers provide 2 out of the 4 dE/dx samples required for particle identification in the ITS. Each sensor has a sensitive area of 70.17 mm ($r\phi$) x 75.25 mm (z), which is split into two drift regions separated by a central cathode. Three rows of MOS¹ charge injectors perpendicular to the drift direction monitor the drift velocity. The latter has a variation of 0.8%/K at room temperature. The injectors are triggered on regular intervals during the data taking for on-line calibration of the drift velocity.

The double-sided Silicon Strip Detector (SSD) is responsible for the matching of TPC tracks with the ITS. It provides a 2 dimensional measurement of the track position and dE/dx information. Each sensor has an active area of 73 mm ($r\phi$) x 40 mm (z) and a thickness of 300 μm . Strips are nearly parallel to the magnetic field to achieve optimal resolution in the bending direction.

The spatial resolution of the various ITS sub-systems is summarized in Tab. 2.1, together with the number of active cells and read-out channels.

2.2.1.3 V0A and V0C

V0A and V0C are two arrays of scintillator counters mounted on either sides of the interaction point. They provide minimum bias triggers for the central barrel detectors and a rough centrality trigger based on multiplicity. The latter exploits the monotonic dependence between the number of particles registered by the V0

¹Metal Oxide Semiconductor

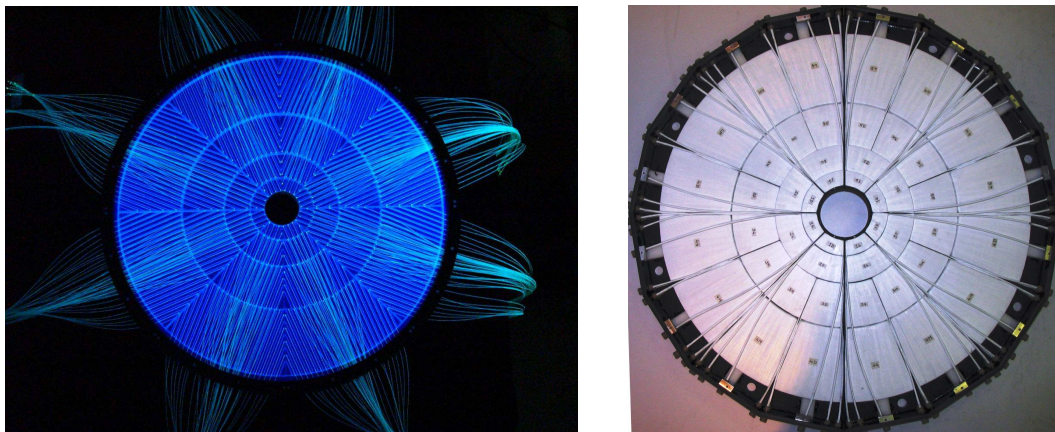


Figure 2.6: Front view of V0A (left) and V0C (right) arrays.

arrays and the number of emitted primary particles. Moreover, a p-Gas off-line trigger (PG) eliminates false events coming from interactions of protons with the residual gas in the vacuum pipe.

The V0A detector is installed at 340 cm from the nominal interaction point, on the side opposite to the muon spectrometer, and covers the pseudo-rapidity range $2.8 < \eta < 5.1$. The V0C system is located on the opposite side with respect to the interaction point, at a distance of 90 m, and covers the range $-3.7 < \eta < -1.7$. Both detectors are segmented into 32 individual counters, each distributed in 4 rings and 8 sectors of 45° (see Fig. 2.6). The scintillating material is 2.5 and 2.0 cm thick in the case of V0A and V0C, respectively, and is coupled to Wave-Length Shifting (WLS) fibres with a diameter of 1 mm.

2.2.2 Trigger system

The Central Trigger Processor (CTP) is designed for the optimal use of all the ALICE sub-systems, which are busy for quite different periods. Moreover, it can handle different running modes: ions, pA and pp, with counting rates varying by almost two orders of magnitude.

Tracking detectors need to cope with the high multiplicities in PbPb collisions,

2. THE ALICE DETECTOR AT THE LHC

Detector	η acceptance	ϕ acceptance	Technology	Physics
ITS (SPD)	$\pm 2 / \pm 1.4$	full azimuth	<ul style="list-style-type: none"> silicon detectors with different technologies 	<ul style="list-style-type: none"> vertex reconstruction PID at low p_T
ITS (SDD)	± 0.9			<ul style="list-style-type: none"> tracking at low p_T
ITS (SSD)	± 0.9			<ul style="list-style-type: none"> improved momentum resolution improved impact parameter resolution
TPC	± 0.9 at $r = 2.8$ m ± 1.5 at $r = 1.4$ m	full azimuth with intra-sector gaps	<ul style="list-style-type: none"> gas time projection chamber 	<ul style="list-style-type: none"> tracking PID also in relativistic rise
TRD	± 0.84	full azimuth	<ul style="list-style-type: none"> carbon fibre radiator multi-wire proportional gas chambers 	<ul style="list-style-type: none"> electron identification improved momentum resolution improved position resolution
V0A	$2.8 < \eta < 5.1$	full azimuth	<ul style="list-style-type: none"> scintillating counters 	<ul style="list-style-type: none"> MB trigger
V0C	$-3.7 < \eta < -1.7$		<ul style="list-style-type: none"> wave-length shifting fibres photo-multipliers 	<ul style="list-style-type: none"> beam-gas rejection centrality trigger luminosity

Table 2.2: Summary of detectors used in this thesis.

2.2 A Large Ion Collider Experiment (ALICE)

which in some cases require the use of non pipelined electronics and a strobe at $1.2 \mu s$. Therefore the fast part of the trigger is split into two levels: a Level 0 (L0) signal that reaches some detectors at $1.2 \mu s$ but is too fast to receive all the trigger inputs and a Level 1 (L1) signal at $6.5 \mu s$ that receives the remaining fast inputs. The L0 latency is almost entirely determined by the generation time of the input signals and by cable delays, while the CTP decisions are made in only 100 ns.

In high multiplicity PbPb collisions events containing more than one central collision are not reconstructable. For this reason, the ALICE trigger system also implements past-future protection. The final Level 2 (L2) of trigger waits for the end of the past-future protection interval ($88 \mu s$ determined by the TPC drift time) before the following event can be taken.

2.2.3 Off-line framework

The ALICE off-line framework is called AliRoot [6] and is based on Object-Oriented techniques. Its basic design features are modularity and re-usability. For instance it is possible to change the event generator or the transport Monte Carlo without affecting the user code. The codes from different detectors are independent and can be developed concurrently with minimal interference. Moreover, a maximum amount of backward compatibility is ensured while the system evolves.

AliRoot is developed starting from the supporting structure of the ROOT system [2], which provides integrated I/O, hierarchical object store, a C++ interpreter and advanced statistical analysis tools like multidimensional histograms, random number generators, multi-parametric fits etc. It also includes advanced visualization tools. The ROOT system is extended with modular software packages to support event generation, detector simulation, event reconstruction and data analysis. These libraries are loaded dynamically and the contained classes share the native ROOT services like object browsing and dictionary.

The ROOT system is interfaced with the Grid Middleware via the AliEn [125] system (developed by ALICE). Moreover, the PROOF [55] system extends ROOT

2. THE ALICE DETECTOR AT THE LHC

capabilities in parallel computing. Together AliEn and PROOF provide a distributed parallel computing platform for large scale production and analysis. Both systems have been used to obtain the results presented in this thesis. The entire AliRoot framework is written in C++ with some external programs, hidden to the user, in FORTRAN (i.e. PYTHIA 6 and other Monte Carlo generators).

The event simulation is provided via the interface to external generators or simple parametrizations of transverse momentum and rapidity spectra defined in function libraries. The physics processes at the parton level and the fragmentation results created by event generators are stored in a *kinematics tree*.

The detector response is simulated via different transport Monte Carlo packages and in particular in this analysis we used GEANT 3 [68]. The external magnetic fields are described by a parametrization based on measurement obtained with an accuracy of the order of 1.0 Gauss. The transport procedure simulates the detector response to each crossing particle. The energy deposition at a given point and time is called *hit*. The hits are converted into *digits* which take into account the detector and associated electronics response function. Finally, the digits are stored as *raw data* in hardware formats specific to each detector.

At this point the reconstruction can start. As a first step the different detectors perform local reconstruction such as clusterization, then a seeding procedure is used to start tracking based on Kalman filter [59, 60, 61, 102] (the tracking procedure will be further discussed in Sect. 2.2.4). Simulated events can be processed through the whole cycle and the reconstructed particles are compared to the generated ones. This allows us to study the software and detector performance.

The output of the reconstruction of both real and simulated events is the Event Summary Data (ESD): an object container which accommodates the reconstructed tracks, PID information, various decay topologies and particles reconstructed in the calorimeters.

The data analysis starts from the ESD. Additionally, analysis tasks can produce and take as input Analysis Object Datas (AODs) which contain condensed information from the ESD or specific information relative to each analysis. The

2.2 A Large Ion Collider Experiment (ALICE)

analysis framework is implemented in such a way that the user code is independent on the used computing scheme (local, PROOF or Grid) and permits the splitting of each analysis into a tree of dependent tasks. Each task is data oriented: it registers the required input data and publishes its output. Moreover, the AliRoot framework allows to include the Monte Carlo truth so that it can be used for correction studies such as efficiency or acceptance.

2.2.4 Performance

The track-finding procedure starts with the reconstruction of the primary vertex. The position of the primary vertex is then used as a constraint to initiate the tracking of primary particles in the TPC and subsequent detectors. Secondary tracks are found during a further tracking pass. Finally the reconstruction of secondary vertexes is performed.

2.2.4.1 Primary vertex reconstruction

The reconstruction of the primary vertex is based on the information from the two innermost ITS layers (SPD). We select pairs of reconstructed points in the two layers, which are close in azimuthal angle in the transverse plane (called *tracklets*). The position along z of the primary vertex comes from a linear extrapolation of the z coordinates of the two points. On the transverse plane a similar procedure is performed, though in this case the linear extrapolation is only an approximation due to the track bending in the magnetic field. However, since the transverse distance from the interaction point is small, the vertex position can be determined with enough accuracy to be used as a constraint in the first tracking pass. The resolution on the position of the primary vertex depends on the charged-particle density and is parametrized by the expression:

$$\sigma = \frac{\alpha}{\sqrt{dN_{ch}/d\eta}} + K \quad (2.4)$$

where the parameters α and K depend essentially on the residual misalignment of the pixel layers. In Fig. 2.7 we show the resolution of the primary-vertex position (along x and z coordinates) determined from measured data in PbPb collisions at $\sqrt{s} = 2.76$ ATeV. Instead of the track multiplicity, the resolution is plotted as

2. THE ALICE DETECTOR AT THE LHC

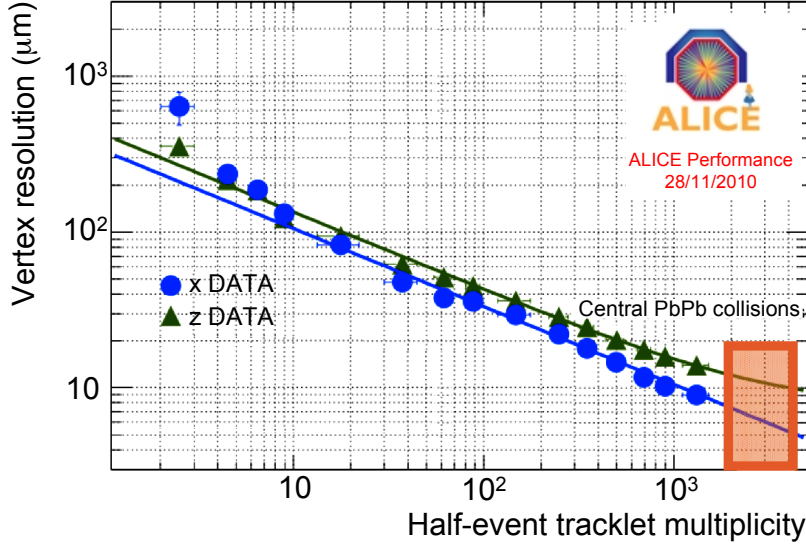


Figure 2.7: Primary vertex resolution in PbPb collisions at $\sqrt{s} = 2.76$ ATeV as a function of half of the ITS tracklet-multiplicity in the event. The resolution along the x and z coordinates is obtained dividing the tracks of the event in two random samples and reconstructing two vertices for the two samples. The difference between these two vertices is the measure of the resolution as a function of the half tracklet-multiplicity. Fit according to Eq. 2.4. More details in the text.

a function of the ITS tracklet multiplicity. The event is divided in two random samples, each containing half of the total tracklet multiplicity. For each sample a primary vertex is reconstructed. The difference between the position of the two vertices is a measure of the vertex position resolution. In the figure we also show a fit of the measured values according to Eq. 2.4. In an average pp event at $\sqrt{s} = 7$ TeV ALICE measured an average multiplicity of about 6 charged particles [19], which corresponds to a vertex resolution of about $200 \mu\text{m}$ along both coordinates. The resolution in central PbPb collisions is indicated in the orange box in Fig. 2.7 and it is an order of magnitude smaller than in the pp case.

2.2.4.2 Track reconstruction

Track finding and fitting in ALICE is based on the Kalman filter technique [59, 60, 61, 102]. The procedure starts with a set of initial seed values for the track parameters and their covariance matrix. The seeds are determined from space points reconstructed in the TPC. The space points positions are calculated from the center of gravity of the two dimensional clusters (in the pad-row and time directions). The seeding is done twice: once assuming that the track originated from the primary vertex and once assuming it originated elsewhere. In the first pass we combine the space points from a few outermost pad rows constraining them with the primary vertex position. The procedure is repeated several times, using sets of pad rows closer and closer to the TPC center. From every seed the tracking proceeds by propagating the track state vector of parameters and its covariance matrix to the next pad row. Then a noise term is added to take into account stochastic processes such as multiple scattering or energy loss fluctuations. If in the new pad row a space point is found compatible with the track prolongation, the track parameters and the covariance matrix are updated with the new information from this point. Finally, the seeding is repeated a second time, without the primary vertex constraint.

After this first step involving only the TPC, tracks are propagated to the outer layers of the ITS, starting with the highest momentum tracks, which have smaller ambiguities in the assignment of space points. If more than one space point candidate is found in the search window around the prolongation of a track, all possible assignments are used as different hypotheses. A decision is made only at the end based on the sum of the χ^2 along the track path in the ITS.

When tracking in the ITS is completed, we follow the tracks from the inner ITS layers outwards, always using a Kalman filter. In this case, we start with more precise track parameters and we try to eliminate improperly assigned points (outliers). The procedure continues beyond the TPC, assigning space points in the TRD and other outer detectors. It is then possible to perform a final *re-fit* procedure from outside inwards, in order to obtain the values of the track parameters near the primary vertex.

2. THE ALICE DETECTOR AT THE LHC

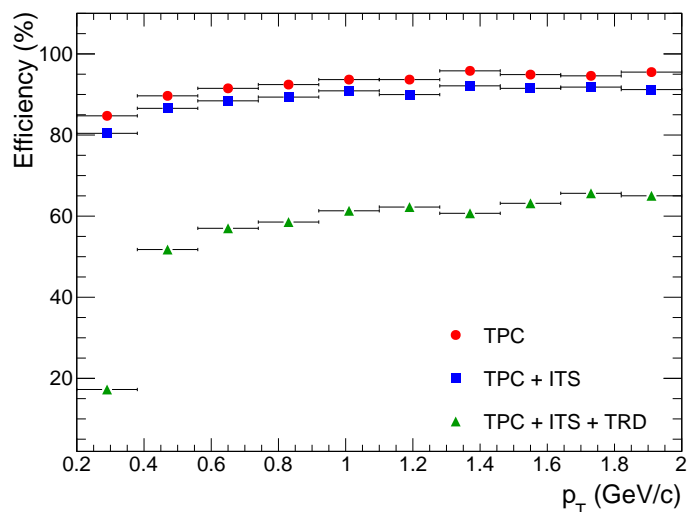


Figure 2.8: Track-finding efficiency in pp collisions for different combinations of the tracking detectors. The efficiency is largely reduced by the requirement of hits in the TRD. Figure adapted from [15].

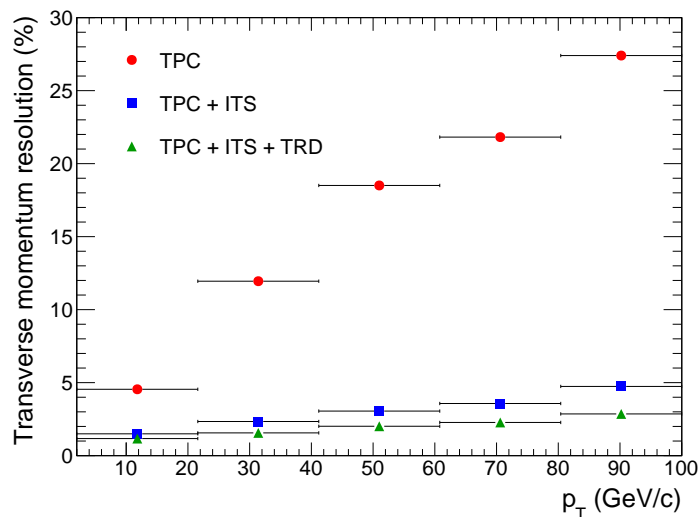


Figure 2.9: Transverse momentum resolution in pp collisions for different combinations of the tracking detectors. The TPC resolution is significantly improved by requiring also the ITS information. Figure adapted from [15].

2.2 A Large Ion Collider Experiment (ALICE)

In Fig. 2.8 we show the tracking efficiency as function of the particle transverse momentum for different combinations of detectors. In Fig. 2.9 we show the transverse momentum resolution. Both plots refer to pp collisions. These results justify the choice made in this thesis to consider only tracks which come from the combined information of ITS and TPC. In particular the ITS information largely improves the TPC momentum resolution of about a factor 3 for p_T below 20 GeV/c, having only a 5% effect on the tracking efficiency. On the other hand we decided to neglect the TRD information since it has a large impact on the tracking efficiency, without improving significantly the momentum resolution.

2. THE ALICE DETECTOR AT THE LHC

3

Transition Radiation Detector and Read-out Board testing

The Transition Radiation Detector (TRD) [1] serves the main purpose to provide electron identification for momenta above 1 GeV/ c , a domain in which the energy loss measurement of the TPC loses its electron/pion discriminating power. This is achieved by exploiting the Transition Radiation¹ (TR) produced by electrons traversing a radiator and their specific energy loss in a Xe/CO₂ gas mixture. A pion rejection factor of 100 (for 90% electron efficiency) can be achieved in this way [50]. Moreover, the TRD can trigger on high-transverse-momentum charged-particles, contributing to the ALICE L1 trigger. As already mentioned in Sect. 2.2.4, the TRD also improves the combined ITS and TPC tracking resolution by increasing the lever arm. The TRD momentum resolution (at a multiplicity of $dN_{ch}/d\eta = 2000$) for a 5 GeV/ c particle is 3.5% [15].

In this chapter we give a short description of the TRD system, with particular emphasis on its read-out electronics and on the Read-Out Board (ROB) testing procedure. The reason is that part of this thesis work was dedicated to the

¹TR [84] is produced by relativistic charged-particles when they traverse the boundary between two media with different dielectric constants. The energy loss depends on the particle's Lorentz factor γ and produces photons in the keV range mostly directed in the direction of motion of the particle, peaked at an angle of the order of $1/\gamma$. The intensity of the emitted radiation is roughly proportional to the particle's energy.

3. TRANSITION RADIATION DETECTOR AND READ-OUT BOARD TESTING

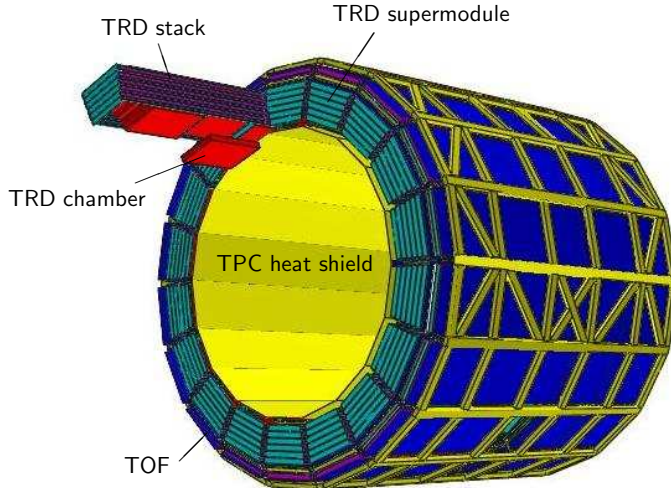


Figure 3.1: Schematic representation of the TRD system layout. Shown are 18 supermodules, containing 30 read-out chambers each (red) and arranged in 6 radial layers. Figure from [15].

optimization of this testing procedure. In the following sections we refer to large extent to [1, 15, 121].

3.1 Detector design

The TRD consists of 540 individual detector modules, arranged in cylindrical geometry outside the TPC barrel. They form a cylindrical shell with an inner radius of 2.9 m, an outer radius of 3.68 m and extending 7 m along the beam direction. The system covers the pseudo-rapidity range $|\eta| < 0.8$ and the full azimuth (for complete installation). The single modules are arranged in 18 trapezoidal elements (supermodules), each containing 30 modules grouped in 5 stacks along z and in six layers in radial direction. The TRD layout is sketched in Fig. 3.1.

Each TRD module consists of a layer of radiating material (Rohacell/polypropylene sandwich, 48 mm thick) on the side facing the interaction point, followed by a gas drift volume (30 mm thick) and a multi-wire proportional section (7 mm

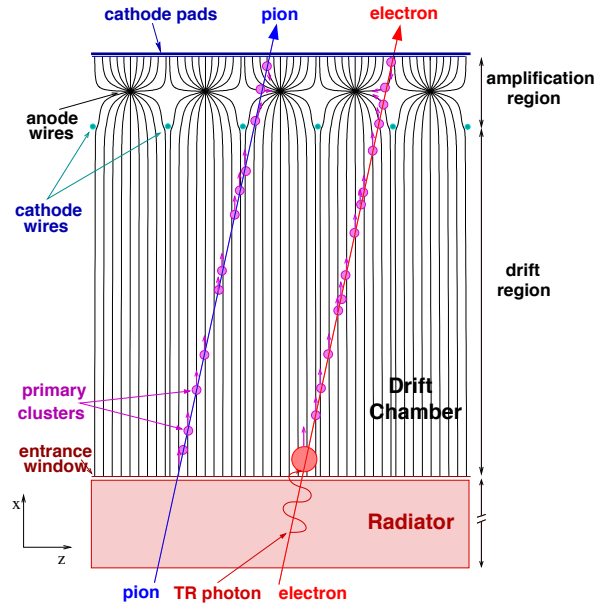


Figure 3.2: Schematic rz cross-section of a TRD module illustrating the detector working principle. Charged particles traversing the gas volume create pairs of electrons and ions. The ionization electrons start drifting under the effect of an electric field. Electrons also give rise to TR (more details in the text). The ALICE r coordinate is indicated here with x , in the local detector reference system. Figure from [15].

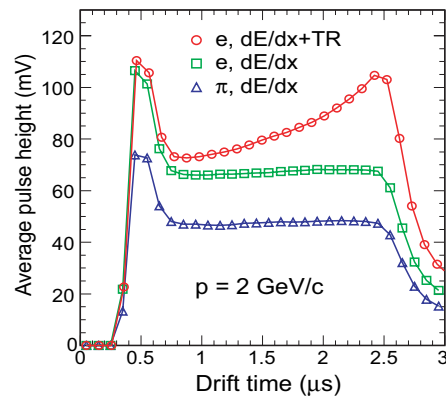


Figure 3.3: Average pulse height as a function of drift time for electrons with radiator (red dots), electrons without radiator (green squares) and pions (blue triangles). Beam-test data. Figure from [15].

3. TRANSITION RADIATION DETECTOR AND READ-OUT BOARD TESTING

thick) with pad read-out. The counting gas is a mixture of 85% Xe and 15% CO₂.

In Fig. 3.2 we show a schematic rz cross-section of a TRD module, illustrating the detector working principle. When charged particles traverse the gas volume, pairs of electrons and ions are created and start drifting under the effect of an electric field towards their respective electrodes (the electrons move toward the amplification region). In addition, particles exceeding the threshold for TR production (Lorentz factor of about 1000) give rise to X-ray photons in the energy range of 1–30 keV. In the particular gas mixture chosen¹, the conversion probability of such photons is maximal at the very beginning of the drift region. In proximity of the anode wires, the signal from both the initial ionizing particle and eventually the TR, is induced on the read-out pads. The TRD system is immersed in the L3 magnetic field, which causes a bending of the tracks in the $r\phi$ plane. The radius of curvature of a track in the bending plane is a direct measurement of its transverse momentum.

In Fig. 3.3 we show the average amplitude of the induced signal versus drift time, measured during a beam-test for particles with a momentum of 2 GeV/ c . Red dots represent the average electron signal in the TRD, while green squares correspond to a configuration without radiator at the chamber entrance. Blue triangles show the pion signal. From this plot we can see the contributions to the pion/electron separation capability. On the one hand electrons have a higher specific energy loss as compared to pions. On the other hand, electrons above 1 GeV/ c have a sufficient Lorentz factor to produce TR, contrary to pions. The TR signal generates an enhancement at high drift times in the electron signal, not present in the pion signal.

3.2 Front-end electronics

The TRD front-end electronics (FEE) is directly mounted on the chambers' back-plane. A single-chamber pad-plane consists of 16 (12 for the most central chambers) rows of 144 pads (in $r\phi$ direction). The overall number of channels is $1.18 \cdot 10^6$. The read-out pads feed the Pre-Amplifier and Shaping Amplifier

¹For a typical TR photon energy of 10 keV, the absorption length in Xe is 1 cm [1].

(PASA) chip [135]. The outputs of the differential amplifier are digitized and pre-processed in order to identify high- p_T track candidates (called *tracklets*). These functionalities are implemented in the TRacklet Processor (TRAP) chip [115]. Both PASA and TRAP are mounted on a single Multi-Chip Module (MCM). Groups of 17–18 MCMs are assembled on the Read-out Board (ROB), a Printed Circuit Board (PCB) described later in more detail. At complete installation the TRD system will count 4,104 ROBs. The TRAP chips are connected via the redundant daisy chained network Slow Control Serial Network (SCSN), used to configure them. Within the SCSN data is exchanged in 76 bits packets called *frames*¹. Moreover, the TRAP chip implements a Network Interface (NI) for data collection from other TRAP chips. The Detector Control system (DCS) is handled by a set of boards (one per chamber) which provide configuration, monitoring and control of the front-end electronics. Among other functionalities, the DCS boards serve as SCSN masters, are responsible for the TRAP configuration and distribute clock and trigger signals. Moreover, two ROBs per chamber carry an Optical Read-out Interface (ORI) board, shipping the data collected by a half chamber to the read-out tree. The TRD signals are read-out with a sampling rate of 10 MHz, so that the signal amplitude on the pads is sampled in time-bins of 100 ns. Each data-point is therefore characterized by four coordinates: chamber, pad-row, pad-column and time-bin.

3.2.1 Pre-amplifier and Shaping Amplifier (PASA)

The PASA circuit is the first element of the TRD read-out chain. Being a charge-sensitive pre-amplifier, its noise is mainly determined by the input capacity. For this reason (and to cope with the high data rate) the FEE is mounted directly on the detector chambers. Each chip has 18 input channels and 21 output channels. The extra outputs are fed into the analog inputs of the TRAPs belonging to neighbouring MCMs, this signal duplication allows a continuous tracklet calculation across MCM boundaries.

The PASA is a folded cascode with differential output. It has an amplification

¹In each frame only 32 bits are dedicated to the data, the rest contains addresses, commands etc.

3. TRANSITION RADIATION DETECTOR AND READ-OUT BOARD TESTING

of about 12 mV/fC per channel [135] and shapes each signal to a semi-Gaussian distribution. The pulse width is 120 ns (FWHM) with a peaking time of about 110 ns and a maximum peak-to-peak amplitude of 2 V. The equivalent noise at the input capacity of 25 pF is 850 electrons and the power consumption is about 15 mW/channel. The PASA chip is developed with the 0.35 μm Complementary Metal Oxide Semiconductor (CMOS) technology and covers an area of 21 mm².

3.2.2 Tracking Processor (TRAP)

The Tracking Processor (TRAP) is a mixed-mode chip, which comprises 21 10-bits Analog to Digital Converters (ADCs) with a sampling frequency of 10 MHz, a digital filter and processing units. The core of the TRAP chip is a group of 4 RISC¹ CPUs that calculate the slope of a tracklet in the bending plane and the charge deposited along the track in configurable windows. The chip design is realized in the UMC² 0.18 μm process.

For testing purposes, the PASA chip implements a programmable test-pattern generator, allowing the TRAP chip to program a charge amount to be injected into the PASA input of specific channels. Moreover, the event buffer in the TRAP can be pre-loaded with test events and used as a defined data source instead of the ADCs to test the read-out chain.

3.2.3 Multi Chip Module (MCM)

The Multi Chip Module (MCM) is the basic building-block of the TRD FEE, hosting the PASA and TRAP chips. The MCM is a custom-designed PCB with an area of 4x4 cm². It is designed as Ball Grid Array (BGA) soldered directly to the ROB. The silicon chips are glued to the PCB substrate and are interconnected by gold wires with a diameter of 25 μm . The PASA outputs are bonded chip-to-chip to the TRAP ADC inputs. An encapsulation resin called *glob-top* covers

¹Reduced Instruction Set Computing

²<http://www.umc.com/English/>

the chips in order to guarantee stability against thermal and mechanical stress. The cooling system, circulating water at a temperature of about 18° , is glued directly onto the glob-top. Fig. 3.4 shows the PASA and TRAP chips assembled on the MCM without the protecting glob-top (left) and the MCM final realization (right) including the glob-top .

3.2.4 Read-out Board (ROB)

The MCMs are hosted by custom-designed Read-out Boards (ROBs [124]), which are PCBs with an area of $46 \times 30 \text{ cm}^2$, integrating voltage regulators, detector control interface boards and optical data links. Moreover, they distribute system clock and trigger signals. Each board carries 12 voltage regulators with fast-response and ultra low drop-out voltage. They provide the nominal voltages to power-up the MCMs. Namely 3.3 V are required by the PASA chip and some digital component of the TRAP chip and 1.8 V are required by the ADCs and other digital components of the TRAP chip. The analog and digital supplies are partially isolated on the ROB. Each board hosts 17 or 18 MCMs, interconnected via the SCSN network. Of those, 16 MCMs are connected to the read-out pads and one is responsible for merging the data produced by the ROB: the so-called Board Merger (BM). Fig. 3.5 shows an example ROB. The main components are also indicated in the picture.

One of the critical aspects of the ROB design is the minimization of noise, therefore the supply voltage and ground routings are distributed over four planes: two carrying analog voltages (for PASA and ADCs) and two carrying digital voltages (for TRAP). The analog PASA ground is fully decoupled. Moreover, since the various ROB components operate at different frequencies, to reduce the overall noise and interference a decoupling capacitive network is created by small groups of capacitors below each MCM.

The TRD read-out chambers have 12 different sizes and either 6 or 8 ROBs can be adjusted on each chamber according to its size. Each ROB provides the infrastructure to perform different tasks according to its position on the chamber. This leads to 7 different ROB types called: 1A, 3A, 4A, 1B, 2B, 3B and 4B (type 2A does not exist). Each chamber is locally divided into an A- and B- side along

3. TRANSITION RADIATION DETECTOR AND READ-OUT BOARD TESTING

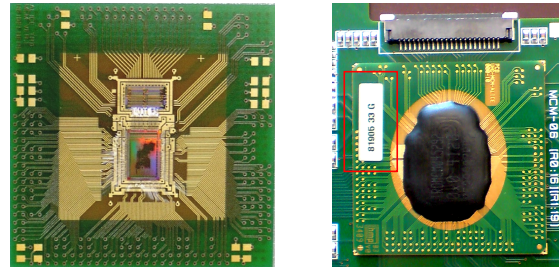


Figure 3.4: The TRD MCM, integrating the PASA (top chip in left image) and TRAP (bottom chip in left image) chips without protective glob-top and MCM fully assembled on the ROB (right image). The MCM label number is also indicated in the figure (right).

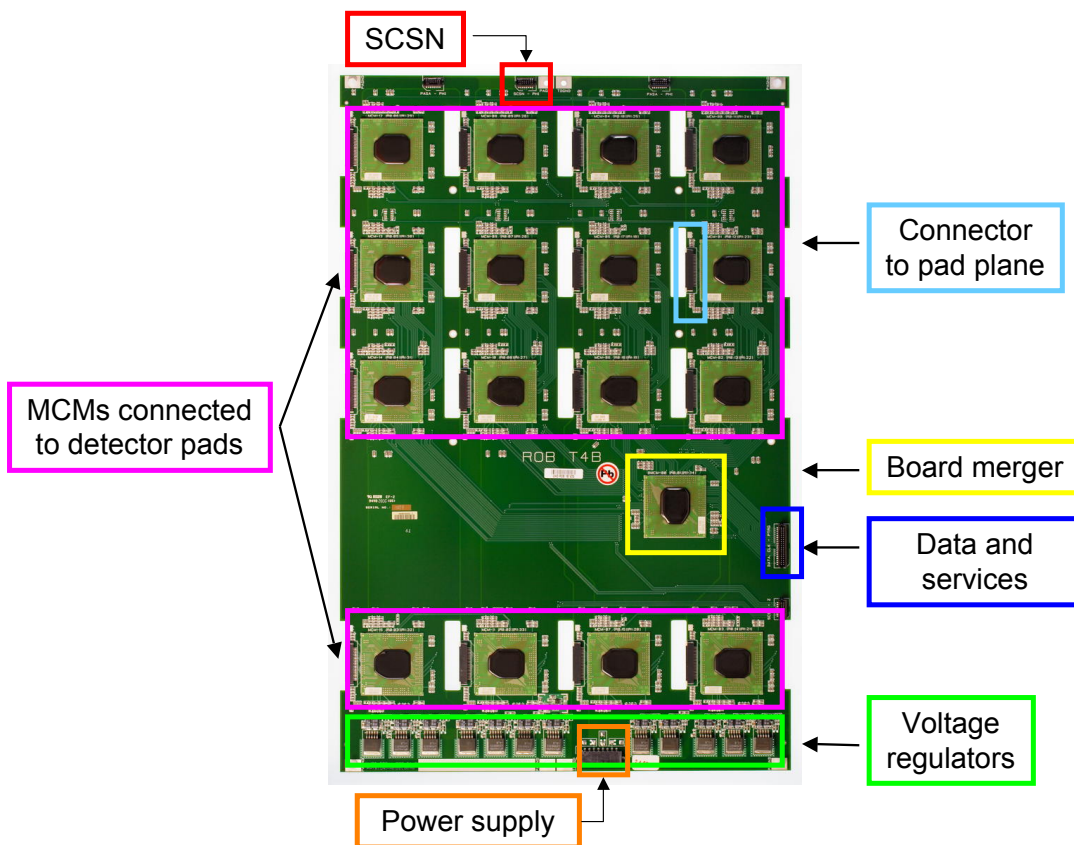


Figure 3.5: A TRD ROB integrating 17 MCMs. The functionalities of the different MCMs are indicated, as well as the main elements implemented on the board.

the ϕ direction in order to label the different ROB types. Boards of the type 3A and 3B have an additional MCM called Half Chamber Merger (HCM) that collects the data from up to 3 neighbouring boards and ships it to the ORI board, mounted on the same ROB. The ROB type 2B includes the DCS board.

3.3 Read-out Board testing procedure

Each TRD FEE component is subject to a set of stringent quality tests since it is supposed to work reliably for about 10 years under the high radiation exposure at the LHC [97]. Indeed, after the installation in the ALICE barrel the electronics components will not be easily accessible. The various testing steps included a radiation-tolerance analysis aimed to test the FEE design. Moreover, we test the performance of each silicon wafer hosting the chips. The MCMs undergo an autonomous testing and classification procedure at the production site. The classification is used to mount the MCMs in strategic locations of the ROBs, for instance lowest quality MCMs become BM or HCM. An automatic and comprehensive testing of the ROB functionalities was designed and implemented at the University of Heidelberg and is described in [121]. In this section we summarize the main aspects of the ROB testing procedure. The new feature introduced during this thesis is the implementation of the automated tests of the ROB's analog part (described in Sect. 3.3.3). Moreover, we investigated a new strategy to identify MCMs with missing ID (see Sect. 3.3.4). Some other miscellaneous activities include the on-line documentation of the testing procedure¹, an automated backup of all test results and software maintenance activities.

The testing routine requires a comprehensive assessment of the ROB performance at different levels. At the MCM level, the PASA and TRAP chips are tested in parallel. In particular this includes a diagnostics of all the internal functional blocks of the TRAP chip (for a detailed description see [121]). At the single-ROB level, the interconnection between MCMs and the integrity of the transferred data are tested. In the special case of ROB types 2B (hosting a

¹Available at (password protected):

https://wiki.kip.uni-heidelberg.de/ti/TRD/index.php/ROB_production_monitoring

3. TRANSITION RADIATION DETECTOR AND READ-OUT BOARD TESTING

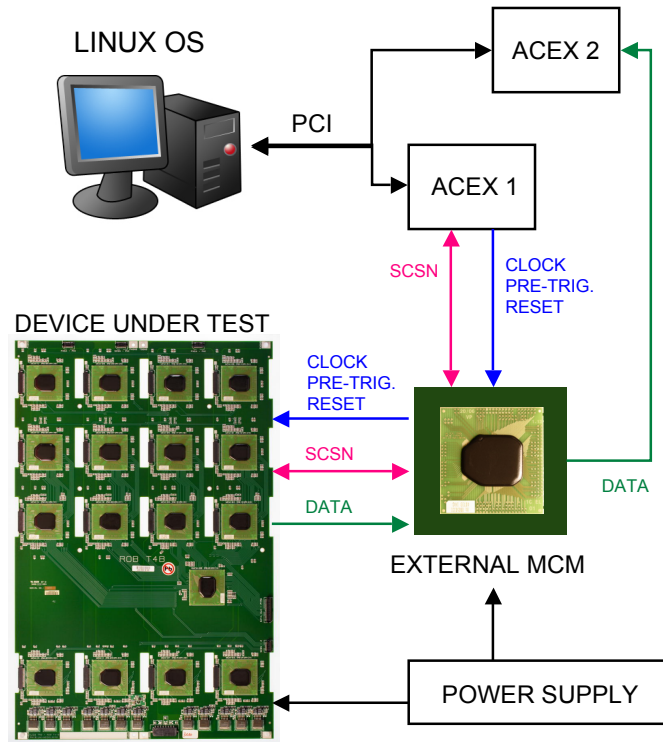


Figure 3.6: Schematic layout of the most simple ROB test system set-up.

DCS board) and 3A and 3B (hosting an ORI board) the boards' connectivity to the relevant MCMs is also tested.

The half-chamber configuration needs to be tested as well since it provides the output read out by the TRD Global Tracking Unit (GTU) [1]. Nevertheless, the half-chamber arrangement is not suitable for an automated mass-test environment and its conditions are emulated electronically (more in Sect. 3.3.1).

3.3.1 System set-up

The chamber-level configuration of the SCSN and of the read-out tree have been adapted to allow the operation of a single stand-alone ROB. In this case the DCS boards are not used and the SCSN controller is located on a custom general-

3.3 Read-out Board testing procedure

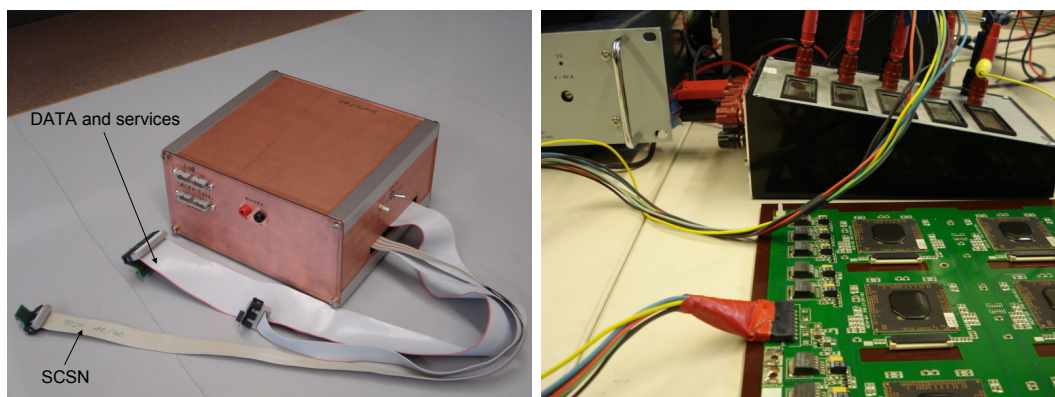


Figure 3.7: Box containing the single-MCM external PCB (left) and connection of the power supply lines to the ROB (right).

purpose PCI¹ card based on an FPGA² of type ACEX-EP1K100. In the following it will be called *ACEX board (card)* [121]. The ACEX board serves as interface between the test software and the device under test (DUT). It features a PCI connector that allows direct connection to a suitable computer mother board, used in the ROB-test system. Also clock, trigger and reset signals are generated by the ACEX board and sent to the HCM in opposite direction to the data flow. The HCM distributes those signals to the BM, which finally propagates them to all other MCMs on the board. Note that HCM and BM are not connected to the detector pads, therefore their analog performance is irrelevant.

In the test set-up, for board types 1A, 1B, 2B, 4A and 4B (without HCM) data is read-out by a dedicated external single-MCM board, hosting an ORI board. The ORI optical link is received by a second ACEX card, equipped with a custom optical receiver, which ships the received information to the computer via PCI. The single-MCM board also distributes control signals generated by the first ACEX card. This configuration constitutes the first class of test set-up. The set-up is illustrated in Fig. 3.6. Fig. 3.7 shows the box containing the single-MCM external PCB (left) and the connection of the power supply lines to the

¹Peripheral Component Interconnect

²Field Programmable Gate Array

3. TRANSITION RADIATION DETECTOR AND READ-OUT BOARD TESTING

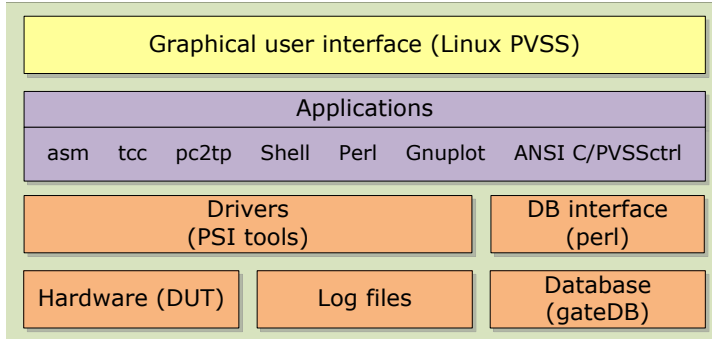


Figure 3.8: The ROB test system software architecture. Figure from [121].

ROB (right).

A second class of test set-up is needed for board types 3A and 3B. These ROBs carry an HCM whose NI ports must be tested. In the full-camber implementation the HCM is interfaced to the BMs of the other three (two) boards belonging to the same half chamber. In the test configuration these external BMs are emulated by 3 external single-MCM boards. Moreover, in this test system class the optical read-out is implemented on board, since ROB types 3A and 3B carry their own ORI as mezzanine board.

3.3.2 System software

The ROB test software architecture is summarized in Fig. 3.8. Software modules are logically grouped into three levels: drivers, applications and user interface. The driver layer handles the communication with the hardware components (i.e. TRAP configuration or ORI read-out). In particular a library called PCI and Shared memory Interface (PSI) [7] was developed at the University of Heidelberg for accessing PCI devices and shared memory from user space programs. The application level acts mainly on the data level: corrupted SCSN frames or data integrity are immediately signalled to these applications. Moreover, the applications layer is responsible for the preparation of the TRAP configuration and for the data-flow control. A custom compiler for the TRAP configuration (the TRAP

3.3 Read-out Board testing procedure

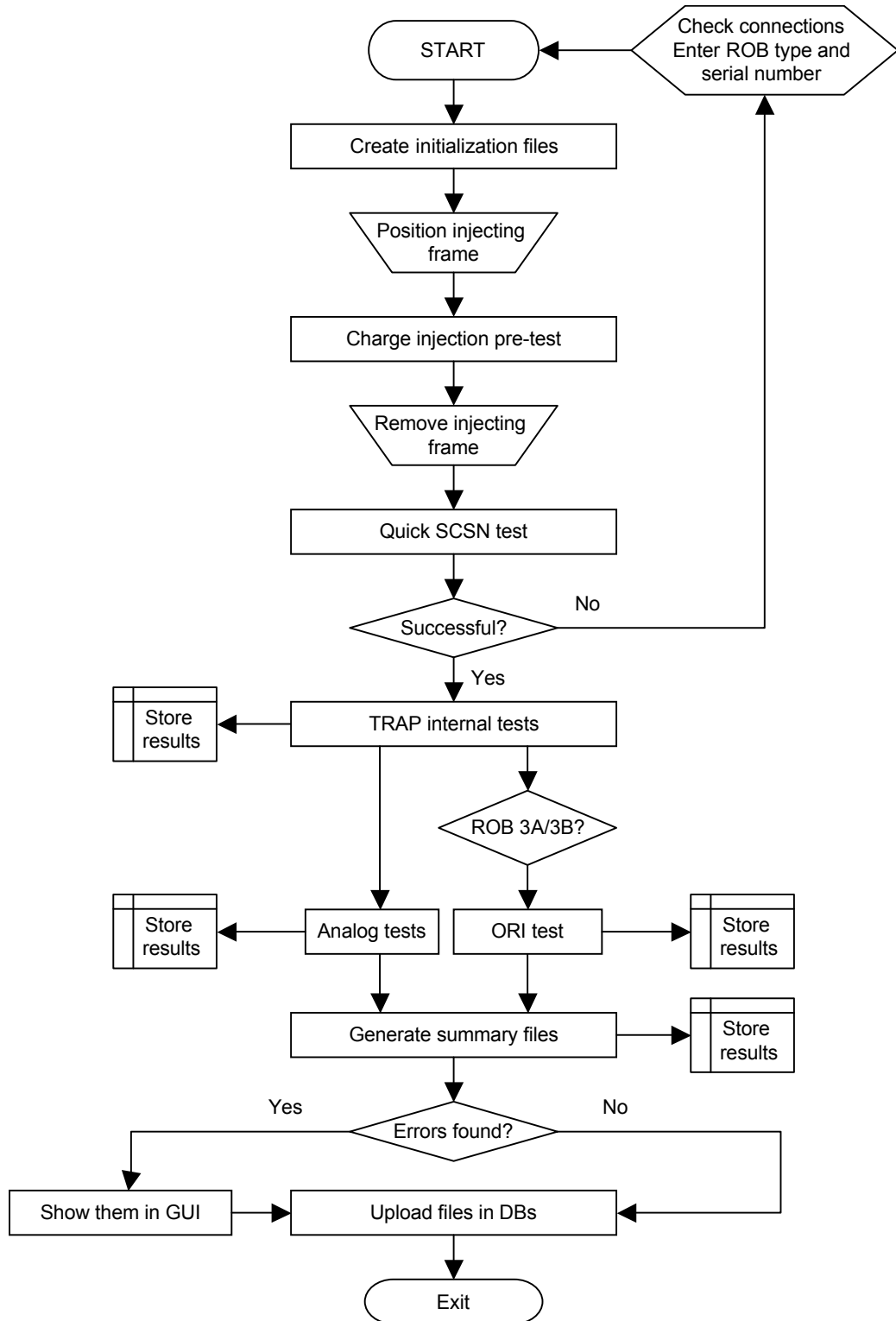


Figure 3.9: Simplified flow diagram of the test routine. Figure adapted and updated from [121].

3. TRANSITION RADIATION DETECTOR AND READ-OUT BOARD TESTING

Configuration Compiler *tcc*) was developed at the University of Heidelberg, as well as a program implementing the interface between the ACEX board and the SCSN (*pc2tp*). The highest level of the software architecture is the Graphical User Interface (GUI) which automatizes the test procedure. In this way, the mass test of the complete ROB production can be handled also by operators which are not expert of the TRD FEE . The ROB test GUI was developed with the SCADA¹ system PVSS² [3].

The automatic testing procedure starts after exposing the ROB to 6 thermal cycles reaching a temperature of 95°. This procedure tests the board resistance to extreme temperatures. The flow diagram of the automatic procedure is simplified in Fig. 3.9. The only human interventions are the connection of the ROB to the testing set-up, the initialization of board type and serial number and the positioning of the frame for the charge-injection test (see Sect. 3.3.3). The *Quick SCSN test* checks if all SCSN slaves are reachable before starting four full runs of *TRAP internal tests*. In the case of ROB types 3A/3B, the optical read-out interface is also tested. The *Analog tests* (see Sect. 3.3.3) verify the correct operation of the signal transmission from the PASA input to the TRAP chip. The summary files produced at the end of the test routine are a filtered text file containing the most relevant informations and a detailed file in PDF format including all messages from TRAP internal tests and the plots from the analog tests. These files, plus a compressed tar archive containing all the files generated during the test, are uploaded to the *global ALICE TRD electronics database* (gateDB). The GUI also offers the opportunity to repeat individual tests or perform manually some additional test for a better diagnose of potential problems.

3.3.3 Analog tests

A schematic view of the critical points in the PASA to TRAP interface is shown in Fig. 3.10. The points labelled with A are the input/output reference voltages

¹Supervisory Control and Data Acquisition

²From German: Prozessvisualisierungs- und Steuerungssystem (Process Visualization and Control System).

3.3 Read-out Board testing procedure

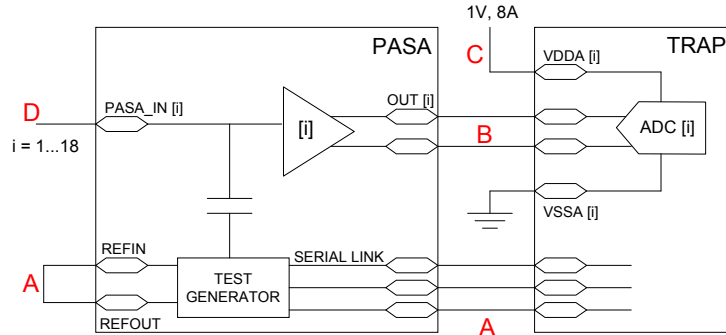


Figure 3.10: Schematic view of the PASA/TRAP interface and critical points. A: reference voltage of the PASA internal test-pattern generator and its serial link to the TRAP chip. B: interface between PASA and TRAP. C: ADCs’ reference voltage. D: PASA input connected to the detector.

of the PASA internal test-pattern generator (see Sect. 3.2.2) and the serial link through which the TRAP chip can program the PASA test-pattern generator. A problem in the points labelled with A leads to a missing test-pulse in all the channels. The label B indicates the bondings between the PASA outputs and the ADC inputs on the TRAP chip. A problem there manifests as a wrong baseline and a high noise in single channels, while we observe constant ADC outputs in single channels in case of problems in C, which is the differential reference voltage of the ADCs. The points labelled with A, B and C can be probed via test pulse. We labelled with D the inputs of the PASA chip, which collect the signals coming from the detector. A faulty connection in D can only be detected by an external signal source at the PASA input. This is done during the *Charge-Injection pre-test*, when a sinusoidal signal is induced at the 18 input channels of every read-out MCM on the ROB. To realize the proper geometrical configuration of the MCM arrangement on the board, we use an *injecting frame* (see Fig. 3.11). The frame is made out of a dielectric plastic material and is equipped with thin metal foil strips placed in correspondence to the MCM input connectors. The signal is induced via these foils through some millimeter of air in between frame and connector. A set of RC-filters between consecutive lines ensures a phase shift of the signals received by the single MCM from two neighbouring ones (for an

3. TRANSITION RADIATION DETECTOR AND READ-OUT BOARD TESTING

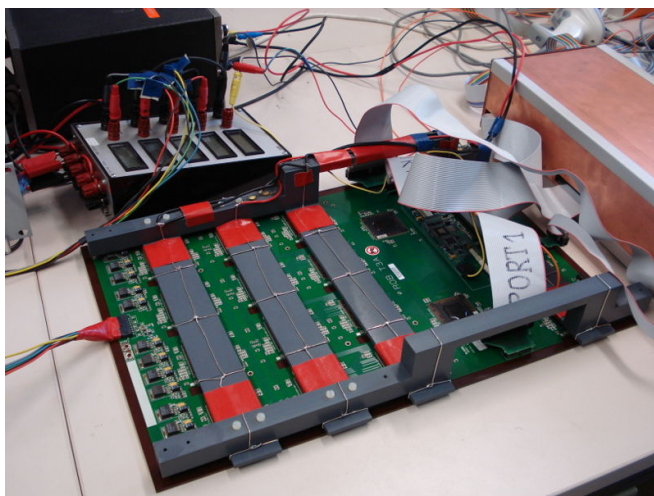


Figure 3.11: Frame used to inject signals at the PASA input positioned on a ROB.

easier visualization of the 18 read-out channels). The ADC output is shipped to the computer via an ORI board and analysed by a C-program. For a given MCM, if at least 5 samples for each channel are over a pre-defined threshold, the test outcome is positive. The threshold value depends on the input signal amplitude. For the typical input signal of 2 V amplitude (and 500 kHz frequency) the threshold value is 100 ADC counts¹. Fig. 3.12 shows an example of test output for a single MCM. The test results are stored in a bi-dimensional matrix representing MCM x ADC-channel. A null entry corresponds to a positive test outcome, while a 1 corresponds to the test failure for that particular MCM and ADC channel.

The charge-injection test proved particularly useful in the diagnose of broken bondings at the PASA input in a batch of boards received in June 2008. The problem was due to the cooling phase of the glob-top implementation on the MCM, which provoked a mechanical stress on the bondings at the edge of the glob-top area. The problem was solved by the MCM manufacturer² by extending

¹An ADC count can range from 1 mV to 1.4 mV, according to the chosen configuration.

²MSC (Microcomputers Systems Components) VERTRIEBS GMBH

<http://www.msc-ge.com/en/home/home/index.html?locale=en>

3.3 Read-out Board testing procedure

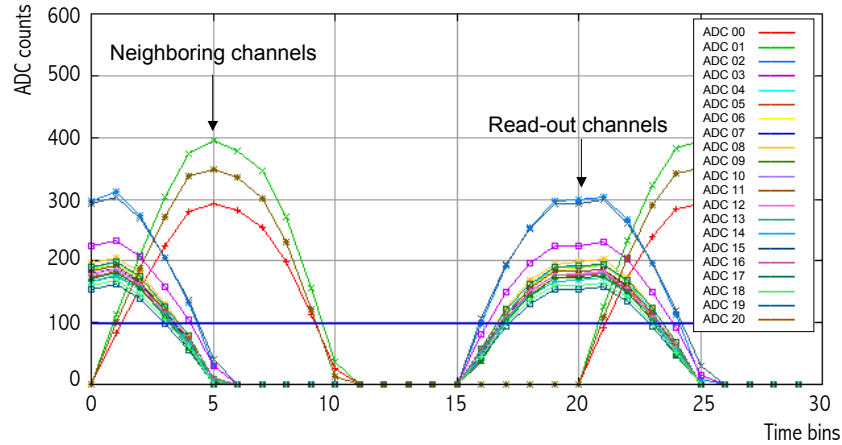


Figure 3.12: Output of the charge-injection test. The applied threshold of 100 ADC counts is also indicated in the plot. In this example there are no faulty channels.

the area covered by the resin further beyond the PASA input bondings.

In order to test points A, B and C a test-pulse is sent to all the ADC channels by configuring the proper TRAP register (PASAPR1) via SCSN with the pc2tp program. This procedure programs the PASA serially to generate a test signal within its own test generator circuit. The TRAP data memories (DMEM) are then read-out via ORI and the test data are stored in a text file for each MCM. Moreover the pc2tp program can be run in the so-called *statistical mode*, which accumulates on-line the sum of the ADC values. From this information, a program reads the DMEM via SCSN and evaluates the signal baseline and area. The baselines and areas of each channel are stored in two additional text files. In a second step, the output text files are analysed by three different C-programs, each aiming to detect specific signal problems. The first program verifies that the signal area falls within an upper and lower threshold. The choice of the allowed range was based on the analysis of a sub-sample of fully operational ROBs and corresponds to 3σ of the area distribution. However this criterion does not allow the detection of other two common signal pathologies: the *baseline shift* and the

3. TRANSITION RADIATION DETECTOR AND READ-OUT BOARD TESTING

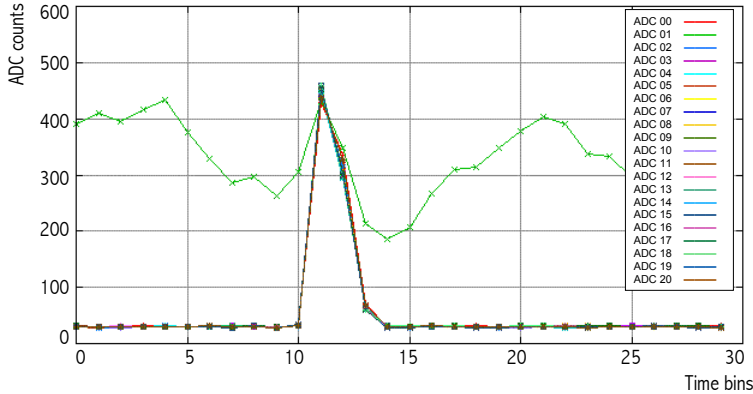


Figure 3.13: Output of the analog test for an MCM with baseline shift in 1 channel.

phase shift. The baseline shift is shown in Fig. 3.13. Coloured lines are the output signals of the 21 ADC channels, the baseline of one channel has a completely different value with respect to the average, indicating a problem in the critical point B for that specific channel. In the normal TRAP configuration during the ROB test, the baseline value should be within 25 and 30 ADC counts.

In some cases we observed a phase shift of the signal from neighbouring MCMs, as shown in Fig. 3.14, which could in principle introduce a bias in the evaluation of the signal centroid. To study this effect we evaluate the average time shift by fitting the signals according to the expected signal shape [51]:

$$S(t) = A \left(\frac{t}{\tau} \right)^n \exp \left\{ -\frac{t}{\tau} \right\} \quad (3.1)$$

where the amplitude A and the time constant τ are the fit parameters. Then we compare the centroid's distribution of a sample of MCMs showing a phase shift with a sample of good MCMs. The analysis of such boards shows that the error introduced is negligible: in average the time shift is 1.5 ns, which corresponds to about $20 \mu\text{m}$ along the drift coordinate (assuming the nominal drift velocity of $1.5 \text{ cm}/\mu\text{m}$), while the nominal resolution in this direction is at least one order of magnitude larger [1]. The test results are stored in a matrix representing MCM x ADC-channel. A null entry corresponds to a positive test outcome, 1 a wrong

3.3 Read-out Board testing procedure

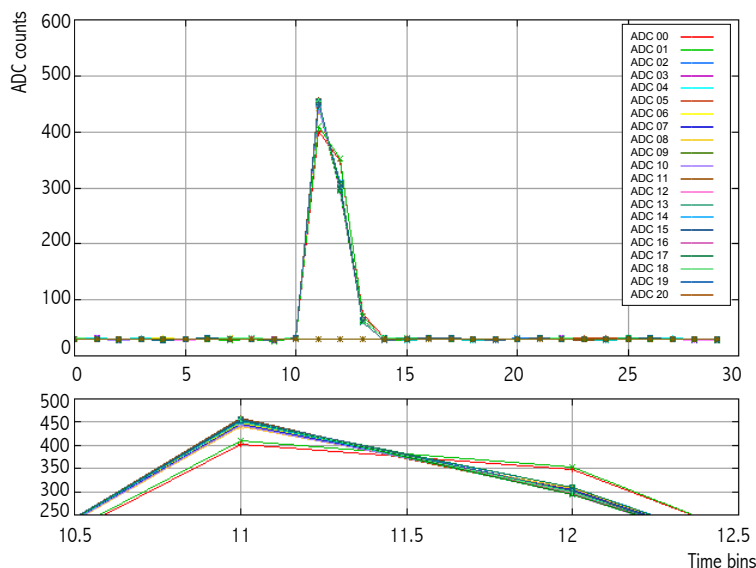


Figure 3.14: Output of the analog test for an MCM with phase shift in 2 channels.

area value, 2 a baseline shift and 3 a phase shift. The test outputs are included in the global ROB-test output files.

Among about 2,500 ROBs tested between 2008 and 2011, 5% failed one of the analog tests described above.

3.3.4 Multi Chip Module identification

Each MCM must be uniquely identified in an automatic way and the ROB on which it is mounted should also be known. In this way in case of failure of an MCM on a specific board, the test results can be retrieved and used to diagnose the problem. Since after their assembly on the MCM the TRAP (and PASA) chips cannot be replaced without destroying the MCM, in the following we will refer equivalently to MCM or TRAP identity. The MCM can be identified by two numbers. The *laser number*¹ is written by laser on a TRAP register (CHIPID) and identifies a single TRAP chip. Since this number can be easily read-out via

¹The laser number is made of 18 bits: the upper 8 refer to the wafer identity, the lower 10 indicate the chip position on the wafer.

3. TRANSITION RADIATION DETECTOR AND READ-OUT BOARD TESTING

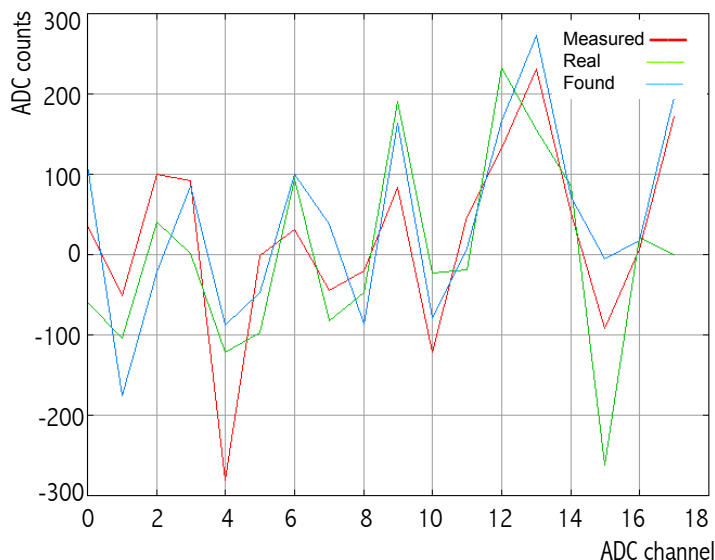


Figure 3.15: Baseline pattern for one TRAP ADC: the average baseline value is plotted as a function of the channel number. Reference from [51].

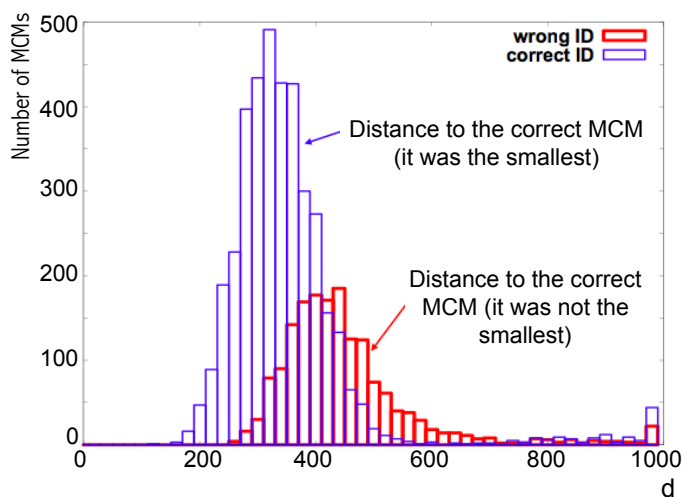


Figure 3.16: Distribution of the squared distance d . Blue histogram: correctly identified MCMs (the reference pattern with smaller distance from our measurement belongs to the same MCM). Red histogram: distance of our measurement from the correct reference pattern, although it is not the smallest (the MCM is wrongly identified). The pedestal correction is not applied in this measurement. Reference from [51].

3.3 Read-out Board testing procedure

software, it is particularly useful to identify automatically an MCM during the ROB test procedure. Unfortunately the laser number can be ambiguous because of writing errors. Moreover, in the last 25 wafers produced (about 20% of all TRAP chips) the CHIPID register was not written.

The *label number* is composed of 7 digits¹ and even though it is not strictly unique, it is the most reliable reference for the MCM identification. This number is written on a label glued to the MCM PCB surface (see Fig. 3.4).

Different strategies have been envisaged to solve the problem of missing laser numbers. The first attempt has been to run a perl script at the end of the test procedure, which would prompt the user to insert manually the label number of ambiguous MCMs. This procedure has the double side effect of increasing the overall test duration and to introduce errors due to the difficulty of reading the small numbers printed on the MCM label.

A second strategy is based on the assumption that the ADC *baseline pattern*² of each MCM is known and does not change with time. Therefore, we can compare the baselines measured during the ROB test with reference measurements. For each MCM that needs to be identified, we evaluate the distance of its baseline pattern from all the reference patterns contained in a local data-base (stored during the single-chip tests, prior to the assembly on the ROB). The squared distance between two patterns is defined as:

$$d = \sum_{i=0}^{17} \left[\left(b_i^{meas} - b_i^{ref} \right)^2 + rms_i^2 \right] \quad (3.2)$$

where b^{meas} is the mean value of the baseline (averaged over the 30 time-bins) measured during the ROB test, b^{ref} is the reference measurement and rms is the statistical noise (root mean square). The sum runs over the 18 read-out ADC channels (the 3 channels from the neighbouring MCMs are not considered). The MCM identity is that of the reference measurement that minimizes d . Fig. 3.15

¹The first 5 digits identify the *nutzen* PCB from which 9 MCMs are cut-out. The last 2 digits indicate the MCM position on the nutzen.

²We call baseline pattern of an ADC the baseline value (averaged over time-bins) as a function of the ADC channel number.

3. TRANSITION RADIATION DETECTOR AND READ-OUT BOARD TESTING



Figure 3.17: EPSON GT 200000 scanner used to take picture of the ROB for the identification of the MCMs.

shows the baseline pattern for one ADC. For this measurement the pedestal correction¹ is not activated, contrary to the normal test procedure, as it can be seen by the baseline values as compared to i.e. Fig. 3.13. The red line is the value measured during the ROB test procedure, the green line is the reference measurement for the same chip and the blue line is the reference baseline pattern with minimal distance from the measured one.

We studied the feasibility of the method with a sample of about 8,300 MCMs with known identity. Fig. 3.16 shows the distribution of the squared distance d . The blue histogram refers to correctly identified MCMs, where the reference pattern with smaller distance from our measurement belongs to the same MCM. The red histogram is the distance of our measurement from the correct reference pattern, even though it is not the smallest measured distance (and therefore the MCM would have been wrongly identified). There is not a clear separation be-

¹The amplification process in the PASA shifts the signal to a pedestal value, which varies strongly from channel to channel. In order to have a small and well defined baseline to prevent undershoots, a configurable pedestal value is added and the actual baseline is determined and subtracted with a recursive first-order filter [106].

3.3 Read-out Board testing procedure



Figure 3.18: Screen-shot of the scanner's GUI.

tween the two distributions, therefore we conclude that the method is not suited to determine the chip identities.

We repeated the study considering the first n minimal distances (with n ranging from 3 to 10) and we concluded that if the right chip does not correspond to the minimum distance between the baseline patterns, it will also not correspond to the n_{th} minimal distance. Moreover, we tried to restrict the search in the reference table to testing dates close ($\pm 3-6$ months) to the testing date of the larger number of MCMs on the board. It is indeed very likely for a batch of MCMs tested in the same day to be also implemented in the same ROB. Unfortunately also this restriction did not improve the efficiency of the MCM identification.

3. TRANSITION RADIATION DETECTOR AND READ-OUT BOARD TESTING

This is due to the fact that single faulty-MCMs can be replaced on the ROB and the testing date of the new MCM is no longer correlated with that of the other chips on the board. Finally, correctly identified MCMs are removed from the reference list.

Among all the MCMs studied, the TRAP identity was wrongly identified in 37% of the cases. A possible reason for such a low yield is that in the ROB test set-up the configuration for the baseline measurement is not optimal, since the board is not grounded properly like in the full-chamber configuration.

It was decided to discard the above mentioned methods for the MCM identification and instead to append to the test results a photograph of the ROB with sufficiently high resolution such that both the ROB serial number and the MCM labels are readable. Before starting the automatic procedure, the board is positioned on a scanner (EPSON GT 20000) fitting exactly its size. A simple graphical interface, implemented in Tcl/Tk¹, allows the operator to insert the ROB serial number and to initialize the scanning. The picture is saved locally on the computer dedicated to this procedure and is automatically retrieved at the end of the automatic ROB test and uploaded to the gateDB. Fig. 3.17 shows the scanner and Fig. 3.18 shows a screen-shot of the GUI.

¹Tool Command Language (Tcl). Tk is the standard graphical user interface toolkit of Tcl.

4

The Transverse regions method

In this chapter we introduce a particular method used to measure the UE: the *Transverse regions* method. In order to study the correlation between the UE and the perturbative QCD interaction, we would like to isolate the two leading partons with topological cuts and to measure the remaining event activity as a function of the transferred momentum scale (Q^2). Experimentally, one can identify the products of the hard scattering, usually the leading jet¹, and study the region azimuthally perpendicular to it as a function of the jet energy. In Section 4.1 we describe the historical measurements of the UE in terms of Transverse regions, from the first proposal of the method by Marchesini and Webber in 1988 [118], to the recent LHC results [10, 11, 81, 108]. In Section 4.2 we discuss the choice of the physics scale. In particular, we compare a p_T scale given by fully reconstructed jets, charged-particles jets or simply the leading track (the latter option is the choice in our final analysis). Finally, in Section 4.3 we investigate the role of different physics processes contributing to the UE (i.e. MPI, QCD radiation and fragmentation of beam remnants) on the final observables.

4.1 Historical overview

A first method to measure the UE in disjoint phase-space regions was outlined in [118]. In this reference the transverse energy E_T produced in a high-energy hadronic collision is plotted against the distance in pseudo-rapidity from the leading-jet axis. A cartoon of the E_T distribution is shown in Fig. 4.1, where the region labelled with E_T^{raw} collects the fragmentation of the leading jet and

¹The leading jet is the reconstructed jet with the highest transverse energy (or p_T) in the event. Similarly, the leading track is the reconstructed track with the highest p_T in the event.

4. THE TRANSVERSE REGIONS METHOD

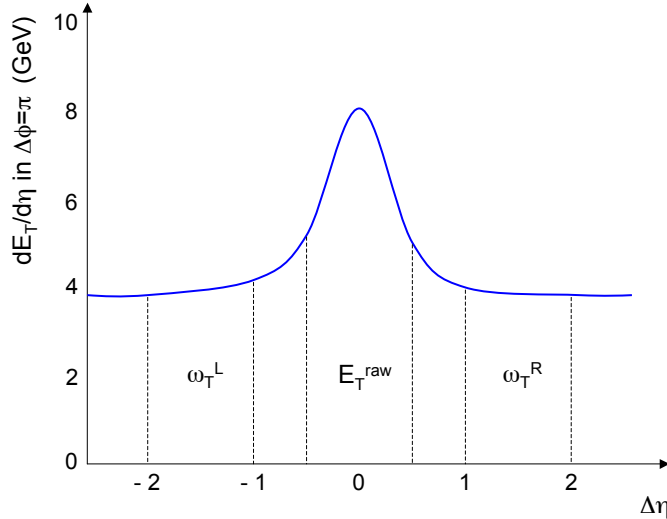


Figure 4.1: Sketch of the transverse energy distribution in jet events as a function of the pseudo-rapidity distance from the leading jet. The distribution is integrated over the azimuthal distance from the leading jet $|\Delta\phi| < \pi/2$. E_T^{raw} is the energy of the leading jet and $\omega_T^{L,R}$ are the transverse energies. The latter provide an estimate of the UE. Figure adapted from [118].

$\omega_T^{L,R}$ are the transverse energies in the rapidity intervals $1 < |\Delta\eta| < 2$. In order to exclude contributions from the recoiling jet, only the range $|\Delta\phi| < \pi/2$ is considered (with $\Delta\phi$ the azimuthal distance from the leading jet). Therefore, a possible estimate of the UE is given by the pedestal energy:

$$\omega_T^{ped} = \frac{1}{2}(\omega_T^L + \omega_T^R) \quad (4.1)$$

The hard component of the pedestal activity is explained in terms of perturbative QCD, from the $2 \rightarrow 3$ matrix elements (at leading order in α_S). In this approximation the third produced jet contributes to only one of the two $\omega_T^{L,R}$ (this consideration will justify the definition of the TransMIN/TransMAX regions described later in this chapter). From the pQCD point of view (neglecting the soft beam remnants and MPI components) the average pedestal energy for the collision of hadrons A and B at a center-of-mass energy \sqrt{s} at LO is given by

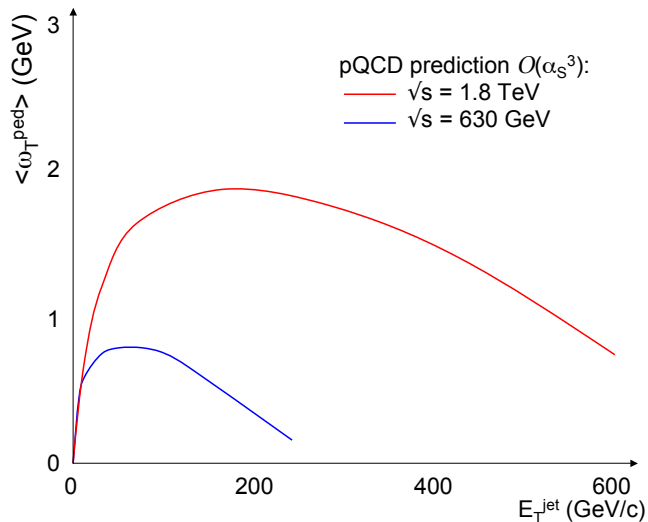


Figure 4.2: LO pQCD prediction of the mean pedestal energy in $p\bar{p}$ collisions as a function of the leading-jet energy. This result is not directly comparable to the measured data since it does not take into account the soft (non perturbative) components of the UE. Figure adapted from [118].

[118]:

$$\langle \omega_T^{ped} \rangle = \frac{d\sigma}{dE_T} = E_T \alpha_S^3(E_T) \frac{1}{4\pi s^2} \int \omega_T^2 d\omega_T d\phi d\eta_1 d\eta_2 d\eta_3 \frac{f_A(x_a)}{x_a} \frac{f_B(x_b)}{x_b} \overline{\sum} |\mathcal{M}(ab \rightarrow 123)|^2 \quad (4.2)$$

where $f_{A,B}(x_{a,b})$ are the PDFs of the incoming partons a and b at the scale E_T . The final state parton 1 gives rise to the leading jet with transverse energy E_T , $|\eta_1| < 1.5$ and zero azimuthal angle. Parton 2 is related to the recoiling jet, with a rapidity η_2 integrated over the full range. Parton 3 contributes to the pedestal energy. It has a transverse energy ω_T , azimuthal angle $|\phi| < \pi/2$ and pseudo-rapidity in the range $1 < |\eta_3 - \eta_1| < 2$. Finally, $\mathcal{M}(ab \rightarrow 123)$ is the matrix element for the $2 \rightarrow 3$ partonic scattering. $\overline{\sum}$ is the average over all spins and colors and the sum over all the possible permutations of final states. The coupling constant has been factored-out of $\mathcal{M}(ab \rightarrow 123)$ to explicitly show its argument (E_T). The pedestal energy according to Eq. 4.2 for $\sqrt{s} = 630$ GeV (SPS

4. THE TRANSVERSE REGIONS METHOD

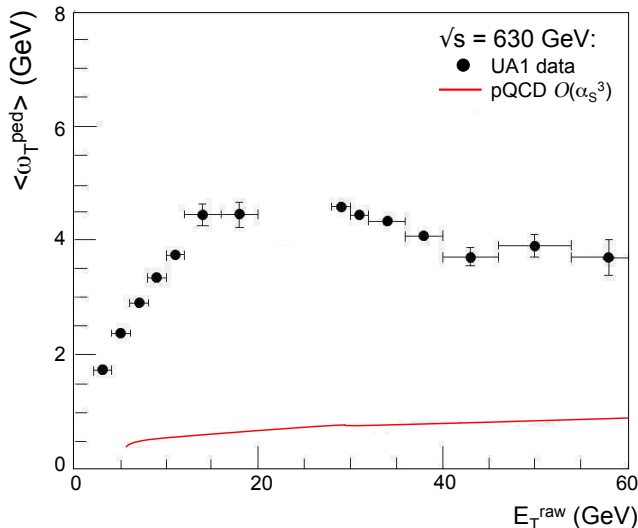


Figure 4.3: Transverse energy density away from the cluster axis ($\Delta\eta = 1.5$) as a function of the cluster transverse energy E_T^{raw} , as measured by the UA1 collaboration at $\sqrt{s} = 630$ GeV [44]. The LO pQCD prediction is also shown in red. Figure adapted from [118].

collider) and 1.8 TeV (Tevatron) are shown in Fig. 4.2 as a function of the leading jet's transverse energy. The average pedestal energy $\langle \omega_T^{ped} \rangle$ rises rapidly at low E_T , has a broad maximum and then vanishes linearly as E_T approaches the kinematic limit $\sqrt{s}/2$. The maximum value reached by $\langle \omega_T^{ped} \rangle$ increases with s as $\alpha_S(E_T)\sqrt{s}$, with E_T around the value at which the maximum pedestal energy occurs [118].

In Fig. 4.3 we show a measurement [44] of the transverse energy density by the UA1 collaboration at $\sqrt{s} = 630$ GeV. In the figure E_T^{raw} is the jet (cluster) transverse energy reconstructed by the UA1 jet-finding algorithm [52] within $|\eta| < 1.5$. The quantity $\langle \omega_T^{ped} \rangle$ is measured in $|\Delta\phi| < \pi/2$ around the cluster axis and at $\Delta\eta = 1.5$ from the cluster axis. Two data sets are plotted in the figure, one recorded with a minimum bias trigger, $E_T^{raw} < 20$ GeV, and one with a jet trigger, $E_T^{raw} > 30$ GeV. More details can be found in [44]. After a steep increase, the distribution tends to flatten at $E_T^{raw} > 15$ GeV. The red line in Fig. 4.3 is

the pQCD prediction from Eq. 4.2. Its quantitative and qualitative discrepancy from the measured data gives an estimate of the other components of the UE. In particular, the disagreement is more pronounced in the E_T^{raw} range 15–35 GeV, where the real event activity is 5–6 times larger than the pQCD prediction.

In 2002 the CDF collaboration introduced [40] a definition of Transverse regions in terms of azimuthal angle which since then is used for UE studies in hadronic collisions. The relevant topological areas are sketched in Fig. 4.4. Each region covers a finite pseudo-rapidity range, generally $|\eta| < 1$. The *Toward* region collects the fragmentation products of the leading jet, while the *Away* region those of the recoiling jet and both regions have an extension of $\pi/3$ radians. The *Transverse* region is composed of two disjoint areas ($\pi/6 + \pi/6$ radians). The one called *TransMAX* is the area for which the summed p_T of the contained particles is maximum. Taking into account the previous considerations in this chapter, we believe that this region is more sensitive to the hard component of the UE (QCD radiation), while the other region (*TransMIN*) collects the fragmentation of the beam remnants and MPI only. Each region is characterized by observables like the charged-particle density or the summed- p_T density.

CDF published various analyses of the UE, among which a first study based on charged-particles jets [40], one in which the Transverse regions are circles in the $\eta\phi$ space centred at $\pi/2$ radians from the leading jet [36], a comparison between jet and di-jet events [99] and a comparison between jet- and Drell-Yan-triggered events [13].

We report here a sample of plots from a CDF analysis [13] of $p\bar{p}$ collisions at $\sqrt{s} = 1.96$ TeV. The analysis considers only charged particles with $p_T > 0.5$ GeV/ c and $|\eta| < 1$. Calorimetric jets are reconstructed with the MidPoint [12] cone-based algorithm and the leading jet is required to be within $|\eta| < 2$.

Fig. 4.5 shows the charged-particle density in the three regions as a function of the leading-jet p_T . In Fig. 4.6 we show the distribution of the summed p_T of charged particles. We note that in both cases the slope is more pronounced in the regions containing the jets (*Toward* and *Away*) than in the *Transverse* region. Moreover, in all the regions after a steep increase for leading-jet $p_T < 20$ GeV/ c , the slope is reduced, almost saturating in the case of the particle density in the

4. THE TRANSVERSE REGIONS METHOD

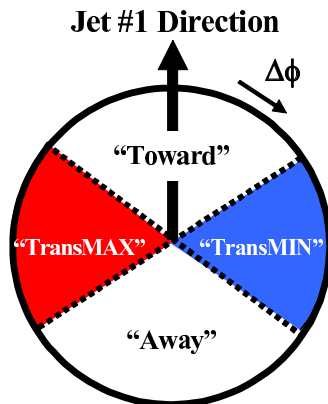


Figure 4.4: Definition of Toward, Away and Transverse (TransMIN + TransMAX) regions by the CDF collaboration. The Toward and Away regions collect the fragmentation products of the leading and recoiling jets, respectively. The Transverse region is composed of two disjoint areas and is more sensitive to the UE. Figure from [99].

Transverse region. The physical interpretation of the low leading-jet- p_T region is quite difficult because a fraction of the entries can come from high multiplicity events without evidence of jet production, in which the jet-finder algorithm nevertheless identifies jet-like structures. We expect the fraction of such events to vanish with increasing leading-jet p_T . The presented results are corrected for detector effects and compared with PYTHIA Tune A, which is one of the preferred models to reproduce the UE at Tevatron energies, and HERWIG [119] without MPI (more details in [13] and references therein).

In Fig. 4.7 and 4.8 we show the number density and summed p_T of charged particles in the regions TransMIN and TransMAX. Of particular interest is the pronounced monotonic increase of the summed p_T in the TransMAX region, possibly due to the QCD radiation.

The STAR experiment at RHIC measured [73] the UE in pp collisions at $\sqrt{s} = 200$ GeV also using the Transverse regions method. The results are not corrected for detector effects, therefore they cannot quantitatively be compared

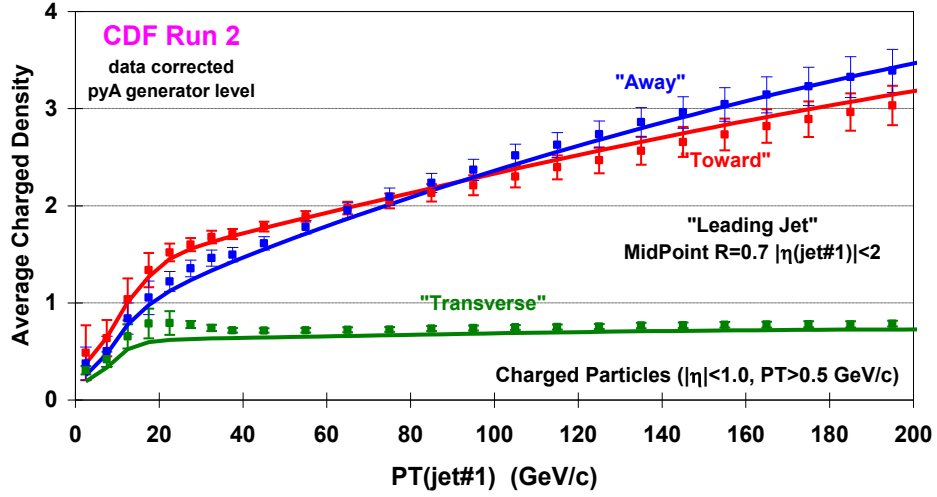


Figure 4.5: Charged-particle density ($p_T > 0.5 \text{ GeV}/c$ and $|\eta| < 1$) as a function of the leading-jet p_T . The data are corrected for detector effects and compared with Pythia Tune A (pyA). Data from the CDF collaboration for $p\bar{p}$ collisions at $\sqrt{s} = 1.96 \text{ TeV}$. Figure from [13].

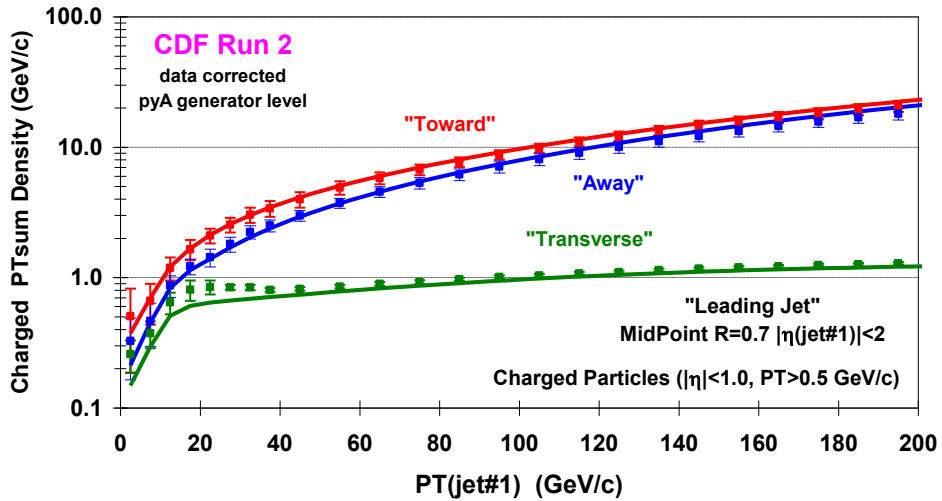


Figure 4.6: Summed- p_T density of charged particles ($p_T > 0.5 \text{ GeV}/c$ and $|\eta| < 1$) as a function of the leading jet p_T . The data are corrected for detector effects and compared with PYTHIA Tune A (pyA). Data from the CDF collaboration for $p\bar{p}$ collisions at $\sqrt{s} = 1.96 \text{ TeV}$. Figure from [13].

4. THE TRANSVERSE REGIONS METHOD

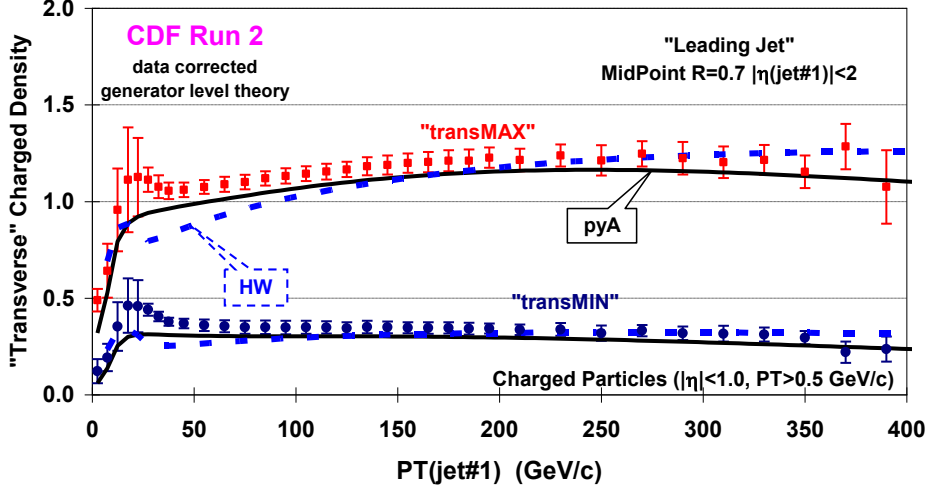


Figure 4.7: Charged-particle density ($p_T > 0.5 \text{ GeV}/c$ and $|\eta| < 1$) as a function of the leading-jet p_T in the TransMIN and TransMAX regions. The data are corrected for detector effects and compared with PYTHIA Tune A (pyA) and HERWIG (without MPI). Data from the CDF collaboration for $p\bar{p}$ collisions at $\sqrt{s} = 1.96 \text{ TeV}$. Figure from [13].

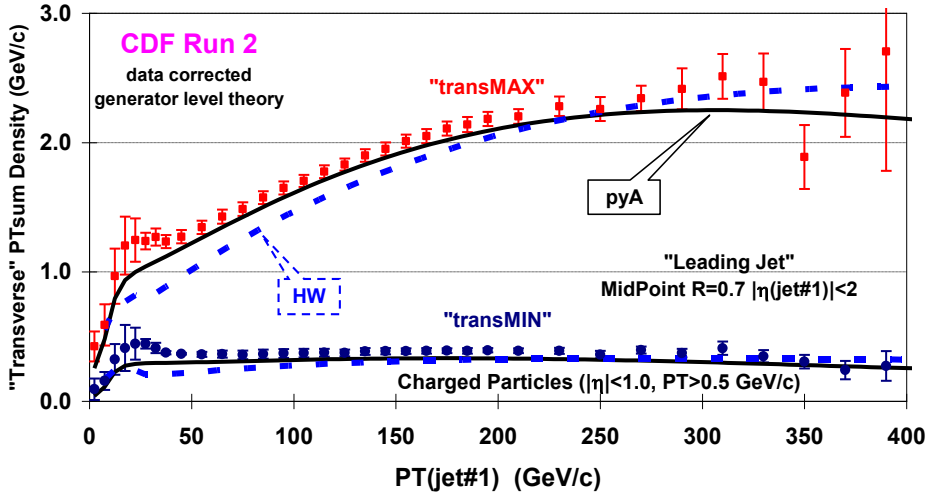


Figure 4.8: Summed- p_T density of charged particles ($p_T > 0.5 \text{ GeV}/c$ and $|\eta| < 1$) as a function of the leading jet p_T in the TransMIN and TransMAX regions. The data are corrected for detector effects and compared with PYTHIA Tune A (pyA, lines) and HERWIG (without MPI). Data from the CDF collaboration for $p\bar{p}$ collisions at $\sqrt{s} = 1.96 \text{ TeV}$. Figure from [13].

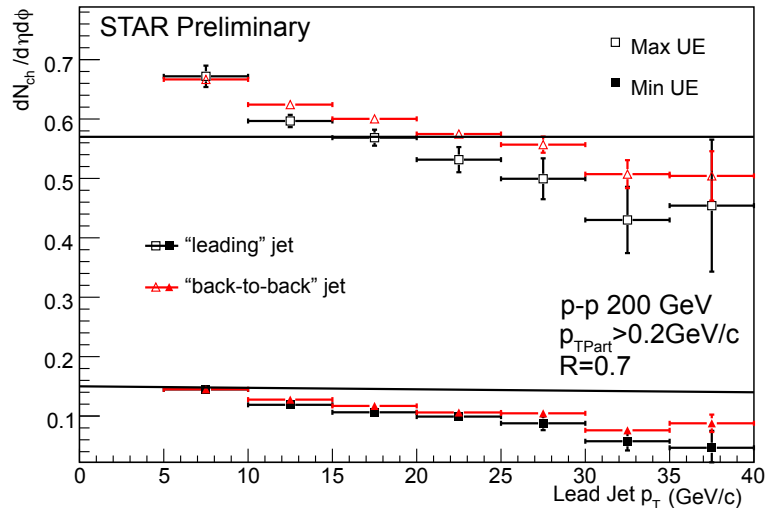


Figure 4.9: Charged-particle density in the TransMIN (Min UE in the legend) and TransMAX (Max UE in the legend) regions measured with the STAR detector. Data are not corrected for detector effects. The two horizontal solid lines are the expected particle densities if the multiplicity in both Transverse regions were a Poissonian distribution (with an average of 0.36). Figure from [73].

to the other results presented in this chapter. Nevertheless, they provide relevant information on the event activity at this collision energy. In Fig. 4.9 we show the uncorrected charged-particle densities in the TransMIN and TransMAX regions as a function of the reconstructed leading-jet p_T . Jets are reconstructed with the seedless cone algorithm SIS Cone [126] with a radius of 0.7 and only tracks with $p_T > 0.2 \text{ GeV}/c$ are considered (more details can be found in [73]). The black points refer to a study based on a sample of events where at least one jet is found in the STAR acceptance ($|\eta| < 1$). Red points represent a sub-set of this sample where two (and only two) back-to-back jets were found, requiring the ratio between the transverse momentum of the away and leading jet to be larger than 0.7 and the azimuthal angle between the two jets' direction to be smaller than 150° . This selection suppresses the probability that one scattered parton has undergone significant QCD radiation. The measured particle densities for the two samples are comparable within the statistical errors (even though the data-points refer-

4. THE TRANSVERSE REGIONS METHOD

ring to the back-to-back analysis are systematically higher). This observation suggests that the hard-scattered partons emit only a small amount of large-angle QCD radiation at RHIC energies, whereas in the Tevatron regime (i.e. $\sqrt{s} = 1.96$ TeV) the ratio between the leading-jet and the back-to-back jets analysis is ~ 0.65 [88]. The two horizontal solid lines shown in the plot are the expected particle densities if the multiplicity in both Transverse regions were a Poissonian distribution (with an average of 0.36) [73]. The similarity of this simple simulation to the data suggests that at RHIC energies the splitting of the TransMIN and TransMAX regions is dominated by a sampling bias. We have performed a similar exercise (not shown here) for the LHC collision energy of 0.9 TeV, coming to similar conclusions.

Recently, also due to the sampling bias mentioned above, the TransMIN/MAX regions have been superseded by a single Transverse region, in which the activity of the two disjoint transverse areas is averaged. Indeed, in the first measurements at the new energies available at the LHC it is advisable to focus on simple observables. For instance, the ATLAS collaboration published two analyses [10, 11] where the physics scale is given by the p_T of the leading-particle in the event instead of the leading reconstructed jet. The first analysis [10] considers the full ATLAS acceptance ($|\eta| < 2.5$) and the second [11] a limited acceptance ($|\eta| < 0.8$) for an easy comparison with the ALICE results. In Fig. 4.10 and 4.11 we show the number density and the summed p_T , respectively, of charged particles in the Transverse region at the collision energies of 0.9 and 7 TeV. Only particles with $p_T > 0.5$ GeV/ c and $|\eta| < 2.5$ are considered. The number density distribution saturates at a value of about 0.4 and 1 for $\sqrt{s} = 0.9$ and 7 TeV, respectively. The summed p_T distribution saturates at a value of about 0.4 and 1.2 GeV/ c for $\sqrt{s} = 0.9$ and 7 TeV, respectively.

The CMS collaboration made [81] a similar analysis of the UE as a function of the leading-particle p_T . We do not show the results here since the measured data are not corrected for detector effects. Nevertheless, we show in Fig. 4.12 the scaling of the UE distributions with the collision energy. Only particles with $p_T > 0.5$ GeV/ c and $|\eta| < 2$ are considered. The left plot shows the ratio of the

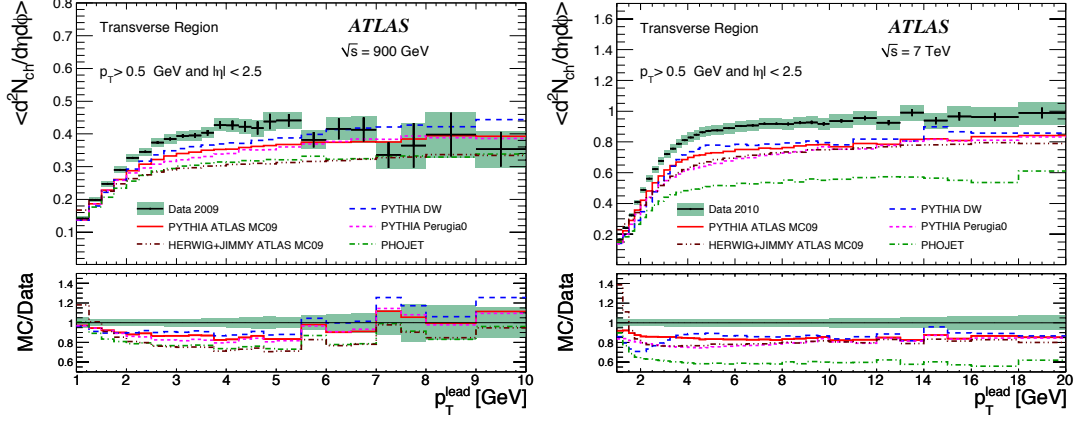


Figure 4.10: Charged-particle density in the Transverse region at $\sqrt{s} = 0.9 \text{ TeV}$ (left) and $\sqrt{s} = 7 \text{ TeV}$ (right) measured with the ATLAS detector. Only particles with $p_T > 0.5 \text{ GeV}/c$ and $|\eta| < 2.5$ are considered. Data are corrected for detector effects. Figure from [10].

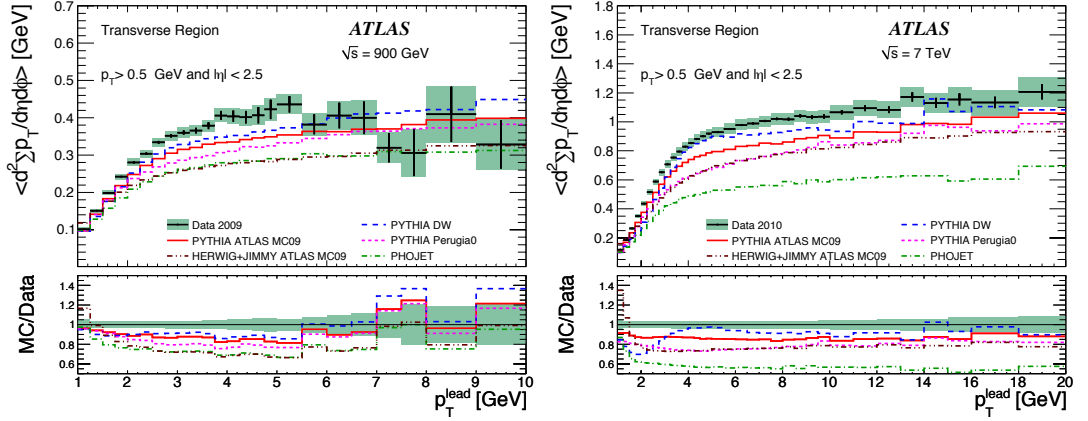


Figure 4.11: Summed- p_T density in the Transverse region at $\sqrt{s} = 0.9 \text{ TeV}$ (left) and $\sqrt{s} = 7 \text{ TeV}$ (right) measured with the ATLAS detector. Only particles with $p_T > 0.5 \text{ GeV}/c$ and $|\eta| < 2.5$ are considered. Data are corrected for detector effects. Figure from [10].

4. THE TRANSVERSE REGIONS METHOD

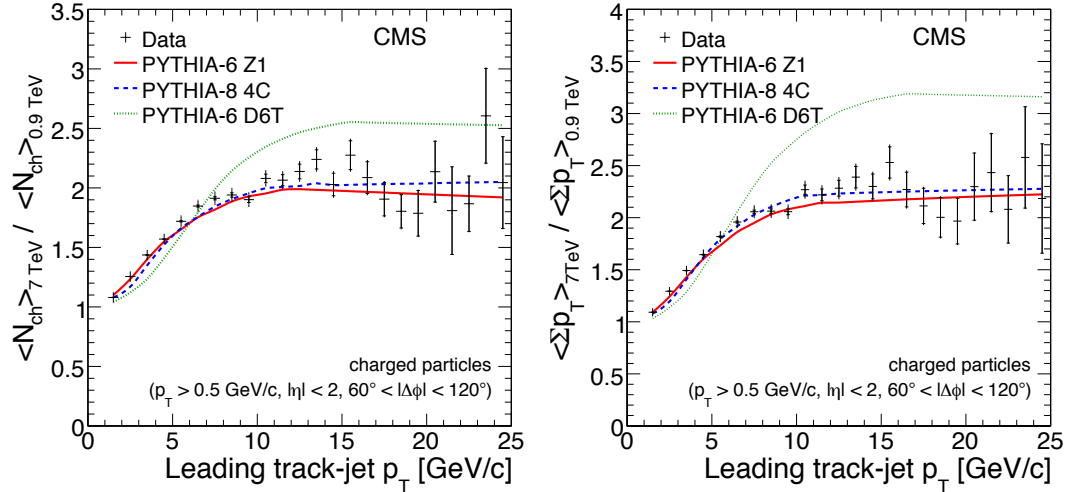


Figure 4.12: Scaling of the UE distributions with the collision energy measured by the CMS collaboration. Only particles with $p_{\text{T}} > 0.5\text{ GeV}/c$ and $|\eta| < 2$ are considered. Figure from [81].

number density distribution between $\sqrt{s} = 0.9$ and 7 TeV , which saturates at a value of about 2. The plot on the right shows the same ratio for the summed p_{T} distribution. In this case the saturation value is about 2.3. Most of the systematic uncertainties are expected to cancel in the ratios, therefore these results can be compared, for instance, with the ALICE measurement (see Sect. 6.5).

4.2 Choice of scale

As already mentioned, jets are the observable counterpart of the perturbative concepts of quarks and gluons. A jet-finding procedure is a way of inverting the quantum mechanical processes of QCD branching and hadronization to obtain an approximate description of the original parton's properties (mass, momentum etc.). In this section we investigate the effect of using the p_{T} of fully reconstructed jets or simply the leading charged particle p_{T} as a scale for the event activity in the Transverse region. The study is based on about 10^8 minimum bias

events generated with PYTHIA 6.4 (tune Perugia 0) at $\sqrt{s} = 7$ TeV. No event selection is applied apart from requiring a leading object with $p_T > 0.15$ GeV/ c in the acceptance. The analysis framework used is the one developed for our final analysis (see Sect. 5) applied to pure Monte Carlo information. We also consider a minimum bias data sample of $25 \cdot 10^6$ events recorded with the ALICE detector (see Sect. 5.2), the same used for our final analysis. The data are not corrected for detector effects (for track and event selections see Sect. 5.3) since at this point we are only interested in the qualitative effects of the scale choice. Jets are reconstructed using the algorithms implemented in the FASTJET [71] package. In particular, we use two sequential-recombination algorithms (anti- k_T [72] and k_T [71]) and two cone algorithms (SISCONE [126] and UA1-cone [52]). Sequential-recombination jet-finders are based on pair-wise recombination of particles and are generally infra-red safe¹. The original idea is to mimic in reversed order the QCD branching sequence and the reconstructed jets naturally tend to collect most of the radiated partons. Cone algorithms identify the dominant energy flow into circles in the $\eta - \phi$ space. They iteratively calculate the jet axis from all particles in the cone until stable cones are found and generally also implement the splitting and merging of overlapping stable cones. The properties of infra-red and collinear² safety are crucial for an accurate comparison of the reconstructed jets with parton-level predictions. Indeed, a jet algorithm should codify the relation between the low-order partonic structure of the event and the observed hadrons. Therefore, the structure of a high- p_T jet should not change radically if a soft or collinear particle is added to the event by hadronization or the UE. The jet-finders used in the analysis are described below.

Anti- k_T [72] and k_T [71] algorithms In both jet-finders one introduces the distances d_{ij} between two objects (particles or pseudo-jets) and d_{iB} between the object i and the beam axis. These distances are defined as follows:

$$d_{i,j} = \min(k_{Ti}^{2p}, k_{Tj}^{2p}) \frac{\Delta_{i,j}^2}{R^2} \quad (4.3)$$

¹A jet-finder algorithm is infra-red safe when the addition of an infinitely soft particle in the event does not lead to a different jet to be found.

²A jet-finder algorithm is collinear-red safe when the emission of a particle at infinitely small angle from the emitting one does not lead to a different jet to be found.

4. THE TRANSVERSE REGIONS METHOD

$$d_{i,B} = k_{Ti}^{2p} \quad (4.4)$$

where $\Delta_{i,j}^2 = (y_i - y_j)^2 + (\phi_i - \phi_j)^2$ and k_{Ti} , y_i and ϕ_i are the transverse momentum, rapidity and azimuth of the particle i , respectively. The main parameters of these algorithms are the radius R and a parameter p , which regulates the scaling of the distances d with the particles' transverse momentum. In the k_T case $p = 1$ and in the anti- k_T case $p = -1$. The clustering procedure identifies the smallest of the distances and if it is a d_{ij} the objects i and j are combined, while if it is a d_{iB} the object i is called a jet and is removed from the list. The procedure is iterated until no objects are left. The main difference between the two algorithms is that in the k_T case soft radiation can provoke irregularities in the shape of the final jets (soft-adaptable boundaries). In the anti- k_T case only hard particles can modify the shape of the jet (soft-resilient boundaries) since soft particles tend to cluster with the hard ones before clustering among themselves. This results in perfectly conical jet shapes. Moreover, besides being infra-red safe, the anti- k_T jet-finder also has the property of collinear-safety. Therefore, in this and the following section we use the anti- k_T jet-finder as the reference algorithm.

SISCONE algorithm [126] It is a seedless, infra-red safe cone jet-finder. First generation cone algorithms take some or all the event particles as *seeds* (trial cone directions). For each seed they evaluate the sum of 4-momenta of the particles contained in the cone. The resulting 4-momentum is then used as a new direction for the trial cone. The procedure is iterated until the cone's direction no longer changes (stable cones). If the seeds are chosen above a certain momentum threshold the procedure will be collinear unsafe. On the other hand, if any particle can act as a seed (seedless algorithm), the procedure is very likely subject to the problem of infra-red unsafety. The solution adopted in the SISCONE algorithm is to use an *exact* seedless algorithm, where exact means that it should be possible to demonstrate mathematically that the algorithm identifies all stable cones. In this way the addition of a soft particle does not lead to new stable cones to be found since all hard stable cones have already been (provably) found. A drawback of this method (critical only in heavy-ions collisions) are the high execution times needed to find a jet, proportional to $N^2 \ln N$ (where N is the number of particles in the event).

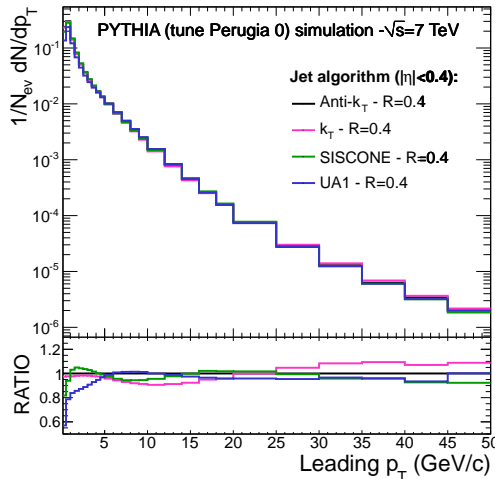


Figure 4.13: Leading-jet spectrum from a selection of jet finders. Distributions are normalized to the number of jets reconstructed with the reference algorithm (anti- k_T). Bottom panel: ratio between each jet finder and the reference one. Simulation from PYTHIA (Perugia 0) at $\sqrt{s} = 7$ TeV.

UA1-cone algorithm [52] This clustering algorithm was adopted for the first time by the UA1 collaboration on calorimeter cells. It is a very simple and robust jet-finder, well suited for the estimate of the jet axis in correlation studies, while for a good energy resolution more elaborate algorithms should be preferred. In this study we use a specific implementation of the UA1-cone algorithm provided by the AliRoot software. The $\eta - \phi$ space is divided in cells of adjustable size and the total transverse energy of the particles contained in each cell is evaluated. The cell with the highest E_T above a threshold (0.15 GeV in our specific case) initiates the procedure. Subsequent cells are clustered with the initiator if they are contained in a circle of radius R in the $\eta - \phi$ space centred around the initiator. After each step the jet-axis is then re-evaluated and the procedure is repeated until stable jets are found.

In the case of cone algorithms the radius parameter R defines the maximum distance from the jet axis of a particle belonging to the jet in the $\eta\phi$ plane: $R = \sqrt{(\Delta\eta)^2 + (\Delta\phi)^2}$.

4. THE TRANSVERSE REGIONS METHOD

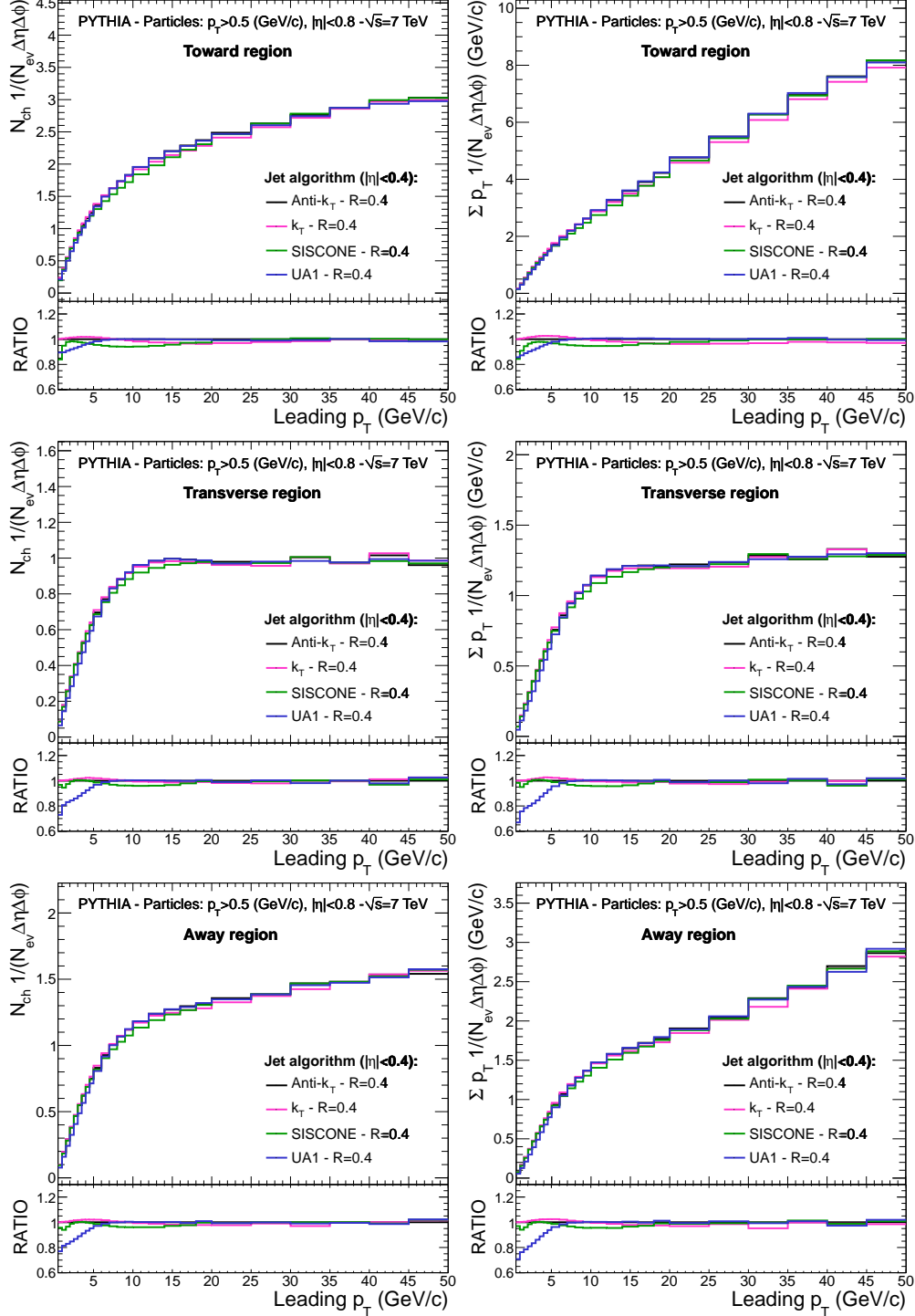


Figure 4.14: Number density (left) and summed p_T (right) for the Toward (top), Transverse (middle) and Away (bottom) regions. Charged particles: $p_T > 0.5$ GeV/c and $|\eta| < 0.8$. Leading jet: $|\eta| < 0.4$. Bottom panel: ratio between each jet finder choice and the reference one (anti- k_T). Simulation from PYTHIA (Perugia 0) at $\sqrt{s} = 7$ TeV.

In Fig. 4.13 we show the p_T distribution of leading-jets with $p_{T,LJ} > 0.15 \text{ GeV}/c$ reconstructed within $|\eta| < 0.4$ using different jet finders. For comparison all the distributions are scaled¹ by the number of entries in the reference case: the anti- k_T algorithm, which we assume to be our best approximation of the leading outgoing-parton. The performance of the k_T and SISCONe algorithms is similar to that of the reference jet-finder, with an average discrepancy of about 10%. The UA1 algorithm agrees within few percent with the reference case for $p_{T,LJ} > 5 \text{ GeV}/c$ and a discrepancy of up to 45% for lower values of leading-track p_T . These distributions are the input for the Transverse regions analysis. In Fig. 4.14 we see the influence of the choice of the jet-finder on the shape of the final UE distributions, considering charged particles with $p_T > 0.5 \text{ GeV}/c$ within $|\eta| < 0.8$. The results obtained with the k_T algorithm are compatible with the reference within few percent in all topological regions. In the case of the SISCONe jet-finder we observe a maximum discrepancy of the order of 5% in the Transverse and Away regions. In the Toward region the discrepancy reaches a maximum of 15% in the first bin ($0.5 < p_{T,LJ} < 1 \text{ GeV}/c$). In the case of the UA1 jet-finder, in all regions we observe an initial discrepancy of up to 35%, which is reduced to few percent for $p_{T,LJ} > 5 \text{ GeV}/c$. A disagreement from the reference in the Toward region indicates that the two jet finders identify different jets. We speculate that in the UA1 case the lower average multiplicity and summed p_T at $p_{T,LJ}$ below $5 \text{ GeV}/c$ indicate that part of the reconstructed jets are just single particles (we remind here that in our specific settings this algorithm considers only particles with $p_T > 0.15 \text{ GeV}/c$), not related to the leading outgoing-parton in a hard scattering. For instance we might be selecting diffractive events. This is further confirmed by the lower activity in the Away region for the same jet-finder with respect to the reference, which indicates that part of the triggered events does not show a clear di-jet structure. As a consequence also the number density and summed p_T distributions in the Transverse region are lower with respect to the reference case, since they are averaged on a smaller amount of events that include QCD

¹In this way the effect of lost events (jets) is visible in the plot. On the contrary, the final UE distributions are normalized (bin-by-bin) by the number of events with a jet reconstructed by the given jet-finder. Events where no jet is reconstructed are not taken into account.

4. THE TRANSVERSE REGIONS METHOD

radiation and MPI associated with a hard scattering.

We now want to assess the effect of further simplifying the leading-parton approximation by considering a scale given by the leading charged-particle's transverse momentum. In Fig. 4.15 we show the p_T distribution of jets reconstructed with the anti- k_T algorithm using charged and neutral or only charged input particles for two values of the radius parameter R : 0.2 and 0.4. The leading-charged particle distribution is also shown.

The leading-particle spectrum drops faster than the reconstructed-jet spectrum since the clustering procedure flattens the slope of the jet spectra. Reducing R or neglecting neutral particles induces a horizontal scaling of the distributions and in the limit $R \rightarrow 0$ the leading-particle spectrum should be recovered.

Fig. 4.16 shows the number density (left) and summed p_T (right) in the Transverse region for these choices of leading objects. The effect of reducing the cone radius, considering only charged-particles in the jet-finding procedure or the leading charged particle is to "squeeze" the distributions towards lower values of transverse momentum (a similar trend is observed in the other two topological regions). Namely, the saturation of the transverse distributions occurs at lower values of the leading-object p_T in the case of the leading charged-particle analysis ($p_{T,LJ} \simeq 4 \text{ GeV}/c$) with respect to the reference algorithm ($p_{T,LJ} \simeq 10 \text{ GeV}/c$). The saturation values have a maximum variation of about 10% from the reference.

To verify that the choice of the leading object has the same effect on real data, in Fig. 4.17 we show the p_T distribution of leading-jets reconstructed with the reference algorithm with two values of the radius parameter ($R=0.2$ and 0.4) run on all tracks with $p_T > 0.15 \text{ GeV}/c$. The leading-track distribution is also shown. In this case the yields for the smaller radius value or the leading-track are always lower than the reference case, due to the tracking inefficiency at low- p_T (see Sect. 5.4). The jet-finder's input are all the reconstructed tracks without any lower p_T cut-off. Therefore it is possible that tracks with $p_T < 0.15 \text{ GeV}/c$ are clustered together to form a jet with $p_T = 0.15 \text{ GeV}/c$, while no leading-track with the same momentum is reconstructed in the acceptance. In Fig. 4.18 we present the number density (left) and summed p_T (right) in the Transverse region for

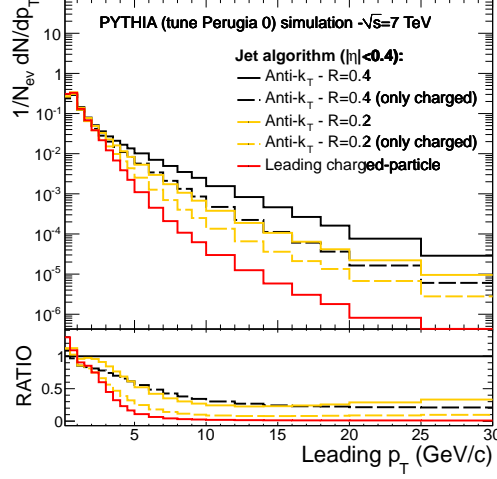


Figure 4.15: Leading-jet spectrum for the anti- k_T algorithm (charged+neutral or charged input) for two values of R and leading-charged-particle spectrum. Scaling factor: number of jets from the reference (anti- k_T on charged+neutral, $R=0.4$). Bottom panel: ratio between each choice of leading object and the reference. PYTHIA (Perugia 0) at $\sqrt{s} = 7$ TeV.

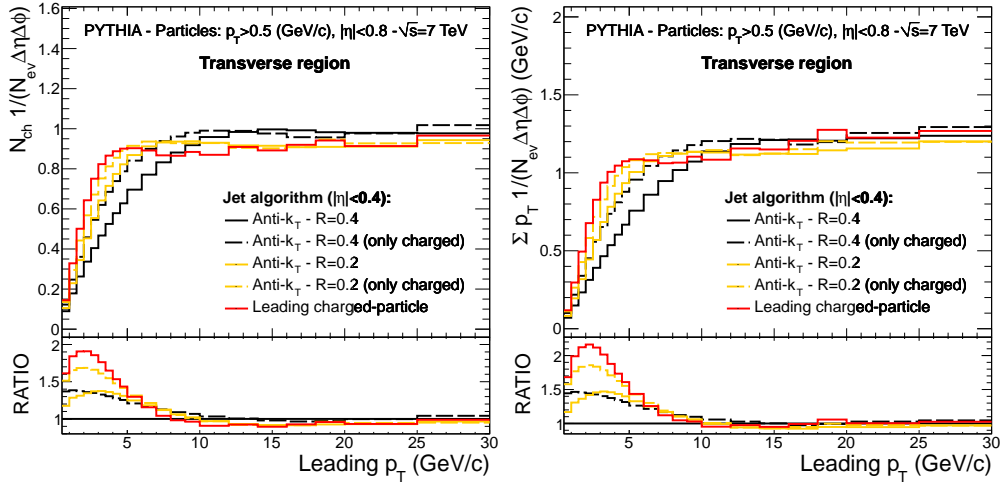


Figure 4.16: Number density (left) and summed p_T (right) in the Transverse region. Leading objects: jets from the anti- k_T algorithm (charged+neutral or charged input, two values of R) or leading charged-particle, $|\eta| < 0.4$. Particles: $p_T > 0.5$ GeV/ c and $|\eta| < 0.8$. Bottom panel: ratio between each choice of leading object and the reference (anti- k_T on charged+neutral input, $R=0.4$). PYTHIA (Perugia 0) at $\sqrt{s} = 7$ TeV.

4. THE TRANSVERSE REGIONS METHOD

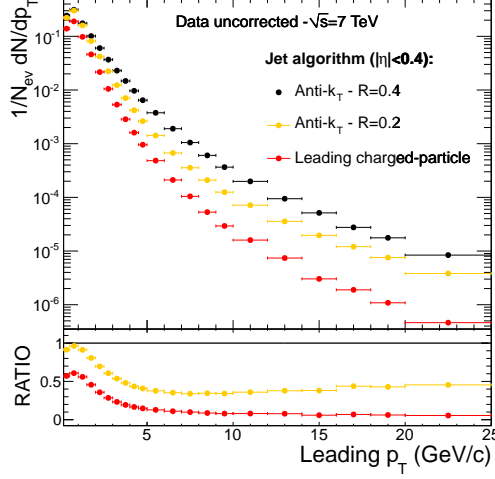


Figure 4.17: Leading-jet spectrum for the anti- k_T algorithm run on all tracks ($p_T > 0.15$ GeV/c) for two values of R . The leading-track distribution is also shown. Distributions are scaled by the number of jets reconstructed with the reference algorithm (anti- k_T with $R=0.4$). Bottom panel: ratio between each choice of leading object and the reference. Uncorrected data at $\sqrt{s} = 7$ TeV.

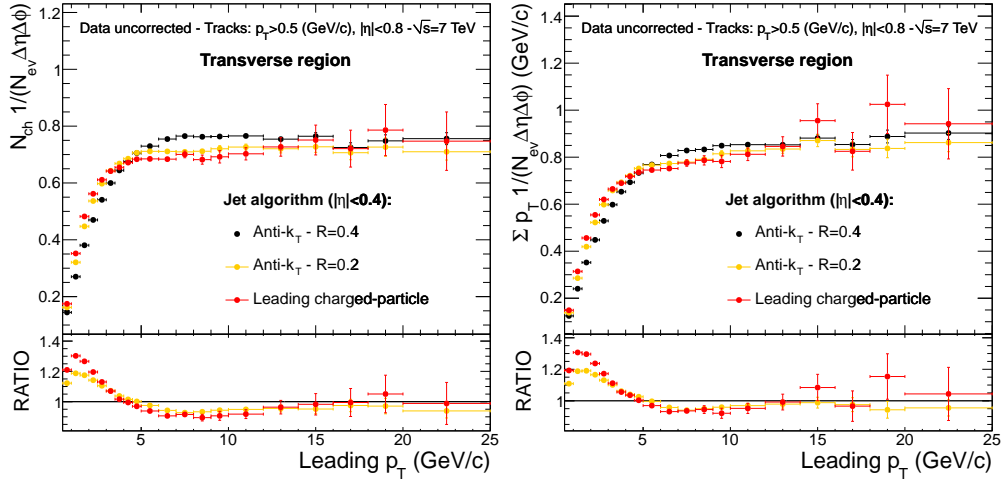


Figure 4.18: Number density (left) and summed p_T (right) in the Transverse region. Leading objects: jets reconstructed with the anti- k_T algorithm (run on all tracks with $p_T > 0.15$ GeV/c for two values of R) or the leading track, $|\eta| < 0.4$. Tracks: $p_T > 0.5$ GeV/c and $|\eta| < 0.8$. Bottom panel: ratio between each choice of leading object and the reference (anti- k_T with $R=0.4$). Uncorrected data at $\sqrt{s} = 7$ TeV.

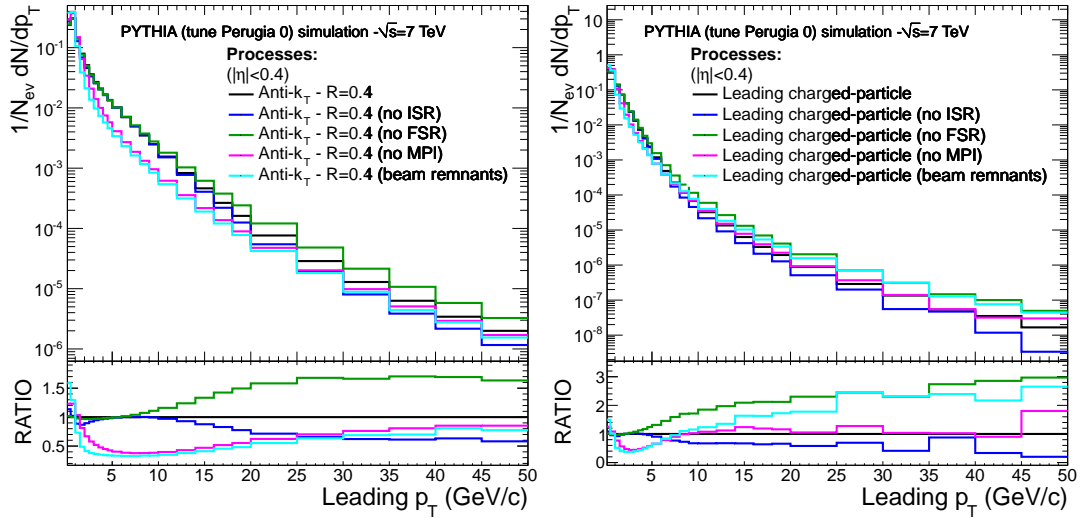


Figure 4.19: Leading-jet spectrum for the anti- k_T algorithm with charged+neutral input (left) and leading charged-particle distribution (right). Various Monte Carlo samples are considered where different physics processes are excluded from the event generation. Distributions are normalized to 1. Bottom panel: ratio between each spectrum and the standard one (all processes included). PYTHIA tune Perugia 0 at $\sqrt{s} = 7$ TeV.

these choices of leading objects. The results show a similar trend than the Monte Carlo prediction. The values obtained for the number density and summed p_T in the saturation region for different choices of leading-object are comparable within 10%. These considerations should be taken into account when comparing different types of analysis.

4.3 Physics processes

In this section we investigate the contribution of different physics processes to the event activity in the Transverse region. The study is based on the Monte Carlo sample described in Sect. 4.2 and four samples of approximately 10^8 minimum bias events generated with PYTHIA 6.4 tune Perugia 0 at $\sqrt{s} = 7$ TeV in which different processes are excluded from the event generation. Namely we turn off ISR (MSTP(61)=0), FSR (MSTP(71)=0), MPI (MSTP(81)=20) and all these

4. THE TRANSVERSE REGIONS METHOD

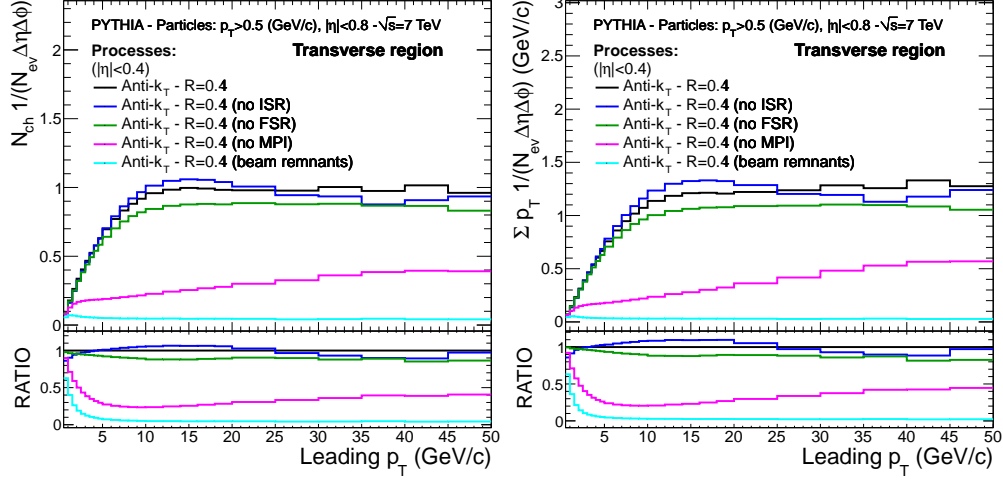


Figure 4.20: Number density (left) and summed p_T (right) in the Transverse region defined by the leading reconstructed jet. Various Monte Carlo samples are considered, where different physics processes are excluded. Particles: $p_T > 0.5 \text{ GeV}/c$ and $|\eta| < 0.8$. Leading jet: $|\eta| < 0.4$. Bottom panel: ratio between each sample and the reference (all processes in). PYTHIA (Perugia 0) at $\sqrt{s} = 7 \text{ TeV}$.

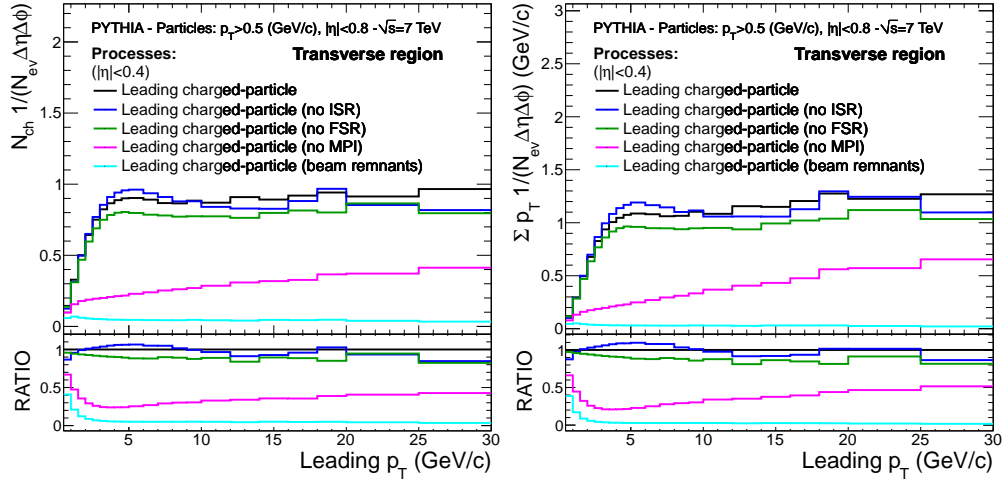


Figure 4.21: Number density (left) and summed p_T (right) in the Transverse region defined by the leading charged-particle. Various Monte Carlo samples are considered, where different physics processes are excluded. Particles: $p_T > 0.5 \text{ GeV}/c$ and $|\eta| < 0.8$. Leading charged-particle: $|\eta| < 0.4$. Bottom panel: ratio between each sample and the reference one (all processes in). Simulation from PYTHIA (Perugia 0) at $\sqrt{s} = 7 \text{ TeV}$.

processes all together (only the fragmentation of beam remnants is left, apart from the hard scattering). In Fig. 4.19 we show the leading-jet distribution (left) and the leading-charged-particle distribution (right) for the different cases. Each distribution is normalized to 1, therefore we can compare the relative changes of the shape of the different distributions. The effect of ISR is to reduce the jet yield at very low jet p_T values ($0.15 < p_{T,LJ} < 0.5 \text{ GeV}/c$) by about 15% and to enhance it up to 40% for higher $p_{T,LJ}$ (note that in the plots the ratio between the case without and with ISR is shown). A similar horizontal scaling towards higher $p_{T,LJ}$ values is due to MPI. In this case the maximum enhancement of about 60% is observed in the intermediate range $5 < p_{T,LJ} < 12 \text{ GeV}/c$. The opposite trend is induced by the presence of FSR, which reduces the jet yield by up to a factor 1.6 in the high $p_{T,LJ}$ region ($p_{T,LJ} > 20 \text{ GeV}/c$). We conclude that dominant jet production mechanism in the intermediate range $5 < p_{T,LJ} < 12 \text{ GeV}/c$ are MPI, while for higher $p_{T,LJ}$ values ($p_{T,LJ} > 30 \text{ GeV}/c$) ISR becomes more important. If the leading charged-particle is considered (Fig. 4.19, right) similar considerations than the case of reconstructed jets hold for the effects of the QCD radiation. In the case of MPI we observe that this process dominates the particle production mechanism only in the range $1 < p_{T,LT} < 6 \text{ GeV}/c$.

In Fig. 4.20 we present the number density (left) and summed p_T (right) in the Transverse region for the different event-samples. The effect of ISR is to enhance the transverse event-activity of 10–15% at high momenta ($p_{T,LJ} > 25 \text{ GeV}/c$) and reducing it of about the same amount in the intermediate-momentum region ($2 < p_{T,LJ} < 20 \text{ GeV}/c$). Excluding FSR causes a reduction of the final values of maximum 20%, with little dependence on the $p_{T,LJ}$ bin. The main contribution to the Transverse region activity, in the model we are considering, is given by MPI. The exclusion of this process reduces the number density and summed- p_T values by up to 80%. In Fig. 4.21 we show a similar picture for the leading charged-particle analysis. The same considerations than for the jet analysis hold true.

Finally, we would like to focus on the low leading-jet (leading charged-particle) region (below $\sim 3 \text{ GeV}/c$). The steep rise of the UE distributions observed in this range is conventionally interpreted as an indication of decreasing impact parameter in the hadronic collision [40]. Higher values of the leading-object p_T are

4. THE TRANSVERSE REGIONS METHOD

related to more central collisions and therefore to an increased probability for MPI, leading to a larger transverse multiplicity. The onset of the multiplicity saturation in the plateau would indicate the occurrence of head-on collisions. Nevertheless, we must be aware of a trivial effect also contributing to the rise of the distributions. At this low scale the leading object is not necessarily related to the leading outgoing parton in a hard scattering (diffractive events can play an important role, as illustrated in Sect. 5.3.1). Nevertheless, the maximum measured value of p_T , averaged over many samples, increases with the sample size. Namely, it is more probable to measure higher values of the leading-object p_T in events with higher multiplicity. At higher values of leading-object p_T the onset of saturation indicates the event-by-event partitioning into azimuthal regions containing the particles from the hard scattering and the UE region. The bulk particle production becomes independent of the hard scale.

5

Measurement of the UE with the ALICE detector

In this chapter we present a measurement of the UE activity in pp collisions at $\sqrt{s} = 0.9$ and 7 TeV. The analysis relies on the Transverse regions method described in the previous chapter and is performed as a function of the p_T of the leading charged particle in the event. We consider charged particles above three different p_T thresholds: 0.15, 0.5 and 1.0 GeV/ c . The data are corrected for detector effects and compared to Monte Carlo predictions. The chapter is organized in the following way: in Section 5.1 we define the relevant observables and the specific settings of the Transverse regions method. The analysis strategy and its software implementation are also illustrated. In Section 5.2 we describe the real and simulated data samples and in Section 5.3 we discuss the event and track selection. The data-correction procedure and the estimation of the systematic uncertainties are described in Section 5.4 and 5.5, respectively. The final results are presented and discussed in Chapter 6.

5.1 Analysis strategy

5.1.1 Settings

The Underlying Event activity is characterized by the following observables:

5. MEASUREMENT OF THE UE WITH THE ALICE DETECTOR

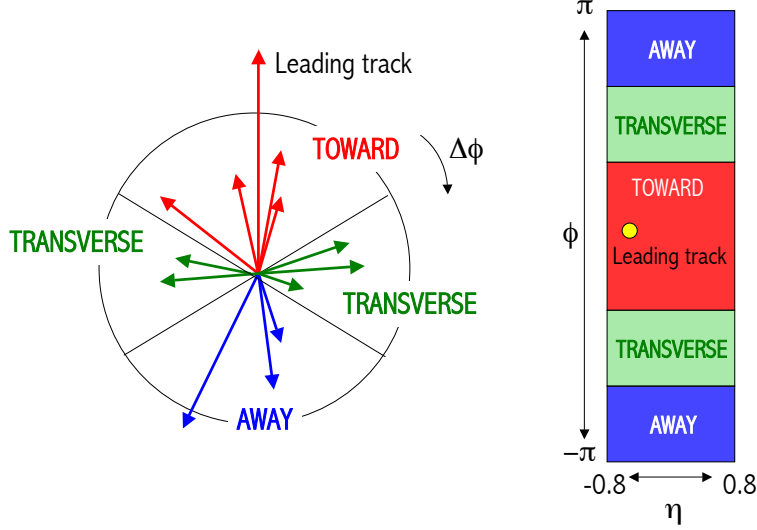


Figure 5.1: Definition of the regions Toward, Transverse and Away with respect to the leading-track direction. In first approximation the Toward and Away regions collect the fragmentation products of the leading and sub-leading jets, respectively. The UE is measured in the Transverse region.

- average charged particle density as a function of leading-track¹ transverse momentum $p_{T,LT}$:

$$\frac{1}{\Delta\eta \cdot \Delta\phi} \frac{1}{N_{ev}(p_{T,LT})} N_{ch}(p_{T,LT}) \quad (5.1)$$

- average summed p_T density as a function of leading track $p_{T,LT}$:

$$\frac{1}{\Delta\eta \cdot \Delta\phi} \frac{1}{N_{ev}(p_{T,LT})} \sum p_T(p_{T,LT}) \quad (5.2)$$

- $\Delta\phi$ -correlation between tracks and the leading track:

$$\frac{1}{\Delta\eta} \frac{1}{N_{ev}(p_{T,LT})} \frac{dN_{ch}}{d\Delta\phi} \quad (5.3)$$

(in bins of leading-track $p_{T,LT}$).

¹A charged particle and a track are two conceptually different objects. Namely, a track is the experimental manifestation of a charged particle traversing the detector and is composed of a set of successive energy depositions in the detector's material. Nevertheless in this thesis we sometimes use the word *leading track* also when referring to the data fully corrected to the particle level.

N_{ev} is the total number of events selected and $N_{\text{ev}}(p_{\text{T,LT}})$ is the number of events in a given leading-track transverse-momentum bin. The first two variables are evaluated in three distinct regions. These regions, illustrated in Fig. 5.1, are defined with respect to the leading-track azimuthal angle:

- Toward: $|\Delta\phi| < 1/3 \pi$
- Transverse: $1/3 \pi < |\Delta\phi| < 2/3 \pi$
- Away: $|\Delta\phi| > 2/3 \pi$

where $\Delta\phi = \phi_{\text{LT}} - \phi$ is defined in $\pm\pi$. Therefore, in Eq.(5.1)-(5.3) $\Delta\phi = 2/3\pi$. $\Delta\eta = 1.6$ is the acceptance in pseudo-rapidity. The leading-track is not included in the final distributions.

5.1.2 Analysis flow

The analysis is performed in three steps, illustrated in Fig. 5.2. The first step is a filtering procedure: the event and track selection cuts are applied to the input data and the filtered information is stored as a *branch* in the AOD output container¹. The input can be reconstructed data (real or simulated) stored in the ESD or pure kinematic information from the Monte Carlo. In the latter case the filtering procedure just selects physical primary particles (this is the case of the simulated results shown in Sect. 4.2 and 4.3). In a second, optional, step the filtered information is processed by one or more jet algorithms and the arrays of reconstructed jets are stored in different AOD branches. Finally, the UE software processes the information stored in the AOD and evaluates the event activity in the different topological regions and the corrections to be applied to the data (if the input was a simulation). The analysis flow is flexible to different options. It is possible to produce and store the AOD object and then to run the UE analysis in a second stage or to concatenate the three steps described above in a single loop over the input data. In this case a virtual AOD is produced which is not saved as a file at the end of the analysis.

¹The AOD container is a ROOT object TTree, containing several sub-structures, called branches. In each branch a relevant piece of information is stored, for instance there is a branch for the reconstructed tracks, jets, vertices etc.

5. MEASUREMENT OF THE UE WITH THE ALICE DETECTOR

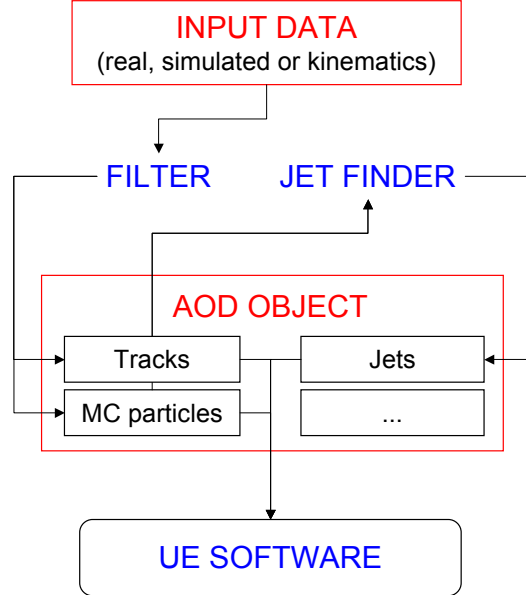


Figure 5.2: Schematic representation of the analysis flow. The input data are pre-selected (FILTER) and stored in an output container (AOD). Eventually, jets are reconstructed (JET FINDER) and stored in the same AOD. The AOD information is finally processed by the UE software to evaluate the event activity in the different regions and the corrections to be applied to the data.

5.1.3 Software implementation

The analysis and correction procedure is based on multi-dimensional histograms in order to preserve correlation information among the relevant observables: leading-track transverse momentum and multiplicity as event level observables and track transverse momentum, pseudo-rapidity and azimuthal angle as track-level observables. Moreover, these quantities are stored for each analysis *step*. A step corresponds to a specific event or track selection. Technically, this is achieved with user-defined data containers based on the ROOT class THnSparse. Tab. 5.1 summarizes the analysis steps, indicating if the stored observables come from Monte Carlo generated information (MC) or after full detector simulation (RECO). For real data only steps 6, 8 and 9 are filled. We call this arrangement of the output container *structure 1*. Ratios of specific quantities at different steps

STEP	Event selection	Leading track	All tracks
0		MC	MC
1	Off-line trigger	MC	MC
2	Reconstructed vertex	MC	MC
3	Leading track in acceptance	MC	MC
4		MC	MC if RECO matched a primary
5		MC	MC if RECO matched any
6		RECO	RECO
7		RECO if matched to MC	RECO
8	Tracking efficiency applied on leading track	RECO	RECO
9	Tracking efficiency applied on leading track in 2 steps	RECO	RECO

Table 5.1: Summary of the analysis steps, corresponding to specific event and track selections. The table also indicates if the stored observables come from Monte Carlo generated information (MC) or from full detector simulation (RECO). This arrangement of the output container is called *structure 1*.

provide the needed information (tracking efficiency, contamination from secondaries etc.) to correct the data back to the particle level, as illustrated in Sect. 5.4.

The code, implemented within the ALICE analysis framework AliRoot, consists of the following classes:

- `AliAnalysisTaskLeadingTrackUE`: master task to execute the analysis
- `AliAnalyseLeadingTrackUE`: analysis algorithms
- `AliUEHist`: defines the output containers
- `AliUEHistograms`: encapsulates several `AliUEHist` objects plus additional control histograms

5. MEASUREMENT OF THE UE WITH THE ALICE DETECTOR

- `AliAnalysisTaskCorrectionsUE`: for standalone study of the contamination correction
- `AliAnalysisTaskTrackCutsSystematicsUE`: to estimate the systematic uncertainty due to the choice of track cuts

Moreover, a set of functions allows the user to apply the correction procedure to the data and to plot the analysis outputs with the systematic uncertainties. These functions are implemented in the macro:

- `correct.C`

Finally, some input files are required which contain the tracking efficiency information needed to estimate the leading-track misidentification bias (Sect. 5.4.1) and the strangeness contamination correction (Sect. 5.4.2).

The analysis fills three main output container types, which belong to the class `AliUEHist`. In the first container type (`fTrackHist[4]`: 4 containers, one per region¹) the track-level information is stored. The relevant variables are: track η and p_T , multiplicity, leading-track p_T and $\Delta\phi$ between tracks and leading track. The container is filled with this set of variables at each of the 10 analysis steps. All the information to plot the final distributions is stored in the container. The second container (`fTrackHistEfficiency`) includes some complementary information to evaluate the tracking efficiency and contamination and the relative systematic uncertainties. Namely, the track p_T and η are stored for different particle species (protons, pions, kaons) at all analysis steps. Finally, the event-level container (`fEventHist`) stores the event multiplicity and the leading-track p_T for all steps. The stored information is used to estimate the event-level corrections (Sect. 5.4.1 and 5.4.4). In addition, the class `AliUEHistograms` contains several histograms useful to check basic distributions and correlations related to the analysis. Those are summarized in the following.

Standard UE distributions:

¹The UE analysis framework always evaluates separately the TransMIN and TransMAX regions. Nevertheless it is possible to merge them into a single Transverse region like in this analysis.

- `fNumberDensitypT`
- `fSumpT`
- `fNumberDensityPhi`

Reconstructed p_T , η , ϕ or R^1 of leading track versus generated:

- `fCorrelationpT`
- `fCorrelationEta`
- `fCorrelationPhi`
- `fCorrelationR`

Azimuthal difference between reconstructed and generated leading-track versus generated p_T :

- `fCorrelationLeading2Phi`

Reconstructed versus generated multiplicity:

- `fCorrelationMultiplicity`

Event count as a function of step and event type (non-diffractive, single or double-diffractive dissociation) for Monte Carlo:

- `fEventCount`: this histogram has one additional step = -1 to account for the number of events before any cut on the vertex longitudinal position
- `fEventCountDifferential`: this histograms accounts for the dependency on leading-track p_T in addition.

Number of tracks contributing to the vertex:

- `fVertexContributors`

5. MEASUREMENT OF THE UE WITH THE ALICE DETECTOR

Collision energy: 0.9 TeV					
Data period	Events	Anchor	Generator	Tune	Events
LHC10c	5,515,184	LHC10e13	PYTHIA	D6T	4,188,258
		LHC10e12	PHOJET		4,182,576
Collision energy: 7 TeV					
Data period	Events	Anchor	Generator	Tune	Events
LHC10b	25,137,512	LHC10d1	PYTHIA	Perugia 0	18,831,361
		LHC10d2	PHOJET		13,676,884

Table 5.2: Data samples considered classified in terms of LHC data-taking periods and corresponding Monte Carlo anchor runs.

5.2 Data samples

We consider two sets of data corresponding to the collision energies of $\sqrt{s} = 0.9$ and 7 TeV and the related simulations (PYTHIA 6 tunes D6T and Perugia 0 and PHOJET after full detector simulation with GEANT 3). In May 2010 ALICE recorded about $6 \cdot 10^6$ good-quality minimum-bias events at $\sqrt{s} = 0.9$ TeV. The luminosity was of the order of $10^{26} \text{ cm}^{-2} \text{ s}^{-1}$ and the probability for pile-up events in the same bunch crossing was negligible. Data underwent 3 iterations of the calibration/reconstruction procedure (referred to as pass3). The $\sqrt{s} = 7$ TeV sample of about $25 \cdot 10^6$ events was collected in April 2010, with a luminosity of $10^{27} \text{ cm}^{-2} \text{ s}^{-1}$. In this case the mean number μ (see Sect. 2.1.1) of interactions per bunch crossing has been estimated to range from 0.005 to 0.035. A set of high pile-up probability runs ($\mu = 0.2 - 2$) has also been analysed in order to study our pile-up rejection procedure and to determine the related uncertainty (see Sect. 5.3.1.1). Those runs are excluded from the analysis. The calibration/reconstruction procedure was iterated 2 times (pass2). Tab. 5.2 summarizes the details of the considered data and Monte Carlo samples. The number of events reported corresponds to the off-line triggered events.

For each data-taking period we consider only those runs flagged as good (quality

$${}^1R = \sqrt{\Delta\phi^2 + \Delta\eta^2}$$

flag = 1) according to the official ALICE run condition table¹ with no voltage trips in the TPC and no TPC sectors with occupancy above the tolerated upper limit. The same runs are considered in the *anchor*² simulations. Namely, for the 0.9 TeV sample (LHC10c) we considered the following runs: 121040, 121039, 118561, 118560, 118558, 118512, 118507, 118506.

For the 7 TeV sample (LHC10b): 117222, 117220, 117116, 117112, 117109, 117099, 117086, 117077, 117065, 117063, 117060, 117059, 117054, 117053, 117052, 117050, 117048, 116645, 116643, 116574, 116571, 116562, 116403, 116402, 116288, 116102, 115414, 115401, 115393, 115193, 115186, 114931.

Data are compared to three Monte Carlo models: PYTHIA 6.4 (tune Perugia-0), PYTHIA 8.1 (tune 1) and PHOJET 1.12 (see Sect. 1.3.2 for an overview on these models).

5.3 Event and track selection

5.3.1 Event selection

In this analysis we consider events fulfilling the standard ALICE minimum bias trigger³, based on the on-line information from the SPD and the V0A and V0C detectors. Namely this trigger selects events with at least one chip fired in the SPD or in one of the two V0s, in coincidence with the nominal LHC interacting bunches. An additional off-line selection is made following the same criteria but considering clusters of hits instead of a single chip fired⁴. Moreover, the arrival time of particles in the V0A and V0C scintillators is used to reject beam-gas interactions occurring outside the nominal interaction region [105].

¹<http://alimonitor.cern.ch/configuration/>

²Anchor runs are sets of simulated events in which the detector configuration reproduces that of the corresponding experimental runs. Namely, the same calibration parameters are applied during the reconstruction and the same modules switched-off during the data taking are excluded.

³CINT1B level-0 trigger class.

⁴This is achieved with the `AliPhysicsSelection` class in the AliRoot framework.

5. MEASUREMENT OF THE UE WITH THE ALICE DETECTOR

For each event a reconstructed vertex is required. We accept vertices reconstructed with global tracks (combined ITS and TPC information) or with the SPD only (as described in Sect. 2.2.4.1). Only vertices within ± 10 cm of the nominal interaction point along the beam axis are considered. Moreover, we require at least one track with $p_T > 0.15, 0.5$ or $1.0 \text{ GeV}/c$ in the acceptance $|\eta| < 0.8$.

In the set of data taken at $\sqrt{s} = 7 \text{ TeV}$ a pile-up rejection procedure is applied: events with more than one distinct reconstructed primary vertex are rejected as well as single tracks with a distance of closest approach¹ to the primary vertex in the beam direction (DCA_Z) larger than 2 cm. The effects of this selection are discussed and quantified in Sect. 5.3.1.1.

No explicit rejection of cosmic-ray events is applied since cosmic particles are efficiently suppressed by our track selection cuts [20]. This is confirmed by the absence of a sharp enhanced correlation at $\Delta\phi = \pi$ from the leading track which would be caused by almost straight high- p_T tracks crossing the detector. Tab. 5.3 summarizes the percentage of events remaining after each event selection step.

Finally, some word should be spent about the class of events selected with the above criteria. We are interested in the study of inelastic non-diffractive events. Nevertheless, the ALICE minimum-bias trigger is also efficient for diffractive events. The fraction of accepted diffractive events can be evaluated with Monte Carlo and strongly depends on the model. In Fig. 5.3 we show the probability for Non Diffractive (ND), Single Diffractive (SD) dissociation and Double Diffractive (DD) dissociation events as a function of the leading-track p_T for PYTHIA 6 and PHOJET. All the event-selection cuts have been applied, except for the

¹The Distance of Closest Approach (DCA) or *impact-parameter* of a track to the primary vertex is generally considered separately in the transverse plane (XY) and in the longitudinal direction (Z) with respect to the beam axis. The two projections are defined as: $\text{DCA}_{XY} = \rho - \sqrt{(x_v - x_0)^2 + (y_v - y_0)^2}$ and $\text{DCA}_Z = (z_{\text{track}} - z_v)$, where ρ and (x_0, y_0) are the radius and the centre of the track projection in the transverse plane, (x_v, y_v, z_v) is the position of the primary vertex and z_{track} is the longitudinal position of the track after it has been propagated to the distance of closest approach in the transverse plane [85].

Collision energy: 0.9 TeV		
	Events	% of all
Offline trigger	5,515,184	100.0
Reconstructed vertex	4,482,976	81.3
Leading track $p_T > 0.15$ GeV/ c	4,043,580	73.3
Leading track $p_T > 0.5$ GeV/ c	3,013,612	54.6
Leading track $p_T > 1.0$ GeV/ c	1,281,269	23.2
Collision energy: 7 TeV		
	Events	% of all
Offline trigger	25,137,512	100.0
Reconstructed vertex	22,698,200	90.3
Leading track $p_T > 0.15$ GeV/ c	21,002,568	83.6
Leading track $p_T > 0.5$ GeV/ c	17,159,249	68.3
Leading track $p_T > 1.0$ GeV/ c	9,873,085	39.3

Table 5.3: Events remaining after each event-selection step.

cut on the leading-track p_T . In case of PHOJET, diffraction contributes significantly up to higher transverse momenta than PYTHIA. For instance, we see that at $\sqrt{s} = 7$ TeV for a leading track p_T of 10 GeV/ c the number of diffractive events is about half of the non-diffractive events, while in the PYTHIA 6 case the diffractive contribution is negligible. This is due to the fact that PHOJET, as opposed to PYTHIA 6, implements hard and central diffraction. The initial fraction of diffractive events, prior to any event selection, is of the order of 19–35% (considering PYTHIA 6 and PHOJET at both collision energies) of all inelastic processes. After our event selection, the fraction of diffractive events is reduced to an amount that depends on the cut applied on the leading-track p_T . In Tab. 5.4 we summarize the fraction of ND, DD and SD events accepted by the analysis for the three different values of the $p_{T,LT}$ threshold. For $p_{T,LT} > 1$ GeV/ c the diffractive contribution is reduced to 0.4–8% of the total inelastic events. We do not correct for this remaining contribution.

5. MEASUREMENT OF THE UE WITH THE ALICE DETECTOR

Collision energy: 0.9 TeV			
	ND % of INEL	SD % of INEL	DD % of INEL
	$p_{T,LT} > 0.15 \text{ GeV}/c$		
PYTHIA 6	83.9	10.2	5.9
PHOJET	84.5	10.9	4.6
	$p_{T,LT} > 0.5 \text{ GeV}/c$		
PYTHIA 6	92.0	5.2	2.8
PHOJET	87.3	9.1	3.6
	$p_{T,LT} > 1.0 \text{ GeV}/c$		
PYTHIA 6	99.5	0.3	0.2
PHOJET	91.7	6.1	2.2
Collision energy: 7 TeV			
	ND % of INEL	SD % of INEL	DD % of INEL
	$p_{T,LT} > 0.15 \text{ GeV}/c$		
PYTHIA 6	84.1	9.3	6.6
PHOJET	88.7	7.8	3.5
	$p_{T,LT} > 0.5 \text{ GeV}/c$		
PYTHIA 6	92.2	4.6	3.2
PHOJET	90.2	6.9	2.9
	$p_{T,LT} > 1.0 \text{ GeV}/c$		
PYTHIA 6	99.6	0.2	0.2
PHOJET	93.4	4.8	1.8

Table 5.4: Percentage of non-diffractive (ND), single-diffractive dissociation (SD) and double-diffractive dissociation (DD) events with respect to all inelastic collisions (INEL) accepted by the analysis.

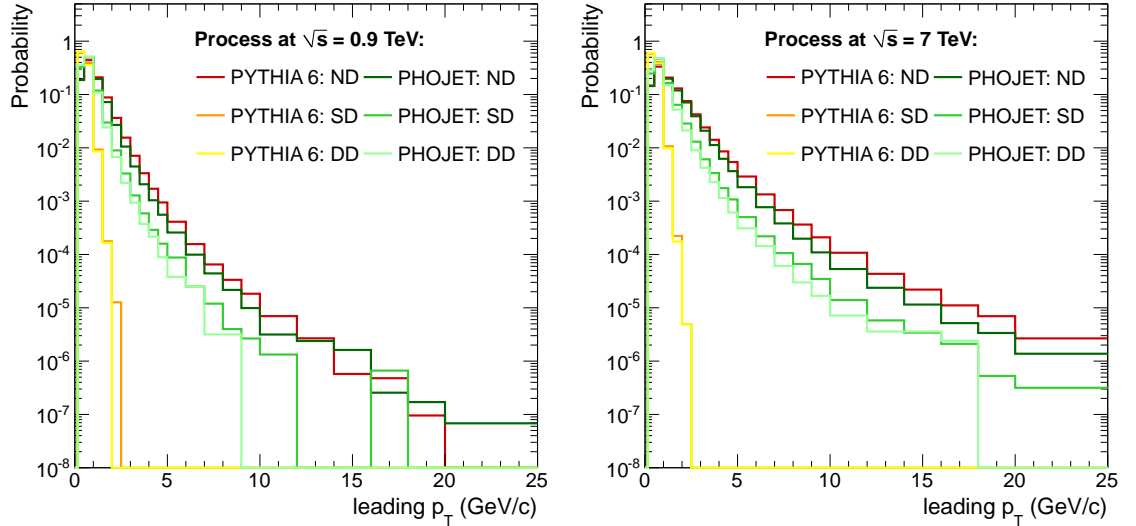


Figure 5.3: Fraction of non-diffractive (ND), double-diffractive dissociation (DD) and single-diffractive dissociation (SD) events in the considered samples as predicted by PYTHIA 6 and PHOJET. $\sqrt{s} = 0.9$ TeV (left), $\sqrt{s} = 7$ TeV (right).

5.3.1.1 Pile-up and beam-gas events

At the collision energy of 7 TeV, due to the high number of protons per bunch it can happen that more than one pair of protons per bunch interacts, while this effect is negligible in the data sample at $\sqrt{s} = 0.9$ TeV. The pile-up rejection procedure is explained in the previous section. Those cuts have a negligible effect on Monte Carlo samples, where no pile-up is implemented: only 0.06 % of the events are removed. In Fig. 5.4 we show the effect of the pile-up rejection on the number density distribution in the Transverse region for two sets of events: the reference sample used in the UE analysis ($\mu = 0.05$ – 0.035) and a set of high pile-up probability runs¹ ($\mu = 0.2$ – 2). At this stage the data are not yet corrected for detector effects. For the high- μ sample the bias (i.e. the discrepancy from the reference sample) is reduced from 20–25% to less than 2%, while the cuts have barely any effect on the reference sample. This is better seen in the left panel of Fig. 5.5, where we show the effect of the rejection on the reference sample alone. In the right panel of Fig. 5.5 we show the effect of the cuts on

¹Runs in the range: 124183–124750.

5. MEASUREMENT OF THE UE WITH THE ALICE DETECTOR

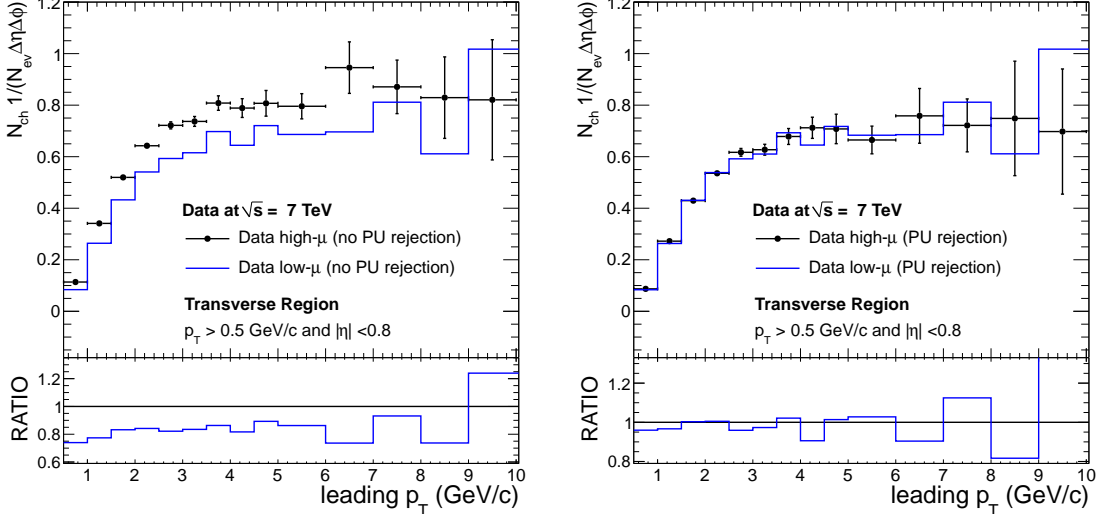


Figure 5.4: Reference and high pile-up probability samples without (left) and with (right) pile-up (PU) rejection cuts. In the high- μ sample (black points) the rejection procedure reduces the bias from 20–25% to less than 2%. The reference sample is unchanged. Non-corrected data at $\sqrt{s} = 7$ TeV.

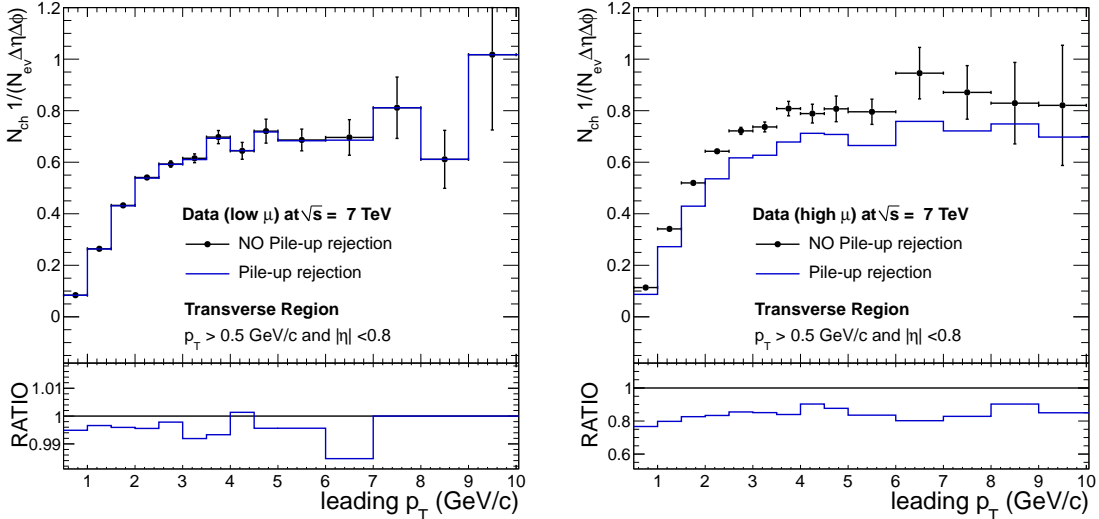


Figure 5.5: Effect of pile-up rejection cuts on the reference (left) and high pile-up probability (right) samples. The cuts barely have any effect on the reference sample and a 20–25% effect on the high- μ sample. Non-corrected data at $\sqrt{s} = 7$ TeV.

Selection criteria	Value
Detectors required	ITS,TPC
Minimum number of TPC clusters	70
Maximum χ^2 per TPC cluster	4
Minimum number of ITS clusters	3
Minimum number of SPD or 1 st layer SDD clusters	1
Maximum DCA_Z	2 cm
Maximum $DCA_{XY}(p_T)$	7σ

Table 5.5: Main track-selection criteria. For more details see text.

the high pile-up sample (we remind here that these runs are excluded from the UE analysis). Taking into account these considerations, we conclude that the contribution from pile-up events in our sample is negligible and we do not apply any further correction.

For what concerns beam-gas events, other studies within the collaboration [105] have shown that the fraction of those remaining after the off-line rejection, mentioned in Sect. 5.3.1, is negligible.

5.3.2 Track selection

Only charged particles are considered in this analysis. Tracks are reconstructed with the two main tracking detectors in the ALICE central barrel: the TPC and the ITS (see Sect. 2.2). The selection criteria described here were optimized during the LHC 2010 data-taking period in order to minimize the contamination from secondary tracks. They are summarized in Tab. 5.5 and explained in more detail in the following:

- require at least 1 cluster in one of the first 3 ITS layers (any SPD layer or the first SDD layer): this cut is meant to reduce the contamination from secondary particles produced in the interaction with the silicon layers or coming from decays of strange particles (which are produced at large distance from the primary interaction point)

5. MEASUREMENT OF THE UE WITH THE ALICE DETECTOR

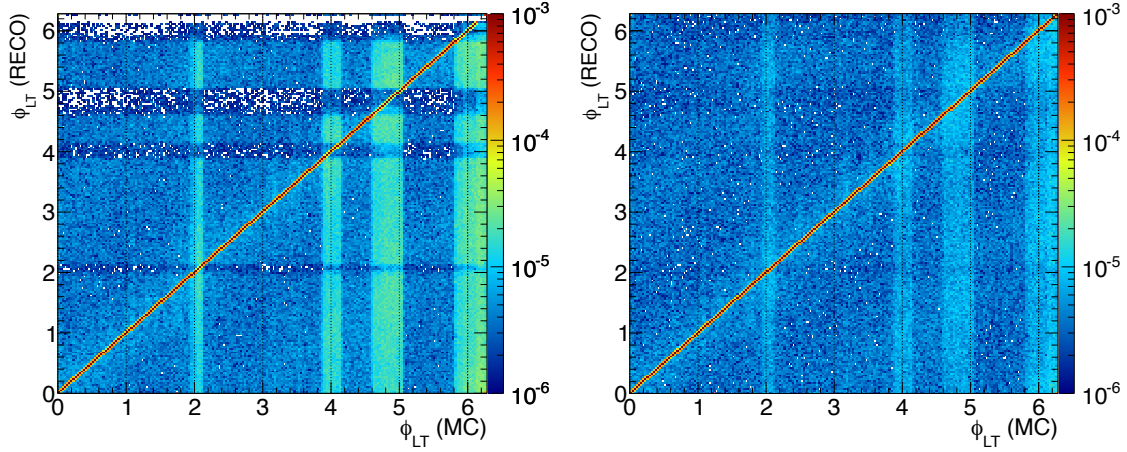


Figure 5.6: Azimuthal correlation between reconstructed (RECO) and generated (MC) leading track. Standard cuts (left) and customized cuts (right). In case of our customized cuts the bias due to the missing ITS modules is reduced (light-blue vertical bands). $p_{p_T} > 0.15 \text{ GeV}/c$ and $|\eta| < 0.8$. PYTHIA 6 and GEANT 3 at $\sqrt{s} = 0.9 \text{ TeV}$.

-
- require at least 70 clusters in the TPC drift volume
 - require a successful re-fit procedure for the TPC and ITS detectors, as described in Sect. 2.2.4.2
 - the quality of the track TPC fitting, measured in terms of χ^2 per space point, is required to be less than 4. The χ^2 measures the dispersion of the fired pads in a cluster with respect to the evaluated centroid
 - p_T -dependent selection on the distance of closest approach to the primary vertex in the transverse plane (DCA_{XY}). The cut corresponds to 7σ of the inclusive probability distribution
 - distance of closest approach to the primary vertex along the beam direction (DCA_Z) smaller than 2 cm
 - reject particles from *kinks* (i.e. charged decay products of charged particles going into charged/neutral pairs)

5.4 Data correction procedure

These are standard cuts also used in other ALICE analyses (i.e. [20]) with only one difference: we require an energy deposition in one of the first 3 ITS layers, while the standard requirement is restricted to the first 2 layers. The standard choice would result in the loss of basically all tracks in the regions where both SPD layers are not active. The effect is illustrated in Fig. 5.6, where we plot the azimuthal position of the generated leading-track versus the one reconstructed by the detector simulation. Apart from a clear correlation between the two quantities (red line), the ITS dead areas are also clearly visible (light-blue vertical bands). As a consequence, most of the events with the leading track in this regions are misidentified, which is unfortunate for this analysis. On the other hand, dropping the standard requirement can lead to a larger number of secondary particles. Fig. 5.7 shows the ratio between the contamination with standard and customized track-cuts. The contamination is defined as the ratio between all reconstructed-tracks and reconstructed primary-tracks. At $\sqrt{s} = 0.9$ TeV we observe a maximum difference of 1.5% for tracks with $p_T < 0.2$ GeV/ c , while for $p_T > 0.5$ GeV/ c the difference saturates at a negligible value (about 0.1%). At 7 TeV the effect is negligible. Therefore, we can safely replace the tight standard cut with the looser requirement of either a cluster in the SPD system or one in the first SDD layer (third ITS layer). In this way the misidentification is reduced from about 16% to about 11.3% (at $\sqrt{s} = 0.9$ TeV and similarly for $\sqrt{s} = 7$ TeV). The track p_T resolution is not significantly different: Fig. 5.8 shows the difference between reconstructed and generated transverse momentum for the standard and customized cuts. The resolution is given by the standard deviation of the distribution's Gaussian fit. The maximum difference in the resolution between the two sets of cuts is about 0.7% in the range $0.2 < p_T < 1$ GeV/ c and 10.5% in the range $5 < p_T < 10$ GeV/ c . In Fig. 5.9 we show the position resolution, which is given by a Gaussian fit to the DCA_{XY} distribution of primary tracks with respect to the simulated vertex. The position resolution in the plane perpendicular to the beam axis deteriorates at maximum by 20%.

5. MEASUREMENT OF THE UE WITH THE ALICE DETECTOR

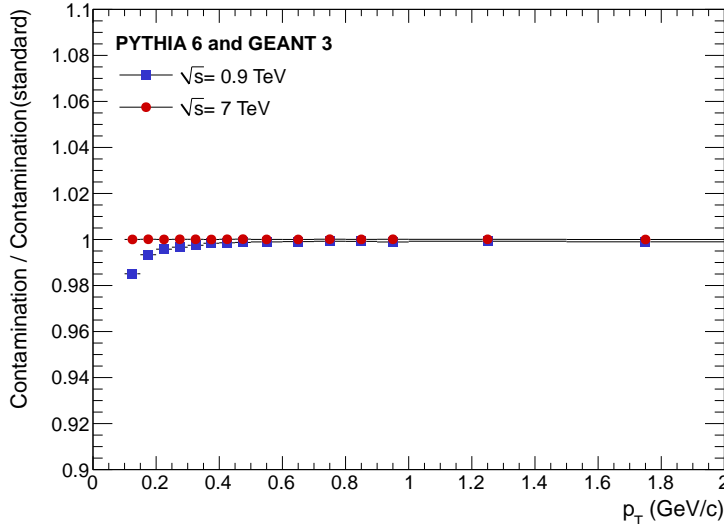


Figure 5.7: Contamination from secondaries: ratio between custom and standard track cuts ($|\eta| < 0.8$). PYTHIA 6 and GEANT 3.

5.4 Data correction procedure

At the event level we correct for the vertex reconstruction efficiency and for the misidentification of the leading track. We do not correct for the trigger efficiency since its value is basically 100% for events which have at least one particle with $p_T > 0.15$ GeV/ c in the range $|\eta| < 0.8$ [105]. At the track level we correct for the tracking efficiency and for the contamination from secondary particles.

The flow of the correction procedure is shown in Fig. 5.10. Each experimental bias is evaluated from the relevant analysis steps (see Tab. 5.1) from the simulated output, then the corresponding correction factor is applied to the data (or Monte Carlo after full detector simulation) and the corrected distributions are stored in a different data-container at a step corresponding to the applied correction. Each step also includes the corrections applied in all the previous ones. The output structure containing the corrected data is illustrated in Tab. 5.6 and is called *structure 2*. In practice, the correction mechanism proceeds backwards with respect to the data analysis flow and fills a container object similar to the one used for the analysis. In this way the effect of each single correction step

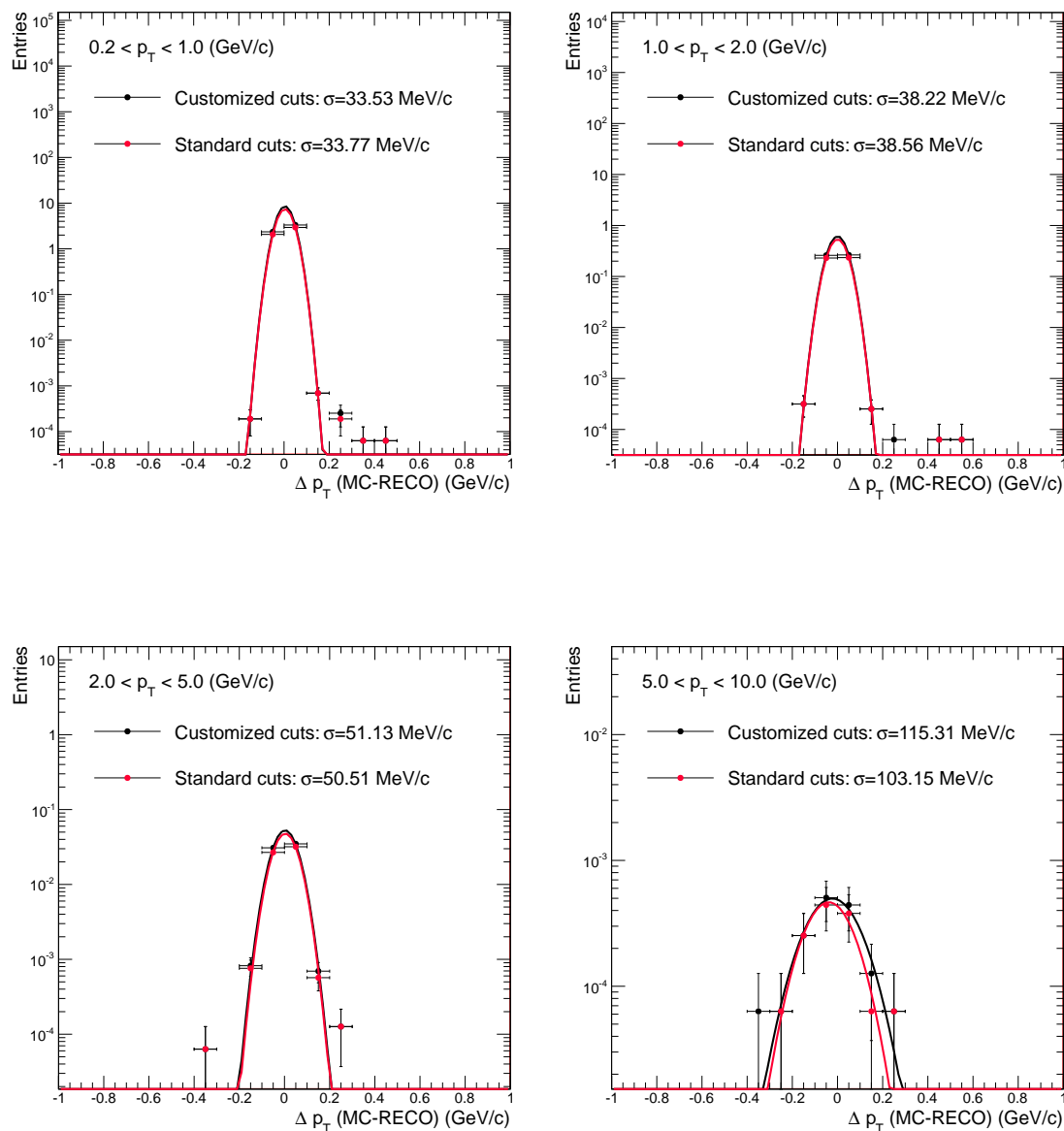


Figure 5.8: Transverse momentum resolution for standard and customized track cuts ($|\eta| < 0.8$). Distributions are normalized to unity and fitted with a Gaussian. The maximum difference in the resolution (σ of Gaussian fit) between the two sets of cuts is about 10.5%. PHOJET and GEANT 3 at $\sqrt{s} = 0.9$ TeV.

5. MEASUREMENT OF THE UE WITH THE ALICE DETECTOR

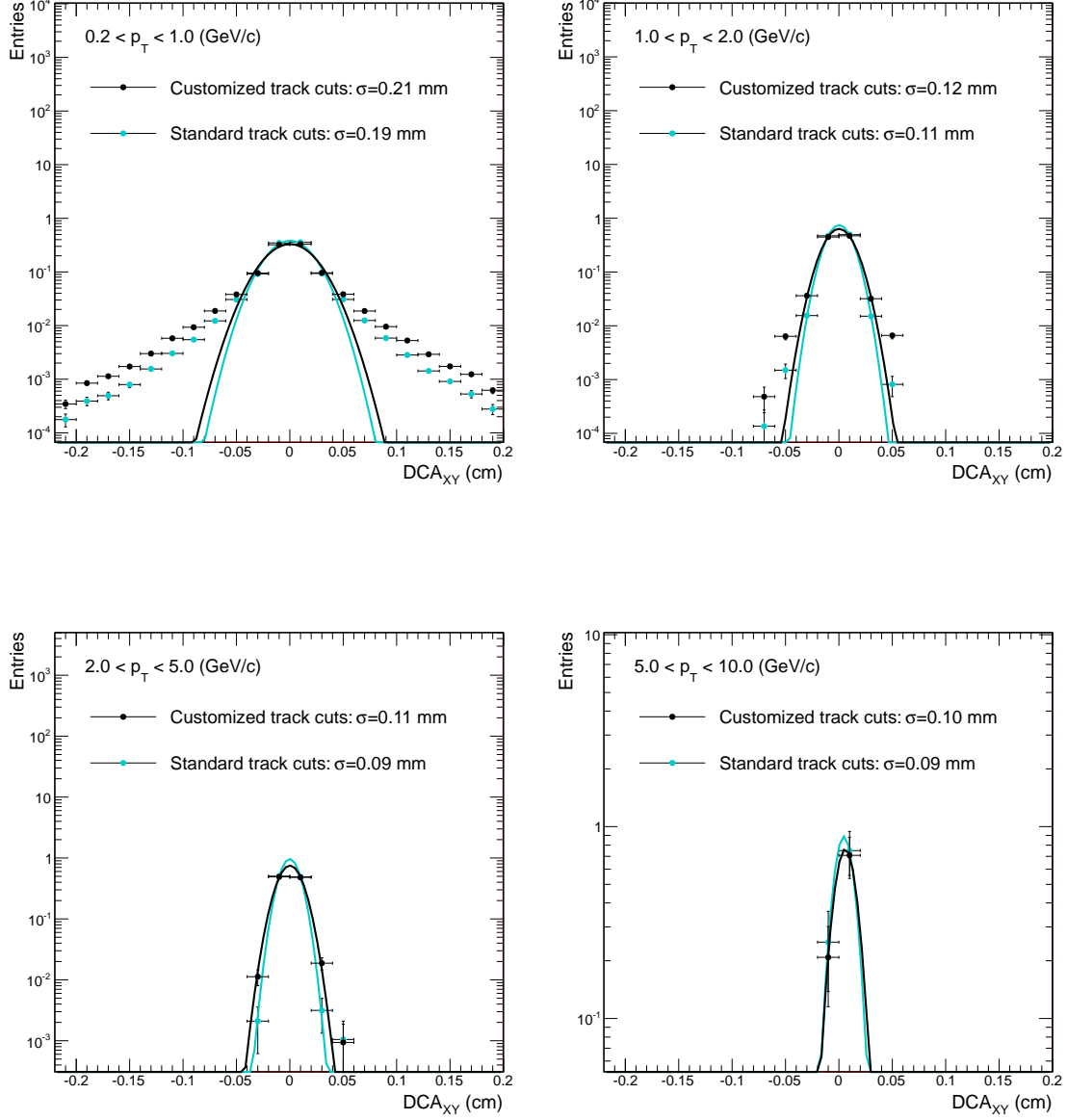


Figure 5.9: Position resolution of primary tracks for standard and customized track cuts ($|\eta| < 0.8$). Distributions are normalized to unity and fitted with a Gaussian. The maximum difference in the resolution (σ of Gaussian fit) between the two sets of cuts is about 20% in the highest p_T bins. PHOJET and GEANT 3 at $\sqrt{s} = 0.9$ TeV.

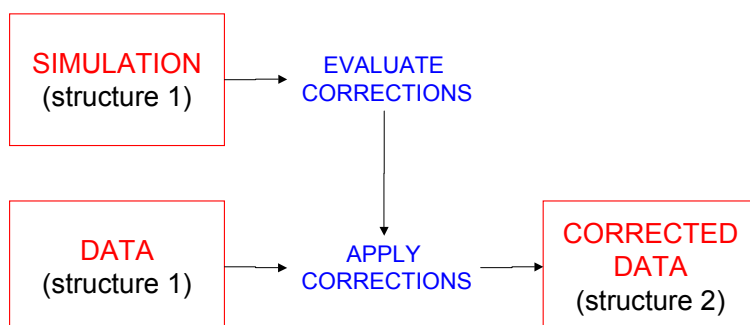


Figure 5.10: Schematic representation of the data correction procedure. Each experimental bias is evaluated from the simulated output, then the corresponding correction factor is applied to the data and the corrected distributions are stored in a different data-container.

is stored separately, which facilitates the estimate of the systematic uncertainty related to that particular correction.

The first correction applied accounts for the misidentification of the leading track (see Sect. 5.4.1). This bias is estimated from the ratio between steps 8 and 6 of structure 1. The corrected distributions fill the step number 5 of structure 2.

In first approximation (see Sect. 5.4.2) the contamination from secondary particles is estimated from the ratio between steps 5 and 4 of structure 1. Corrected quantities fill step 4 of structure 2.

The tracking efficiency (see Sect. 5.4.3) comes from the ratio between steps 4 and 3 of structure 1; step 3 of structure 2 is filled with the corrected quantities.

Similarly, the correction for the vertex reconstruction efficiency comes from the ratio between steps 2 and 1 of structure 1 and the corrected data fill step 1 of structure 2. This last step corresponds to a number of events corrected down to all the off-line triggers and to track distributions where detector effects have been accounted for and which can be compared to model predictions.

5. MEASUREMENT OF THE UE WITH THE ALICE DETECTOR

STEP	Events and tracks corrected for:
9	
8	
7	
6	(Uncorrected)
5	Leading track misidentification
4	Contamination from secondaries
3	Tracking efficiency
2	
1	Vertex reconstruction efficiency
0	

Table 5.6: Structure of the output container (*structure 2*) accommodating the corrected data.

5.4.1 Leading-track misidentification

Experimentally, we can fail to detect the real leading-track because of the finite acceptance of the detector or tracking inefficiency. In these cases another track (i.e. the sub-leading or sub-sub-leading etc.) is interpreted as the leading one, biasing the analysis in two possible ways. On the one hand the sub-leading track can have a different transverse momentum than the leading one (leading-track p_T bin migration). It has been verified with simulations that this effect is negligible due to the weak dependence of the final distributions on the leading-track p_T . Moreover, the reconstructed leading-track can have a significantly different orientation with respect to the real one, resulting in a rotation of the overall event topology. The most dramatic case is when the misidentified leading-track falls in the actual Transverse region. Fig. 5.11 shows the difference in azimuthal angle between real and reconstructed leading-tracks in $|\eta| < 0.8$ and $p_{T,LT} > 0.15 \text{ GeV}/c$ from a PYTHIA simulation at a collision energy of 7 TeV. In about 5% of the analysed events the reconstructed leading-track falls in the *true* Transverse region.

The probability to misidentify the leading track mostly depends on its p_T . Therefore we can evaluate the correction factors as a function of leading-track

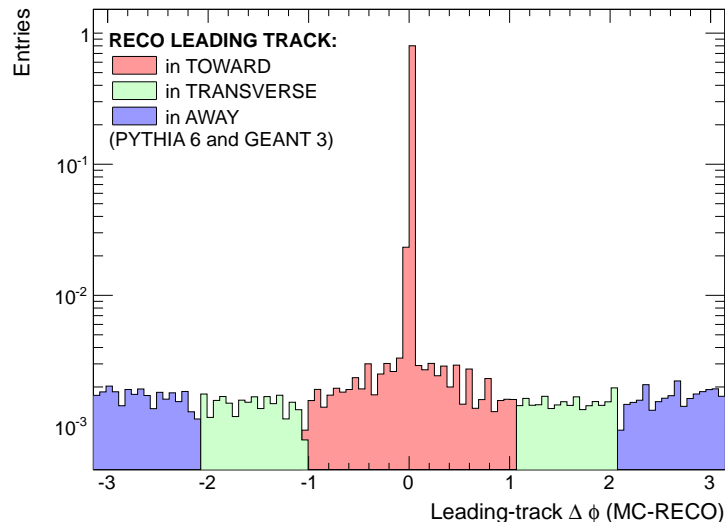


Figure 5.11: Azimuthal distance between real and reconstructed leading track ($p_{T,LT} > 0.15 \text{ GeV}/c$, $|\eta| < 0.8$). In about 5% of the events the reconstructed leading track falls in the true Transverse region. PYTHIA and GEANT at $\sqrt{s} = 7 \text{ TeV}$.

p_T only. The correction is then applied to both event and track-level measured observables, separately for each topological region. The misidentification bias can be evaluated either from simulations or with a data driven procedure. In the first scenario the corrections come from the ratio between events defined by true or reconstructed leading track (steps 6 and 7 of structure 1). The data-driven procedure is illustrated in Fig. 5.12: starting from the measured distributions, for each event the tracking inefficiency is applied a second time on the data (the first time being applied naturally by the detector). Namely, with the help of a random number generator and the efficiency information (previously evaluated with Monte Carlo as a function of η and p_T) we determine if the leading track is reconstructed. In the positive case it is used to define the topological regions. Otherwise the sub-leading track is used. Since the tracking inefficiency is quite small (about 20%) applying it on the reconstructed data a second time does not alter the results significantly. In order to verify this assertion we compare our results with a two-steps procedure. In this case the inefficiency is applied two times

5. MEASUREMENT OF THE UE WITH THE ALICE DETECTOR

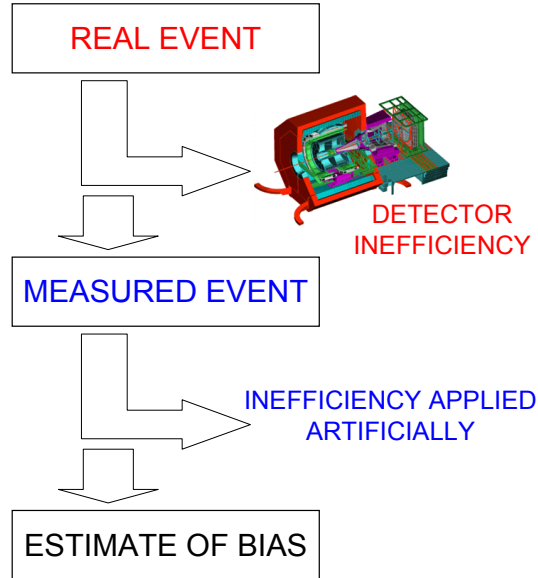


Figure 5.12: Data-driven estimate of the leading-track misidentification bias. The tracking inefficiency is applied on the data a second time, the first time being naturally applied by the detector.

on the measured data, the half of its value at the time¹. The correction factor thus obtained is compatible with the one-step procedure. As an example, the comparison between the correction factor for the number density in the Transverse region obtained with the one and two-steps procedures is shown in Fig. 5.13 (left).

The data-driven procedure is validated by its consistency with the Monte Carlo procedure, though a discrepancy is present at low leading-track p_T values. As an example Fig. 5.13 (right) shows the correction factor for the number density in the Transverse region for tracks with $p_T > 0.15 \text{ GeV}/c$ for the Monte Carlo and data-driven procedures. The discrepancy between the two methods is maximal in the first bin ($0.15 < p_{T,LT} < 0.5 \text{ GeV}/c$), indicating that in this range other effects

¹Strictly speaking the square root of the inefficiency should be applied two times in this case. For technical reasons this is not done in the filling of step 9 of structure 1. We have verified that this approximation has an effect below 1% and in any case this step is only used for testing purposes.

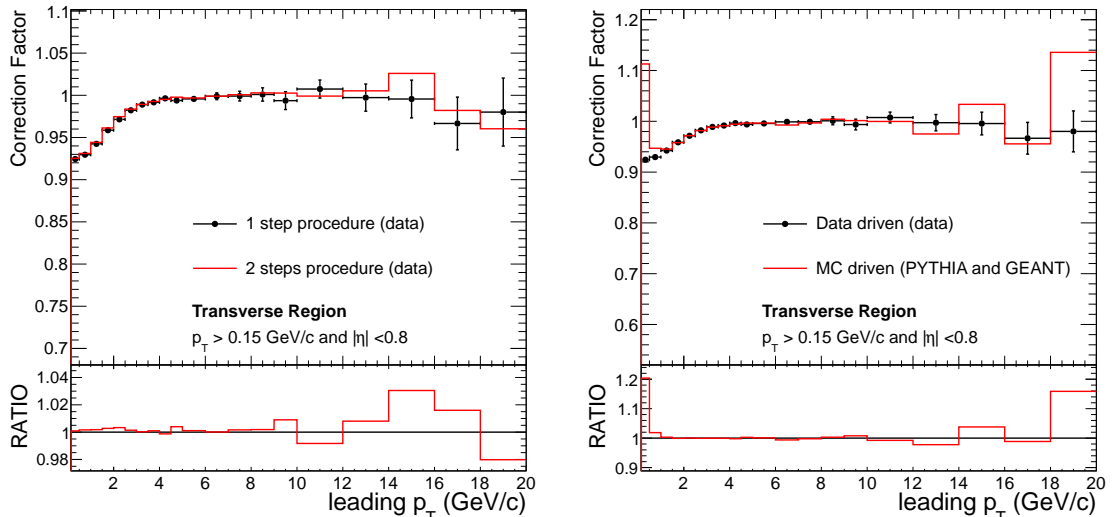


Figure 5.13: Leading-track misidentification bias for the number density in the Transverse region: correction factor as a function of leading-track p_T for the data-driven method with one or two steps (left) and for Monte Carlo and data-driven procedures (right). PYTHIA 6 and GEANT 3 at $\sqrt{s} = 7$ TeV.

than the tracking inefficiency contribute to the bias like, for instance, the momentum resolution. Our final results are obtained with the one-step data-driven procedure.

In Appendix A we present the effect of the leading-track misidentification correction on the measured data. We consider all the topological regions and the two collision energies for the track p_T threshold of 0.15 GeV/ c . The corrections applied for the other threshold values are always smaller. At $\sqrt{s} = 0.9$ TeV the bias extends up to a leading track p_T of about 3 GeV/ c and at $\sqrt{s} = 7$ TeV up to about 4 GeV/ c . The maximum value of the applied correction is -8% .

5.4.2 Contamination from secondaries

We correct for secondary tracks that pass the selection cuts and are wrongly identified as primaries. The relevant observables for this correction are the track's transverse momentum and pseudo-rapidity, therefore we evaluate a two-

5. MEASUREMENT OF THE UE WITH THE ALICE DETECTOR

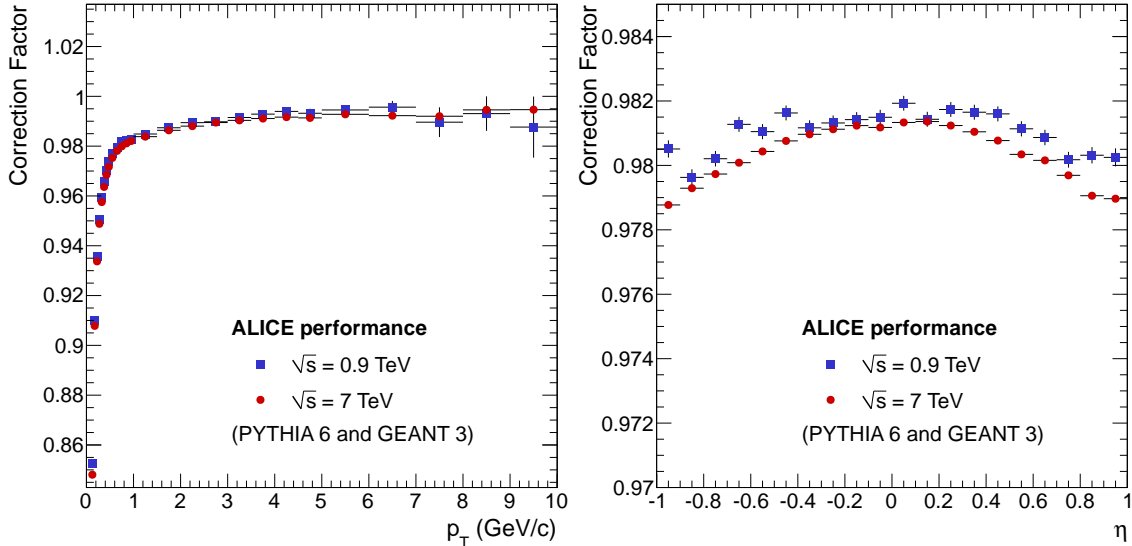


Figure 5.14: Contamination correction: correction factor as a function of track p_T (left, $|\eta| < 0.8$) and η (right, $p_T > 0.5 \text{ GeV}/c$) from a PYTHIA and GEANT simulation.

dimensional array of correction factors as a function of these variables. Relying on Monte Carlo information, the factors are obtained from the ratio between the number of reconstructed tracks (after full detector simulation) matching a generated primary and the number of reconstructed tracks matching any generated particle. Fig. 5.14 shows these correction factors projected on the relevant variables p_T and η at the two considered collision energies. The correction has a maximum value of $\sim 15\%$ in the first track- p_T bin ($0.15\text{--}0.2 \text{ GeV}/c$) and is below 1% for track $p_T > 3 \text{ GeV}/c$.

Moreover, we introduce an additional data-driven correction that takes into account the underestimation of the strangeness yields in Monte Carlo. Secondary tracks are mostly produced by weak decays of strange particles (K_s^0 , Λ etc.), photon conversions, hadronic interactions in the detector material and decays of charged pions. Fig. 5.15 shows the relative abundance of tracks coming from different processes as predicted by PYTHIA 6 and GEANT 3 at a collision energy of 7 TeV . The inclusive yield from real data is also shown. The plot shows that the

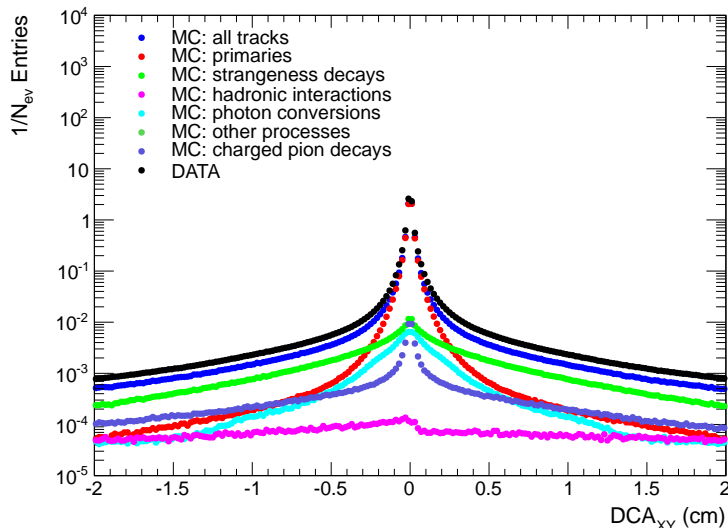


Figure 5.15: Different contributions to secondary tracks yield. Track $p_T > 0.15 \text{ GeV}/c$ and $|\eta| < 0.8$. PYTHIA 6 and GEANT 3 and uncorrected data at $\sqrt{s} = 7 \text{ TeV}$.

simulated inclusive yield (dark-blue points) does not reproduce the measured one (black points), especially in the tails of the DCA_{XY} distribution, where secondary tracks dominate. The most relevant contribution in the tails of the DCA_{XY} distribution is given by the decay products of strange particles (light-green dots), while photon conversions and charged-pion decays have on average smaller opening angles (therefore smaller $|DCA_{XY}|$). We attribute the discrepancy between data and simulations at high DCA_{XY} absolute values to a too low strangeness production in PYTHIA, as already observed in other studies [22] and we use a data-driven method to account for this discrepancy. First we determine a normalization factor $N(p_T)$ to estimate the difference between data and Monte Carlo in primary-particles production. This factor is evaluated in the central DCA_{XY} region, the one accepted by the p_T -dependent cut, and is given by the ratio between the track yields in data and simulation. In Fig. 5.16 (left) we show the factor $N(p_T)$ for our set of track-cuts and for the standard one (see Sect. 5.3.2) at both considered collision energies. In Fig. 5.17 we show the DCA_{XY} distribution of tracks accepted by our customized cuts in the first (left) and last (right) p_T bins

5. MEASUREMENT OF THE UE WITH THE ALICE DETECTOR

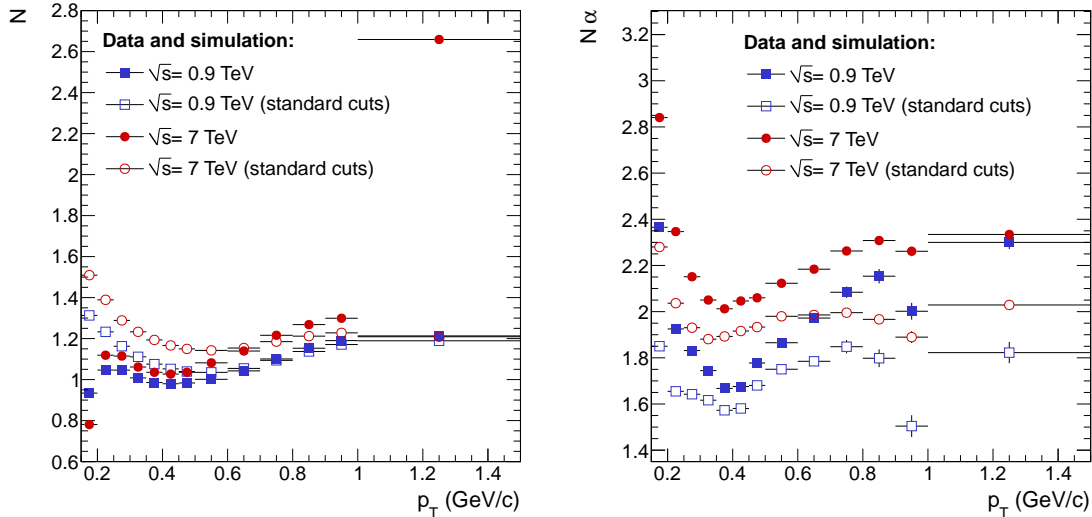


Figure 5.16: Data-driven contamination correction: primaries normalization factor N (left) and strangeness correction factor $N\alpha$ (right) estimated with the constant-fit method ($|\eta| < 0.8$). The track cuts used in this analysis are compared to the standard ones (see Sect. 5.3.2). Data and PYTHIA 6/GEANT 3.

considered in the study. In each plot we compare the measured distribution with the simulated one. The ratio between the integrals of the two distributions gives the normalization factor N in the p_T bin considered. The value of the normalization factor depends on the choice of track cuts since we have observed that the track-selection has a different impact on data and simulations (see Sect. 5.5). This fact is taken into account in the estimate of the systematic uncertainty related to this correction. In particular we note that at the collision energy of 7 TeV, for tracks in the range $1.0 < p_T < 1.5$ GeV/c, our choice of track-cuts leads to a value of $N(p_T)$ about two times larger than in the case of the standard cuts. Moreover, at both collision energies in the very first bin ($0.15 < p_T < 0.2$ GeV/c) the general trend is inverted and the yield is higher in the simulation than in the real data. In a second step we determine the ratio $\alpha(p_T)$ between the strangeness contribution to secondaries from data and simulation:

$$\alpha(p_T) = \frac{Data(p_T) - N(p_T) \cdot OtherSec_{MC}(p_T) - N(p_T) \cdot Prim_{MC}(p_T)}{N(p_T) \cdot SecFromStr_{MC}(p_T)} \quad (5.4)$$

where $Data$ indicates the measured yield, $Prim_{MC}$ the primary tracks from the

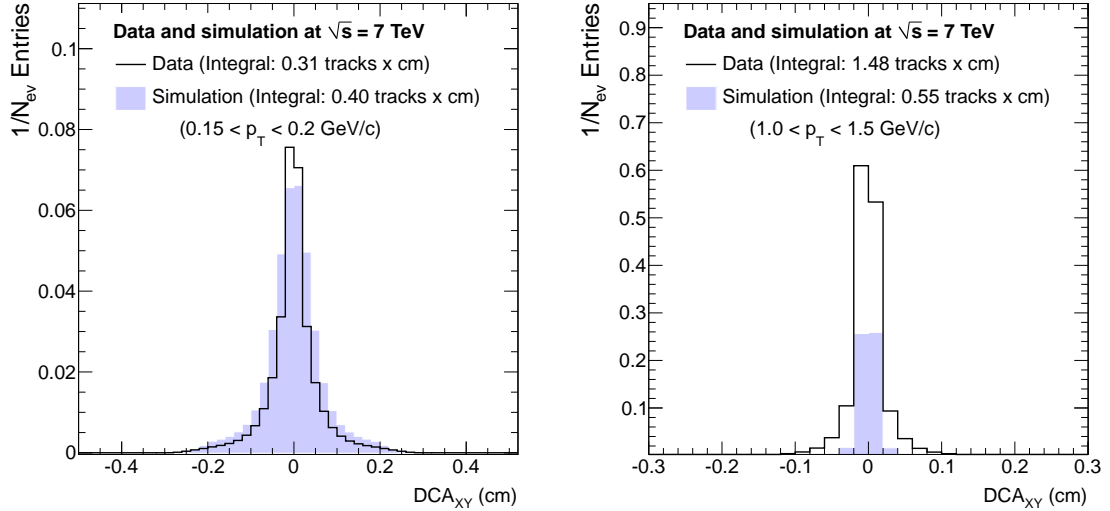


Figure 5.17: Tracks accepted by our customized set of cuts in the first (left) and last (right) p_T bins considered in the determination of the factor N . The ratio between the distribution's integral in the case of real data (black line) and simulation (light-blue area) gives the factor N for the given p_T bin ($|\eta| < 0.8$). Data and PYTHIA 6/GEANT 3 simulation at $\sqrt{s} = 7$ TeV. See text for more details.

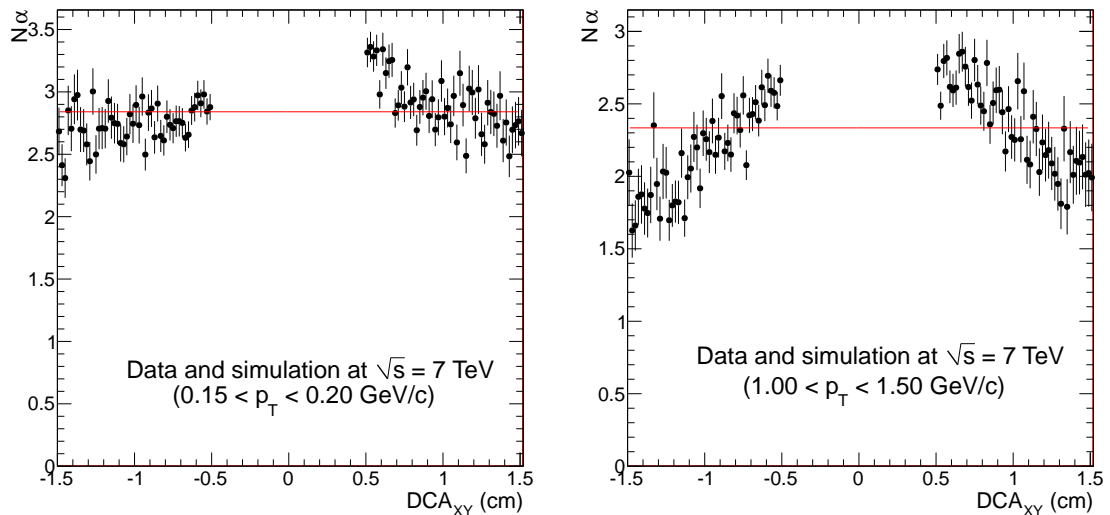


Figure 5.18: Constant fit (red line) to factor $N\alpha$ for the customized set of track cuts: tracks $0.15 < p_T < 0.2$ GeV/ c (left) and $1.0 < p_T < 1.5$ GeV/ c (right), $|\eta| < 0.8$. Data and PYTHIA 6/GEANT 3 simulation at $\sqrt{s} = 7$ TeV. See text for more details.

5. MEASUREMENT OF THE UE WITH THE ALICE DETECTOR

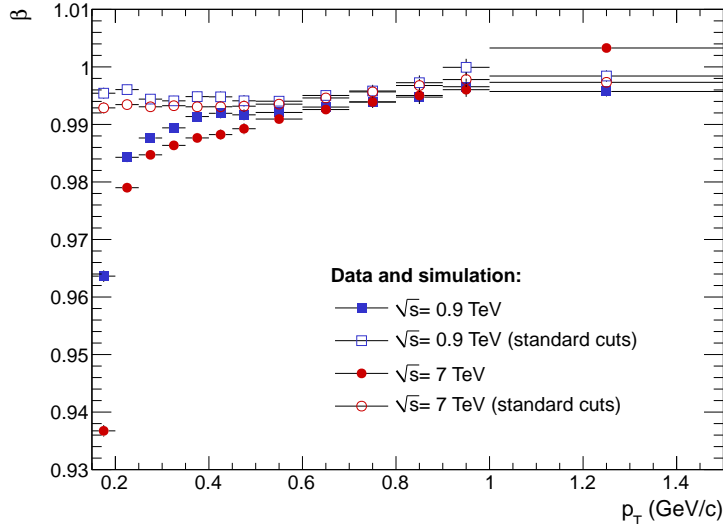


Figure 5.19: Data-driven contamination correction from Eq. 5.6. This quantity multiplies the ratio between primaries and all particles estimated with pure simulation ($|\eta| < 0.8$). The track cuts used in this analysis are compared to the standard ones (see Sect. 5.3.2). Data and PYTHIA 6/GEANT 3.

simulation, $SecFromStr_{MC}$ the secondaries from strangeness decays and $OtherSec_{MC}$ the secondaries from all other processes. The correction factor is evaluated by means of a constant fit to the above quantity (more precisely to $N(p_T)\alpha(p_T) \equiv N\alpha$) in different p_T bins in the range $0.15 < p_T < 1.5 \text{ GeV}/c$, excluding the central region $|DCA_{XY}| < 0.5 \text{ cm}$ which is dominated by primaries. An example of these fits is shown in Fig. 5.18, for the first and the last p_T -bin considered. The factor $N\alpha$ is presented in Fig. 5.16 for the custom and standard track-cuts. Also in this case we observe a discrepancy between the two sets of cuts which is maximal in the first ($0.15 < p_T < 0.2 \text{ GeV}/c$) and last ($1.0 < p_T < 1.5 \text{ GeV}/c$) bins (about a factor 1.3).

In terms of these quantities, the real fraction of primary tracks can be approximated by:

$$\frac{Prim_{TRUE}}{All_{TRUE}} \simeq \frac{N \cdot Prim_{MC}}{N \cdot Prim_{MC} + N \cdot \alpha \cdot SecFromStr_{MC} + N \cdot OtherSec_{MC}} \quad (5.5)$$

where All_{TRUE} is the measured inclusive track yield. In Eq. 5.5 we have omitted the p_T dependence of the various factors. This quantity is obtained by multiplying

the ratio of primaries from Monte Carlo by the correction factor:

$$\beta(p_T) = \frac{All_{MC}(p_T)}{Prim_{MC}(p_T) + \alpha(p_T) \cdot SecFromStr_{MC}(p_T) + OtherSec_{MC}(p_T)} \quad (5.6)$$

Fig. 5.19 shows the factor $\beta(p_T)$ at the two energies considered, the results for the standard cuts are also shown. For the set of cuts used in this analysis, in the lower track p_T bin ($0.15 < p_T < 0.2 \text{ GeV}/c$) the correction has a maximum value of about 3.6% and 6.5% at the collision energies of $\sqrt{s} = 0.9$ and 7 TeV respectively. For $p_T > 0.3 \text{ GeV}/c$ its value is below 2%. We do not estimate this correction factor for higher values of track p_T because statistical fluctuations dominate over any systematic effect.

In Appendix A we show the real data corrected for the contamination from secondaries for the track p_T threshold of $0.15 \text{ GeV}/c$, including both the Monte Carlo and the data-driven corrections. The contamination estimate from Monte Carlo has been multiplied by the data driven correction factor. In the first bin ($0.15 < p_{T,LT} < 0.5 \text{ GeV}/c$) the maximum effect on the final distributions is -8% at both collision energies. For $p_{T,LT} > 1.0 \text{ GeV}/c$ at $\sqrt{s} = 0.9 \text{ TeV}$ and $p_{T,LT} > 4.0 \text{ GeV}/c$ at $\sqrt{s} = 7 \text{ TeV}$ the effect saturates at a maximum value of about -4.5% .

An alternative way to estimate the strangeness contamination correction is to fit the DCA_{XY} distribution with the sum of two Monte Carlo template histograms: one containing the decay products of strange particles and one with all other tracks (primaries and secondaries from other processes). The fit is performed in the region $|DCA_{XY}| > 0.3$ and in different track p_T bins. The results obtained with this method are used to estimate the systematic uncertainty on the data-driven correction (see Sect. 5.5).

5.4.3 Tracking efficiency

The tracking efficiency depends on the track-level observables η and p_T . In Fig. 5.20 we present the efficiency projected on the two relevant observables separately, at the two considered energies. The dip of about 1% at $\eta = 0$ in the pseudo-rapidity projection is due to the absorption of particles in the central

5. MEASUREMENT OF THE UE WITH THE ALICE DETECTOR

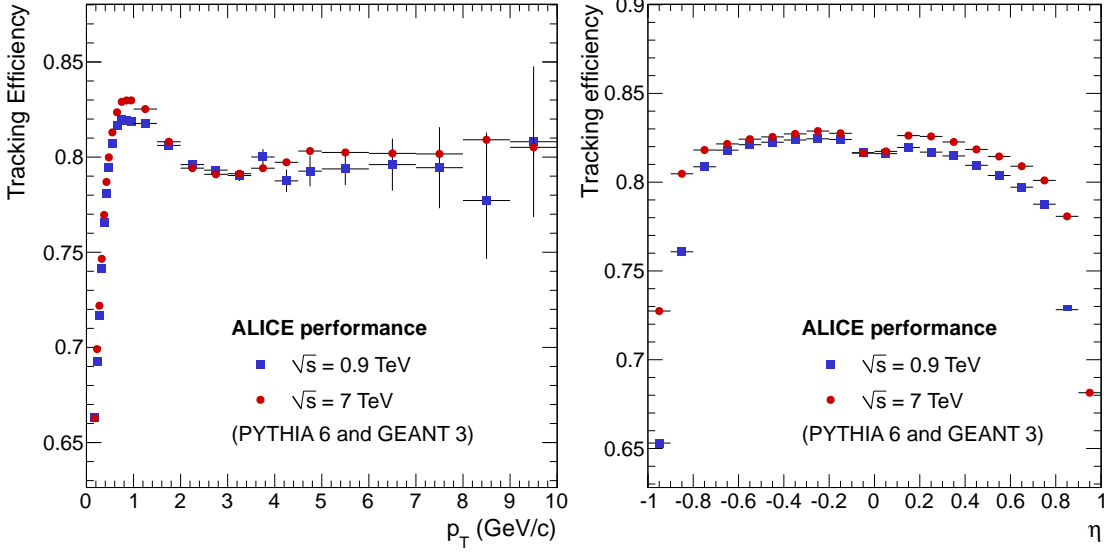


Figure 5.20: Tracking efficiency as a function of track p_T (left, $|\eta| < 0.8$) and η (right, $p_T > 0.5$ GeV/c). The decrease in the range 1–3 GeV/c is due to straight (high- p_T) tracks falling in the dead areas between TPC sectors. The dip at $\eta = 0$ in the pseudo-rapidity projection is due to the central TPC cathode. PYTHIA and GEANT simulation.

TPC cathode. The decrease in efficiency in the range 1–3 GeV/c is explained by the presence of straight (high- p_T) tracks falling in the dead areas between TPC sectors. Therefore, at high p_T the efficiency is dominated by geometry and has a constant value of about 80% at both collision energies. In order to extend the efficiency correction to high p_T without being dominated by statistical fluctuations, the estimated efficiency is fitted with a constant in the range $5 < p_T < 15$ GeV/c. The obtained value is used to correct the yields for $p_T > 10$ GeV/c (considered only at $\sqrt{s} = 7$ TeV). Additionally, the efficiency estimate from Monte Carlo is reduced by a factor 1% to account for some residual inaccuracy of the ITS description in simulations. The discrepancy between the results at $\sqrt{s} = 0.9$ and 7 TeV is due to the different configuration of detector modules excluded in the two data-taking periods.

The effect of the correction applied on real data for the track p_T threshold of

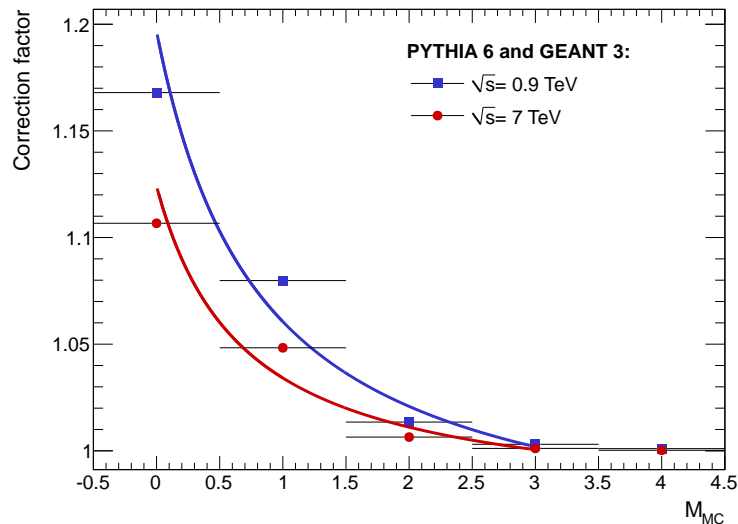


Figure 5.21: Vertex reconstruction correction factor as a function of the generated multiplicity. The fit according to Eq. 5.7 is also shown. PYTHIA 6 and GEANT 3 simulation.

0.15 GeV/ c is shown in Appendix A. In the first bin ($0.15 < p_{T,LT} < 0.5$ GeV/ c) the maximum correction applied is 40% and is reduced to 30% for $p_{T,LT} > 2$ GeV/ c at both collision energies.

5.4.4 Vertex reconstruction

The correction for the finite vertex reconstruction efficiency is performed as function of the event multiplicity. The correction as a function of the generated multiplicity within $|\eta| < 0.8$ (M_{MC}) is obtained from the ratio between the analysis steps 1 and 2 of structure 1 and extends up to $M_{MC} = 3$ (see Fig. 5.21). This correction factor is fitted with the function:

$$Correction\ factor = A + \frac{B}{M_{MC} - C} \quad (5.7)$$

where A , B and C are the fit parameters. The fit results are also shown in Fig. 5.21. This particular function has been chosen empirically since it reproduces well the shape of the correction distribution.

The correction to the real data should be applied as a function of the reconstructed

5. MEASUREMENT OF THE UE WITH THE ALICE DETECTOR

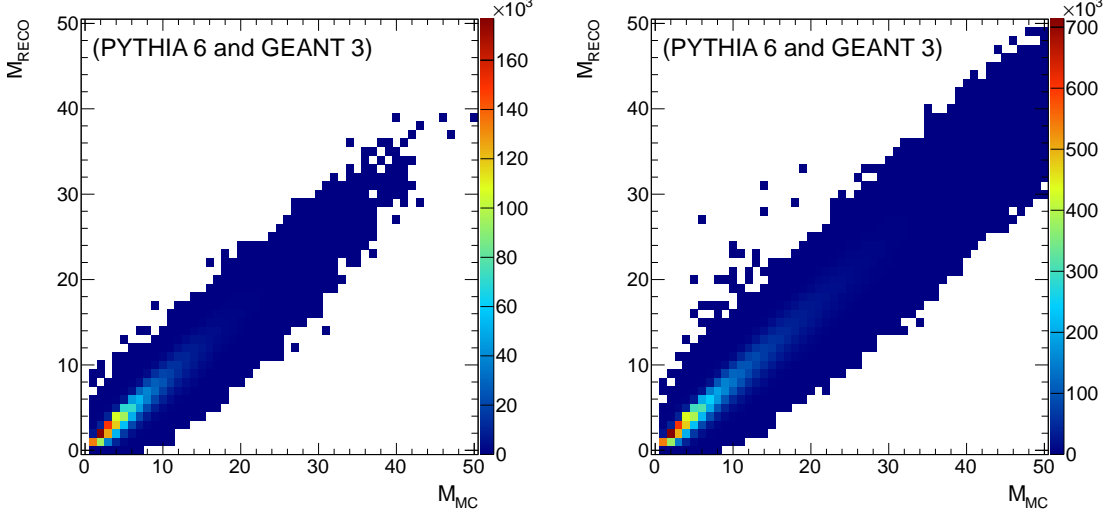


Figure 5.22: Multiplicity response matrix at $\sqrt{s} = 0.9$ TeV (left) and $\sqrt{s} = 7$ TeV (right). The multiplicity of reconstructed tracks is plotted against the multiplicity of generated particles. The profile of these distributions gives a conversion factor of 0.77 between M_{RECO} and M_{MC} . PYTHIA 6 and GEANT 3 simulation.

multiplicity (M_{RECO}). Therefore we convert the generated multiplicity into the measured one via a conversion factor extracted from the profile of the response matrix (shown in Fig. 5.22). The value of this conversion factor (M_{RECO}/M_{MC}) is 0.77 at both collision energies. In this way we obtain fractional values of the multiplicity, from which derives the need to fit the correction factor as a function of M_{MC} . The final correction is obtained by scaling the fit result from Eq. 5.7 by the conversion factor along the multiplicity (horizontal) axis.

In Appendix A we show the effect of this correction on the final distributions for the track p_T threshold of $0.15 \text{ GeV}/c$. The maximum correction is applied to the first bin ($0.15 < p_{T,LT} < 0.5 \text{ GeV}/c$) and has a value of about -2% at $\sqrt{s} = 0.9 \text{ TeV}$ and -1% at $\sqrt{s} = 7 \text{ TeV}$. For higher values of leading-track transverse-momentum the correction is negligible.

5.4.5 Two tracks effects

By comparing simulated events corrected for single-particle efficiencies with the input Monte Carlo, we observe a 0.5% discrepancy around $\Delta\phi = 0$. This effect is called non-closure in Monte Carlo (it will be further discussed in Sect. 5.5) and in this case is related to small two-track resolution¹ effects. Data are corrected for this discrepancy.

In Tab. 5.7 we summarize the maximum amount of each correction considering all final observables and regions at the two collision energies. We note here that the maximum corrections are applied only to the first or second-first leading-track p_T bins.

5.5 Systematic uncertainties

In Tables 5.9, 5.10 and 5.11 we summarize the systematic uncertainties evaluated in the analysis for the three track thresholds: $p_T > 0.15, 0.5$ and $1.0 \text{ GeV}/c$. Each uncertainty is explained in more detail in the following paragraphs. Uncertainties which are constant as a function of leading-track p_T are listed in Table 5.9. Leading-track p_T dependent uncertainties are summarized in Tables 5.10 and 5.11 for $\sqrt{s} = 0.9 \text{ TeV}$ and 7 TeV , respectively.

Particle composition

The tracking efficiency and contamination corrections depend slightly on the particle species, mainly due to their decay length and absorption in the material. The ALICE collaboration has measured [21] identified particle spectra in pp collisions at $\sqrt{s} = 0.9 \text{ TeV}$ and a similar study is under preparation [14] at $\sqrt{s} = 7 \text{ TeV}$. These results indicate a maximum integrated discrepancy of about 30% in pion and proton yields between data and simulation (PYTHIA 6 tunes D6T and Perugia 0 at $\sqrt{s} = 0.9$ and 7 TeV , respectively) in the range $0.1 < p_T < 2.5 \text{ GeV}/c$. In the case of kaons the measured distributions exceed the Monte Carlo predictions

¹The two-track resolution measures the capability to reconstruct two particles produced close to each other in space as two separate tracks.

5. MEASUREMENT OF THE UE WITH THE ALICE DETECTOR

Correction	$\sqrt{s} = 0.9 \text{ TeV}$	$\sqrt{s} = 7 \text{ TeV}$
	$p_T > 0.15 \text{ GeV}/c$	
Leading track misidentification	-8%	-8%
Contamination from secondaries	-8%	-8%
Tracking efficiency	+40%	+40%
Vertex reconstruction efficiency	-2%	-1%
	$p_T > 0.5 \text{ GeV}/c$	
Leading track misidentification	-4%	-8%
Contamination from secondaries	-2%	-2%
Tracking efficiency	+25%	+25%
Vertex reconstruction efficiency	-0.7%	-0.3%
	$p_T > 0.1 \text{ GeV}/c$	
Leading track misidentification	-4%	-8%
Contamination from secondaries	-2%	-2%
Tracking efficiency	+25%	+25%
Vertex reconstruction efficiency	-0.3%	-0.1%

Table 5.7: Upper limit of each correction for all considered p_T thresholds and collision energies. The maximum corrections are applied only to the first or second-first leading-track p_T bins. The values consider all final observables and regions.

up to a factor 2 and in Sect. 5.4.2 we have discussed a special correction for this effect. Therefore in order to assess the consequences of the incorrect description of the particle abundances in the Monte Carlo, we vary the relative yields of pions, protons, kaons, and other particles by 30% relative to the default Monte Carlo predictions in the full p_T range considered in our analysis (up to 10 or 25 GeV/ c for the lower and upper collision energies respectively). In Fig. 5.23 we show the tracking efficiency (left) and the contamination correction factor¹ (right) for different combinations of relative yields. The biggest effect is due to the variation of particles other than protons and kaons (mainly pions) since their yield is roughly one order of magnitude higher [21]. The maximum variation of the final UE dis-

¹The contamination correction factor is the quantity that multiplies the data to correct them for the contamination from secondaries. Therefore it is the inverse of the contamination itself.

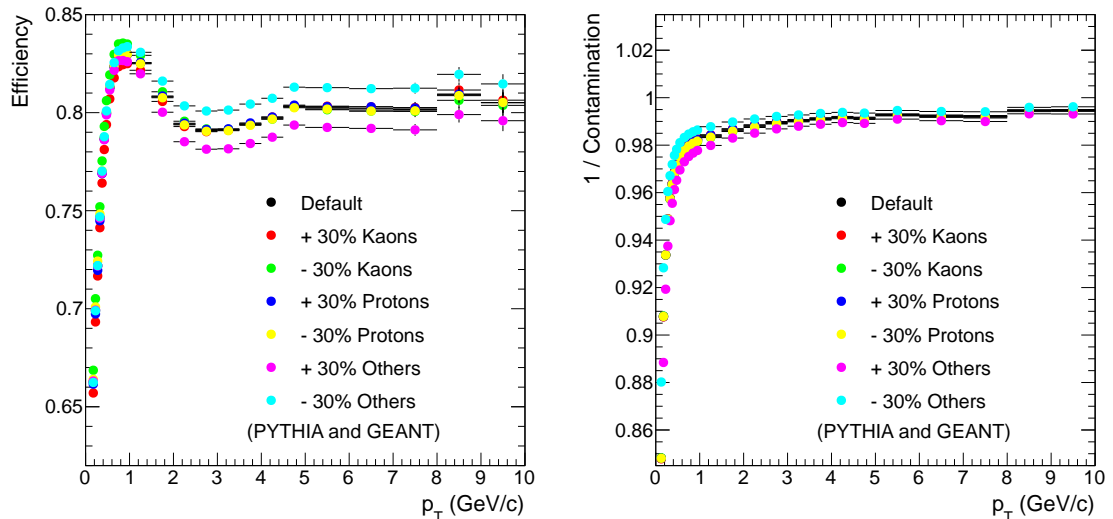


Figure 5.23: Efficiency (left) and contamination corrections (right) as a function of track p_T for different choices of particle composition for the estimate of systematic uncertainties ($|\eta| < 0.8$). For an explanation see text. PYTHIA 6 and GEANT 3 at $\sqrt{s} = 7$ TeV.

tributions induced by these modified efficiency/contamination corrections is 0.9% and represents the systematic uncertainty related to the particle composition (see Table 5.9).

Strangeness estimation

As mentioned in Sect. 5.4.2, we have developed two alternative methods to estimate the discrepancy in the strangeness yields between data and Monte Carlo: a constant-fit technique (used in the final analysis) and one based on histogram templates. A third possibility is to take the values measured by the ALICE collaboration [22]. In Fig. 5.24 we compare the quantity $1/(N\alpha)$, with α and N as defined in Sect. 5.4.2, obtained with the three methods at $\sqrt{s} = 0.9$ TeV. For the constant-fit method we show the results for the two sets of track-cuts considered (Sect. 5.4.2). The open stars represent the ratio between the measured yields of strange particles (K, Λ , ϕ and Ξ) and the Monte Carlo prediction (PYTHIA 6 tune D6T) from [22]. The full red stars represent the average of the various

5. MEASUREMENT OF THE UE WITH THE ALICE DETECTOR

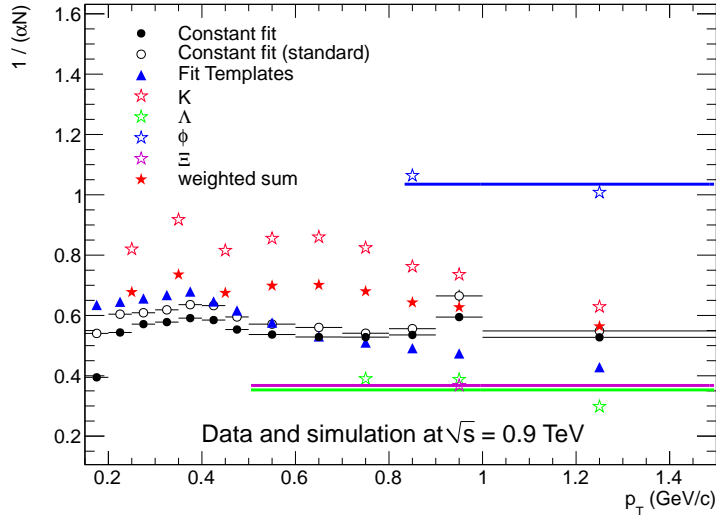


Figure 5.24: Comparison between different methods to estimate the strangeness contamination correction. Stars represent the ALICE measurement [22] for different particle species and dots and triangles our study based on two different methods and different track-cuts. More details in the text. Data and PYTHIA/GEANT at $\sqrt{s} = 0.9$ TeV. Statistical errors are indicated only for the constant fit method.

particle species weighted for the relative yields from [22]. In the case of Λ , ϕ and Ξ the measurement is limited to a restricted p_T range ($p_T > 0.5$ GeV/c), therefore we fit the values with a constant in that range (the fit is also shown in the figure) in order to extrapolate them to the full range considered in this study. The maximum discrepancy between the different methods gives the variation to be applied to the correction factor in order to estimate the systematic uncertainty on the strangeness yield correction. We assign a systematic uncertainty of 0–2.3% depending on the p_T threshold and collision energy, see Tables 5.10 and 5.11.

In the procedure described in Sect. 5.5 the effect of the wrong estimate of strangeness yields in Monte Carlo is already partially taken into account since we also let the relative kaon yields vary of 30%. Nevertheless in that case the main contribution to the systematic uncertainty is due to pions and the variation of the strangeness yield has no contribution to the uncertainty.

Selection criteria	Lower	Standard	Upper
Minimum number of TPC clusters	60	70	80
Maximum χ^2 per TPC cluster	3	4	5
Maximum $\text{DCA}_{XY}(p_T)$	4σ	7σ	10σ

Table 5.8: Variation of the most relevant track-cuts for the estimate of the systematic uncertainty.

ITS and TPC efficiency

The tracking efficiency depends on the level of precision of the description of the ITS and TPC detectors in the simulation. After detector alignment with survey methods, cosmic-ray events and pp collision events [17], the uncertainty on the efficiency due to the ITS description is estimated [89] to be below -2% and affects only tracks with $p_T < 0.3 \text{ GeV}/c$. The uncertainty due to the TPC reaches 4.5% at very low p_T and is smaller than 1.2% for tracks with $p_T > 0.5 \text{ GeV}/c$. The resulting maximum uncertainty on the UE final distributions is below 1% . Moreover, an uncertainty of 1% is included to account for uncertainties in the MC description of the matching between TPC and ITS tracks (see Table 5.9).

Track cuts

By applying the efficiency and contamination corrections we correct for those particles which are lost due to detector effects and for secondary tracks which have not been removed by the selection cuts. These corrections rely on detector simulations and therefore we need to estimate the systematic uncertainty introduced in the correction procedure by one particular choice of track cuts. To do so we have to repeat the analysis assigning some extreme (but still reasonable) lower and upper values to the most relevant track cuts, both for simulations and real data. The discrepancy between data and simulations in the variation of the final UE distributions gives the systematic uncertainty. In practice, with the class `AliAnalysisTaskTrackCutsSystematics`, for every relevant track-cut we evaluate the factors:

5. MEASUREMENT OF THE UE WITH THE ALICE DETECTOR

$$R_{low,high}(p_T, \eta) = \frac{DATA_{low,high}(p_T, \eta)}{DATA_{standard}(p_T, \eta)} \cdot \frac{MC_{standard}(p_T, \eta)}{MC_{low,high}(p_T, \eta)} \quad (5.8)$$

where *DATA* and *MC* are the two-dimensional distributions of track p_T and η for the extreme choices of track cuts (low, high) or for the standard choice. In order to evaluate the variation of the final observables, we multiply the tracks' distributions used as input for the UE analysis by these factors. The cuts considered in this procedure are: the minimum number of TPC clusters, the maximum χ^2 per cluster and the number of standard deviations accepted in the DCA_{XY} distribution. The values used to evaluate the systematic uncertainty are summarized in Table 5.8: the lower and upper values of the cut on the number of TPC clusters are set to 60 and 80 respectively (the default is 70), the maximum accepted χ^2 per cluster varies between 3 and 5 (the default is 4) and the number of standard deviations accepted in the DCA_{XY} distribution is set to 4 and 10 (the default is 7). The lower cuts on the number of TPC clusters and χ^2 per cluster are the major contributions to the systematic uncertainty. The overall effect, considering all cuts and different UE distributions, is smaller or equal to 3.5 % at both collision energies (Table 5.9).

Misidentification bias

The uncertainty on the leading-track misidentification correction is estimated from the discrepancy between the data-driven correction used in the analysis and that based on simulations. Both methods are applied on simulations in order to disentangle the effect of a different p_T spectrum in the data with respect to Monte Carlo. The effect influences only the first two leading-track p_T bins at both collision energies. The maximum uncertainty ($\sim 18\%$) affects the first leading-track p_T bin for the track p_T cut-off of 0.15 GeV/ c . In all other bins this uncertainty is of the order of few percent. As summarized in Tables 5.10 and 5.11, the uncertainty has slightly different values for the various UE distributions.

Vertex-reconstruction efficiency

The analysis accepts reconstructed vertices with at least one contributing track. We repeat the analysis and the correction procedure requiring at least two contributing tracks. The systematic uncertainty related to the vertex reconstruction efficiency is given by the maximum variation in the final distributions between the cases of one and two contributing tracks and its value is below 2.4% (see Tables 5.10 and 5.11). The effect is only visible in the first leading-track p_T bin, where the events have lower multiplicity and therefore the choice of minimum number of contributors is more relevant.

Non-closure in Monte Carlo

By correcting a Monte Carlo prediction after full detector simulation with corrections extracted from the same generator, we expect to obtain the input Monte Carlo prediction within the statistical uncertainty. This consideration holds true only if each correction is evaluated with respect to all the variables to which the given correction is sensitive. For instance, if we estimate the tracking efficiency only as a function of the track p_T , neglecting its η dependence, the correction factors will be only averaged over this second variable, resulting in a less precise result. The imprecision is higher for a stronger dependence of the correction on the neglected observable. Any statistically significant difference between input and corrected distributions is referred to as *non-closure in Monte Carlo*. In the assessment of this uncertainty we use the Monte Carlo driven procedure for the estimate of the leading-track misidentification (which is the first correction applied) in order to isolate the non-closure effect from the uncertainty already evaluated (see Tables 5.10 and 5.11).

The overall non-closure effect is sizeable ($\sim 17\%$) in the first leading-track p_T bin and is 0.6–5% in all other bins at both collision energies.

Monte-Carlo dependence

We observe a difference in the final distributions when correcting the data with PYTHIA 6.4 or PHOJET generators, possibly due to the different spectra and

5. MEASUREMENT OF THE UE WITH THE ALICE DETECTOR

particle composition in the two models. The discrepancy is of the order of 1% and equally affects all the leading-track p_T bins (Table 5.9).

Material budget

Uncertainties in the knowledge of the material budget of the detector are assessed by varying the material density in the detector simulation according to the estimated uncertainty on the material budget knowledge obtained with a measurement of photon conversions (-6.2% , 3.4% [63]). The effect on our observables is $0.2\text{--}0.6\%$ depending on the p_T threshold considered (Table 5.9).

		$\sqrt{s} = 0.9 \text{ TeV}$	
		$p_T > 0.15 \text{ GeV}/c$	$p_T > 0.5 \text{ GeV}/c$
Particle composition		$\pm 0.9\%$	$\pm 0.7\%$
ITS efficiency		$\pm 0.6\%$	–
TPC efficiency		$\pm 1.9\%$	$\pm 0.8\%$
Track cuts		$+ 3.0\%$ $- 1.1\%$	$+ 2.0\%$ $- 1.1\%$
ITS/TPC matching		$\pm 1.0\%$	$\pm 1.0\%$
MC dependence		$+ 1.1\%, + 1.1\%, + 1.6\%$	$+ 0.9\%$
Material budget		$\pm 0.6\%$	$\pm 0.2\%$
		$\sqrt{s} = 7 \text{ TeV}$	
		$p_T > 0.15 \text{ GeV}/c$	$p_T > 0.5 \text{ GeV}/c$
Particle composition		$\pm 0.9\%$	$\pm 0.7\%$
ITS efficiency		$\pm 0.5\%$	–
TPC efficiency		$\pm 1.8\%$	$\pm 0.8\%$
Track cuts		$+ 2.1\%$ $- 2.3\%$	$+ 1.6\%$ $- 3.2\%$
ITS/TPC matching		$\pm 1.0\%$	$\pm 1.0\%$
MC dependence		$+ 0.8\%, + 0.8\%, + 1.2\%$	$+ 0.8\%$
Material budget		$\pm 0.6\%$	$\pm 0.2\%$
		$p_T > 1.0 \text{ GeV}/c$	
			$\pm 0.4\%$
			–
			$\pm 0.4\%$
			$+ 0.9\%$ $- 1.5\%$
			$\pm 1.0\%$
			$+ 0.9\%, + 0.9\%, + 1.3\%$
			$\pm 0.2\%$
		$p_T > 1.0 \text{ GeV}/c$	
			$\pm 0.5\%$
			–
			$\pm 0.5\%$
			$+ 2.5\%$ $- 3.5\%$
			$\pm 1.0\%$
			$+ 1.0\%$
			$\pm 0.2\%$

Table 5.9: Constant systematic uncertainties at both collision energies. When more than one number is quoted, separated by a comma, the first value refers to the number density distribution, the second to the summed p_T and the third to the azimuthal correlation. Some of the uncertainties are quoted asymmetrically.

5. MEASUREMENT OF THE UE WITH THE ALICE DETECTOR

		$\sqrt{s} = 0.9 \text{ TeV}$		
		Number density		
		$p_T > 0.15 \text{ GeV}/c$	$p_T > 0.5 \text{ GeV}/c$	$p_T > 1.0 \text{ GeV}/c$
Lead. track misid.	$p_T, 1^{\text{st}}$ bin	+ 17.8%, + 16.3%, + 16.3%	+ 4.6%, + 3.5%, + 3.5%	+ 4.2%, + 2.9%, + 1.7%
	2^{nd} bin	+ 2.9%	+ 1.3%	-
MC non closure	1^{st} bin	- 17.2%	- 3.6%	- 1.2%
	2^{nd} bin	- 3.2%	- 0.8%	- 1.2%
Strangeness	others	- 0.6%	- 0.8%	- 1.2%
	1^{st} bin	$\pm 1.9\%$	$\pm 0.2\%$	-
Vertex reco.	others	$\pm 1.0\%$	$\pm 0.2\%$	-
	1^{st} bin	- 2.4%	- 0.7%	- 0.5%
Summed p_T				
Lead. track misid.	$p_T, 1^{\text{st}}$ bin	$p_T > 0.15 \text{ GeV}/c$ + 20.0%, + 18.1%, + 18.1%	$p_T > 0.5 \text{ GeV}/c$ + 5.3%, + 4.1%, + 4.1%	$p_T > 1.0 \text{ GeV}/c$ + 4.8%, + 3.4%, + 3.4%
	2^{nd} bin	+ 3.7%	+ 1.6%	-
MC non closure	1^{st} bin	- 17.0%	- 2.8%	- 1.1%
	2^{nd} bin	- 3.0%	- 1.0%	- 1.1%
Strangeness	others	- 0.7%	- 1.0%	- 1.1%
	1^{st} bin	$\pm 1.9\%$	$\pm 0.2\%$	-
Vertex reco.	others	$\pm 1.0\%$	$\pm 0.2\%$	-
	1^{st} bin	- 2.4%	- 0.7%	- 0.5%
Azimuthal correlation				
Lead. track misid.	$p_T, 1^{\text{st}}$ bin	$p_T > 0.15 \text{ GeV}/c$ + 12.0%	$p_T > 0.5 \text{ GeV}/c$ + 3.9%	$p_T > 1.0 \text{ GeV}/c$ + 2.5%
	2^{nd} bin	+ 2.6%	+ 1.1%	-
MC non closure	1^{st} bin	- 17.1%	- 3.3%	- 1.6%
	2^{nd} bin	- 3.5%	- 3.0%	- 1.6%
Strangeness	others	- 2.4%	- 3.0%	- 1.6%
	1^{st} bin	$\pm 1.9\%$	$\pm 0.2\%$	-
Vertex reco.	others	$\pm 1.0\%$	$\pm 0.2\%$	-
	1^{st} bin	- 2.4%	- 0.4%	-
	others	- 0.5%	- 0.4%	-

Table 5.10: Systematic uncertainties vs. leading track p_T at $\sqrt{s} = 0.9 \text{ TeV}$. When more than one number is quoted, separated by a comma, the first value refers to the Toward, the second to the Transverse and the third to the Away region. The second column denotes the leading track p_T bin for which the uncertainty applies. The numbering starts for each case from the first bin above the track p_T threshold.

		$\sqrt{s} = 7 \text{ TeV}$		
		Number density		
		$p_T > 0.15 \text{ GeV}/c$	$p_T > 0.5 \text{ GeV}/c$	$p_T > 1.0 \text{ GeV}/c$
Lead. track misid.	$p_{T,LT}$	$+ 17.9\%, + 16.3\%, + 16.3\%$	$+ 4.0\%, + 3.2\%, + 3.2\%$	$+ 2.5\%, 1.2\%, 1.2\%$
	1^{st} bin	$+ 2.7\%$	–	$+ 0.7\%$
MC non closure	1^{st} bin	$- 16.8\%$	$- 2.6\%$	$- 1.9\%$
	2^{nd} bin	$- 2.9\%$	$- 1.4\%$	$- 1.9\%$
Strangeness	others	$- 0.6\%$	$- 1.0\%$	$- 1.9\%$
	1^{st} bin	$\pm 1.8\%$	$\pm 2.3\%$	–
Vertex reco.	others	$\pm 1.0\%$	$\pm 2.3\%$	–
	1^{st} bin	$- 2.4\%$	$- 0.7\%$	$- 0.5\%$
		Summed p_T		
Lead. track misid.	$p_{T,LT}$	$p_T > 0.15 \text{ GeV}/c$	$p_T > 0.5 \text{ GeV}/c$	$p_T > 1.0 \text{ GeV}/c$
	1^{st} bin	$+ 20.0\%, + 17.9\%, + 17.9\%$	$+ 4.9\%, + 3.8\%, + 3.8\%$	$+ 3.4\%, + 1.9\%, + 1.9\%$
MC non closure	2^{nd} bin	$+ 3.4\%$	$+ 0.8\%$	$+ 1.1\%$
	1^{st} bin	$- 16.7\%$	$- 2.7\%$	$- 1.5\%$
Strangeness	2^{nd} bin	$- 2.6\%$	$- 1.2\%$	$- 1.5\%$
	others	$- 0.8\%$	$- 1.0\%$	$- 1.5\%$
Vertex reco.	1^{st} bin	$\pm 1.8\%$	$\pm 2.3\%$	–
	others	$\pm 1.0\%$	$\pm 2.3\%$	–
Vertex reco.	1^{st} bin	$- 2.4\%$	$- 0.7\%$	$- 0.5\%$
			Azimuthal correlation	
Lead. track misid.	$p_{T,LT}$	$p_T > 0.15 \text{ GeV}/c$	$p_T > 0.5 \text{ GeV}/c$	$p_T > 1.0 \text{ GeV}/c$
	1^{st} bin	$+ 16.8\%$	$+ 3.4\%$	$+ 0.9\%$
MC non closure	2^{nd} bin	$+ 2.5\%$	–	–
	1^{st} bin	$- 25.3\%$	$- 4.3\%$	$- 1.2\%$
Strangeness	2^{nd} bin	$- 5.3\%$	$- 2.1\%$	$- 1.2\%$
	others	$- 2.1\%$	$- 2.1\%$	$- 1.2\%$
Vertex reco.	1^{st} bin	$\pm 1.8\%$	$\pm 2.3\%$	–
	others	$\pm 1.0\%$	$\pm 2.3\%$	–
Vertex reco.	1^{st} bin	$- 2.4\%$	$- 0.4\%$	–
	others	$- 0.5\%$	$- 0.4\%$	–

Table 5.11: Systematic uncertainties vs. leading track p_T at $\sqrt{s} = 7 \text{ TeV}$. When more than one number is quoted, separated by a comma, the first value refers to the Toward, the second to the Transverse and the third to the Away region. The second column denotes the leading track p_T bin for which the uncertainty applies. The numbering starts for each case from the first bin above the track p_T threshold.

5. MEASUREMENT OF THE UE WITH THE ALICE DETECTOR

6

Results

In this section we present and discuss the corrected results [16] for the three UE distributions in all regions at $\sqrt{s} = 0.9$ TeV and $\sqrt{s} = 7$ TeV. Three different track- p_T lower thresholds are considered: $p_{T,\min} = 0.15, 0.5$ and 1 GeV/ c . The final distributions are shown in Figures 6.1-6.17. The upper part of each plot shows the relevant measured distribution (black points) compared to a set of Monte Carlo predictions (coloured curves). Shaded bands represent the systematic uncertainty only. Bars along the x axis indicate the bin width. The lower part shows the ratio between Monte Carlo and data. In this case the shaded band is the quadratic sum of statistical and systematic uncertainties.

We consider three Monte Carlo models: PYTHIA 6.4 (tune Perugia 0), PYTHIA 8 (tune 1) and PHOJET 1.12 (see Sect. 1.3.2 for an overview). The overall agreement of data and simulations is of the order of 10–30% and we are not able to identify a preferred model that can reproduce all measured observables. In general, all three generators underestimate the event activity in the Transverse region. Nevertheless, an agreement of the order of 20% has to be considered a success, considering the complexity of the system under study. Even though an exhaustive comparison of data with the latest models available is beyond the scope of this thesis, in the next sections we will indicate some general trends observed in the comparison with the chosen models.

In the following discussion we define the leading-track p_T range from 4 to 10 GeV/ c at $\sqrt{s} = 0.9$ TeV and from 10 to 25 GeV/ c at $\sqrt{s} = 7$ TeV as the *plateau*.

6. RESULTS

$\sqrt{s} = 0.9 \text{ TeV}$				
	Number density		Summed p_T	
	Slope $(\text{GeV}/c)^{-1}$	Mean	Slope	Mean (GeV/c)
$p_T > 0.15 \text{ GeV}/c$	0.00 ± 0.02	1.00 ± 0.04	0.00 ± 0.01	0.62 ± 0.02
$p_T > 0.5 \text{ GeV}/c$	0.00 ± 0.01	0.45 ± 0.02	0.01 ± 0.01	0.45 ± 0.02
$p_T > 1.0 \text{ GeV}/c$	0.003 ± 0.003	0.16 ± 0.01	0.006 ± 0.005	0.24 ± 0.01
$\sqrt{s} = 7 \text{ TeV}$				
	Number density		Summed p_T	
	Slope $(\text{GeV}/c)^{-1}$	Mean	Slope	Mean (GeV/c)
$p_T > 0.15 \text{ GeV}/c$	0.00 ± 0.01	1.82 ± 0.06	0.01 ± 0.01	1.43 ± 0.05
$p_T > 0.5 \text{ GeV}/c$	0.005 ± 0.007	0.95 ± 0.03	0.01 ± 0.01	1.15 ± 0.04
$p_T > 1.0 \text{ GeV}/c$	0.001 ± 0.003	0.41 ± 0.01	0.008 ± 0.006	0.76 ± 0.03
$\sqrt{s} = 1.8 \text{ TeV (CDF)}$				
	Number density (at leading charged jet $p_T = 20 \text{ GeV}/c$)			
$p_T > 0.5 \text{ GeV}/c$	0.60			

Table 6.1: Saturation values in the Transverse region for the two collision energies. The result from CDF is also given, for details see text.

6.1 Number density

In Fig. 6.1-6.3 we show the multiplicity density as a function of leading-track p_T in the three regions: Toward, Transverse and Away. Toward and Away regions are expected to collect the fragmentation products of the two back-to-back outgoing partons from the elementary hard scattering. As expected [34], we observe that the multiplicity density in these regions increases monotonically with the $p_{T,LT}$ scale. In the highest leading-track p_T bins the activity in the Toward and Away regions is comparable within the uncertainties at the collision energy of $\sqrt{s} = 0.9 \text{ TeV}$. At $\sqrt{s} = 7 \text{ TeV}$, always in the highest leading-track p_T bins, the charged-particle density in the Toward region is roughly a factor 1.3 higher than in the Away region (we remind here that the leading-track is not included in the Toward region). In the Transverse region, after a monotonic increase at low leading track p_T , the distribution tends to flatten out (see Sect. 4.3). The same

behaviour is observed at both collision energies and all values of $p_{T,\min}$.

The plateau range is fitted with a line. The fit slopes and mean values for the three p_T thresholds are reported in Table 6.1. In the fit, potential correlations of the systematic uncertainties in different p_T bins are neglected. The fit slopes are consistent with zero.

For the lowest track threshold $p_T > 0.15 \text{ GeV}/c$ all models underestimate the charged multiplicity in the Transverse and Away regions. In particular at $\sqrt{s} = 7 \text{ TeV}$ PHOJET predictions largely underestimate the measurement in the Transverse region (up to $\sim 50\%$), the discrepancy being more pronounced with increasing p_T cut-off value. PYTHIA 8 correctly describes the Toward region at both collision energies and PHOJET only at $\sqrt{s} = 0.9 \text{ TeV}$. For track $p_T > 1 \text{ GeV}/c$, PYTHIA 8 systematically overestimates the event activity in the jet fragmentation regions (Toward and Away).

6.2 Summed p_T

In Fig. 6.4-6.6 we show the summed p_T density as a function of leading track p_T in the three topological regions. The shape of the distributions follows a trend similar to that discussed above for the number density. Also in this case at $\sqrt{s} = 0.9 \text{ TeV}$ the activity in the Toward and Away regions is comparable in the highest $p_{T,LT}$ bins, while at $\sqrt{s} = 7 \text{ TeV}$ there is about a factor 1.6 difference between the two regions. The summed p_T in these two regions is not expected to be comparable. First of all the leading track is not included in the Toward region. Moreover, due to the k_T smearing¹ of the initial partons the two outgoing jets from the hard scattering can have a different value of η . Therefore the sub-leading jet can fall partially (or completely) outside our experimental acceptance ($|\eta| < 0.8$). As a consequence, the total transverse-momentum measured in the Away region will be lower than in the Toward region. A second effect that can produce a loss of

¹With k_T *smearing* we refer to the primordial transverse-momentum carried by the partons inside the proton. Due to this the p_T of the outgoing partons is not exactly balanced in the laboratory frame and as a consequence the produced jets are observed at different values of η .

6. RESULTS

energy in the Away region is FSR. In this case QCD radiation can be emitted at a large azimuth and therefore be collected in the Transverse region.

The general trend of PYTHIA 8 is to overestimate the fragmentation in the Toward region at all p_T cut-off values. Also in this case at $\sqrt{s} = 7$ TeV PHOJET largely underestimates the measurement in the Transverse region (up to $\sim 50\%$), especially at higher values of p_T cut-off. Other systematic trends are not very pronounced.

In Table 6.1 we report the mean value of a linear fit in the plateau range. The summed p_T density in the Transverse region can be interpreted as a measurement of the UE activity in a given leading track p_T bin. Therefore, its value in the plateau can be used, for example, to correct jet spectra.

6.3 Azimuthal correlations

In Fig. 6.7-6.17 2-particle azimuthal correlations with respect to the leading track are shown in different ranges of leading-track p_T . The range $1/3\pi < |\Delta\phi| < 2/3\pi$ corresponds to the Transverse region. The regions $-1/3\pi < \Delta\phi < 1/3\pi$ (Toward) and $2/3\pi < |\Delta\phi| < \pi$ (Away) collect the fragmentation products of the leading and sub-leading jets. In general, all considered Monte Carlo simulations fail to reproduce the shape of the measured distributions. PYTHIA 8 provides the best prediction for the Transverse activity in all leading track p_T ranges considered. Unfortunately, the same model significantly overestimates the jet fragmentation regions. The general trend shown by the Monte Carlo models considered is to enhance the event activity in the jet-fragmentation regions ($\Delta\phi = 0$ and π). This can be seen by the sharper correlation peaks at these angles in the models with respect to the measured distributions. By contrast, our measurement shows that a larger fraction of the observed multiplicity is produced at larger angles (i.e. $1/3\pi < |\Delta\phi| < 2/3\pi$) from the leading-particle direction, suggesting a more prominent MPI activity than the one predicted by the models considered.

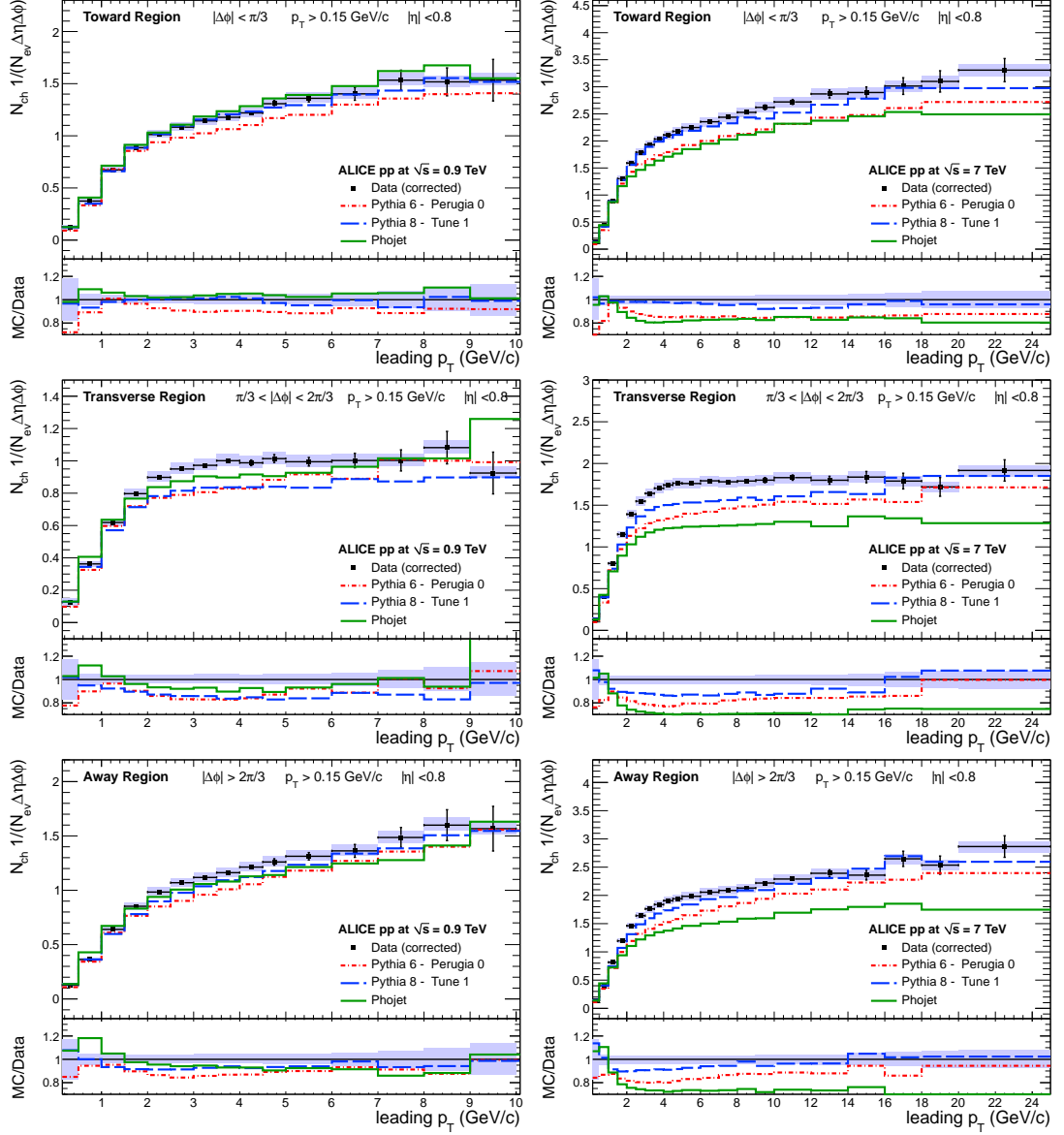
Number Density - particle $p_T > 0.15 \text{ GeV}/c$ 

Figure 6.1: Number density in Toward (top), Transverse (middle) and Away (bottom) regions at $\sqrt{s} = 0.9 \text{ TeV}$ (left) and $\sqrt{s} = 7 \text{ TeV}$ (right). Right and left vertical scales differ by a factor 2. Shaded area in upper plots: systematic uncertainties. Shaded areas in bottom plots: sum in quadrature of statistical and systematic uncertainties. Horizontal error bars: bin width.

6. RESULTS

Number Density - particle $p_T > 0.5 \text{ GeV}/c$

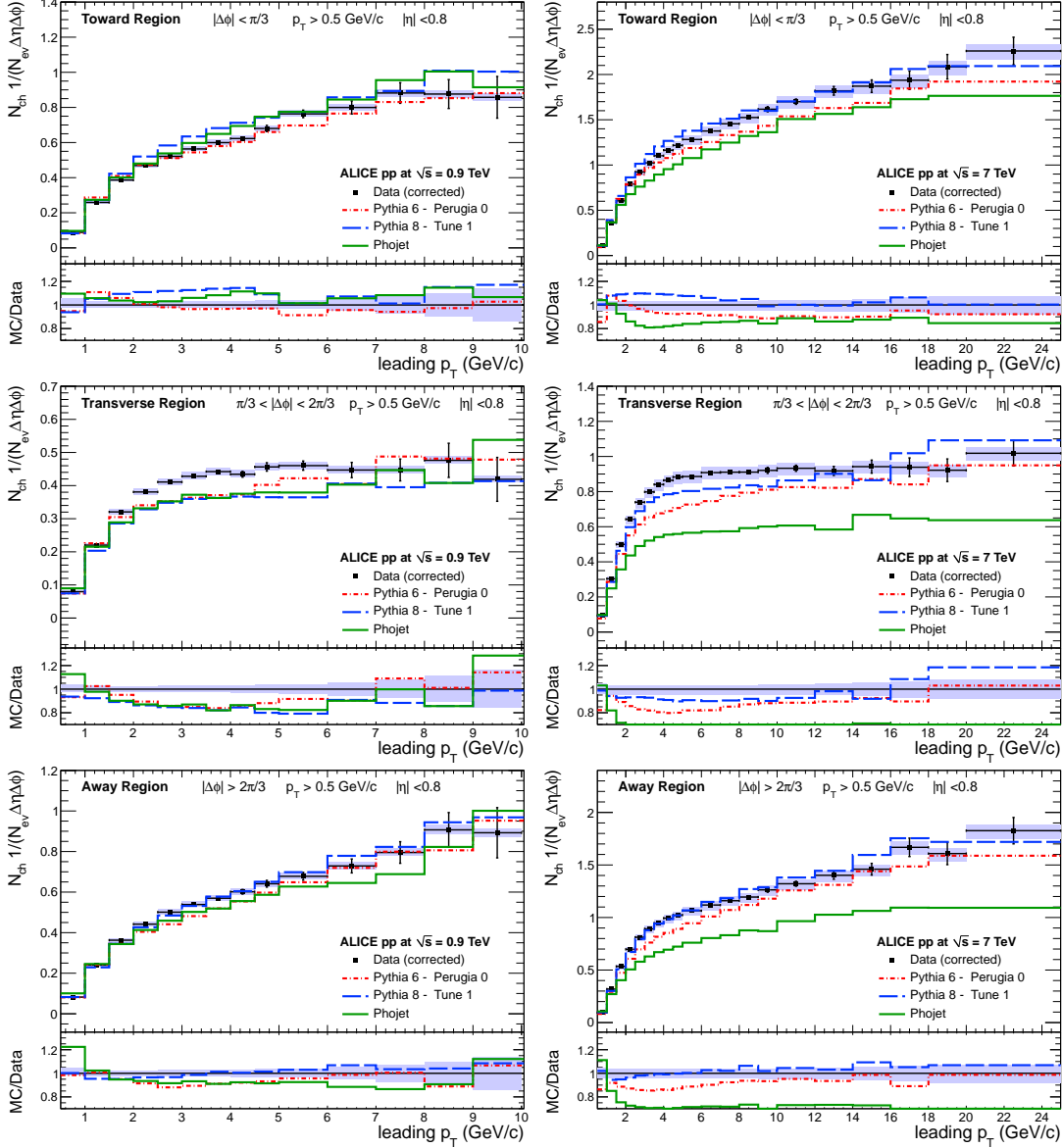


Figure 6.2: Number density in Toward (top), Transverse (middle) and Away (bottom) regions at $\sqrt{s} = 0.9 \text{ TeV}$ (left) and $\sqrt{s} = 7 \text{ TeV}$ (right). Right and left vertical scales differ by a factor 2. Shaded area in upper plots: systematic uncertainties. Shaded areas in bottom plots: sum in quadrature of statistical and systematic uncertainties. Horizontal error bars: bin width.

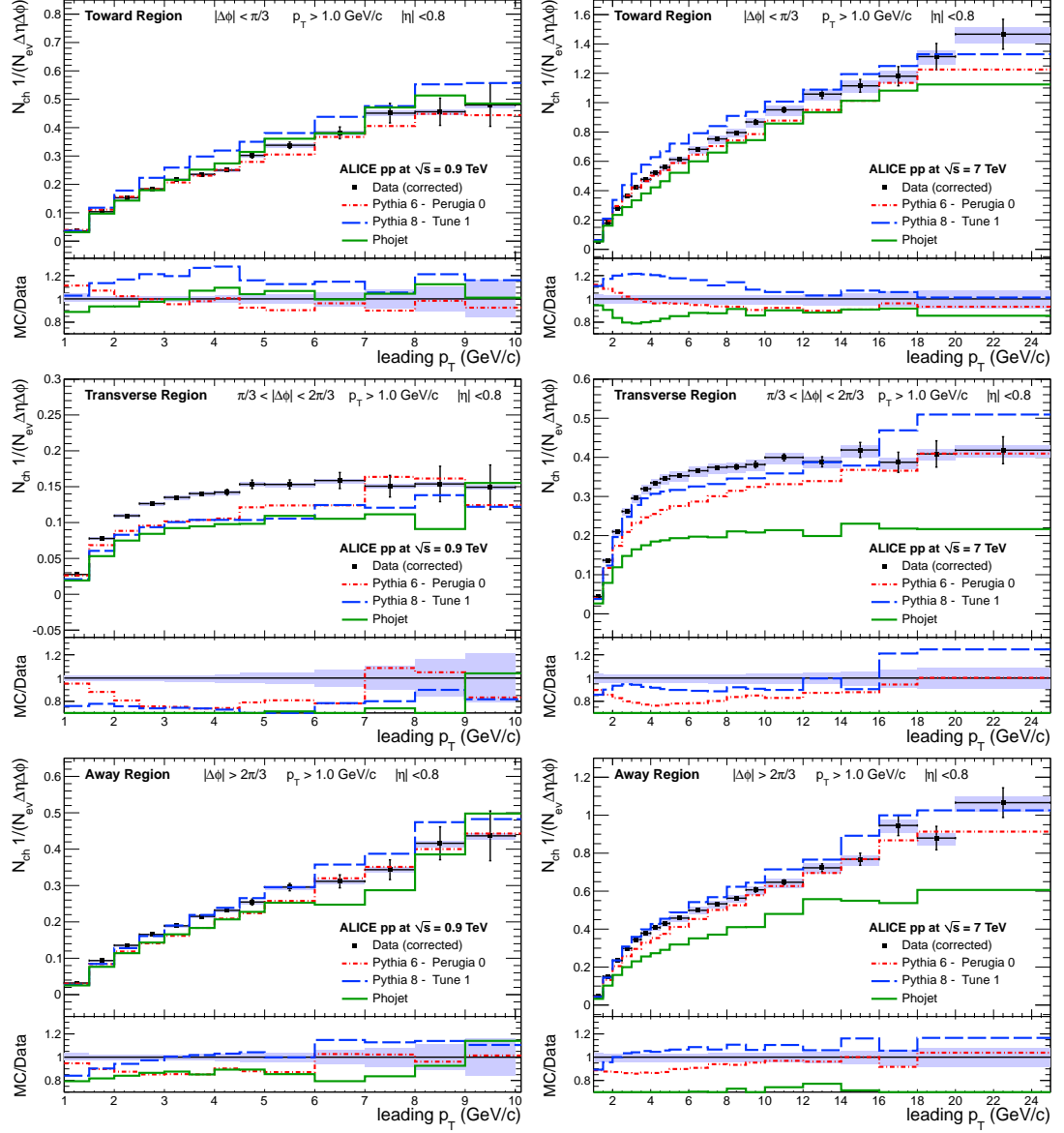
Number Density - particle $p_T > 1.0 \text{ GeV}/c$ 

Figure 6.3: Number density in Toward (top), Transverse (middle) and Away (bottom) regions at $\sqrt{s} = 0.9 \text{ TeV}$ (left) and $\sqrt{s} = 7 \text{ TeV}$ (right). Right and left vertical scales differ by a factor 2. Shaded area in upper plots: systematic uncertainties. Shaded areas in bottom plots: sum in quadrature of statistical and systematic uncertainties. Horizontal error bars: bin width.

6. RESULTS

Summed p_T - particle $p_T > 0.15 \text{ GeV}/c$

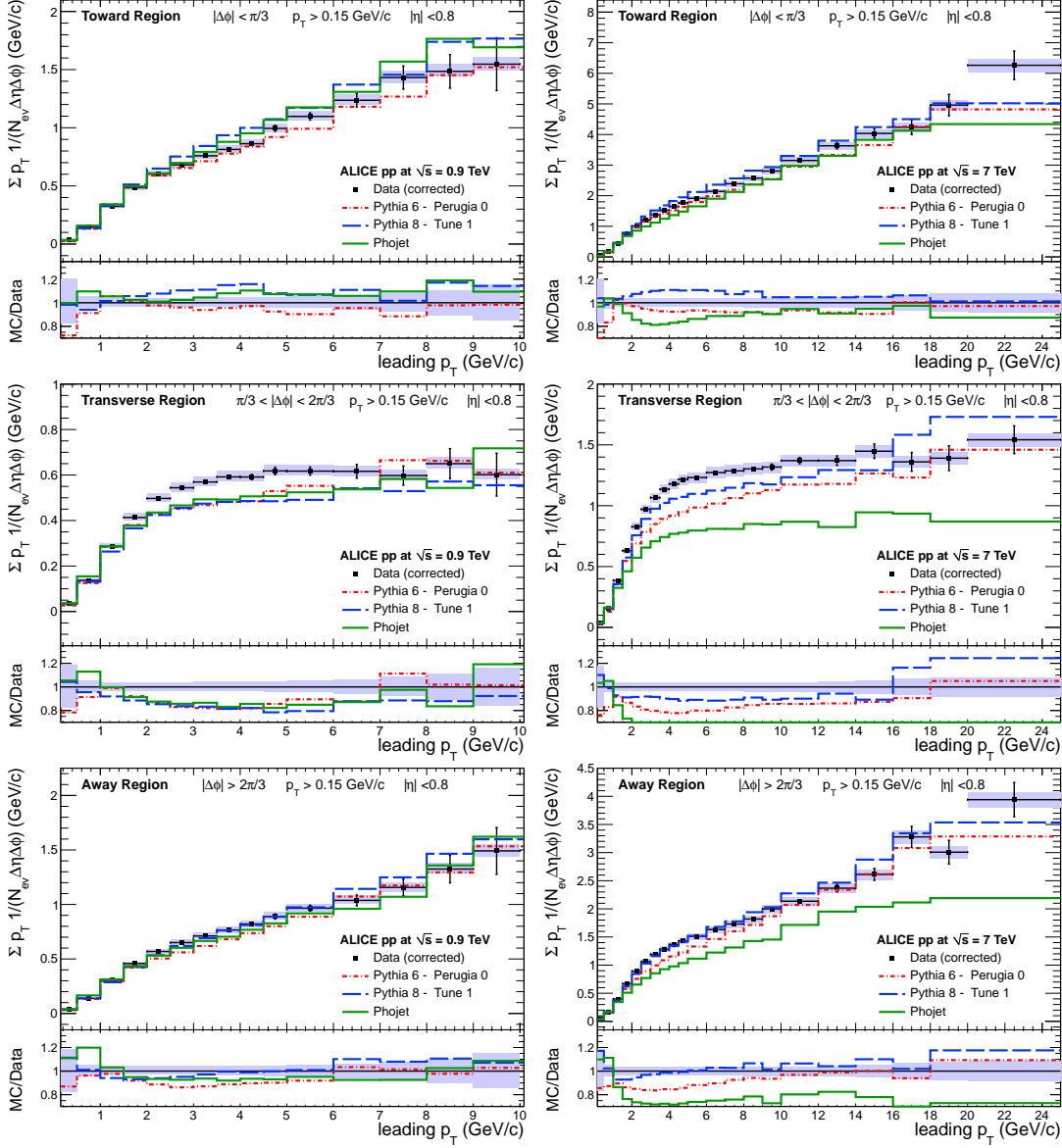


Figure 6.4: Summed p_T in Toward (top), Transverse (middle) and Away (bottom) regions at $\sqrt{s} = 0.9 \text{ TeV}$ (left) and $\sqrt{s} = 7 \text{ TeV}$ (right). Right and left vertical scales differ by a factor 4 (2) in the top (middle and bottom) panel. Shaded area in upper plots: systematic uncertainties. Shaded areas in bottom plots: sum in quadrature of statistical and systematic uncertainties. Horizontal error bars: bin width.

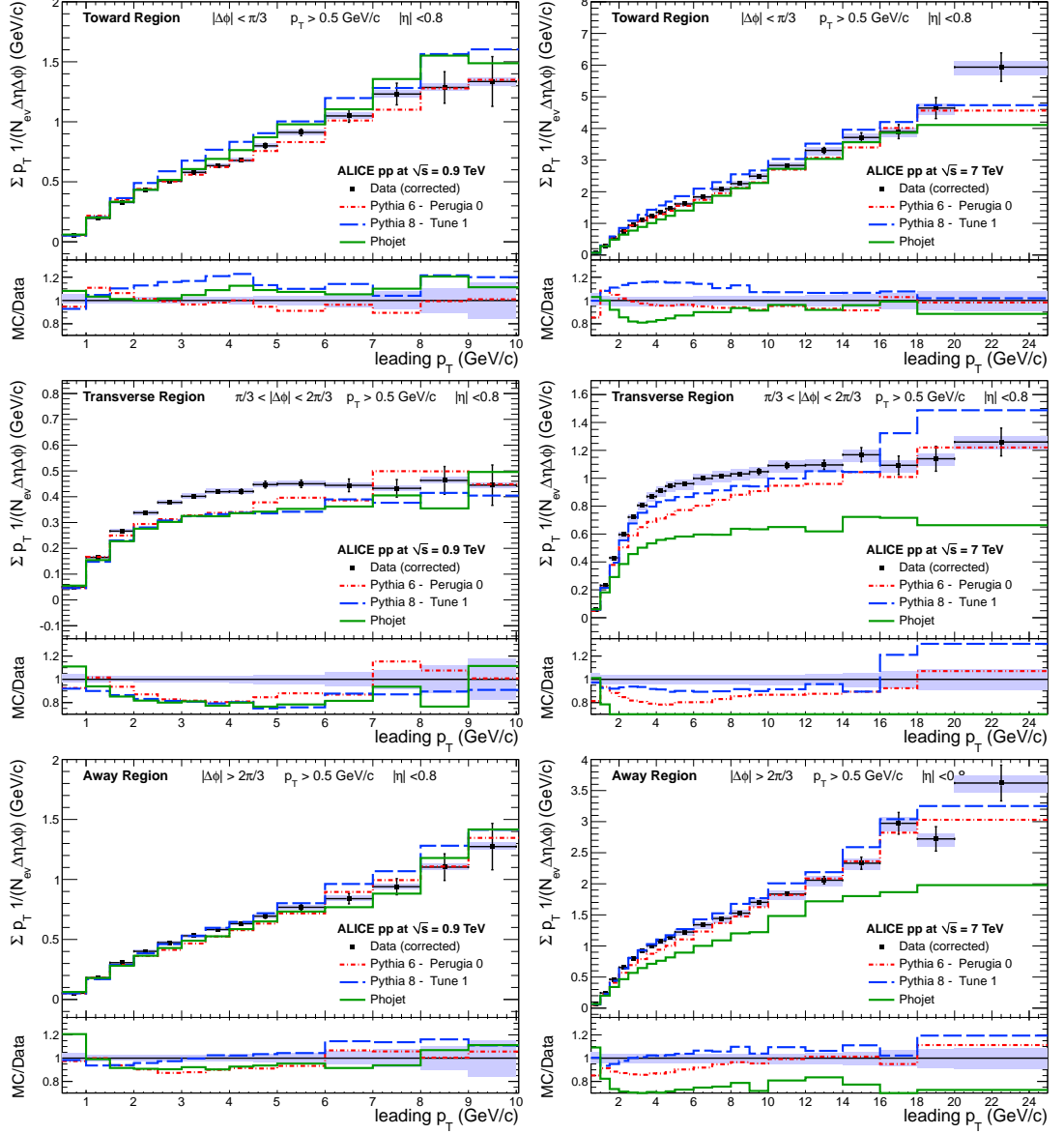
Summed p_T - particle $p_T > 0.5 \text{ GeV}/c$ 

Figure 6.5: Summed p_T in Toward (top), Transverse (middle) and Away (bottom) regions at $\sqrt{s} = 0.9 \text{ TeV}$ (left) and $\sqrt{s} = 7 \text{ TeV}$ (right). Right and left vertical scales differ by a factor 4 (2) in the top (middle and bottom) panel. Shaded area in upper plots: systematic uncertainties. Shaded areas in bottom plots: sum in quadrature of statistical and systematic uncertainties. Horizontal error bars: bin width.

6. RESULTS

Summed p_T - particle $p_T > 1.0 \text{ GeV}/c$

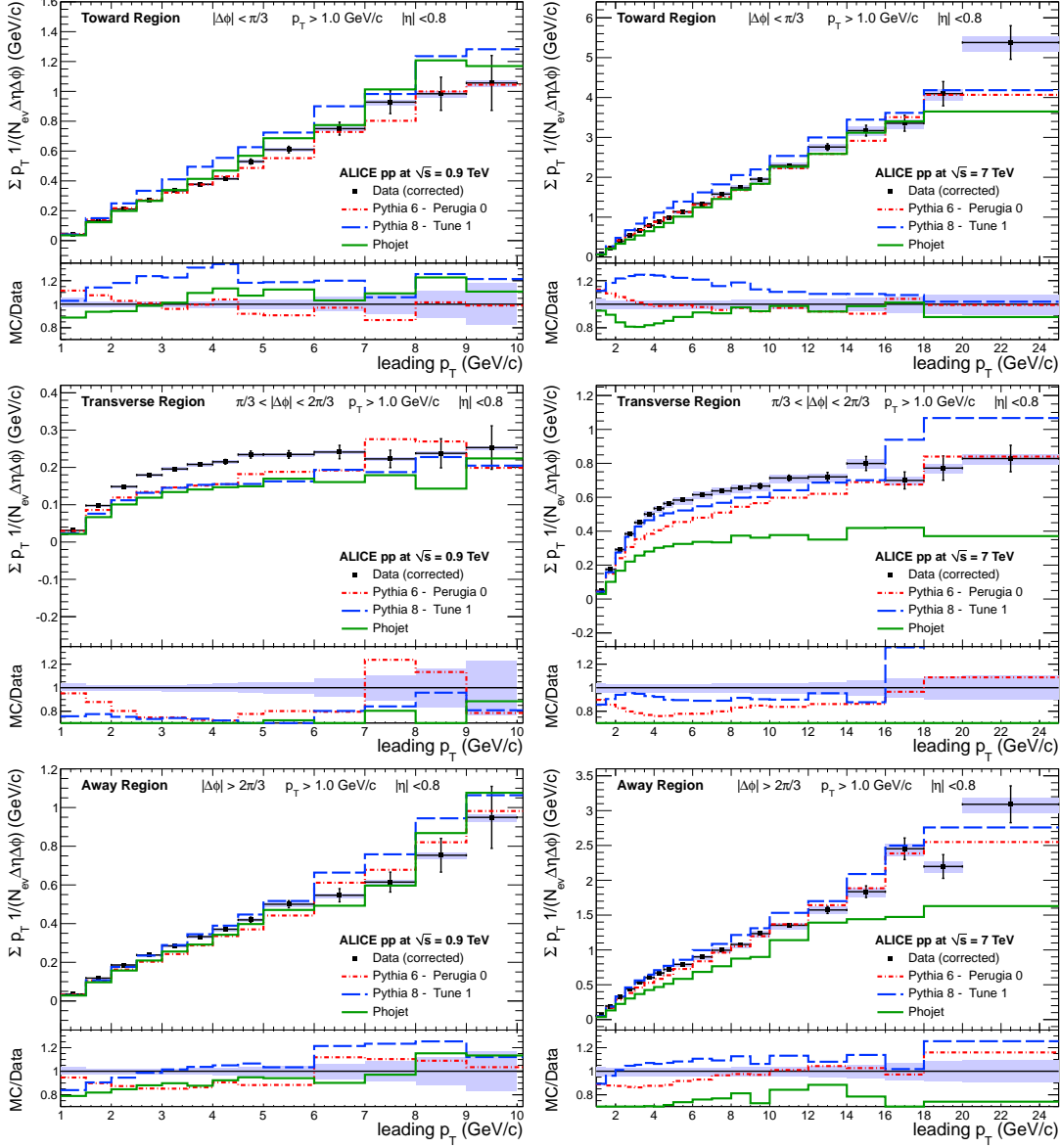


Figure 6.6: Summed p_T in Toward (top), Transverse (middle) and Away (bottom) regions at $\sqrt{s} = 0.9 \text{ TeV}$ (left) and $\sqrt{s} = 7 \text{ TeV}$ (right). Right and left vertical scales differ by a factor 4 (3) in the top (middle and bottom) panel. Shaded area in upper plots: systematic uncertainties. Shaded areas in bottom plots: sum in quadrature of statistical and systematic uncertainties. Horizontal error bars: bin width.

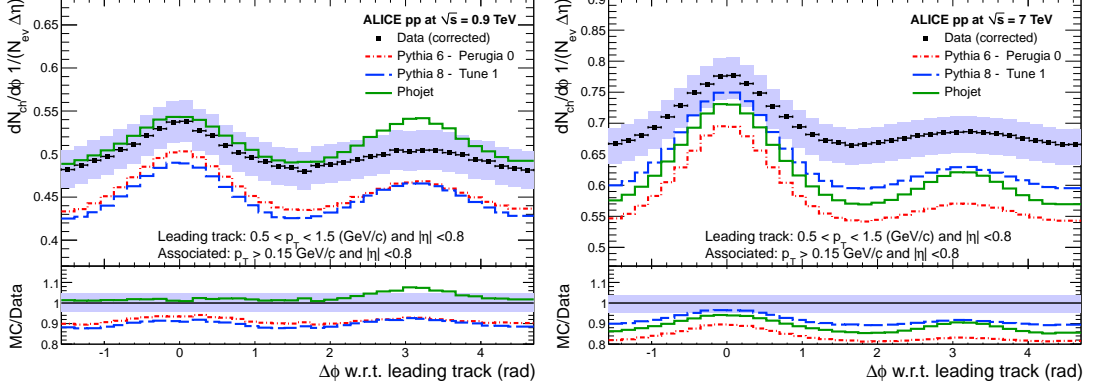
Azimuthal correlations - particle $p_T > 0.15 \text{ GeV}/c$ 

Figure 6.7: Azimuthal correlation at $\sqrt{s} = 0.9 \text{ TeV}$ (left) and $\sqrt{s} = 7 \text{ TeV}$ (right). Leading-track: $0.5 < p_{T,LT} < 1.5 \text{ GeV}/c$. For visualization purposes the $\Delta\phi$ axis is not centered around 0. Shaded area in upper plots: systematic uncertainties. Shaded areas in bottom plots: sum in quadrature of statistical and systematic uncertainties. Horizontal error bars: bin width.

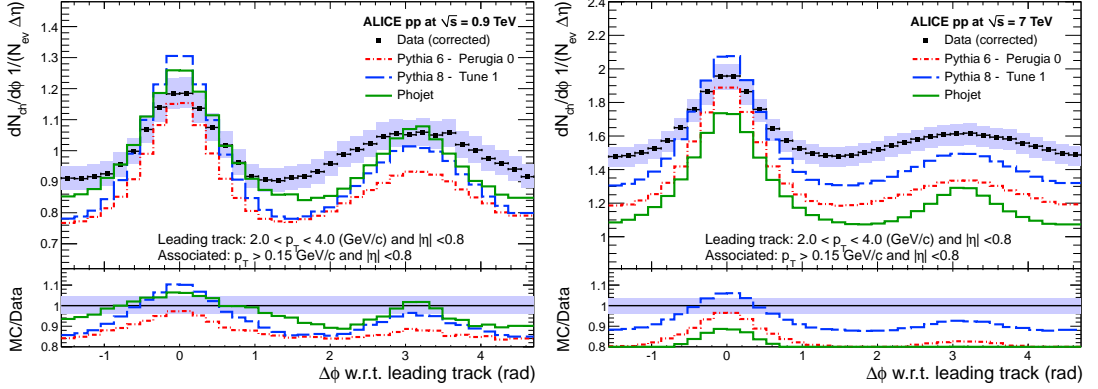


Figure 6.8: Azimuthal correlation at $\sqrt{s} = 0.9 \text{ TeV}$ (left) and $\sqrt{s} = 7 \text{ TeV}$ (right). Leading-track: $2.0 < p_{T,LT} < 4.0 \text{ GeV}/c$. For visualization purposes the $\Delta\phi$ axis is not centered around 0. Shaded area in upper plots: systematic uncertainties. Shaded areas in bottom plots: sum in quadrature of statistical and systematic uncertainties. Horizontal error bars: bin width.

6. RESULTS

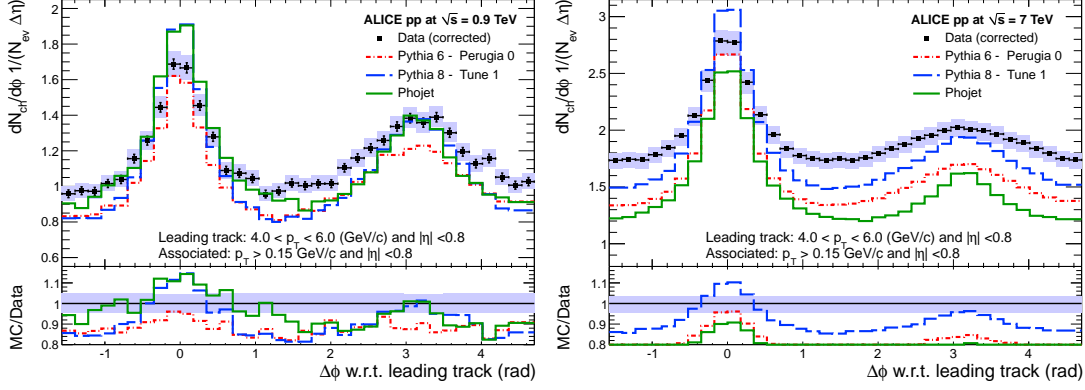


Figure 6.9: Azimuthal correlation at $\sqrt{s} = 0.9$ TeV (left) and $\sqrt{s} = 7$ TeV (right). Leading-track: $4.0 < p_{T,LT} < 6.0$ GeV/c. For visualization purposes the $\Delta\phi$ axis is not centered around 0. Shaded area in upper plots: systematic uncertainties. Shaded areas in bottom plots: sum in quadrature of statistical and systematic uncertainties. Horizontal error bars: bin width.

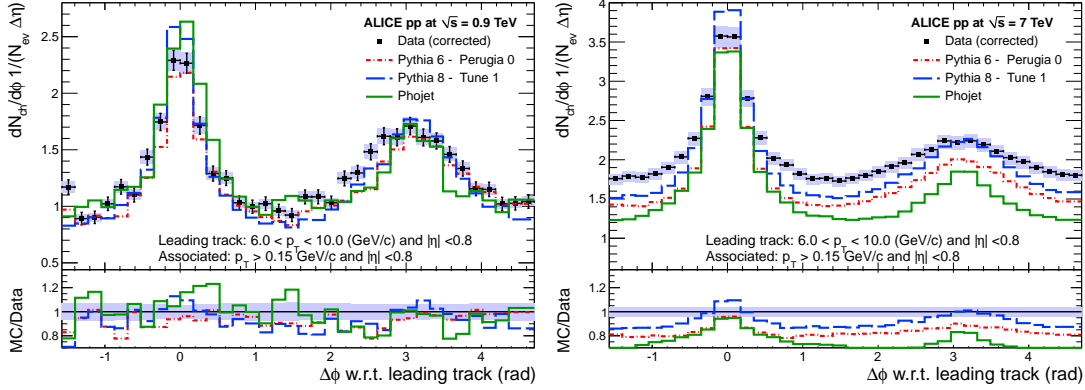


Figure 6.10: Azimuthal correlation at $\sqrt{s} = 0.9$ TeV (left) and $\sqrt{s} = 7$ TeV (right). Leading-track: $6.0 < p_{T,LT} < 10.0$ GeV/c. For visualization purposes the $\Delta\phi$ axis is not centered around 0. Shaded area in upper plots: systematic uncertainties. Shaded areas in bottom plots: sum in quadrature of statistical and systematic uncertainties. Horizontal error bars: bin width.

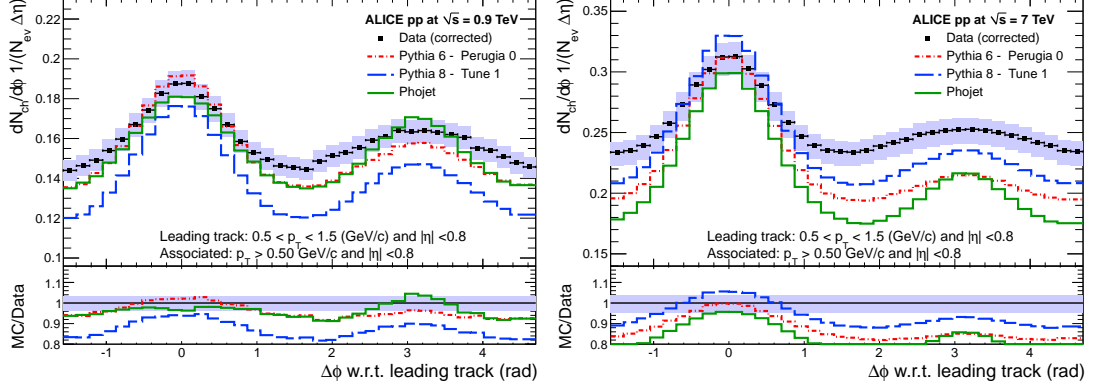
Azimuthal correlations - particle $p_T > 0.5 \text{ GeV}/c$ 

Figure 6.11: Azimuthal correlation at $\sqrt{s} = 0.9 \text{ TeV}$ (left) and $\sqrt{s} = 7 \text{ TeV}$ (right). Leading-track: $0.5 < p_{T,LT} < 1.5 \text{ GeV}/c$. For visualization purposes the $\Delta\phi$ axis is not centered around 0. Shaded area in upper plots: systematic uncertainties. Shaded areas in bottom plots: sum in quadrature of statistical and systematic uncertainties. Horizontal error bars: bin width.

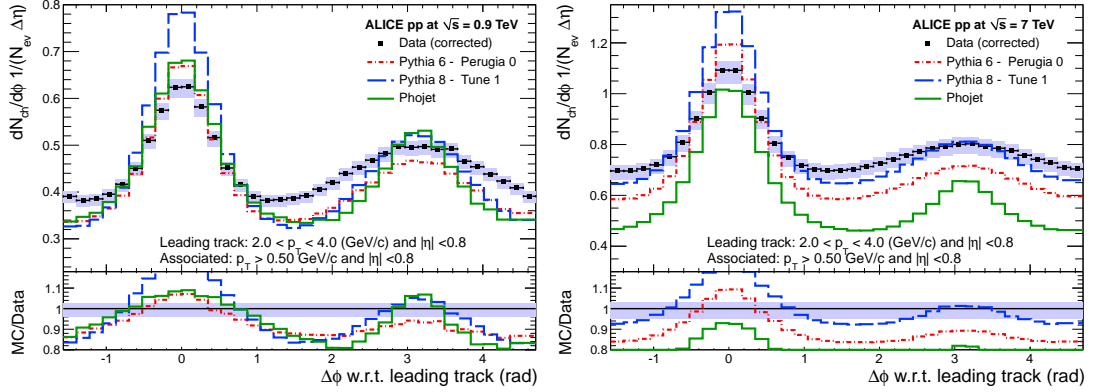


Figure 6.12: Azimuthal correlation at $\sqrt{s} = 0.9 \text{ TeV}$ (left) and $\sqrt{s} = 7 \text{ TeV}$ (right). Leading-track: $2.0 < p_{T,LT} < 4.0 \text{ GeV}/c$. For visualization purposes the $\Delta\phi$ axis is not centered around 0. Shaded area in upper plots: systematic uncertainties. Shaded areas in bottom plots: sum in quadrature of statistical and systematic uncertainties. Horizontal error bars: bin width.

6. RESULTS

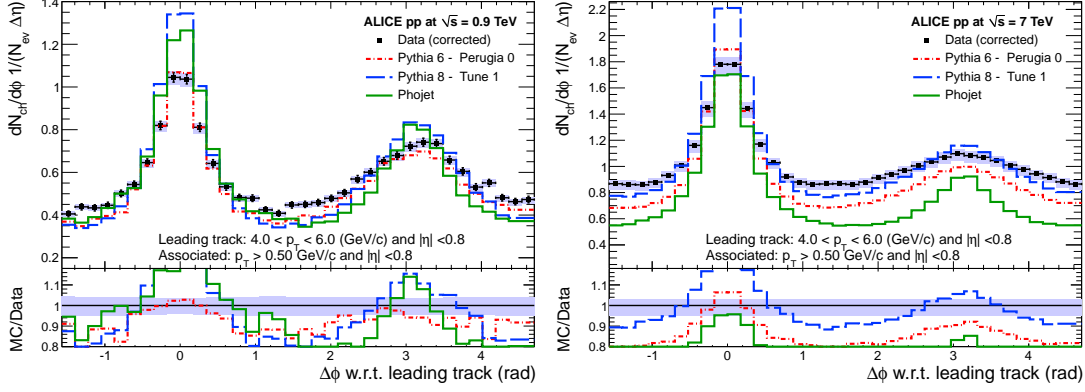


Figure 6.13: Azimuthal correlation at $\sqrt{s} = 0.9$ TeV (left) and $\sqrt{s} = 7$ TeV (right). Leading-track: $4.0 < p_{T,LT} < 6.0$ GeV/c. For visualization purposes the $\Delta\phi$ axis is not centered around 0. Shaded area in upper plots: systematic uncertainties. Shaded areas in bottom plots: sum in quadrature of statistical and systematic uncertainties. Horizontal error bars: bin width.

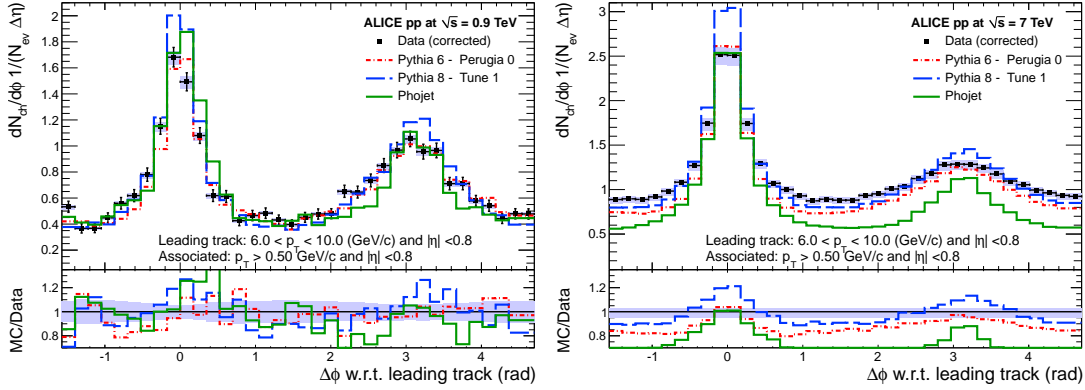


Figure 6.14: Azimuthal correlation at $\sqrt{s} = 0.9$ TeV (left) and $\sqrt{s} = 7$ TeV (right). Leading-track: $6.0 < p_{T,LT} < 10.0$ GeV/c. For visualization purposes the $\Delta\phi$ axis is not centered around 0. Shaded area in upper plots: systematic uncertainties. Shaded areas in bottom plots: sum in quadrature of statistical and systematic uncertainties. Horizontal error bars: bin width.

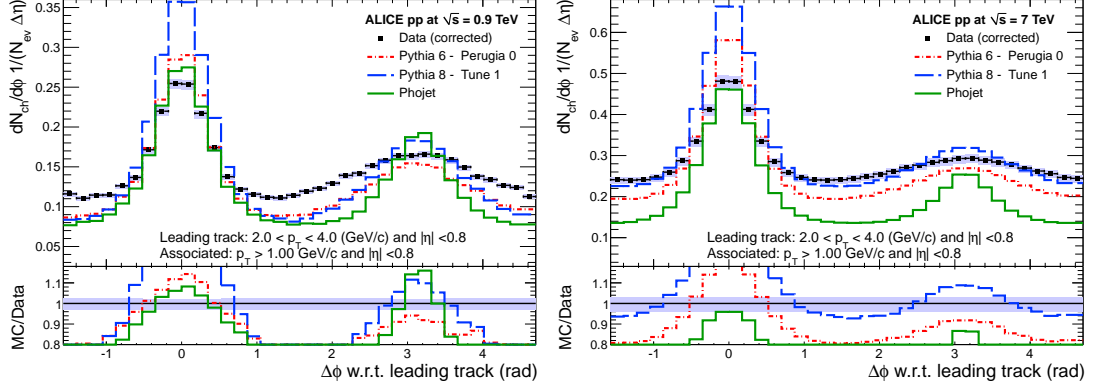
Azimuthal correlations - particle $p_T > 1.0 \text{ GeV}/c$ 

Figure 6.15: Azimuthal correlation at $\sqrt{s} = 0.9 \text{ TeV}$ (left) and $\sqrt{s} = 7 \text{ TeV}$ (right). Leading-track: $2.0 < p_{T,LT} < 4.0 \text{ GeV}/c$. For visualization purposes the $\Delta\phi$ axis is not centered around 0. Shaded area in upper plots: systematic uncertainties. Shaded areas in bottom plots: sum in quadrature of statistical and systematic uncertainties. Horizontal error bars: bin width.

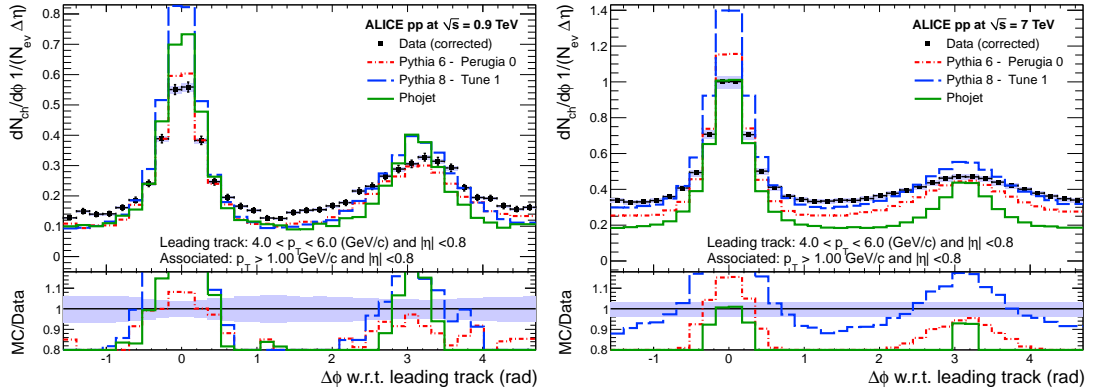


Figure 6.16: Azimuthal correlation at $\sqrt{s} = 0.9 \text{ TeV}$ (left) and $\sqrt{s} = 7 \text{ TeV}$ (right). Leading-track: $4.0 < p_{T,LT} < 6.0 \text{ GeV}/c$. For visualization purposes the $\Delta\phi$ axis is not centered around 0. Shaded area in upper plots: systematic uncertainties. Shaded areas in bottom plots: sum in quadrature of statistical and systematic uncertainties. Horizontal error bars: bin width.

6. RESULTS

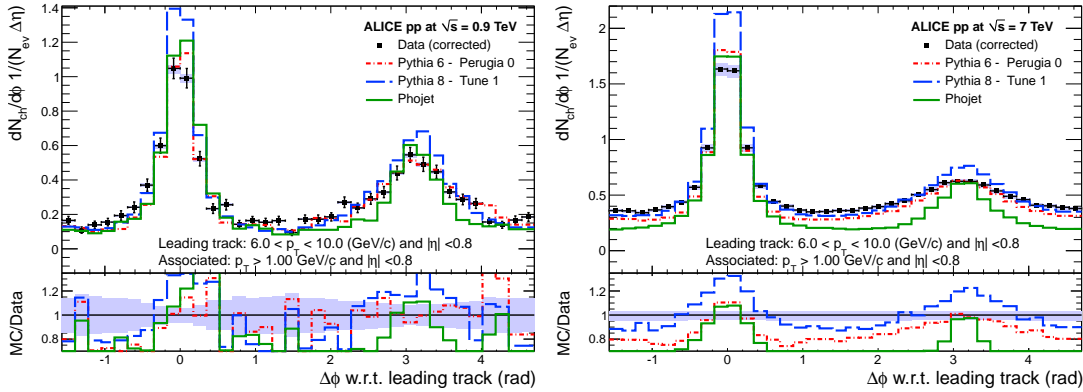


Figure 6.17: Azimuthal correlation at $\sqrt{s} = 0.9$ TeV (left) and $\sqrt{s} = 7$ TeV (right). Leading-track: $6.0 < p_{T,LT} < 10.0$ GeV/ c . For visualization purposes the $\Delta\phi$ axis is not centered around 0. Shaded area in upper plots: systematic uncertainties. Shaded areas in bottom plots: sum in quadrature of statistical and systematic uncertainties. Horizontal error bars: bin width.

6.4 Comparison with ATLAS results

We are interested in comparing independent measurements with different systematic uncertainties from the various LHC experiments. For this purpose the LHC-wide *Minimum Bias and Underlying Event working-group* [5] has defined some common settings for a combined analysis. These settings are the ones used in our measurement and are outlined in Sect. 5.1. So far the ATLAS collaboration has published an analysis [11] fulfilling these criteria: the hard scale is given by the leading-track p_T and the acceptance considered is $|\eta| < 0.8$. Only charged particles with $p_T > 0.5$ or 1 GeV/ c are considered. The leading-track is not included in the Toward region and in the azimuthal correlations. The comparison between ALICE and ATLAS results is shown in Appendix B.1, where we plot the ratio of the number density and summed p_T measured by the two experiments in all the topological regions at both collision energies. The overall agreement is within 3 standard deviations of the statistical error. Nevertheless at $\sqrt{s} = 7$ TeV the ALICE measurement tends to systematically underestimate the ATLAS results by about 5%.

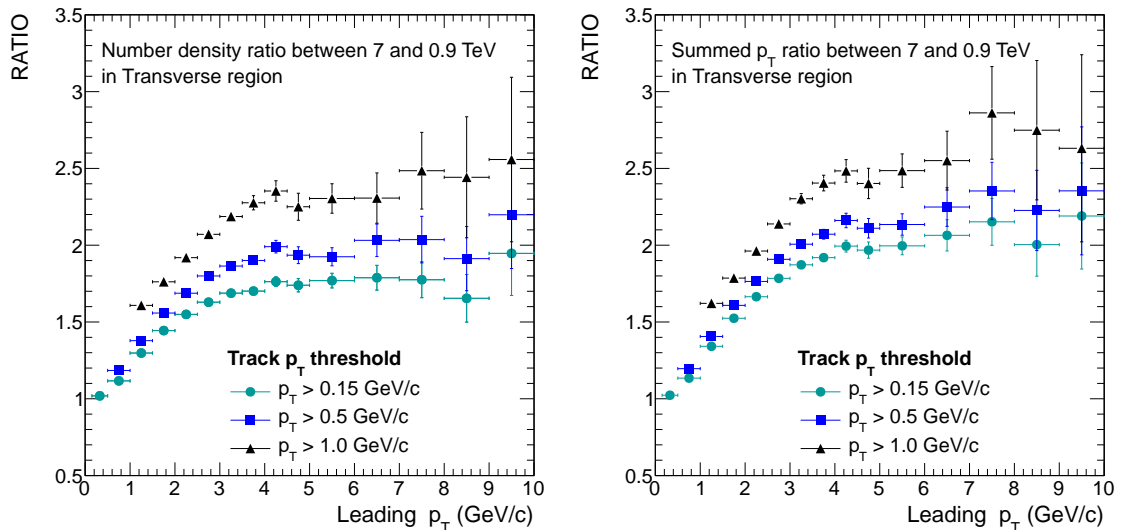


Figure 6.18: Ratio between $\sqrt{s} = 0.9$ TeV and $\sqrt{s} = 7$ TeV for number density (left) and summed p_T (right) distributions in the Transverse region. Statistical uncertainties only.

Moreover, ATLAS has published an UE measurement in the detector's full pseudo-rapidity coverage of $|\eta| < 2.5$ [10]. The comparison with our measurement is shown in Appendix B.2, for track $p_T > 0.5$ GeV/ c . Given the different pseudo-rapidity ranges considered in the two measurements, the results in the Toward and Away regions are not comparable. Moreover, in the ATLAS case the leading track is included in the Toward region. On the other hand, the mean values of the Transverse plateaus are in good agreement, indicating an independence of the UE activity on the pseudo-rapidity in the $p_{T,LT}$ range considered (even though in this case our measurement tends to slightly overestimate the ATLAS measurement at $\sqrt{s} = 0.9$ TeV). The discrepancy at lower values of $p_{T,LT}$ in this region is explained by the different acceptance [100].

6.5 Energy scaling

In Fig. 6.18 (left) we show the ratio between the number density distribution at $\sqrt{s} = 7$ TeV and $\sqrt{s} = 0.9$ TeV. Most of the systematic uncertainties are expected

6. RESULTS

	Number density	Summed p_T
$p_T > 0.15 \text{ GeV}/c$	1.76 ± 0.02	2.00 ± 0.03
$p_T > 0.5 \text{ GeV}/c$	1.97 ± 0.03	2.16 ± 0.03
$p_T > 1.0 \text{ GeV}/c$	2.32 ± 0.04	2.48 ± 0.05

Table 6.2: Constant fit in $4 < p_{T,LT} < 10 \text{ GeV}/c$ to the ratio between $\sqrt{s} = 0.9 \text{ TeV}$ and $\sqrt{s} = 7 \text{ TeV}$ for number density (left) and summed p_T (right) distributions in the Transverse region.

to be correlated between the two energies, therefore we consider only statistical uncertainties. The ratio saturates for leading-track $p_T > 4 \text{ GeV}/c$. The results of a constant fit in the range $4 < p_{T,LT} < 10 \text{ GeV}/c$ are reported in Table 6.2. The measured scaling factor for a p_T threshold of $0.5 \text{ GeV}/c$ is in agreement with the observations of ATLAS [10, 11] and CMS [81].

In Fig. 6.18 (right) we show the ratio between the distribution at $\sqrt{s} = 7 \text{ TeV}$ and $\sqrt{s} = 0.9 \text{ TeV}$, considering only statistical errors as before. The results of a constant fit in the range $4 < p_{T,LT} < 10 \text{ GeV}/c$ are reported in Table 6.2. Also in this case the scaling factor is in agreement with ATLAS and CMS results.

The summed p_T distribution rises slightly faster as a function of \sqrt{s} than the number density distribution, indicating that the available energy tends to increase the particles' transverse momentum in addition to the multiplicity. This is in qualitative agreement with an increased relative contribution of hard processes to the Underlying Event with increasing collision energy.

In Table 6.1 we compared our results on the UE activity in the plateau (in the Transverse region) with a measurement by the CDF collaboration [40]. CDF measured the UE as a function of charged-particle-jet p_T at a collision energy of 1.8 TeV . The particle p_T threshold is $0.5 \text{ GeV}/c$ and the acceptance $|\eta| < 1$. In the Transverse region CDF measures 3.8 charged particles per unit pseudorapidity above the p_T threshold at leading-jet $p_T = 20 \text{ GeV}/c$, which falls in the plateau region. This number needs to be divided by 2π in order to be compared with the average number of particles in the plateau from Table 6.1 at the same

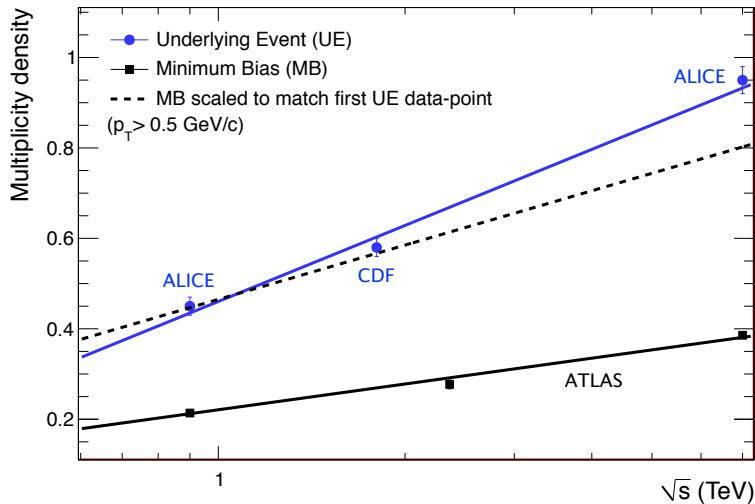


Figure 6.19: Comparison of number density in the plateau of the Transverse region (blue points, see Table 6.2) and $dN_{\text{ch}}/d\eta$ at mid-rapidity (scaled by $1/2\pi$) in minimum-bias events measured by the ATLAS collaboration [9] (black points). The CDF measurement [40] of the UE is also shown (second blue full-point). In all cases only particles with $p_{\text{T}} > 0.5 \text{ GeV}/c$ are considered. The full lines show fits with the functional form $a + b \ln \sqrt{s}$. The dotted line is the minimum-bias measurement scaled to match the first UE data-point. More details in the text.

threshold value. The scaled CDF result is 0.60, also shown in Table 6.1 for comparison. As expected, it falls between our two measurements at $\sqrt{s} = 0.9 \text{ TeV}$ and $\sqrt{s} = 7 \text{ TeV}$. Interpolating between our measurements assuming a logarithmic dependence on \sqrt{s} results in 0.62 charged particles per unit area at 1.8 TeV, consistent with the CDF result.

Figure 6.19 presents the number density in the plateau of the Transverse region for $p_{\text{T}} > 0.5 \text{ GeV}/c$ compared with $dN_{\text{ch}}/d\eta$ at mid-rapidity (scaled by $1/2\pi$) measured by the ATLAS collaboration [9]. The $dN_{\text{ch}}/d\eta$ value is measured in events with at least one charged particle in the ATLAS acceptance ($|\eta| < 2.5$) and for particles with $p_{\text{T}} > 0.5 \text{ GeV}/c$. The CDF data-point for the UE measurement is also shown in Fig. 6.19. We fit both measurements, UE and Minimum Bias (MB), with a logarithmic dependence on the collision energy ($a + b \ln \sqrt{s}$),

6. RESULTS

also shown in Fig. 6.19 as solid lines. We observe that at $\sqrt{s} = 7$ TeV the multiplicity density in the UE is about 2.5 times larger than in the minimum-bias case. This is due to the fact that the UE measurement is performed in a sub-sample of the minimum-bias events, in which we require the leading particle to be in a limited p_T range: $4 < p_{T,LT} < 10$ GeV/ c at $\sqrt{s} = 0.9$ TeV and $10 < p_{T,LT} < 25$ GeV/ c at $\sqrt{s} = 7$ TeV. The lower threshold on the leading-particle p_T reduces the amount of diffractive events considered (see Sect. 5.3.1), while enhancing the case of 2-to-2 hard scatterings.

Moreover, this comparison points out that the slope of the UE multiplicity-density scaling with $\ln \sqrt{s}$ is much steeper in the UE than in the MB case. This observation confirms the idea that different physics processes contribute to different extent to the UE or MB activity.

6.6 Conclusions

We have characterized the Underlying Event in pp collisions at $\sqrt{s} = 0.9$ and 7 TeV by measuring the number density, the summed- p_T and the azimuthal correlation of charged particles with respect to the leading particle. The first two quantities are evaluated in three topological regions: Toward, Transverse and Away. Three different track- p_T lower thresholds are considered: $p_{T,\min} = 0.15$, 0.5 and 1 GeV/ c . The analysis is based on about $6 \cdot 10^6$ minimum bias events at $\sqrt{s} = 0.9$ TeV and $25 \cdot 10^6$ events at $\sqrt{s} = 7$ TeV recorded by the ALICE detector during the data-taking periods from April to July 2010. Measured data have been corrected for detector-related effects; in particular we applied a data-driven correction to account for the misidentification of the leading particle and for the contamination from secondaries produced in the decays of strange particles. The systematic uncertainties related to our correction procedure have also been estimated. The fully-corrected final distributions are compared with PYTHIA 6.4, PYTHIA 8 and PHOJET, showing that pre-LHC tunes have difficulties describing the data. These results are an important ingredient in the required retuning of those generators.

Out of the presented distributions, the Transverse region is particularly sensitive to the Underlying Event. The event activity in this region has a steep increase for leading particle $p_{T,LT}$ below ~ 3 GeV/ c . For higher $p_{T,LT}$ the distributions tend to saturate at different values depending on $p_{T,\min}$. For the number density distribution at $\sqrt{s} = 0.9$ TeV these values are 1.00 ± 0.04 , 0.45 ± 0.02 and 0.16 ± 0.01 for $p_{T,\min} = 0.15$, 0.5 and 1 GeV/ c , respectively. At $\sqrt{s} = 7$ TeV the saturation values are 1.82 ± 0.06 , 0.95 ± 0.03 and 0.41 ± 0.01 . The summed- p_T distribution at 0.9 TeV saturates at 0.62 ± 0.02 GeV/ c , 0.45 ± 0.02 GeV/ c and 0.24 ± 0.01 GeV/ c for $p_{T,\min} = 0.15$, 0.5 and 1 GeV/ c , respectively. At 7 TeV the values are 1.43 ± 0.05 GeV/ c , 1.15 ± 0.04 GeV/ c and 0.76 ± 0.03 GeV/ c . The saturation indicates the onset of the event-by-event partitioning into azimuthal regions containing the particles from the hard scattering and the UE region. The bulk particle production becomes independent of the hard scale.

6. RESULTS

We observe that the ratio between the distributions at $\sqrt{s} = 0.9$ and 7 TeV in this region saturates at a value of about 2 for track $p_T > 0.5 \text{ GeV}/c$. The summed- p_T distribution rises slightly faster as a function of \sqrt{s} than the number density distribution, indicating that the available energy tends to increase the particles' transverse momentum in addition to the multiplicity. This is in qualitative agreement with an increased relative contribution of hard processes to the Underlying Event with increasing \sqrt{s} . Moreover, the average number of particles at large $p_{T,LT}$ in the Transverse region scales logarithmically with the collision energy faster than $dN_{\text{ch}}/d\eta$ in minimum-bias events, indicating that different physics processes contribute to different extent to the UE or minimum bias activity. Therefore models aiming at a correct reproduction of these minimum-bias and Underlying Event distributions need a precise description of the interplay of the hard process, the associated initial and final-state radiation and multiple parton interactions.

In general our results are in good qualitative and quantitative agreement with measurements from other LHC experiments (ATLAS and CMS) and show similar trends to that of the Tevatron (CDF).

Appendix A

Corrections on real data

In this Appendix we present the effect of each correction on the real data. Black dots represent the data prior to any correction step, solid lines are the data corrected for the mentioned correction step (including the previous ones). The correction factors are evaluated with PYTHIA. We show only results for the track p_T threshold of $0.15 \text{ GeV}/c$ since this is the case in which the maxima corrections are applied.

A. CORRECTIONS ON REAL DATA

A.1 Number density

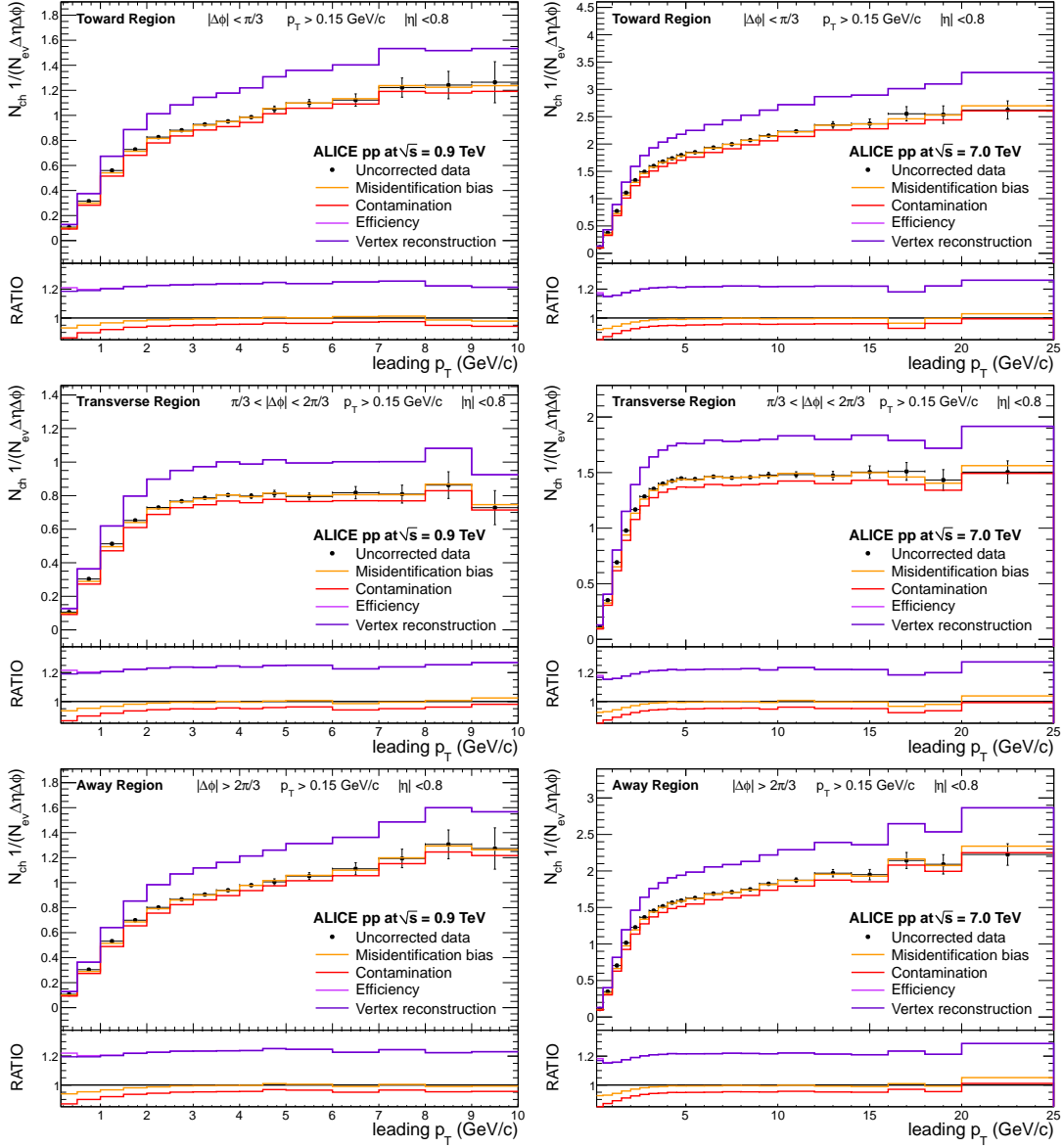


Figure A.1: Number density at $\sqrt{s} = 0.9$ TeV (left) and $\sqrt{s} = 7$ TeV (right) in Toward (top), Transverse (middle) and Away (bottom) regions. Track $p_T > 0.15$ GeV/c.

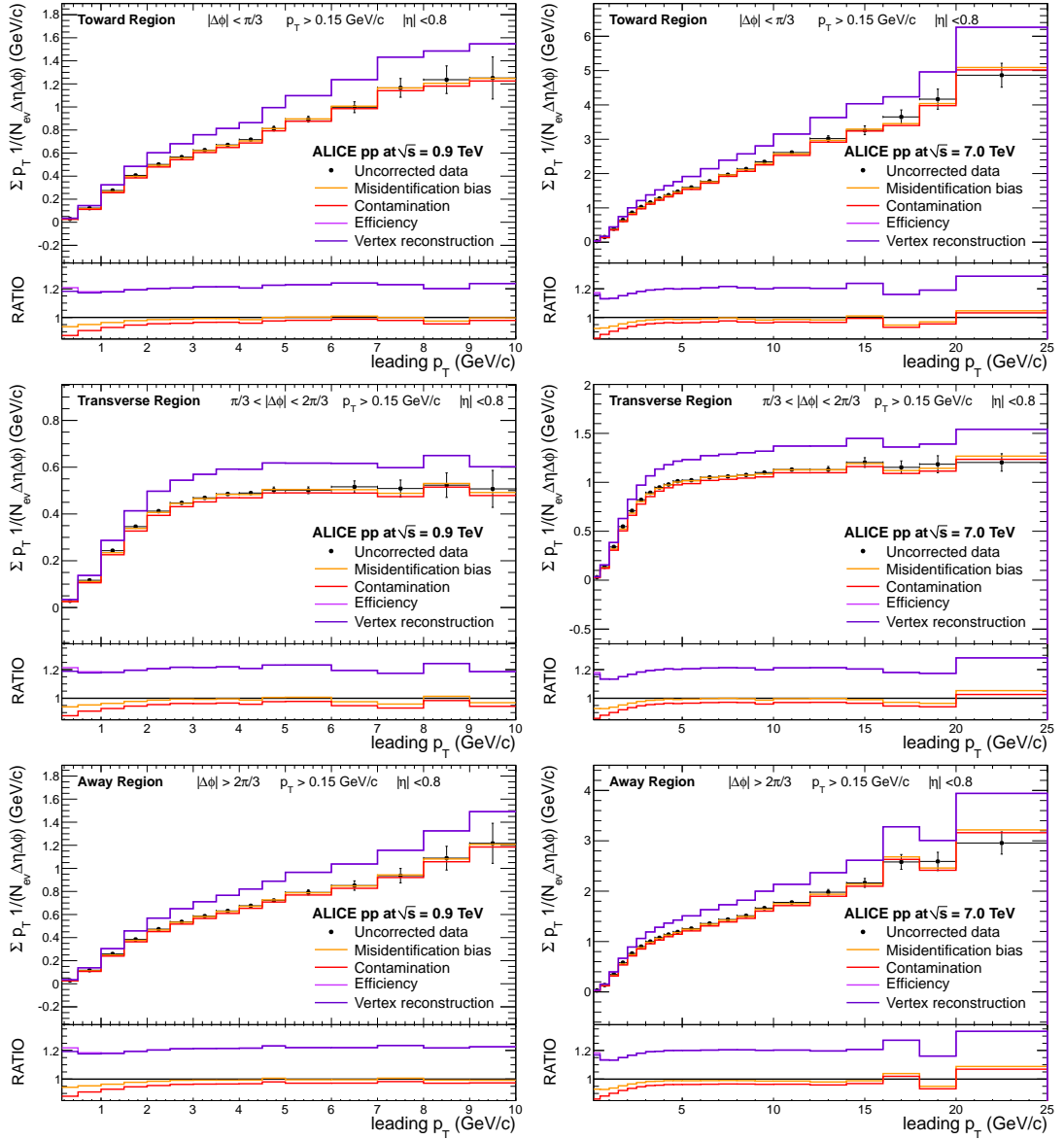
A.2 Summed p_T 

Figure A.2: Summed p_T at $\sqrt{s} = 0.9$ TeV (left) and $\sqrt{s} = 7$ TeV (right) in Toward (top), Transverse (middle) and Away (bottom) regions. Track $p_T > 0.15$ GeV/c.

A. CORRECTIONS ON REAL DATA

A.3 Azimuthal correlations

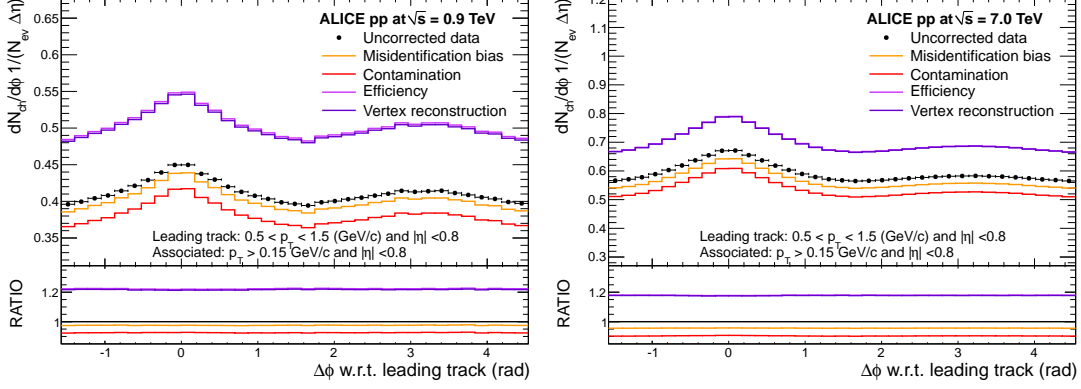


Figure A.3: Azimuthal correlation between tracks and leading track at $\sqrt{s} = 0.9$ TeV (left) and $\sqrt{s} = 7$ TeV (right). Leading track: $0.5 < p_T < 1.5$ GeV/c. Tracks: $p_T > 0.15$ GeV/c.

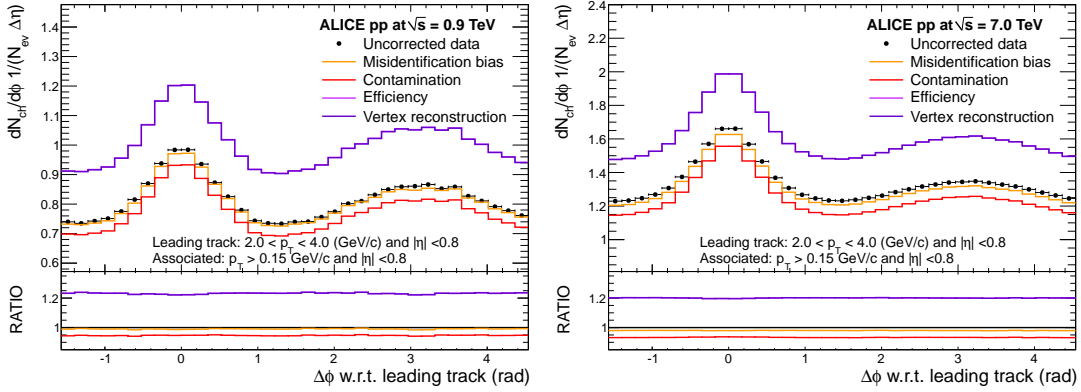


Figure A.4: Azimuthal correlation between tracks and leading track at $\sqrt{s} = 0.9$ TeV (left) and $\sqrt{s} = 7$ TeV (right). Leading track: $2.0 < p_T < 4.0$ GeV/c. Tracks: $p_T > 0.15$ GeV/c.

A.3 Azimuthal correlations

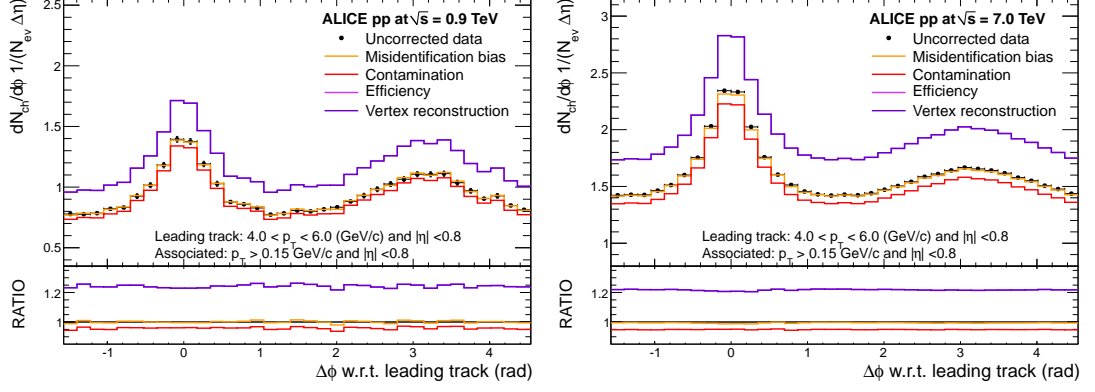


Figure A.5: Azimuthal correlation between tracks and leading track at $\sqrt{s} = 0.9$ TeV (left) and $\sqrt{s} = 7$ TeV (right). Leading track: $4.0 < p_T < 6.0$ GeV/c. Tracks: $p_T > 0.15$ GeV/c.

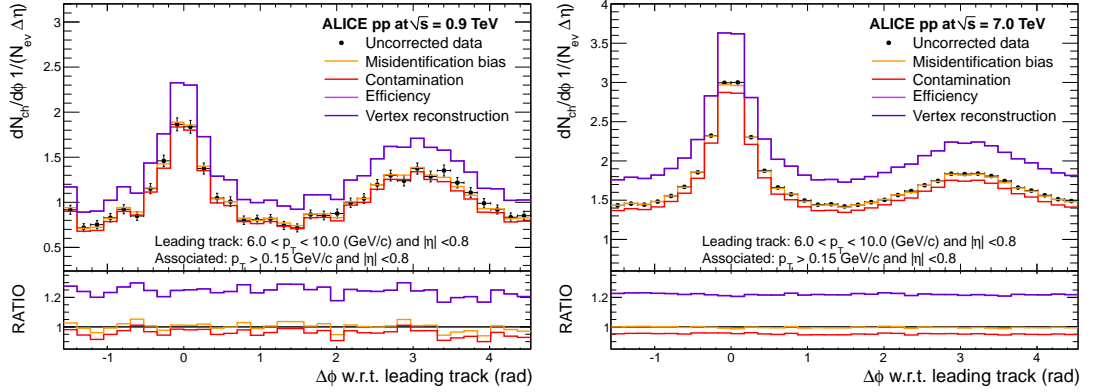


Figure A.6: Azimuthal correlation between tracks and leading track at $\sqrt{s} = 0.9$ TeV (left) and $\sqrt{s} = 7$ TeV (right). Leading track: $6.0 < p_T < 10.0$ GeV/c. Tracks: $p_T > 0.15$ GeV/c.

A. CORRECTIONS ON REAL DATA

Appendix B

Comparison with ATLAS results

In this Appendix we show a comparison between our measurement of the UE and the results from the ATLAS collaboration. In Appendix B.1 the results from both experiments are considered in the acceptance $|\eta| < 0.8$. ATLAS data-points are extracted with a graphical digitizer from [11]. In Appendix B.2 the full ATLAS acceptance $|\eta| < 2.5$ is considered (for ALICE $|\eta| < 0.8$). The leading particle is included in the Toward region in the ATLAS measurement but not in the ALICE measurement. In this case the ATLAS results are published in [10] and the data-points available at [4].

B. COMPARISON WITH ATLAS RESULTS

B.1 ATLAS limited phase-space: $|\eta| < 0.8$

Particle $p_T > 0.5 \text{ GeV}/c - \sqrt{s} = 0.9 \text{ TeV}$

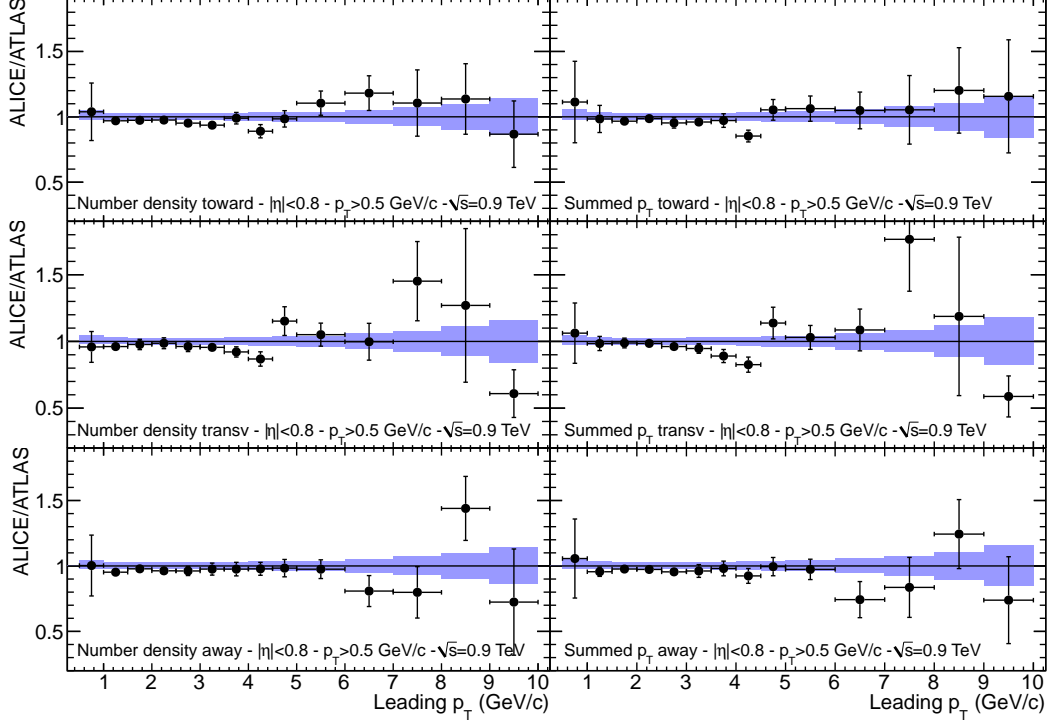


Figure B.1: Ratio between ALICE and ATLAS [11] results for the number density (left) and summed p_T (right) distributions in the Toward (top), Transverse (middle) and Away (bottom) regions. The leading particle is not included in the Toward region. In the ratio ATLAS errors are statistical and systematic added in quadrature and ALICE data-points have no error. The coloured band represents the ALICE statistical and systematic errors added in quadrature. Particle $p_T > 0.5 \text{ GeV}/c$ and $|\eta| < 0.8$ for both experiments. $\sqrt{s} = 0.9 \text{ TeV}$.

Particle $p_T > 0.5 \text{ GeV}/c - \sqrt{s} = 7 \text{ TeV}$

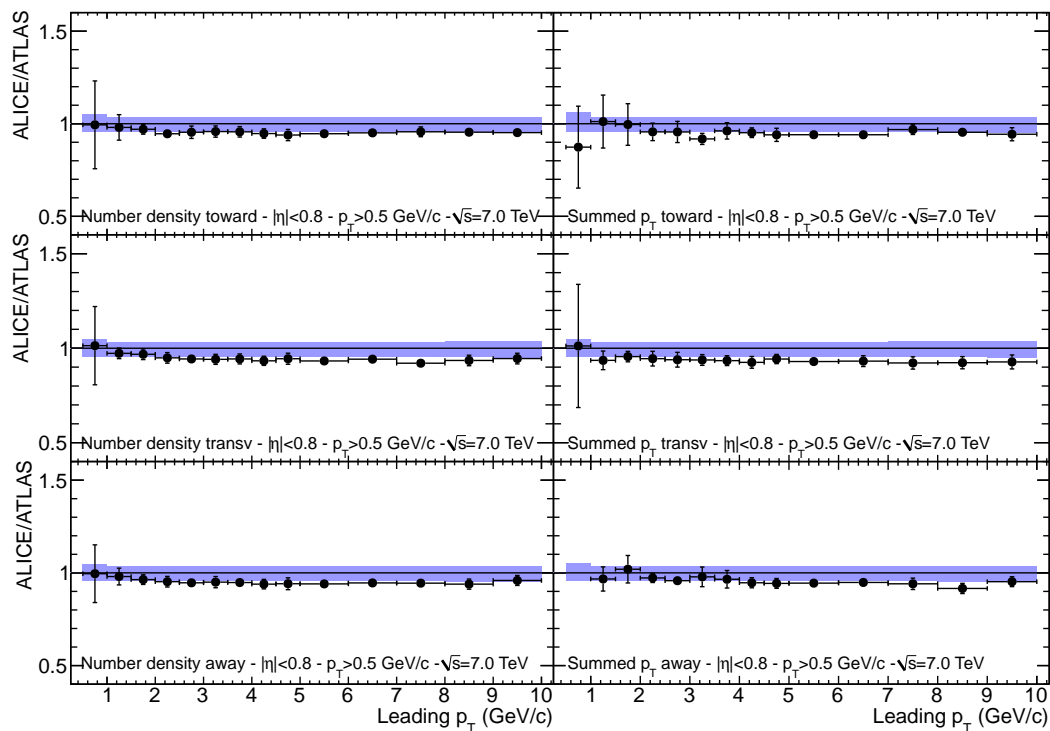


Figure B.2: Ratio between ALICE and ATLAS [11] results for the number density (left) and summed p_T (right) distributions in the Toward (top), Transverse (middle) and Away (bottom) regions. The leading particle is not included in the Toward region. In the ratio ATLAS errors are statistical and systematic added in quadrature and ALICE data-points have no error. The coloured band represents the ALICE statistical and systematic errors added in quadrature. Particle $p_T > 0.5 \text{ GeV}/c$ and $|\eta| < 0.8$ for both experiments. $\sqrt{s} = 7 \text{ TeV}$.

B. COMPARISON WITH ATLAS RESULTS

Particle $p_T > 1 \text{ GeV}/c - \sqrt{s} = 0.9 \text{ TeV}$

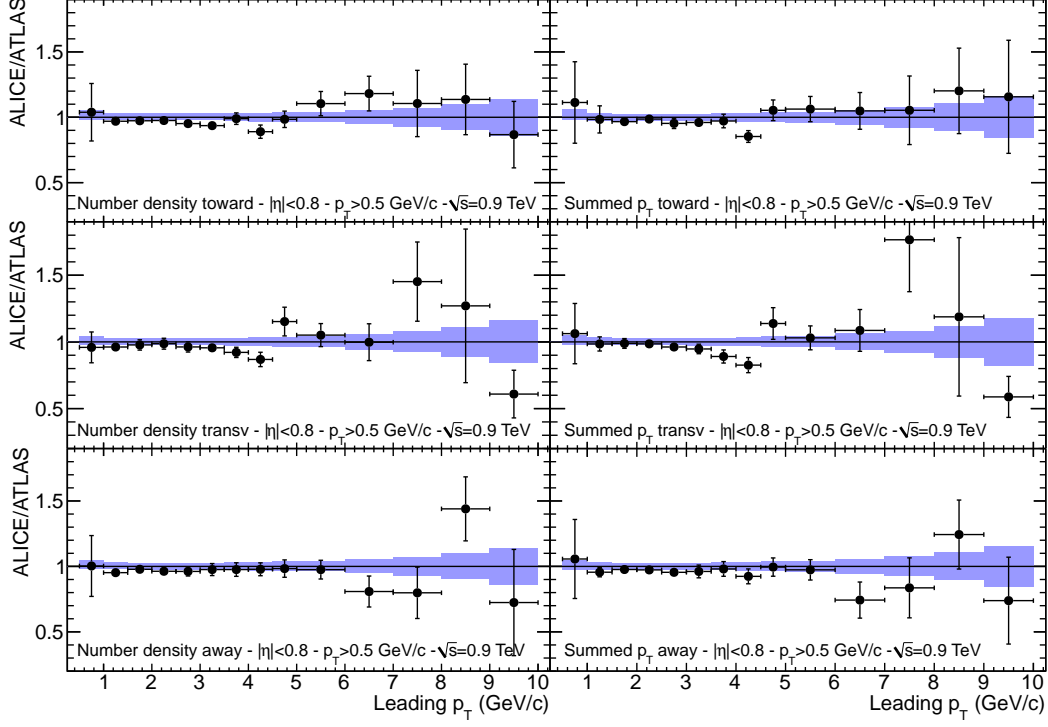


Figure B.3: Ratio between ALICE and ATLAS [11] results for the number density (left) and summed p_T (right) distributions in the Toward (top), Transverse (middle) and Away (bottom) regions. The leading particle is not included in the Toward region. In the ratio ATLAS errors are statistical and systematic added in quadrature and ALICE data-points have no error. The coloured band represents the ALICE statistical and systematic errors added in quadrature. Particle $p_T > 1 \text{ GeV}/c$ and $|\eta| < 0.8$ for both experiments. $\sqrt{s} = 0.9 \text{ TeV}$.

Particle $p_T > 1 \text{ GeV}/c$ - $\sqrt{s} = 7 \text{ TeV}$

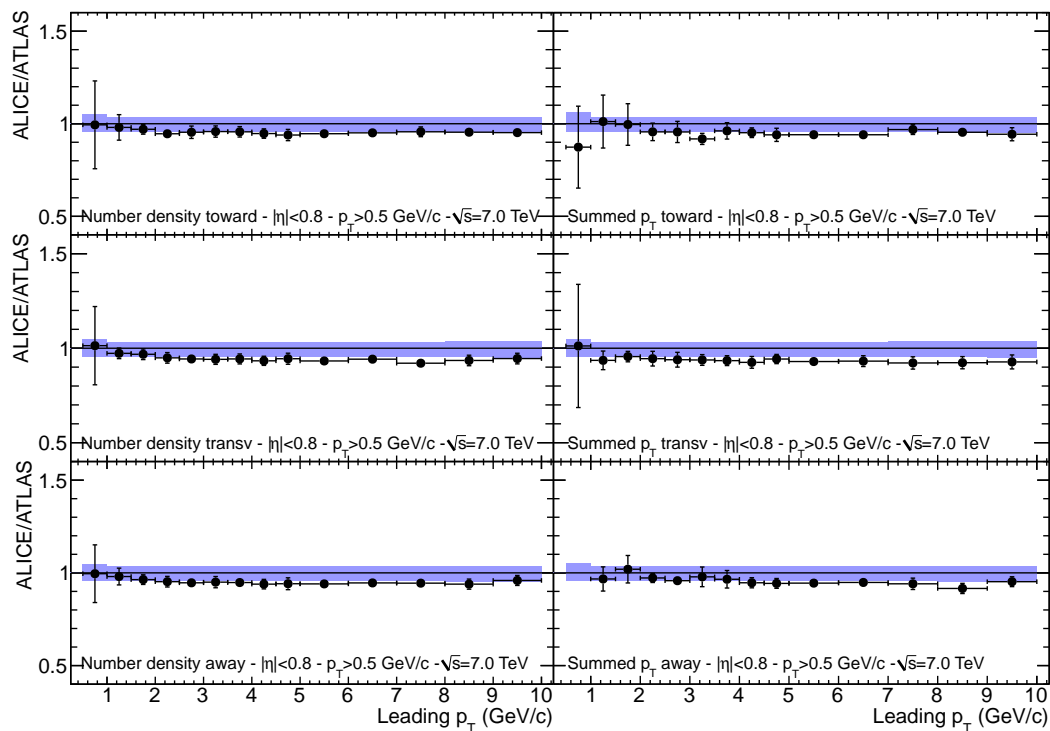


Figure B.4: Ratio between ALICE and ATLAS [11] results for the number density (left) and summed p_T (right) distributions in the Toward (top), Transverse (middle) and Away (bottom) regions. The leading particle is not included in the Toward region. In the ratio ATLAS errors are statistical and systematic added in quadrature and ALICE data-points have no error. The coloured band represents the ALICE statistical and systematic errors added in quadrature. Particle $p_T > 1 \text{ GeV}/c$ and $|\eta| < 0.8$ for both experiments. $\sqrt{s} = 7 \text{ TeV}$.

B. COMPARISON WITH ATLAS RESULTS

B.2 ATLAS full phase-space: $|\eta| < 2.5$

Particle $p_T > 0.5 \text{ GeV}/c - \sqrt{s} = 0.9 \text{ TeV}$

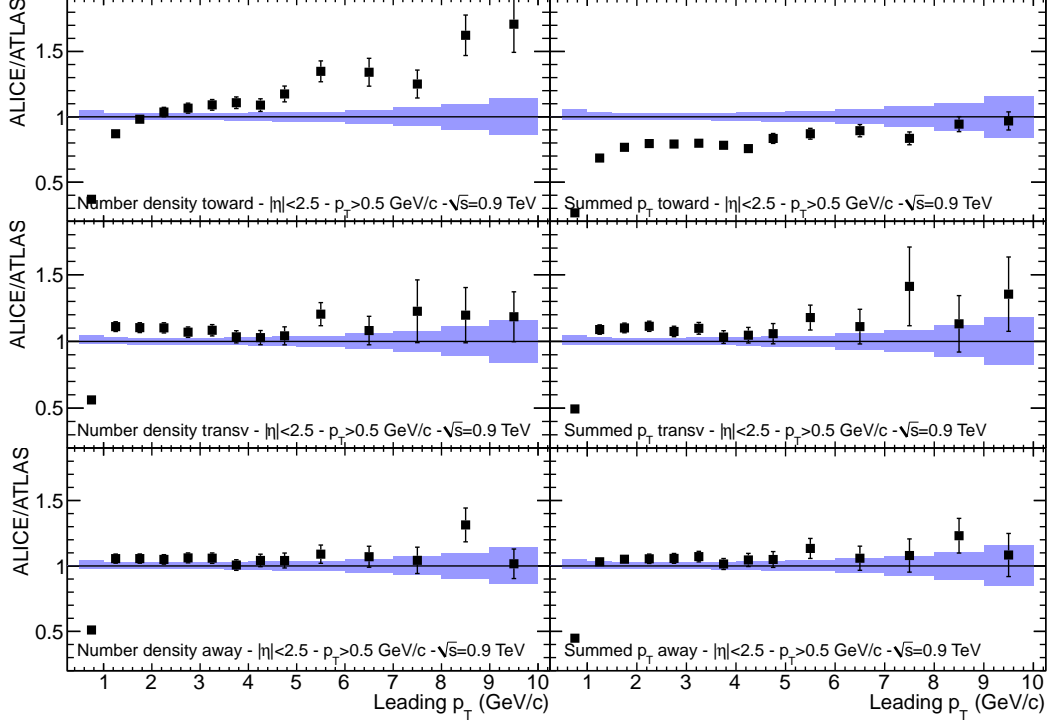


Figure B.5: Ratio between ALICE and ATLAS [10] results for the number density (left) and summed p_T (right) distributions in the Toward (top), Transverse (middle) and Away (bottom) regions. The leading particle is included in the Toward region only in the ATLAS measurement. In the ratio ATLAS errors are statistical and systematic added in quadrature and ALICE data-points have no error. The coloured band represents the ALICE statistical and systematic errors added in quadrature. Particle $p_T > 0.5 \text{ GeV}/c$, $|\eta| < 0.8$ for ALICE and $|\eta| < 2.5$ for ATLAS. $\sqrt{s} = 0.9 \text{ TeV}$.

Particle $p_T > 0.5 \text{ GeV}/c - \sqrt{s} = 7 \text{ TeV}$

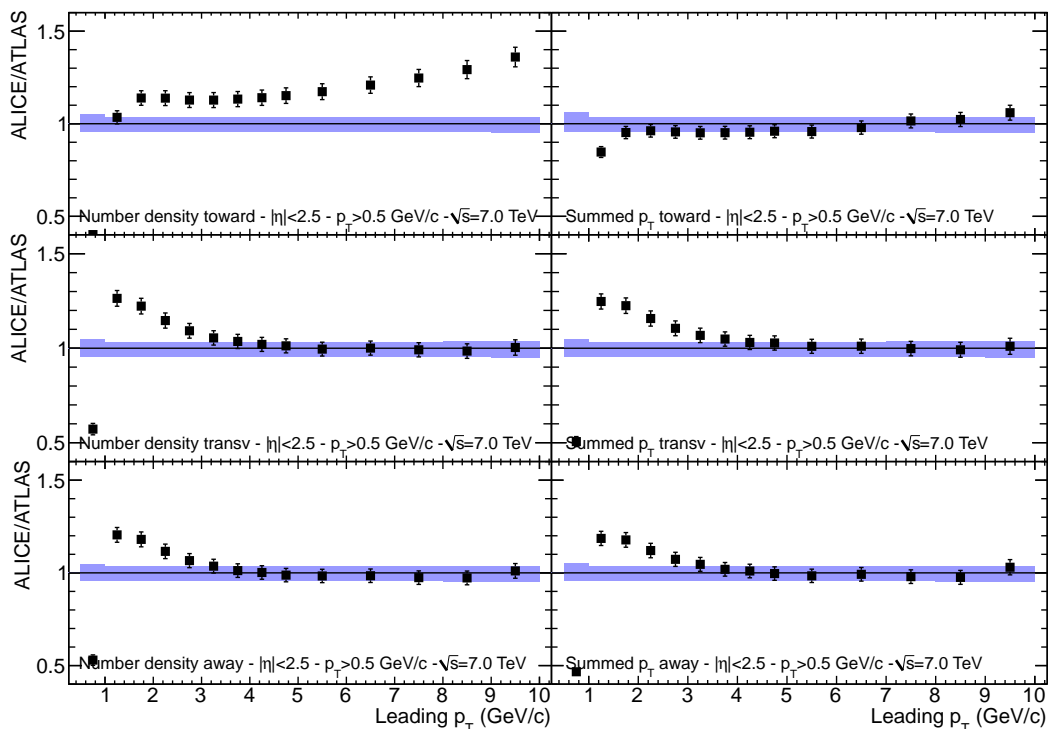


Figure B.6: Ratio between ALICE and ATLAS [11] results for the number density (left) and summed p_T (right) distributions in the Toward (top), Transverse (middle) and Away (bottom) regions. The leading particle is included in the Toward region only in the ATLAS measurement. In the ratio ATLAS errors are statistical and systematic added in quadrature and ALICE data-points have no error. The coloured band represents the ALICE statistical and systematic errors added in quadrature. Particle $p_T > 0.5 \text{ GeV}/c$, $|\eta| < 0.8$ for ALICE and $|\eta| < 2.5$ for ATLAS. $\sqrt{s} = 7 \text{ TeV}$.

B. COMPARISON WITH ATLAS RESULTS

Acronyms

ADC Analog to Digital Converter. 58

ALICE A Large Ion Collider Experiment. 34

AOD Analysis Object Data. 46

BGA Ball Grid Array. 58

BM Board Merger. 59

CMOS Complementary Metal Oxide Semiconductor. 58

CPV Charged Particle Veto. 36

CTP Central Trigger Processor. 43

DCA Distance of Closest Approach. 110

DCS Detector Control system. 57

DD Double Diffractive. 110

DIS Deep Inelastic Scattering. 5

DPM Dual Parton Model. 21

DY Drell Yan. 13

EMCal ElectroMagnetic Calorimeter. 36

ESD Event Summary Data. 46

Acronyms

- FEE** Front End Electronics. 39
- FF** Fragmentation Function. 15
- FMD** Forward Multiplicity Detector. 37
- FSR** Final State Radiation. 17
- GTU** Global Tracking Unit. 62
- GUI** Graphical User Interface. 66
- HCM** Half Chamber Merger. 61
- HMPID** High Multiplicity PID. 36
- ISR** Initial State Radiation. 17
- ITS** Inner Tracking System. 34
- LHC** Large Hadron Collider. 1
- LO** Leading Order. 5
- MB** Minimum Bias. 165
- MCM** Multi-Chip Module. 57
- MPI** Multi Partonic Interactions. 1
- MRPC** Multi-gap Resistive Plate Chamber. 35
- ND** Non Diffractive. 110
- NI** Network Interface. 57
- NLO** next-to-leading order. 11
- NNLO** next-to-next-to-leading order. 12
- ORI** Optical Read-out Interface. 57

PASA Pre-Amplifier and Shaping Amplifier. 57

PCB Printed Circuit Board. 57

PDF Parton Distribution Function. 5

PHOS PHOton Spectrometer. 36

PID Particle IDentification. 34

PMD Photon Multiplicity Detector. 37

pQCD perturbative QCD. 6

PSI PCI and Shared memory Interface. 64

QCD Quantum ChromoDynamics. 1

RF Radio Frequency. 32

RFT Regge Field Theory. 22

ROB Read-Out Board. 53

RPC Resistive Plate Chambers. 36

SCSN Slow Control Serial Network. 57

SD Single Diffractive. 110

SDD Silicon Drift Detector. 42

SM Standard Model. 1

SPD Silicon Pixel Detector. 42

SSD Silicon Strip Detector. 42

TOF Time Of Flight. 35

TPC Time Projection Chamber. 34

Acronyms

TRAP TRacklet Processor. 57

TRD Transition Radiation Detector. 2

UV ultra-violet. 6

ZDC Zero Degree Calorimeter. 37

List of Figures

1.1	Schematic representation of the hard cross-section factorization. . .	7
1.2	Schematic representation of a 2-to-2 scattering.	9
1.3	Lowest order diagrams contributing to the two jets cross-section. .	10
1.4	Inclusive jet cross-section measured with the CMS detector. . . .	11
1.5	Parton kinematics at LHC ($\sqrt{s} = 7$ TeV).	14
1.6	Di-jet event in e^+/e^- collisions at LEP and hadronic collision seen by the ALICE detector.	16
1.7	Sketch of a realistic pp collision.	17
1.8	Schematic representation of an interaction with two 2-to-2 hard scatterings.	20
1.9	Graphical representation of the optical theorem.	22
1.10	Schematic representation of a 2-to-2 scattering followed by a rescat- tering.	27
2.1	Schematic view of the LHC circumference.	32
2.2	Schematic representation of the ALICE detector and coordinate system.	35
2.3	Schematic view of the TPC field cage.	38
2.4	Picture of the TPC detector.	38
2.5	Layout of the ITS system.	41
2.6	Picture of the V0A and V0C detectors.	43
2.7	Vertex resolution as a function of tracklet multiplicity.	48
2.8	Track-finding efficiency for different combinations tracking detectors.	50
2.9	Transverse-momentum resolution for different combinations track- ing detectors.	50

LIST OF FIGURES

3.1	Schematic representation of the TRD system layout.	54
3.2	Working principle of the TRD detector.	55
3.3	Electron and pion signal in the TRD from beam-test data.	55
3.4	The TRD MCM integrating the PASA and TRAP chips.	60
3.5	Picture of a TRD ROB. The MCMs' functionalities are indicated.	60
3.6	Schematic layout of the most simple ROB test system set-up.	62
3.7	Box containing the single-MCM external PCB and connection of the power supply lines to the ROB.	63
3.8	The ROB test system software architecture.	64
3.9	Simplified flow diagram of the test routine.	65
3.10	Schematic view of the PASA/TRAP interface and critical points.	67
3.11	Frame used to inject signals at the PASA input.	68
3.12	Output of the charge-injection test.	69
3.13	Output of the analog test for an MCM with baseline shift.	70
3.14	Output of the analog test for an MCM with phase shift.	71
3.15	Baseline pattern for one TRAP ADC.	72
3.16	Distribution of the squared distance d	72
3.17	Scanner used for the identification of the MCMs.	74
3.18	Screen-shot of the scanner's GUI.	75
4.1	Sketch of the transverse-energy distribution in jet events as a function of $\Delta\eta$ from the leading jet.	78
4.2	LO pQCD prediction of the mean pedestal energy	79
4.3	Pedestal energy measured by the UA1 collaboration at $\sqrt{s} = 630$ GeV.	80
4.4	Definition of the Toward, Transverse and Away regions by the CDF collaboration.	82
4.5	Charged-particle density as a function of the leading-jet p_T measured by the CDF collaboration. Regions: Toward, Transverse and Away.	83
4.6	Summed- p_T density of charged particles as a function of the leading-jet p_T measured by the CDF collaboration. Regions: Toward, Transverse and Away.	83

4.7	Charged-particle density as a function of the leading-jet p_T measured by the CDF collaboration. Regions: TransMIN and TransMAX.	84
4.8	Summed- p_T density of charged particles as a function of the leading-jet p_T measured by the CDF collaboration. Regions: TransMIN and TransMAX.	84
4.9	Charged-particle density in the TransMIN and TransMAX regions measured with the STAR detector.	85
4.10	Charged-particle density in the Transverse region at $\sqrt{s} = 0.9$ TeV and $\sqrt{s} = 7$ TeV measured with the ATLAS detector.	87
4.11	Summed- p_T density in the Transverse region at $\sqrt{s} = 0.9$ TeV and $\sqrt{s} = 7$ TeV measured with the ATLAS detector.	87
4.12	Scaling of the UE distributions with the collision energy measured by the CMS collaboration.	88
4.13	Leading-jet spectrum from a selection of jet finders. Simulation from PYTHIA at $\sqrt{s} = 7$ TeV.	91
4.14	Number density and summed p_T for the Toward, Transverse and Away regions defined by different jet algorithms. PYTHIA at $\sqrt{s} = 7$ TeV.	92
4.15	Leading-jet spectrum for the anti- k_T algorithm with different settings and leading-charged-particle spectrum. PYTHIA at $\sqrt{s} = 7$ TeV.	95
4.16	Number density and summed p_T in the Transverse region defined by the anti- k_T algorithm with different settings or by the leading charged-particle. PYTHIA at $\sqrt{s} = 7$ TeV.	95
4.17	Leading-jet spectrum for the anti- k_T algorithm with different settings or leading-track distribution. ALICE data uncorrected at $\sqrt{s} = 7$ TeV.	96
4.18	Number density and summed p_T in the Transverse region defined by jets reconstructed with the anti- k_T algorithm with different settings or the leading track. ALICE data uncorrected at $\sqrt{s} = 7$ TeV.	96

LIST OF FIGURES

4.19	Leading-jet spectrum for the anti- k_T algorithm and leading charged-particle distribution. PYTHIA at $\sqrt{s} = 7$ TeV. Different processes are excluded from the simulation.	97
4.20	Number density and summed p_T in the Transverse region defined by the leading reconstructed jet. PYTHIA at $\sqrt{s} = 7$ TeV. Different processes are excluded from the simulation.	98
4.21	Number density and summed p_T in the Transverse region defined by the leading charged-particle. PYTHIA at $\sqrt{s} = 7$ TeV. Different processes are excluded from the simulation.	98
5.1	Definition of the regions Toward, Transverse and Away with respect to the leading-track direction.	102
5.2	Schematic representation of the analysis flow.	104
5.3	Fraction of diffractive events as a function of the leading-track p_T	113
5.4	Reference and high pile-up probability samples without and with pile-up rejection cuts.	114
5.5	Effect of pile-up rejection cuts on the reference and high pile-up probability samples.	114
5.6	Azimuthal correlation between reconstructed and generated leading track for different sets of track-cuts.	116
5.7	Contamination from secondaries: ratio between custom and standard track cuts.	118
5.8	Transverse momentum resolution for standard and customized track cuts.	119
5.9	Position resolution of primary tracks for standard and customized track cuts.	120
5.10	Schematic representation of the data correction procedure.	121
5.11	Azimuthal distance between real and reconstructed leading track. PYTHIA and GEANT at $\sqrt{s} = 7$ TeV.	123
5.12	Sketch of the data-driven estimate of the leading-track misidentification bias.	124
5.13	Leading-track misidentification bias for the number density in the Transverse region.	125
5.14	Monte Carlo driven contamination correction.	126

LIST OF FIGURES

5.15	Different contributions to secondary tracks yield.	127
5.16	Data-driven contamination correction-factors N and $N\alpha$	128
5.17	Estimation of the contamination correction factor N	129
5.18	Estimation of the contamination correction factor $N\alpha$	129
5.19	Final data-driven contamination correction.	130
5.20	Tracking efficiency as a function of track p_T and η	132
5.21	Vertex-reconstruction correction factor.	133
5.22	Multiplicity response matrix at $\sqrt{s} = 0.9$ TeV and $\sqrt{s} = 7$ TeV.	134
5.23	Efficiency and contamination corrections for different choices of particle composition.	137
5.24	Comparison between different methods to estimate the strangeness contamination correction.	138
6.1	Number density in the different topological regions for particle $p_T > 0.15$ GeV/ c	151
6.2	Number density in the different topological regions for particle $p_T > 0.5$ GeV/ c	152
6.3	Number density in the different topological regions for particle $p_T > 1.0$ GeV/ c	153
6.4	Summed p_T in the different topological regions for particle $p_T >$ 0.15 GeV/ c	154
6.5	Summed p_T in the different topological regions for particle $p_T >$ 0.5 GeV/ c	155
6.6	Summed p_T in the different topological regions for particle $p_T >$ 1.0 GeV/ c	156
6.7	Azimuthal correlation. Tracks: $p_T > 0.15$ GeV/ c . Leading-track: $0.5 < p_{T,LT} < 1.5$ GeV/ c	157
6.8	Azimuthal correlation. Tracks: $p_T > 0.15$ GeV/ c . Leading-track: $2.0 < p_{T,LT} < 4.0$ GeV/ c	157
6.9	Azimuthal correlation. Tracks: $p_T > 0.15$ GeV/ c . Leading-track: $4.0 < p_{T,LT} < 6.0$ GeV/ c	158
6.10	Azimuthal correlation. Tracks: $p_T > 0.15$ GeV/ c . Leading-track: $6.0 < p_{T,LT} < 10.0$ GeV/ c	158

LIST OF FIGURES

6.11	Azimuthal correlation. Tracks: $p_T > 0.5 \text{ GeV}/c$. Leading-track: $0.5 < p_{T,LT} < 1.5 \text{ GeV}/c$	159
6.12	Azimuthal correlation. Tracks: $p_T > 0.5 \text{ GeV}/c$. Leading-track: $2.0 < p_{T,LT} < 4.0 \text{ GeV}/c$	159
6.13	Azimuthal correlation. Tracks: $p_T > 0.5 \text{ GeV}/c$. Leading-track: $4.0 < p_{T,LT} < 6.0 \text{ GeV}/c$	160
6.14	Azimuthal correlation. Tracks: $p_T > 0.5 \text{ GeV}/c$. Leading-track: $6.0 < p_{T,LT} < 10.0 \text{ GeV}/c$	160
6.15	Azimuthal correlation. Tracks: $p_T > 1.0 \text{ GeV}/c$. Leading-track: $2.0 < p_{T,LT} < 4.0 \text{ GeV}/c$	161
6.16	Azimuthal correlation. Tracks: $p_T > 1.0 \text{ GeV}/c$. Leading-track: $4.0 < p_{T,LT} < 6.0 \text{ GeV}/c$	161
6.17	Azimuthal correlation. Tracks: $p_T > 1.0 \text{ GeV}/c$. Leading-track: $6.0 < p_{T,LT} < 10.0 \text{ GeV}/c$	162
6.18	Ratio between $\sqrt{s} = 0.9 \text{ TeV}$ and $\sqrt{s} = 7 \text{ TeV}$ for number density and summed p_T distributions in the Transverse region.	163
6.19	Energy scaling of number density in the plateau of the Transverse region compared to the minimum bias case.	165
A.1	Corrections on real data: number density in all topological regions at $\sqrt{s} = 0.9$ and 7 TeV	170
A.2	Corrections on real data: summed p_T in all topological regions at $\sqrt{s} = 0.9$ and 7 TeV	171
A.3	Corrections on real data: azimuthal correlation at $\sqrt{s} = 0.9$ and 7 TeV. Leading track: $0.5 < p_T < 1.5 \text{ GeV}/c$	172
A.4	Corrections on real data: azimuthal correlation at $\sqrt{s} = 0.9$ and 7 TeV. Leading track: $2.0 < p_T < 4.0 \text{ GeV}/c$	172
A.5	Corrections on real data: azimuthal correlation at $\sqrt{s} = 0.9$ and 7 TeV. Leading track: $4.0 < p_T < 6.0 \text{ GeV}/c$	173
A.6	Corrections on real data: azimuthal correlation at $\sqrt{s} = 0.9$ and 7 TeV. Leading track: $6.0 < p_T < 10.0 \text{ GeV}/c$	173
B.1	Ratio between ALICE and ATLAS results in comparable phase space ($ \eta < 0.8, p_T > 0.5 \text{ GeV}/c$). $\sqrt{s} = 0.9 \text{ TeV}$	176

LIST OF FIGURES

B.2	Ratio between ALICE and ATLAS results in comparable phase space ($ \eta < 0.8, p_T > 0.5 \text{ GeV}/c$). $\sqrt{s} = 7 \text{ TeV}$	177
B.3	Ratio between ALICE and ATLAS results in comparable phase space ($ \eta < 0.8, p_T > 1.0 \text{ GeV}/c$). $\sqrt{s} = 0.9 \text{ TeV}$	178
B.4	Ratio between ALICE and ATLAS results in comparable phase space ($ \eta < 0.8, p_T > 1.0 \text{ GeV}/c$). $\sqrt{s} = 7 \text{ TeV}$	179
B.5	Ratio between ALICE ($ \eta < 0.8$) and ATLAS ($ \eta < 2.5$) results. $p_T > 0.5 \text{ GeV}/c$. $\sqrt{s} = 0.9 \text{ TeV}$	180
B.6	Ratio between ALICE ($ \eta < 0.8$) and ATLAS ($ \eta < 2.5$) results. $p_T > 0.5 \text{ GeV}/c$. $\sqrt{s} = 7 \text{ TeV}$	181

LIST OF FIGURES

List of Tables

2.1	Synopsis of ITS characteristics.	41
2.2	Summary of detectors used in this thesis.	44
5.1	Summary of the analysis steps, corresponding to specific event and track selections.	105
5.2	Data samples considered and corresponding Monte Carlo anchor runs.	108
5.3	Events remaining after each event-selection step.	111
5.4	Percentage of diffractive events accepted by the analysis.	112
5.5	Main track-selection criteria.	115
5.6	Structure of the output container accommodating the corrected data.	122
5.7	Upper limit of each correction for all considered p_T thresholds and collision energies.	136
5.8	Variation of the most relevant track-cuts for the estimate of the systematic uncertainty.	139
5.9	Constant systematic uncertainties at both collision energies. . . .	143
5.10	Systematic uncertainties vs. leading track p_T at $\sqrt{s} = 0.9$ TeV. . .	144
5.11	Systematic uncertainties vs. leading track p_T at $\sqrt{s} = 7$ TeV. . . .	145
6.1	Saturation values in the Transverse region for $\sqrt{s} = 0.9$ and 7 TeV.	148
6.2	Constant fit to the ratio between $\sqrt{s} = 0.9$ TeV and $\sqrt{s} = 7$ TeV for number density and summed p_T distributions in the Transverse region.	164

LIST OF TABLES

Bibliography

- [1] **ALICE TRD Technical Design Report.** CERN/LHCC 2001-021 (October, 2001). Available from: <http://www-alice.gsi.de/trd/tdr/index.html>. 53, 54, 56, 62, 70
- [2] **An object-oriented data analysis framework.** <http://root.cern.ch>. 45
- [3] **ETM professional control GmbH.** <http://www.pvss.com/>. 66
- [4] **HEP Data: Measurement of underlying event characteristics using charged particles in pp collisions at $\sqrt{s} = 900\text{GeV}$ and 7 TeV with the ATLAS detector .** <http://hepdata.cedar.ac.uk/View/8894728>. 175
- [5] **LHC Physics Centre at CERN (LPCC): Minimum Bias and Underlying Event working group.** http://lpcc.web.cern.ch/LPCC/index.php?page=mb_ue_wg. 162
- [6] **The ALICE experiment offline project.** <http://aliweb.cern.ch/Offline/>. 45
- [7] **University of Heidelberg, Kirchhoff Institute for Physics.** <http://www.kip.uni-heidelberg.de/HLT/software/>. 64
- [8] **G. AAD ET AL. The ATLAS Experiment at the CERN Large Hadron Collider.** *JINST*, **3(08):S08003**, 2008. Available from: <http://stacks.iop.org/1748-0221/3/i=08/a=S08003>. 32, 34

BIBLIOGRAPHY

- [9] G. AAD ET AL. **Charged-particle multiplicities in pp interactions measured with the ATLAS detector at the LHC.** *New J.Phys.*, **13**:053033, 2011. Available from: <http://arxiv.org/abs/1012.5104>. 165
- [10] G. AAD ET AL. **Measurement of underlying event characteristics using charged particles in pp collisions at $\sqrt{s} = 900\text{GeV}$ and 7 TeV with the ATLAS detector.** *Phys. Rev. D*, **83**:112001, 2011. Available from: <http://128.84.158.119/abs/1012.0791v1>. 77, 86, 87, 163, 164, 175, 180
- [11] G. AAD ET AL. **Measurement of underlying event characteristics using charged particles in pp collisions at $\sqrt{s} = 900\text{ GeV}$ and 7 TeV with the ATLAS detector in a limited phase space.** *ATLAS-CONF-2011-009*, Feb 2011. Available from: <http://cdsweb.cern.ch/record/1330721/files/ATLAS-CONF-2011-009.pdf?subformat=6>. 77, 86, 162, 164, 175, 176, 177, 178, 179, 181
- [12] T. AALTONEN ET AL. **Measurement of the inclusive jet cross section at the Fermilab Tevatron $p\bar{p}$ collider using a cone-based jet algorithm.** *Phys. Rev. D*, **78**:052006, Sep 2008. Available from: <http://link.aps.org/doi/10.1103/PhysRevD.78.052006>. 81
- [13] T. AALTONEN ET AL. **Studying the underlying event in Drell-Yan and high transverse momentum jet production at the Tevatron.** *Phys. Rev. D*, **82**:034001, Aug 2010. Available from: <http://link.aps.org/doi/10.1103/PhysRevD.82.034001>. 81, 82, 83, 84
- [14] K. AAMODT ET AL. **Production of pions, kaons and protons in pp collisions at $\sqrt{s} = 7\text{ TeV}$ with ALICE at the LHC.** In preparation. 135
- [15] K. AAMODT ET AL. **The ALICE experiment at the CERN LHC.** *JINST*, **3**:S08002. Available from: <http://iopscience.iop.org/1748-0221/3/08/S08002>. 34, 37, 38, 41, 50, 53, 54, 55

- [16] K. AAMODT ET AL. **Underlying Event measurements in pp collisions at $\sqrt{s} = 0.9$ and 7 TeV with the ALICE experiment at the LHC.** To be published. 3, 147
- [17] K. AAMODT ET AL. **Alignment of the ALICE Inner Tracking System with cosmic-ray tracks.** *JINST*, **5**(03):P03003, 2010. Available from: <http://stacks.iop.org/1748-0221/5/i=03/a=P03003>. 40, 41, 139
- [18] K. AAMODT ET AL. **Charged-Particle Multiplicity Density at Midrapidity in Central Pb-Pb Collisions at $\sqrt{s_{NN}} = 2.76$ TeV.** *Phys. Rev. Lett.*, **105**:252301, Dec 2010. Available from: <http://link.aps.org/doi/10.1103/PhysRevLett.105.252301>. 34
- [19] K. AAMODT ET AL. **Charged-particle multiplicity measurement in protonproton collisions at $\sqrt{s} = 7$ TeV with ALICE at LHC.** *EPJC*, **68**:345–354, 2010. 10.1140/epjc/s10052-010-1350-2. Available from: <http://dx.doi.org/10.1140/epjc/s10052-010-1350-2>. 48
- [20] K. AAMODT ET AL. **Transverse momentum spectra of charged particles in proton-proton collisions at $\sqrt{s} = 900$ GeV with ALICE at the LHC.** *Phys. Lett.*, **B693**:53–68, 2010. 110, 117
- [21] K. AAMODT ET AL. **Production of pions, kaons and protons in pp collisions at $\sqrt{s} = 900$ GeV with ALICE at the LHC.** *Eur. Phys. J.*, **C71**:1655, 2011. Available from: <http://arxiv.org/abs/1101.4110>. 135, 136
- [22] K. AAMODT ET AL. **Strange particle production in proton-proton collisions at $\sqrt{s} = 0.9$ TeV with ALICE at the LHC.** *Eur.Phys.J.*, **C71**:1594, 2011. Available from: <http://arxiv.org/abs/1012.3257>. 127, 137, 138
- [23] V. M. ABAZOV ET AL. **Search for charged Higgs bosons in decays of top quarks.** *Phys. Rev. D*, **80**:051107, 2009. Available from: <http://arxiv.org/abs/0906.5326>. 19

BIBLIOGRAPHY

- [24] G. ABBIENDI ET AL. **QCD studies with e^+e^- annihilation data at 172 GeV - 189 GeV**. *EPJC*, **16**:185–210, 2000. Revised Feb 2000. Available from: <http://arxiv.org/abs/hep-ex/0002012>. 15
- [25] F. ABE ET AL. **Transverse-momentum distributions of charged particles produced in $p\bar{p}$ interactions at $\sqrt{s} = 630$ and 1800 GeV**. *Phys. Rev. Lett.*, **61**:1819–1822, Oct 1988. Available from: <http://link.aps.org/doi/10.1103/PhysRevLett.61.1819>. 15
- [26] F. ABE ET AL. **Double parton scattering in $p\bar{p}$ collisions at $\sqrt{s} = 1.8$ TeV**. *Phys. Rev. D*, **56**:3811–3832, 1997. Available from: http://prd.aps.org/abstract/PRD/v56/i7/p3811_1. 19
- [27] F. ABE ET AL. **Measurement of double parton scattering in $p\bar{p}$ collisions at $\sqrt{s} = 1.8$ TeV**. *Phys. Rev. Lett.*, **79**:584–589, 1997. Available from: http://prl.aps.org/abstract/PRL/v79/i4/p584_1. 19
- [28] K. ABE ET AL. **Production of π^+ , K^+ , K^0 , K^{*0} , ϕ , p and Λ^0 in hadronic Z^0 decays**. *Phys. Rev. D*, **59**:052001, 1999. Available from: <http://arxiv.org/abs/hep-ex/9805029>. 15
- [29] P. ABREU ET AL. **A measurement of α_s from the scaling violation in e^+e^- annihilation**. *Phys. Lett. B*, **398**:194–206, 1997. Available from: <http://www.sciencedirect.com/science/article/pii/S0370269397002566>. 15
- [30] P. ABREU ET AL. **$\pi^{+/-}$, $K^{+/-}$ and p/\bar{p} production in $Z^0 \rightarrow q\bar{q}$, $Z^0 \rightarrow b\bar{b}$, $Z^0 \rightarrow u\bar{u}$, $d\bar{d}$, $s\bar{s}$** . *EPJC*, **5**:585–620, 1998. Available from: <http://www.springerlink.com/content/58165eyptvw6vemf/>. 15
- [31] P. ABREU ET AL. **Energy dependence of inclusive spectra in e^+e^- annihilation**. *Phys. Lett. B*, **459**:397–411, 1999. Available from: <http://www.sciencedirect.com/science/article/pii/S0370269399006012>. 15
- [32] K. ACKERSTAFF ET AL. **Inclusive production of charged hadrons and K_S^0 mesons in photon photon collisions**. *EPJC*, **6**:253–264, 1999. Available from: <http://www.springerlink.com/content/dc3v41v5834gyy0c/>. 15

- [33] K. ACKERSTAFF ET AL. **Measurements of Flavour Dependent Fragmentation Functions in $Z^0 \rightarrow q\bar{q}$ Events.** *EPJC*, **7**:369, 1999. Available from: <http://arxiv.org/abs/hep-ex/9807004>. 15
- [34] D. ACOSTA ET AL. **Momentum distribution of charged particles in jets in dijet events in p anti-p collisions at $\sqrt{s} = 1.8$ TeV and comparisons to perturbative QCD predictions.** *Phys. Rev.*, **D68**:012003, 2003. Available from: <http://prd.aps.org/abstract/PRD/v68/i1/e012003>. 148
- [35] D. ACOSTA ET AL. **The Underlying event in hard interactions at the Tevatron $p\bar{p}$ collider.** *Phys. Rev. D*, **70**:072002, 2004. Available from: <http://arxiv.org/abs/hep-ex/0404004>. 19
- [36] D. ACOSTA ET AL. **Underlying event in hard interactions at the Fermilab Tevatron $\bar{p}p$ collider.** *Phys. Rev. D*, **70**:072002, Oct 2004. Available from: <http://link.aps.org/doi/10.1103/PhysRevD.70.072002>. 81
- [37] C. ADLOFF ET AL. **Charged particle cross-sections in photoproduction and extraction of the gluon density in the photon.** *EPJC*, **10**:363–372, 1999. Available from: <http://arxiv.org/abs/hep-ex/9810020>. 15
- [38] C. ADLOFF ET AL. **Deep inelastic inclusive ep scattering at low x and a determination of α_s .** *EPJC*, **21**:33–61, 2001. Available from: <http://arxiv.org/abs/hep-ex/0012053>. 13
- [39] C. ADLOFF ET AL. **Measurement and QCD analysis of neutral and charged current cross sections at HERA.** *EPJC*, **30**:1–32, 2003. Available from: <http://arxiv.org/abs/hep-ex/0304003>. 13
- [40] T. AFFOLDER ET AL. **Charged jet evolution and the underlying event in proton-antiproton collisions at 1.8 TeV.** *Phys. Rev. D*, **65**:092002, Apr 2002. Available from: <http://link.aps.org/doi/10.1103/PhysRevD.65.092002>. 81, 99, 164, 165

BIBLIOGRAPHY

- [41] H. AIHARA ET AL. **Charged hadron inclusive cross-sections and fractions in e^+e^- annihilation $\sqrt{s} = 29$ GeV.** *Phys. Rev. Lett.*, **61**:1263, 1988. Available from: http://prl.aps.org/abstract/PRL/v61/i11/p1263_1. 15
- [42] T. AKESSON ET AL. **Double parton scattering in pp collisions at $\sqrt{s} = 63$ GeV.** *Z. Phys. C*, **34**(CERN-EP-86-216):163–174. 22 p, Dec 1986. Available from: <http://cdsweb.cern.ch/record/173908>. 19
- [43] M.Z. AKRAWY ET AL. **A study of jet production rates and a test of QCD on the Z^0 resonance.** *Phys. Lett. B*, **235**(3-4):389 – 398, 1990. Available from: <http://www.sciencedirect.com/science/article/pii/037026939091983I>. 16
- [44] C. ALBAJAR ET AL. **Production of low transverse energy clusters in pp collisions at $s=0.20.9$ TeV and their interpretation in terms of QCD jets.** *Nuclear Physics B*, **309**(3):405 – 425, 1988. Available from: <http://www.sciencedirect.com/science/article/pii/0550321388904506>. 80
- [45] H. ALBRECHT ET AL. **Inclusive production of charged pions, charged and neutral kaons and anti-protons in e^+e^- annihilation at 10 GeV and in direct Upsilon decays.** *Z. Phys. C*, **44**:547–555, 1989. 10.1007/BF01549077. Available from: <http://dx.doi.org/10.1007/BF01549077>. 15
- [46] S. ALEKHIN. **Parton distribution functions from the precise NNLO QCD fit.** *JETP Lett.*, **82**:628–631, 2005. Available from: <http://arxiv.org/abs/hep-ph/0508248>. 13
- [47] D. V. ALEKSANDROV ET AL. **A high resolution electromagnetic calorimeter based on lead-tungstate crystals.** *Nucl. Instrum. Meth. A*, **550**(1-2):169 – 184, 2005. Available from: <http://www.sciencedirect.com/science/article/pii/S0168900205012465>. 36

- [48] G. ALTARELLI AND G. PARISI. **Asymptotic Freedom in Parton Language**. *Nucl. Phys. B*, **126**:298, 1977. Available from: <http://www.sciencedirect.com/science/article/pii/0550321377903844>. 12
- [49] B. ANDERSSON, G. GUSTAFSON, G. INGELMAN, AND T. SJOSTRAND. **Parton fragmentation and string dynamics**. *Phys. Rep.*, **97**:31–145, July 1983. Available from: <http://www.sciencedirect.com/science/article/pii/0370157383900807>. 15
- [50] A. ANDRONIC. **Electron identification performance with ALICE TRD prototypes**. *Nucl. Instrum. Meth. A*, **522**(1-2):40 – 44, 2004. TRDs for the Third Millenium. Proceedings of the 2nd Workshop on Advanced Transition Radiation Detectors for Accelerator and Space Applications. Available from: <http://www.sciencedirect.com/science/article/pii/S0168900204000828>. 53
- [51] ANGELOV, V. Private communication. 70, 72
- [52] G. ARNISON ET AL. **Hadronic Jet Production at the CERN Proton - anti-Proton Collider**. *Phys. Lett.*, **B132**:214, 1983. Available from: <http://www.sciencedirect.com/science/article/pii/037026938390254X>. 80, 89, 91
- [53] A. AUGUSTO ALVES JR. ET AL. **The LHCb Detector at the LHC**. *JINST*, **3**(08):S08005, 2008. Available from: <http://stacks.iop.org/1748-0221/3/i=08/a=S08005>. 32
- [54] M. BAHR, S. GIESEKE, AND M. H. SEYMOUR. **Simulation of multiple partonic interactions in Herwig++**. *JHEP*, **07**:076, 2008. Available from: <http://arxiv.org/abs/0803.3633>. 19
- [55] M. BALLINTIJN, R. BRUN, F. RADEMAKERS, AND G. ROLAND. **The PROOF Distributed Parallel Analysis Framework based on ROOT**. 2003. Available from: <http://arxiv.org/abs/physics/0306110>. 45

BIBLIOGRAPHY

- [56] M. BANNER ET AL. **Inclusive particle production in the transverse momentum range between 0.25 GeV/c and 40 GeV/c at the CERN $S\bar{p}\bar{p}S$ collider.** *Z. Phys. C*, **27**:329, 1985. 15
- [57] FOR THE ALICE EMCAL COLLABORATION BELLWIED, R. **ALICE EMCAL Physics Performance Report.** *ArXiv e-prints*, August 2010. Available from: <http://arxiv.org/abs/1008.0413>. 36
- [58] H.U. BENGTSSON AND T. SJOSTRAND. **The Lund Monte Carlo for hadronic processes - PYTHIA version 4.8.** *Comput. Phys. Commun.*, **46**:43–82, July 1987. Available from: <http://www.sciencedirect.com/science/article/pii/0010465587900361>. 23
- [59] P. BILLOIR. **Track fitting with multiple scattering: a new method.** *Nucl. Instrum. Meth. A*, **225**:352–366, 1984. Available from: http://ccdb4fs.kek.jp/cgi-bin/img_index?8309049. 46, 49
- [60] P. BILLOIR. **Progressive track recognition with a Kalman like fitting procedure.** *Comput. Phys. Commun.*, **57**:390–394, 1989. Available from: <http://www.sciencedirect.com/science/article/pii/001046558990249X>. 46, 49
- [61] P. BILLOIR, R. FRUHWIRTH, AND M. REGLER. **Track element merging strategy and vertex fitting in complex modular detectors.** *Nucl. Instrum. Meth. A*, **241**:115–131, 1985. Available from: <http://www.sciencedirect.com/science/article/pii/0168900285905236>. 46, 49
- [62] J. D. BJORKEN AND EMMANUEL A. PASCHOS. **Inelastic Electron Proton and Gamma Proton Scattering and the Structure of the Nucleon.** *Phys. Rev.*, **185**:1975–1982, 1969. Available from: http://prola.aps.org/abstract/PR/v185/i5/p1975_1. 5
- [63] F. BOCK. **ALICE Capabilities for Studying Photon Physics with the Conversion Method at LHC Energies.** Bachelor Thesis (University of Heidelberg, 2010). 142

- [64] G. BOCQUET ET AL. **Transverse momentum spectra of charged particles in $p\bar{p}$ collisions at $\sqrt{s} = 630$ -GeV.** *Phys. Lett. B*, **366**:434–440, 1996. Available from: <http://www.sciencedirect.com/science/article/pii/0370269395014357>. 15
- [65] R. BRANDELIK ET AL. **Charged pion, kaon and nucleon production by e^+e^- annihilation for c.m. energies between 3.6 and 5.2 GeV.** *Nucl. Phys. B*, **148**(3-4):189 – 227, 1979. Available from: <http://www.sciencedirect.com/science/article/pii/0550321379901342>. 15
- [66] P. BRAUN-MUNZINGER AND J. STACHEL. **The quest for the quark gluon plasma.** *Nature*, **448**:302–309, 2007. Available from: <http://www.nature.com/nature/journal/v448/n7151/full/nature06080.html>. 34
- [67] W. BRAUNSCHWEIG ET AL. **Pion, kaon and proton cross-sections in e^+e^- annihilation at 34 GeV and 44 GeV center-of-mass energy.** *Z. Phys. C*, **42**:189, 1989. Available from: <http://www.springerlink.com/content/g426u71147x38863/>. 15
- [68] R. BRUN, F. BRUYANT, M. MAIRE, A. C. MCPHERSON, AND P. ZANARINI. **GEANT3.** CERN-DD-EE-84-1. Available from: <http://cdsweb.cern.ch/record/1119728/files/CERN-DD-EE-84-1.pdf>. 46
- [69] D. BUSKULIC ET AL. **Inclusive $\pi^{+/-}$, $K^{+/-}$ and p/\bar{p} differential cross-sections at the Z resonance.** *Z. Phys. C*, **66**:355–366, 1995. Available from: <http://www.springerlink.com/content/u062552j33v46m85/>. 15
- [70] D. BUSKULIC ET AL. **Measurement of α_s from scaling violations in fragmentation functions in e^+e^- annihilation.** *Phys. Lett. B*, **357**:487–499, 1995. Available from: <http://www.sciencedirect.com/science/article/pii/037026939500917A>. 15
- [71] M. CACCIARI AND G. P. SALAM. **Dispelling the N^3 myth for the k_t jet-finder.** *Phys.Lett.*, **B641**:57–61, 2006. Available from: <http://arxiv.org/abs/hep-ph/0512210>. 89

BIBLIOGRAPHY

- [72] M. CACCIARI, G. P. SALAM, AND G. SOYEZ. **The anti- k_T jet clustering algorithm.** *JHEP*, **2008**(04):063, 2008. Available from: <http://stacks.iop.org/1126-6708/2008/i=04/a=063>. 11, 89
- [73] H. CAINES. **Underlying Event Studies at RHIC.** To be published in the proceedings of DPF-2009, Detroit, MI, July 2009, eConf C090726. Available from: <http://arxiv.org/abs/0910.5203>. 82, 85, 86
- [74] G. CALUCCI AND D. TRELEANI. **Inclusive and exclusive cross sections in the regime of multiple parton collisions.** *Phys. Rev. D*, **79**:034002, 2009. Available from: <http://arxiv.org/abs/0809.4217>. 19
- [75] G. CALUCCI AND D. TRELEANI. **Incoherence and Multiple Parton Interactions.** *Phys. Rev. D*, **80**:054025, 2009. Available from: <http://arxiv.org/abs/0907.4772>. 19
- [76] J. M. CAMPBELL, J.W. HUSTON, AND W.J. STIRLING. **Hard Interactions of Quarks and Gluons: A Primer for LHC Physics.** *Rept. Prog. Phys.*, **70**:89, 2007. Available from: <http://arxiv.org/abs/hep-ph/0611148>. 6, 13
- [77] A. CAPELLA, U. SUKHATME, C.-I. TAN, AND J. TRAN THANH VAN. **Dual parton model.** *Phys. Rep.*, **236**:225–329, January 1994. Available from: <http://www.sciencedirect.com/science/article/pii/0370157394900647>. 21
- [78] S. CATANI, F. KRAUSS, R. KUHN, AND B.R. WEBBER. **QCD matrix elements + parton showers.** *JHEP*, **0111**:063, 2001. Available from: <http://arxiv.org/abs/hep-ph/0109231>. 13
- [79] S. CHATRCHYAN ET AL. **The CMS experiment at the CERN LHC.** *JINST*, **3**(08):S08004, 2008. Available from: <http://stacks.iop.org/1748-0221/3/i=08/a=S08004>. 32, 34
- [80] S. CHATRCHYAN ET AL. **Measurement of the Inclusive Jet Cross Section in pp Collisions at $\sqrt{s} = 7$ TeV.** *Phys. Rev. Lett.*,

- 107:132001, Sep 2011. Available from: <http://link.aps.org/doi/10.1103/PhysRevLett.107.132001>. 11
- [81] S. CHATRCHYAN ET AL. **Measurement of the Underlying Event Activity at the LHC with $\sqrt{s}=7$ TeV and Comparison with $\sqrt{s}=0.9$ TeV.** 2011. CERN-PH-EP-2011-059. Available from: <http://arxiv.org/abs/1107.0330>. 77, 86, 88, 164
- [82] S. CHEKANOV ET AL. **A ZEUS next-to-leading-order QCD analysis of data on deep inelastic scattering.** *Phys. Rev. D*, **67**:012007, 2003. Available from: <http://arxiv.org/abs/hep-ex/0208023>. 13
- [83] S. CHEKANOV ET AL. **An NLO QCD analysis of inclusive cross-section and jet-production data from the zeus experiment.** *EPJC*, **42**:1–16, 2005. Available from: <http://arxiv.org/abs/hep-ph/0503274>. 13
- [84] M. L. CHERRY, G. HARTMANN, D. MÜLLER, AND T. A. PRINCE. **Transition radiation from relativistic electrons in periodic radiators.** *Phys. Rev. D*, **10**:3594–3607, Dec 1974. Available from: <http://link.aps.org/doi/10.1103/PhysRevD.10.3594>. 53
- [85] ALICE COLLABORATION, B. ALESSANDRO, ET AL. **ALICE: Physics Performance Report, Volume II.** *Journal of Physics G: Nuclear and Particle Physics*, **32**(10):1295, 2006. Available from: <http://stacks.iop.org/0954-3899/32/i=10/a=001>. 110
- [86] P.D.B. COLLINS. **An Introduction to Regge Theory and High-Energy Physics.** Cambridge Monographs on Mathematical Physics: 4 (Cambridge University Press, 1977). ISBN: 9780521212458. 22
- [87] R. CORKE. **Multiple Interactions in Pythia 8.** pages 249–259, 2009. Proceedings of the 1st International Workshop on Multiple Partonic Interactions at the LHC, Perugia, Italy (DESY-PROC-2009-06). Available from: <http://arxiv.org/abs/0901.2852>. 12, 15, 21, 27

BIBLIOGRAPHY

- [88] A. CRUZ. **Using Max/Min Transverse Regions to Study the Underlying Event in Proton-Antiproton Collisions at 1.97 TeV**. Doctoral thesis (University of Florida, 2005). 86
- [89] DAINESE, A. Private communication. 139
- [90] D'ENTERRIA, D. Private communication. 14
- [91] M. DERRICK ET AL. **Inclusive transverse momentum distributions of charged particles in diffractive and non-diffractive photoproduction at HERA**. *Z. Phys. C*, **67**:227–238, 1995. Available from: <http://arxiv.org/abs/hep-ex/9503014>. 15
- [92] Y. L. DOKSHITZER. **Calculation of the Structure Functions for Deep Inelastic Scattering and e^+e^- Annihilation by Perturbation Theory in Quantum Chromodynamics**. *Sov. Phys. JETP*, **46**:641–653, 1977. [*Zh.Eksp.Teor.Fiz.*73:1216-1240,1977]. 12
- [93] R. KEITH ELLIS, W. JAMES STIRLING, AND B. R. WEBBER. **QCD and collider physics**. Cambridge Monographs on Particle Physics, Nuclear Physics and Cosmology: 8 (Cambridge University Press, 1996). ISBN: 9780521545891. 6, 7, 9
- [94] R. ENGEL. **Soft interactions**. Proceedings of the XXXI International Symposium on Multiparticle Dynamics: Datong, China (World Scientific, 2011). ISBN: 9789810248444. Available from: <http://www.slac.stanford.edu/econf/C010901/proceedings.html>. 21, 22
- [95] R. ENGEL. **Photoproduction within the two-component Dual Parton Model: Amplitudes and cross sections**. *Z. Phys. C*, **66**:203–214, 1995. 10.1007/BF01496594. Available from: <http://dx.doi.org/10.1007/BF01496594>. 15, 21
- [96] R. ENGEL AND J. RANFT. **Hadronic photon-photon interactions at high-energies**. *Phys. Rev. D*, **54**:4244–4262, 1996. Available from: <http://arxiv.org/abs/hep-ph/9509373>. 15, 21

- [97] L. EVANS AND P. BRYANT. **LHC Machine**. *JINST*, **3**(08):S08001, 2008. Available from: <http://stacks.iop.org/1748-0221/3/i=08/a=S08001>. 31, 33, 61
- [98] R. P. FEYNMAN. **The behavior of hadron collisions at extreme energies**. High Energy Collisions, Proceedings of the Third Topical Conference on High Energy Collisions of Hadrons, Stony Brook, N. Y. (Gordon and Breach, 1969). 5
- [99] R. FIELD. **Min-bias and the underlying event in Run 2 at CDF**. *Acta Phys.Polon.*, **B36**:167–178, 2005. Available from: <http://th-www.if.uj.edu.pl/acta/vol36/abs/v36p0167.htm>. 81, 82
- [100] FIELD, R. Private communication. 163
- [101] M. FROISSART. **Asymptotic Behavior and Subtractions in the Mandelstam Representation**. *Phys. Rev.*, **123**:1053–1057, Aug 1961. Available from: <http://link.aps.org/doi/10.1103/PhysRev.123.1053>. 23
- [102] R. FRUHWIRTH. **Application of Kalman filtering to track and vertex fitting**. *Nucl. Instrum. Meth. A*, **262**:444–450, 1987. Available from: <http://www.sciencedirect.com/science/article/pii/0168900287908874>. 46, 49
- [103] C. GARABATOS. **The ALICE TPC**. *Nucl. Instrum. Meth. A*, **535**:197–200, 2004. Available from: <http://www.sciencedirect.com/science/article/pii/S0168900204016018>. 39
- [104] V. N. GRIBOV AND L. N. LIPATOV. **Deep inelastic ep scattering in perturbation theory**. *Sov. J. Nucl. Phys.*, **15**:438–450, 1972. [Yad.Fiz.15:781-807,1972]. Available from: <http://www.sciencedirect.com/science/article/pii/0370269371905764>. 12
- [105] J. F. GROSSE-OETRINGHAUS. **Measurements of Charged Particle Multiplicity in Proton-Proton Collisions with the ALICE Detector**. Doctoral thesis (University of Muenster,

BIBLIOGRAPHY

- 2009). Available from: <http://cdsweb.cern.ch/record/1175646/files/CERN-THESIS-2009-033.pdf>. 109, 115, 118
- [106] M. GUTFLEISCH. **Local signal processing of the ALICE Transition Radiation Detector at LHC (CERN)**. Doctoral thesis (University of Heidelberg, 2006). Available from: <http://www.kip.uni-heidelberg.de/Veroeffentlichungen/?showgroup=F12>. 74
- [107] J. D. JACKSON. **Classical Electrodynamics**. Hamilton Printing Company, 1999. ISBN: 047130932X. 22
- [108] V. KHACHATRYAN ET AL. **First Measurement of the Underlying Event Activity at the LHC with $\sqrt{s} = 0.9$ TeV**. *Eur. Phys. J., C70*:555–572, 2010. 77
- [109] T. KLUGE, K. RABBERTZ, AND M. WOBISCH. **FastNLO: Fast pQCD calculations for PDF fits**. pages 483–486, 2006. Available from: <http://arxiv.org/abs/hep-ph/0609285>. 11
- [110] B. A. KNIEHL, G. KRAMER, AND B. POTTER. **Testing the universality of fragmentation functions**. *Nucl. Phys. B*, **597**:337–369, 2001. Available from: <http://arxiv.org/abs/hep-ph/0011155>. 15
- [111] B.A. KNIEHL, G. KRAMER, AND B. POTTER. **Fragmentation functions for pions, kaons, and protons at next-to-leading order**. *Nucl. Phys. B*, **582**(1-3):514 – 536, 2000. Available from: <http://www.sciencedirect.com/science/article/pii/S0550321300003035>. 15
- [112] KRAUSS, F. Private communication. 17
- [113] H. L. LAI, M. GUZZI, J. HUSTON, Z. LI, P. M. NADOLSKY, J. PUMPLIN, AND C. P. YUAN. **New parton distributions for collider physics**. *Phys. Rev. D*, **82**:074024, Oct 2010. Available from: <http://link.aps.org/doi/10.1103/PhysRevD.82.074024>. 11
- [114] H. L. LAI, J. HUSTON, S. KUHLMANN, J. MORFIN, F. OLNES, J. F. OWENS, J. PUMPLIN, AND W. K. TUNG. **Global QCD analysis**

- of parton structure of the nucleon: CTEQ5 parton distributions. *EPJC*, **12**:375–392, 2000. Available from: <http://arxiv.org/abs/hep-ph/9903282>. 28
- [115] V. LINDENSTRUTH ET AL. **Final version of the tracklet processor chip (TRAP) for the ALICE TRD.** *GSI Sci. Rep.*, **353**, 2004. Available from: <http://www.gsi.de/informationen/wti/library/scientificreport2004/PAPERS/INSTMETH-25.pdf>. 57
- [116] L. N. LIPATOV. **The parton model and perturbation theory.** *Sov. J. Nucl. Phys.*, **20**:94–102, 1975. 12
- [117] M. L. MANGANO AND S. J. PARKE. **Multiparton amplitudes in gauge theories.** *Phys. Rept.*, **200**:301–367, 1991. Available from: <http://arxiv.org/abs/hep-th/0509223>. 10
- [118] G. MARCHESINI AND B. R. WEBBER. **Associated transverse energy in hadronic jet production.** *Phys. Rev. D*, **38**:3419–3426, Dec 1988. Available from: <http://link.aps.org/doi/10.1103/PhysRevD.38.3419>. 77, 78, 79, 80
- [119] G. MARCHESINI AND B. R. WEBBER. **Monte Carlo Simulation of General Hard Processes with Coherent QCD Radiation.** *Nucl. Phys.*, **B310**:461, 1988. Available from: <http://www.sciencedirect.com/science/article/pii/0550321388900892>. 82
- [120] A. D. MARTIN, R. G. ROBERTS, W. J. STIRLING, AND R. S. THORNE. **Physical gluons and high E_T jets.** *Phys. Lett. B*, **604**:61–68, 2004. Available from: <http://arxiv.org/abs/hep-ph/0410230>. 13
- [121] J. MERCADO. **Development of the control system of the ALICE Transition Radiation Detector and of a test environment for quality-assurance of its front-end electronics.** Doctoral thesis (University of Heidelberg, 2008). Available from: <http://www.phys.uni-heidelberg.de/Publications/>. 54, 61, 63, 64, 65

BIBLIOGRAPHY

- [122] A. MORSCH AND B. PASTIRCAK. **Radiation in ALICE detectors and electronics racks**. Technical Report ALICE Internal Note ALICE-INT-2002-028, CERN, Geneva, 2002. Available from: <https://edms.cern.ch/file/358706/1>. 42
- [123] N. PAVER AND D. TRELEANI. **Multiple parton interactions and multi-jet events at collider and Tevatron energies**. *Phys. Let. B*, **146**(3-4):252 – 256, 1984. Available from: <http://www.sciencedirect.com/science/article/pii/0370269384910293>. 27
- [124] I. RUSANOV AND J. STACHEL. **The new prototype of the ALICE TRD Readout Board**. *GSI Sci. Rep.*, **354**, 2004. Available from: <http://www.gsi.de/informationen/wti/library/scientificreport2004/PAPERS/INSTMETH-26.pdf>. 59
- [125] P. SAIZ, L. APHECETCHE, P. BUNI, R. PISKA, J.-E. REVSBECH, AND V. EGO. **AliEn-ALICE environment on the GRID**. *Nucl. Instrum. Meth. A*, **502**(2-3):437 – 440, 2003. Proceedings of the VIII International Workshop on Advanced Computing and Analysis Techniques in Physics Research. Available from: <http://www.sciencedirect.com/science/article/pii/S0168900203004625>. 45
- [126] G. P. SALAM AND G. SOYEZ. **A practical Seedless Infrared-Safe Cone jet algorithm**. *JHEP*, **05**:086, 2007. Available from: <http://arxiv.org/abs/0704.0292>. 85, 89, 90
- [127] P. SIGMUND. **Particle Radiation and Radiation Effects**. Springer Series in Solid State Sciences: 151 (Springer-Verlag, 2006). ISBN: 3-540-31713-9. 35
- [128] T. SJOSTRAND. **Jet fragmentation of multiparton configurations in a string framework**. *Nucl. Phys. B*, **248**(2):469 – 502, 1984. Available from: <http://www.sciencedirect.com/science/article/pii/0550321384906072>. 15

- [129] T. SJOSTRAND, P. EDN, C. FRIBERG, L. LONNBLAD, G. MIU, S. MRENNNA, AND E. NORRBIN. **High-energy-physics event generation with Pythia 6.1.** *Comput. Phys. Commun.*, **135**(2):238 – 259, 2001. Available from: <http://www.sciencedirect.com/science/article/pii/S0010465500002368>. 12
- [130] T. SJOSTRAND, S. MRENNNA, AND P. Z. SKANDS. **PYTHIA 6.4 Physics and Manual.** *JHEP*, **0605**:026, 2006. Available from: <http://arxiv.org/abs/hep-ph/0603175>. 12, 15, 19, 21, 23
- [131] T. SJOSTRAND, S. MRENNNA, AND P. Z. SKANDS. **A Brief Introduction to PYTHIA 8.1.** *Comput. Phys. Commun.*, **178**:852–867, 2008. Available from: <http://arxiv.org/abs/0710.3820>. 12, 15, 21, 27, 29
- [132] T. SJOSTRAND AND P. Z. SKANDS. **Multiple interactions and the structure of beam remnants.** *JHEP*, **03**:053, 2004. Available from: <http://arxiv.org/abs/hep-ph/0402078>. 19, 20, 21, 25
- [133] T. SJOSTRAND AND M. VAN ZIJL. **A multiple-interaction model for the event structure in hadron collisions.** *Phys. Rev. D*, **36**:2019–2041, Oct 1987. Available from: <http://link.aps.org/doi/10.1103/PhysRevD.36.2019>. 19
- [134] P. Z. SKANDS. **The Perugia Tunes.** 2009. Proceedings of the 1st International Workshop on Multiple Partonic Interactions at the LHC, Perugia, Italy (DESY-PROC-2009-06). Available from: <http://arxiv.org/abs/0905.3418>. 28, 29
- [135] H. K. SOLTVEIT ET AL. **Final version of the analog front-end electronics for the ALICE TPC-detector and ALICE TRD-detector.** *GSI Sci. Rep.*, **244**, 2003. Available from: <http://www.gsi.de/informationen/wti/library/scientificreport2003/files/213.pdf>. 57, 58
- [136] D. STUMP ET AL. **Inclusive jet production, parton distributions, and the search for new physics.** *JHEP*, **10**:046, 2003. Available from: <http://arxiv.org/abs/hep-ph/0303013>. 13

- [137] B. R. WEBBER. **A QCD Model for Jet Fragmentation Including Soft Gluon Interference.** *Nucl. Phys. B*, **238**:492, 1984. Available from: <http://www.sciencedirect.com/science/article/pii/055032138490333X>. 15
- [138] J. WIECHULA, P. BRAUN-MUNZINGER, H. DAUES, U. FRANKENFELD, C. GARABATOS, ET AL. **High-precision measurement of the electron drift velocity in NeCO₂.** *Nucl. Instrum. Meth. A*, **548**:582–589, 2005. Available from: <http://www.sciencedirect.com/science/article/pii/S0168900205011289>. 39

Acknowledgements

I would like to thank Prof. Dr. Johanna Stachel for giving me the opportunity to join her group and to participate in the exciting task of analysing the very first LHC data. The work described in this thesis would not have been possible without the valuable help of many people along the way. In particular I would like to acknowledge: Jan Fiete Grosse-Oetringhaus, Christian Klein-Boesing, Andreas Morsch, Klaus Reygers and Oliver Busch.